



**NAVAL
POSTGRADUATE
SCHOOL**

MONTEREY, CALIFORNIA

DISSERTATION

**DETERMINING SNOW DEPTH USING AIRBORNE
MULTI-PASS INTERFEROMETRIC SYNTHETIC
APERTURE RADAR**

by

Jack R. Evans

September 2013

Dissertation Supervisor:

Fred A. Kruse

Approved for public release: distribution is unlimited

THIS PAGE INTENTIONALLY LEFT BLANK

REPORT DOCUMENTATION PAGE
Form Approved OMB No. 0704-0188

Public reporting burden for this collection of information is estimated to average 1 hour per response, including the time for reviewing instruction, searching existing data sources, gathering and maintaining the data needed, and completing and reviewing the collection of information. Send comments regarding this burden estimate or any other aspect of this collection of information, including suggestions for reducing this burden, to Washington Headquarters Services, Directorate for Information Operations and Reports, 1215 Jefferson Davis Highway, Suite 1204, Arlington, VA 22202-4302, and to the Office of Management and Budget, Paperwork Reduction Project (0704-0188) Washington DC 20503.

1. AGENCY USE ONLY (Leave blank)	2. REPORT DATE September 2013	3. REPORT TYPE AND DATES COVERED Dissertation	
4. TITLE AND SUBTITLE DETERMINING SNOW DEPTH USING AIRBORNE MULTI-PASS INTERFEROMETRIC SYNTHETIC APERTURE RADAR		5. FUNDING NUMBERS	
6. AUTHOR(S) Jack R. Evans			
7. PERFORMING ORGANIZATION NAME(S) AND ADDRESS(ES) Naval Postgraduate School Monterey, CA 93943-5000		8. PERFORMING ORGANIZATION REPORT NUMBER	
9. SPONSORING /MONITORING AGENCY NAME(S) AND ADDRESS(ES) N/A		10. SPONSORING/MONITORING AGENCY REPORT NUMBER	
11. SUPPLEMENTARY NOTES The views expressed in this thesis are those of the author and do not reflect the official policy or position of the Department of Defense or the U.S. government. IRB protocol number ____N/A____.			
12a. DISTRIBUTION / AVAILABILITY STATEMENT Approved for public release: distribution is unlimited		12b. DISTRIBUTION CODE A	
13. ABSTRACT (maximum 200 words) Snow accumulation is a significant factor for hydrological planning, flood prediction, trafficability, avalanche control, and numerical weather/climatological modeling. Current snow depth methods fall short of requirements. This research explores a new approach for determining snow depth using airborne interferometric synthetic aperture radar (InSAR). Digital elevation models (DEM) are produced for Snow Off and Snow On cases and differenced to determine elevation change from accumulated snow. Interferograms are produced using Multi-pass Single Look Complex airborne Ku-band SAR. Two approaches were attempted. The first is a classical method similar to spaceborne InSAR and relies on determining the baseline of the interferometric pair. The second used a perturbation method that isolates and compares high frequency terrain phase to elevation to generate a DEM. Manual snow depth measurements were taken to verify the results. The first method failed to obtain a valid baseline and therefore failed. The second method resulted in representative DEMs and average snow depth errors of -8cm, 95cm, -49cm, 176cm, 87cm, and 42cm for six SAR pairs respectively. Furthermore, Ku-band appeared to be a high enough frequency to avoid significant penetration of the snow. Results show that this technique has promise but still requires more research to refine its accuracy.			
14. SUBJECT TERMS Airborne SAR, digital elevation model, interferometric, InSAR, remote sensing, synthetic aperture radar, snow depth, Mammoth Mountain, snow volume		15. NUMBER OF PAGES 221	
16. PRICE CODE			
17. SECURITY CLASSIFICATION OF REPORT Unclassified	18. SECURITY CLASSIFICATION OF THIS PAGE Unclassified	19. SECURITY CLASSIFICATION OF ABSTRACT Unclassified	20. LIMITATION OF ABSTRACT UU

THIS PAGE INTENTIONALLY LEFT BLANK

Approved for public release: distribution is unlimited

**DETERMINING SNOW DEPTH USING AIRBORNE MULTI-PASS
INTERFEROMETRIC SYNTHETIC APERTURE RADAR**

Jack R. Evans
Lieutenant Colonel, United States Air Force
B.S., Texas A&M University, 1998
M.S., Naval Postgraduate School, 2007

Submitted in partial fulfillment of the
requirements for the degree of

DOCTOR OF PHILOSOPHY IN METEOROLOGY

from the

NAVAL POSTGRADUATE SCHOOL
September 2013

Author: _____
Jack R. Evans

Approved by:

Fred A. Kruse Research Professor of Physics Dissertation Supervisor	Wendell Nuss Professor of Meteorology Dissertation Committee Chair
Philip Durkee Professor of Meteorology Dean of GSEAS	Peter Guest Research Professor of Meteorology
<hr/>	
Qing Wang Professor of Meteorology	

Approved by: _____
Wendell Nuss, Chair, Department of Meteorology

Approved by: _____
Douglas Moses, Vice Provost for Academic Affairs

THIS PAGE INTENTIONALLY LEFT BLANK

ABSTRACT

Snow accumulation is a significant factor for hydrological planning, flood prediction, trafficability, avalanche control, and numerical weather/climatological modeling. Current snow depth methods fall short of requirements. This research explores a new approach for determining snow depth using airborne interferometric synthetic aperture radar (InSAR). Digital elevation models (DEM) are produced for Snow Off and Snow On cases and differenced to determine elevation change from accumulated snow. Interferograms are produced using Multi-pass Single Look Complex airborne Ku-band SAR. Two approaches were attempted. The first is a classical method similar to spaceborne InSAR and relies on determining the baseline of the interferometric pair. The second used a perturbation method that isolates and compares high frequency terrain phase to elevation to generate a DEM. Manual snow depth measurements were taken to verify the results. The first method failed to obtain a valid baseline and therefore failed. The second method resulted in representative DEMs and average snow depth errors of -8cm, 95cm, -49cm, 176cm, 87cm, and 42cm for six SAR pairs respectively. Furthermore, Ku-band appeared to be a high enough frequency to avoid significant penetration of the snow. Results show that this technique has promise but still requires more research to refine its accuracy.

THIS PAGE INTENTIONALLY LEFT BLANK

TABLE OF CONTENTS

I.	INTRODUCTION.....	1
II.	BACKGROUND	5
A.	SNODEP	5
B.	SIR-C/X-SAR	7
1.	SIR-C/X-SAR Description.....	7
2.	Snow Analysis Using SIR-C/X-SAR.....	7
C.	GROUND PENETRATING RADAR.....	9
D.	LIDAR.....	10
E.	INSAR AND TOMOGRAPHIC SAR.....	11
III.	METHODOLOGY	25
A.	RESEARCH APPROACH.....	25
B.	SAR DATA COLLECTION AND FIELD WORK	27
1.	Aircraft SAR Collection	27
2.	Site Selection and Preparation.....	28
3.	Site Survey	38
4.	Validation.....	38
C.	DATA PROCESSING (BASELINE METHOD)	39
1.	Data Preparation.....	40
2.	Complex Image Generation	40
3.	Registration	41
4.	Interferogram Generation.....	43
5.	Phase Unwrapping.....	46
6.	Baseline Determination	49
7.	Flat Earth Removal.....	62
8.	Height to Phase Scaling	70
9.	Snow On Snow Off Differencing	74
10.	Baseline Method Summary	74
D.	DATA PROCESSING (BEST FIT PLANE REMOVAL METHOD).....	76
1.	Best Fit Plane Generation	79
2.	Best Fit Plane Removal.....	80
3.	Mean Slope Generation from Low Resolution DEM.....	84
4.	Control Point Elevation Difference from Average Slope	85
5.	Phase to Elevation Linear Regression.....	85
6.	Apply Linear Regression Equation to BFPR Image.....	87
7.	Add Linearized Image to Average Slope	87
8.	Snow On/Off Differencing.....	89
9.	Best Fit Plan Removed Summary.....	91
E.	VERIFICATION.....	93
IV.	BASELINE METHOD RESULTS.....	95
A.	PROCESSED IMAGERY	95
1.	Snow Off Pair 21/22	95

2.	Snow On Pair 01/02	99
3.	Snow On Pair 01/03	104
4.	Snow On Pair 01/04	108
B.	BASELINE METHOD ANALYSIS	112
V.	BEST FIT PLANE REMOVAL METHOD RESULTS.....	117
A.	PROCESSED IMAGERY	117
1.	Low Resolution DEM Processing	117
2.	Snow Off DEM Generation.....	118
3.	Snow On 01/02 DEM Generation and Snow Depth Calculation .	123
4.	Snow On 01/03 DEM Generation and Snow Depth Calculation .	129
5.	Snow On 01/04 DEM Generation and Snow Depth Calculation .	135
6.	Snow On 02/03 DEM Generation and Snow Depth Calculation .	141
7.	Snow On 02/04 DEM Generation and Snow Depth Calculation .	149
8.	Snow On 03/04 DEM Generation and Snow Depth Calculation .	155
B.	BEST FIT PLANE REMOVED ANALYSIS	161
VI.	COHERENCE OBSERVATION	171
VII.	CONCLUSIONS, RECOMMENDATIONS AND FUTURE WORK	175
A.	CONCLUSIONS	175
1.	Baseline Method	175
2.	Best Fit Plane Removed Method	176
3.	Coherence Observation	178
4.	Implications	178
B.	RECOMMENDATIONS AND FUTURE WORK	179
1.	Baseline Recommendations.....	179
2.	Explore the causes of the Best Fit Plane Removed Biases.....	179
3.	Circumvent the biases.....	179
4.	Bistatic Antenna	180
5.	Negation of ground data.....	180
6.	Snow conditions.....	180
7.	Collection method	180
8.	Perturbation isolation	180
APPENDIX A.	BASELINE TO M/RAD SENSITIVITY	183
APPENDIX B.	BASELINE COMPONENT SENSITIVITY TO GROUND DIFFERENCE ERROR	185
APPENDIX C.	CALCULATED SNOW DEPTH	187
APPENDIX D.	SNOW DEPTH ERROR	189
LIST OF REFERENCES	191	
INITIAL DISTRIBUTION LIST	195	

LIST OF FIGURES

Figure 1.	The electromagnetic spectrum and the indicative transmittance of the atmosphere on a path between space and the earth (Richards 2009).....	12
Figure 2.	The microwave portion of the electromagnetic spectrum is broken down into bands with L- (1.0-2.0 GHz), C- (4.0-8.0 GHz), and X-bands (8.0-12.5 GHz) as those most commonly used for remote sensing (Richards 2009).	13
Figure 3.	Imaging scenario depicting the cross-range resolvability issue. Targets lying on the same constant-range line but separated in cross range cannot be distinguished in the return of a single pulse when a broad beam is used to illuminate the entire ground patch, where L represents the patch radius and $p(y)$ represents range on the ground in the direction perpendicular to the flight path (Jakowatz, 1996).....	15
Figure 4.	The concept of using the platform motion to synthesize an effectively long antenna; the footprint of the real antenna on the ground is shown as rectangular for simplicity, where " L_a " represents the length of the synthetic antenna, " l_a " represents the physical length of the antenna, " R_0 " represents the range, " λ " represents the wave length and " θ_a " is the beamwidth (Richards 2009).....	16
Figure 5.	Geometry for computing range resolutions. " r_g " represents the difference in ground range with respect to the radar antenna, " r_r " is the slant range resolution, " Δr " the difference in the slant range between targets A and B, and " θ " is the incidence angle between the incoming beam and the normal to the surface. (Richards 2009)	17
Figure 6.	(a) Even though the topographic variation between a and b is resolvable, there is ambiguity between a and c (b) resolving the a and c ambiguity by changing the radar position, but causing ambiguity at a and d (Richards 2009).	19
Figure 7.	Geometry for single baseline SAR interferometry, in which the look and incidence angles are assumed to be the same. " R_1 " and " R_2 " are the respective ranges from antennas 1 and 2. " B " represents the baseline between the two antenna locations. " B_{\perp} " represent the orthogonal baseline between the two radar beam paths. " θ " and " $\delta\theta$ " represent the incidence angle and the change in incidence angle respectively (Richards 2009).....	20
Figure 8.	Determining the relationship between topographic height "h" and incidence angle " θ " with a platform altitude of " H " and range to the target of " R_0 " (Richards 2009).....	22
Figure 9.	Penetration depth as a function of frequency. Ulaby et al. 1982 demonstrates that as frequency increase, the penetration into the snowpack decreases. In contrast, lower frequencies will penetrate further into the snowpack.....	26
Figure 10.	Map depicting relationship between General Atomics home airfield and Snow study site at Mammoth Mountain, CA (Google Earth 2012).	29

Figure 11.	Google Earth 3D perspective view of Elysian Fields collection area looking northward towards Mammoth Mountain, CA (Google Earth 2012).	30
Figure 12.	Backscatter from various shapes and corresponding radar cross section equations (Granit Island Group, 2013).	31
Figure 13.	Lightweight portable corner reflectors were designed to be broken down for use in the field. Five of these along with their stands could easily be put in to a backpack and either skied or hiked in to the SAR collection areas.	32
Figure 14.	Corner reflector orientation at Elysian Fields collection site during Snow On SAR collection ($37^{\circ}37.7'N$, $119^{\circ}02.7'N$). The image area is 312 x 176m with the N-S corner reflectors 80m apart and the E-W corner reflectors 100m apart. Magnitude image provided by General Atomics Aeronautical.	34
Figure 15.	Deployment of corner reflectors used as ground control points at Elysian Fields collection site.	35
Figure 16.	Corner reflector deployment for Snow Off SAR collection.	36
Figure 17.	Corner reflector orientation at Elysian Fields (312 x 176m) collection site during Snow Off SAR collection ($37^{\circ}37.7'N$, $119^{\circ}02.7'N$). The ninth corner reflector is outside the image area. Magnitude image provided by General Atomics Aeronautical.	37
Figure 18.	An avalanche snow analysis pit was dug during the SAR collection. A vertical profile of the snowpack's temperature, crystal size, crystal type, and snow density was recorded.	39
Figure 19.	Magnified Snow On SAR magnitude image showing two corner reflectors. In addition to the reflectors, the walking paths can be seen in the snow as bright linear tracks. Image size 45x77m, Mammoth Mountain study site, ($37^{\circ}37.7'N$, $119^{\circ}02.7'N$).	42
Figure 20.	Example of interferogram generated during the Snow Off SAR collection. The repeating fringe pattern is derived from the subtraction of the phases of the two interferometric datasets. Both datasets record values between $-\pi$ and π . Therefore the phase difference between the fringes can never be greater than 2π . Mammoth Mountain study site, ($37^{\circ}37.7'N$, $119^{\circ}02.7'N$).	44
Figure 21.	Example of coherence image generated from the Snow Off SAR collection. Mammoth Mountain study site, ($37^{\circ}37.7'N$, $119^{\circ}02.7'N$).	46
Figure 22.	Unwrapped total phase generated from interferometric image collected during Snow On SAR collection. The repeating 2π pattern has been removed and the full range of phase difference can be seen. Mammoth Mountain study site, ($37^{\circ}37.7'N$, $119^{\circ}02.7'N$).	48
Figure 23.	Geometry for Multi-pass Single Look Complex interferometric SAR collection. “ r_1 ” and “ r_2 ” are the respective ranges from antennas 1 and 2. “ B ” represents the baseline between the two antenna locations. “ B_{\perp} ” represents the orthogonal baseline between the two radar beam paths. SRP is the scene reference point. “ θ ” represent the angle between the baseline and the orthogonal baseline. “ $\delta\alpha$ ” represents the angle between	

the two range vectors. (After Richards 2009; with input from Douglas Bickel personal communication, 2013)	51
Figure 24. Comparing the physical change in location and phase of multiple points to a reference point “RP” enables the construction of a system of equations to solve for the baseline. The given ranges to the reference point “ r_0 ” and the other points “ r_a ”, is also required for the solving the system of equations. (After Douglas Bickel, personal communication, 2013).....	53
Figure 25. This approximately 200x300m scene depicts a reference point ”RP” defined by the SE corner reflector and the relative positions of the other three known positional points defined by the other three emplaced corner reflectors at positions “a”, “b”, and “c”. Mammoth Mountain study site (312 x 176m), (37°37.7’N, 119°02.7’N).	55
Figure 26. In order to correctly determine the baseline, an accurate representation of the x, y, and z changes must be known. Those changes were computed in a reference frame where the x axis was east/west and the y axis was north/south. The radar reference frame does not line up, thereby requiring an adjustment to the x and y components in the baseline calculation equations.....	57
Figure 27. Demonstration of the correction required for a given rotation of α° rotation in reference frames (From Mathematics-Online Lexicon, 2013).	58
Figure 28. Header data provided with each SAR acquisition provides specifics on the aircraft flight path orientation and the orientation of the radar with respect to the flight information. In addition to the flight data, the header provides the calculated pixel size for the given image or the ground resolution.	59
Figure 29. SCLA represents the flight path relative to true north.....	60
Figure 30. Theta in the header data represents the squint angle or the angle that the radar is looking relative to the flight path. In this case theta is 82.9342°.....	61
Figure 31. This figure shows all the relevant angles required to determine the rotation angle “ α ” used in calculating the change in x and y for the rotation of the reference frame. “ θ ” represents the squint angle. “ $\theta_{(true)}$ ” represents the squint angle adjust for true north. SCLA represents the flight heading.....	62
Figure 32. Geometry shows that θ changes as the distance from the antenna “ r_0 ” changes. This change in θ is required to determine the interferometric phase angle and is calculated using the known altitude “ h ” above the scene reference point (SRP) and the ground distance “ y ”.....	64
Figure 33. This notional figure demonstrates the unwrapped change in phase in the “y” direction due to the change in range (range aspect of the flat earth phase).	65
Figure 34. This notional figure demonstrates the wrapped change in phase in increments of 2π radians in the “y” direction due to the change in range (range aspect of the flat earth phase).	66
Figure 35. This notional figure demonstrates the unwrapped change in phase in the “x” or azimuth aspect of the flat earth phase.	67
Figure 36. This figure demonstrates the unwrapped change in phase in increments of 2π radians in the “x” or azimuth aspect of the flat earth phase.....	68

Figure 37.	The flat earth phase is sum of the range and azimuth phases. Subtracting the flat earth phase from the total unwrapped phase results in the terrain phase.	69
Figure 38.	Subtracting the flat earth phase from the total unwrapped interferometric phase results in a phase array or flattened phase that represents terrain phase only (right image).	69
Figure 39.	Geometry involved in determining phase to elevation scaling where “ r_0 ” represents the radar range to an imaginary plane, “T” represents a point on the terrain that is at the same range as r_0 but at a height of “z” above the imaginary plane. “ θ_0 ” represent the incidence angle to a given point “O” on the imaginary plane that is at the same range as that of point T. “ $\delta\theta$ ” is the angle between the vectors to point O and T. “ α ” is the angle between the baseline in the y-z plane and the horizontal (After Rosen 2009; with input from Douglas Bickel, personal communication, 2013).	70
Figure 40.	“ $\delta\theta$ ” or the angle between the vectors that point toward points “O” and “T” is required to determine the phase to height relationship. An equation can be derived by introducing “n” for the distance between “O” and “T” and recognizing that “ θ_0 ”, incidence angle, is the same as the angle between “n” and the imaginary plane. (After Rosen 2009; with input from Douglas Bickel, personal communication, 2013)	72
Figure 41.	Snow Off DEM. Mammoth Mountain study site ($37^{\circ}37.7'N$, $119^{\circ}02.7'N$).	74
Figure 42.	Baseline method flow chart.	75
Figure 43.	The Best Fit Plane Removed (BFPR) method subtracts the best fit plane (BFP) from the total unwrapped phase. The BFPR isolates the portion of the total unwrapped phase that is due to the deviation of the terrain from the average slope of the terrain and is signified as “ $\delta\Delta\phi$ ”. This can then be compared to ground data to establish a relationship between this phase and elevation.	79
Figure 44.	Best fit plane generated from an unwrapped interferogram showing the average slope of the phase image. Mammoth Mountain study site, ($37^{\circ}37.7'N$, $119^{\circ}02.7'N$).	80
Figure 45.	Unwrapped interferogram. Mammoth Mountain study site, ($37^{\circ}37.7'N$, $119^{\circ}02.7'N$).	81
Figure 46.	Best Fit Plane generated from the unwrapped interferogram. Mammoth Mountain study site, ($37^{\circ}37.7'N$, $119^{\circ}02.7'N$).	82
Figure 47.	This figure represents the phase that is left after subtracting the BFP from the unwrapped interferogram and is referred to as Best Fit Plane Removed (BFPR). Mammoth Mountain study site, ($37^{\circ}37.7'N$, $119^{\circ}02.7'N$).	82
Figure 48.	Path to the BFPR. Mammoth Mountain study site, ($37^{\circ}37.7'N$, $119^{\circ}02.7'N$).	83
Figure 49.	3D representation of a 10 meter resolution DEM used to determine average slope of the terrain. Mammoth Mountain study site, ($37^{\circ}37.7'N$, $119^{\circ}02.7'N$).	84

Figure 50.	3D representation of 10m DEM BFP (average terrain slope in meters). Mammoth Mountain study site, (37°37.7'N, 119°02.7'N).....	85
Figure 51.	Perspective view of BFPR with tie points and accompanying elevations depicted. Mammoth Mountain study site, (37°37.7'N, 119°02.7'N)	86
Figure 52.	Linear regression for Snow On 01/02 SAR image pair shows the relationship between the phase and elevation.....	86
Figure 53.	Adding the BFPR after it has had the linear regression equation applied to the low resolution DEM BFP (terrain slope in meters) results in a DEM that is measured in meters. Mammoth Mountain study site, (37°37.7'N, 119°02.7'N)	88
Figure 54.	Subtracting the Snow Off DEM from the Snow On DEM results in a snow depth image. Mammoth Mountain study site, (37°37.7'N, 119°02.7'N)	90
Figure 55.	Best fit plane removed method flow chart.....	92
Figure 56.	Manual snow depth measurements were taken throughout the scene and are represented by the circles in the above snow depth image. The circle size also demonstrates the 5m radius area that was used to average the snow depth in that location. Corner reflector locations are also shown and labeled (red outlined circles). Mammoth Mountain study site (312 x 176m), (37°37.7'N, 119°02.7'N).....	94
Figure 57.	Snow Off SAR image pair 21 and 22 interferogram and the resulting unwrapped interferogram. Mammoth Mountain study site, (37°37.7'N, 119°02.7'N)	96
Figure 58.	The summation of the range phase correction and azimuth phase correction results in the total flat earth phase correction that will be applied to the unwrapped interferogram. Mammoth Mountain study site, (37°37.7'N, 119°02.7'N)	97
Figure 59.	Subtracting the flat earth correction from the unwrapped phase results in a phase that is entirely due to the snow covered terrain and is known as the flattened phase. Mammoth Mountain study site, (37°37.7'N, 119°02.7'N)...	98
Figure 60.	Once the scaling factor is applied to the flattened phase, the resulting image is a DEM of the area being sampled. The image on the right is the SAR-calculated DEM while the image on the left is the low resolution DEM for comparison. Mammoth Mountain study site, (37°37.7'N, 119°02.7'N)	99
Figure 61.	Snow On SAR image pair 01 and 02 interferogram and the resulting unwrapped interferogram. Mammoth Mountain study site, (37°37.7'N, 119°02.7'N)	100
Figure 62.	The summation of the range phase correction and azimuth phase correction results in the total flat earth phase correction that will be applied to the unwrapped interferogram. Mammoth Mountain study site, (37°37.7'N, 119°02.7'N)	101
Figure 63.	Subtracting the flat earth correction from the unwrapped phase results in a phase that is entirely due to the snow covered terrain and is known as the flattened phase. Mammoth Mountain study site, (37°37.7'N, 119°02.7'N).	102

Figure 64.	Once the scaling factor is applied to the flattened phase, the resulting image is a DEM of the area being sampled. The image on the right is the SAR-calculated DEM while the image on the left is the low resolution DEM for comparison. Mammoth Mountain study site, (37°37.7'N, 119°02.7'N).	103
Figure 65.	Subtracting the Snow Off DEM from the Snow On DEM should result in an image representing the snow depth. Mammoth Mountain study site, (37°37.7'N, 119°02.7'N).	104
Figure 66.	Snow On SAR image pair 01 and 03 interferogram and the resulting unwrapped interferogram. Mammoth Mountain study site, (37°37.7'N, 119°02.7'N).	105
Figure 67.	The summation of the range phase correction and azimuth phase correction results in the total flat earth phase correction that will be applied to the unwrapped interferogram. Mammoth Mountain study site, (37°37.7'N, 119°02.7'N).	106
Figure 68.	Subtracting the flat earth correction from the unwrapped phase results in a phase that is entirely due to the snow covered terrain and is known as the flattened phase. Mammoth Mountain study site, (37°37.7'N, 119°02.7'N).	107
Figure 69.	Once the scaling factor is applied to the flattened phase, the resulting image is a DEM of the area being sampled. The image on the right is the SAR-calculated DEM while the image on the left is the low resolution DEM for comparison. Mammoth Mountain study site, (37°37.7'N, 119°02.7'N).	107
Figure 70.	Subtracting the Snow Off DEM from the Snow On DEM should result in an image representing or the snow depth. Mammoth Mountain study site, (37°37.7'N, 119°02.7'N).	108
Figure 71.	Snow On SAR image pair 01 and 04 interferogram and the resulting unwrapped interferogram. Mammoth Mountain study site, (37°37.7'N, 119°02.7'N).	109
Figure 72.	The summation of the range phase correction and azimuth phase correction results in the total flat earth phase correction that will be applied to the unwrapped interferogram. Mammoth Mountain study site, (37°37.7'N, 119°02.7'N).	110
Figure 73.	Subtracting the flat earth correction from the unwrapped phase results in a phase that is entirely due to the snow covered terrain and is known as the flattened phase. Mammoth Mountain study site, (37°37.7'N, 119°02.7'N).	111
Figure 74.	Once the scaling factor is applied to the flattened phase, the resulting image is a DEM of the area being sampled. The image on the right is the SAR-calculated DEM while the image on the left is the low resolution DEM for comparison. Mammoth Mountain study site, (37°37.7'N, 119°02.7'N).	111
Figure 75.	Subtracting the Snow Off DEM from the Snow On DEM results in an image representing or the snow depth. Mammoth Mountain study site, (37°37.7'N, 119°02.7'N).	112

Figure 76.	A relatively low resolution 10m DEM of the survey area was obtained from the USDA NAIP and then geocorrected to match the SAR image area. Centered on Mammoth Mountain study site, (37°37.7'N, 119°02.7'N).	117
Figure 77.	Best fit Plane of low resolution 10m DEM of survey area. This represents the generalized terrain slope for the Elysian Fields site. Centered on Mammoth Mountain study site, (37°37.7'N, 119°02.7'N).....	118
Figure 78.	A Best Fit Plane (BFP) was generated from the interferometric SAR image pair (total unwrapped phase) 21 and 22. After generating the BFP, it was subtracted from the total phase resulting in a Best Fit Plane Removed (BFPR) image. Mammoth Mountain study site, (37°37.7'N, 119°02.7'N).	119
Figure 79.	Linear regression of the BFPR phase and mean slope perturbation results in an equation that is applied to change BFPR image from phase to elevation for SAR image pair 21 and 22.....	120
Figure 80.	Addition of BFPRL to the 10m DEM BFP results in the Snow Off SAR image pair 21 and 22 DEM. Mammoth Mountain study site, (37°37.7'N, 119°02.7'N).	121
Figure 81.	The BFPR derived DEM (left) generally resembles the low resolution DEM (right), however, it exhibits higher detail and fine terrain variability..	122
Figure 82.	A Best Fit Plane (BFP) was generated from the interferometric SAR image pair (total unwrapped phase) 01 and 02 . After generating the BFP, it was subtracted from the total phase resulting in a Best Fit Plane Removed (BFPR) image. Mammoth Mountain study site, (37°37.7'N, 119°02.7'N).	124
Figure 83.	Linear regression of the BFPR phase and mean slope perturbation results in an equation that is applied to change BFPR image from phase to elevation for SAR image pair 01 and02.....	125
Figure 84.	Addition of BFPRL to the 10m DEM BFP results in the Snow On SAR image pair 01 and 02 DEM. The snow covered DEM assumes minimal SAR penetration. Mammoth Mountain study site, (37°37.7'N, 119°02.7'N).	126
Figure 85.	Subtracting the Snow Off DEM from the Snow On DEM generated from the SAR image pair 01 and 02 results in a snow depth image. Mammoth Mountain study site, (37°37.7'N, 119°02.7'N).	128
Figure 86.	A Best Fit Plane (BFP) was generated from the interferometric SAR image pair (total unwrapped phase) 11 and 03 . After generating the BFP, it was subtracted from the total phase resulting in a Best Fit Plane Removed (BFPR) image. Mammoth Mountain study site, (37°37.7'N, 119°02.7'N).	130
Figure 87.	Linear regression of the BFPR phase and mean slope perturbation results in an equation that is applied to change BFPR image from phase to elevation for SAR image pair 01 and 03.....	131
Figure 88.	Addition of BFPRL to the 10m DEM BFP results in the Snow On SAR image pair 01 and 03 DEM. The snow covered DEM assumes minimal	

SAR penetration. Mammoth Mountain study site, (37°37.7'N, 119°02.7'N).	132
Figure 89.	
Subtracting the Snow Off DEM from the Snow On DEM generated from the SAR image pair 01 and 03 results in a snow depth image. Mammoth Mountain study site, (37°37.7'N, 119°02.7'N).	134
Figure 90.	
A Best Fit Plane (BFP) was generated from the interferometric SAR image pair (total unwrapped phase) 01 and 04. After generating the BFP, it was subtracted from the total phase resulting in a Best Fit Plane Removed (BFPR) image. Mammoth Mountain study site, (37°37.7'N, 119°02.7'N).	136
Figure 91.	
Linear regression of the BFPR phase and mean slope perturbation results in an equation that is applied to change BFPR image from phase to elevation for SAR image pair 01 and 04.....	137
Figure 92.	
Addition of BFPRL to the 10m DEM BFP results in the Snow On SAR image pair 01 and 04 DEM. The snow covered DEM assumes minimal SAR penetration. Mammoth Mountain study site, (37°37.7'N, 119°02.7'N).	138
Figure 93.	
Subtracting the Snow Off DEM from the Snow On DEM generated from the SAR image pair 01 and 04 results in a snow depth image. Mammoth Mountain study site, (37°37.7'N, 119°02.7'N).	140
Figure 94.	
A Best Fit Plane (BFP) was generated from the interferometric SAR image pair (total unwrapped phase) 02 and 03. After generating the BFP, it was subtracted from the total phase resulting in a Best Fit Plane Removed (BFPR) image. Mammoth Mountain study site, (37°37.7'N, 119°02.7'N).	142
Figure 95.	
Linear regression of the BFPR phase and mean slope perturbation results in an equation that is applied to change BFPR image from phase to elevation for SAR image pair 02 and 03. This SAR pair has a particularly low R ² value of .0102 resulting in a poorly defined DEM.	143
Figure 96.	
Addition of BFPRL to the 10m DEM BFP results in the Snow On SAR image pair 02 and 03 DEM. The snow covered DEM assumes minimal SAR penetration. Mammoth Mountain study site, (37°37.7'N, 119°02.7'N).	145
Figure 97.	
The BFPR derived DEM (left) only partially resemble the low resolution DEM (right)	146
Figure 98.	
Subtracting the Snow Off DEM from the Snow On DEM generated from the SAR image pair 02 and 03 results in a snow depth image. Mammoth Mountain study site, (37°37.7'N, 119°02.7'N).	148
Figure 99.	
A Best Fit Plane (BFP) was generated from the interferometric SAR image pair (total unwrapped phase) 02 and 04. After generating the BFP, it was subtracted from the total phase resulting in a Best Fit Plane Removed (BFPR) image. Mammoth Mountain study site, (37°37.7'N, 119°02.7'N).	150

Figure 100.	Linear regression of the BFPR phase and mean slope perturbation results in an equation that is applied to change BFPR image from phase to elevation for SAR image pair 02 and 04.....	151
Figure 101.	Addition of BFPRL to the 10m DEM BFP results in the Snow On SAR image pair 02 and 04 DEM. The snow covered DEM assumes minimal SAR penetration. Mammoth Mountain study site, (37°37.7'N, 119°02.7'N).	152
Figure 102.	Subtracting the Snow Off DEM from the Snow On DEM generated from the SAR image pair 02 and 04 results in a snow depth image. Mammoth Mountain study site, (37°37.7'N, 119°02.7'N).	154
Figure 103.	A Best Fit Plane (BFP) was generated from the interferometric SAR image pair (total unwrapped phase) 03 and 04. After generating the BFP, it was subtracted from the total phase resulting in a Best Fit Plane Removed (BFPR) image. Mammoth Mountain study site, (37°37.7'N, 119°02.7'N).	156
Figure 104.	Linear regression of the BFPR phase and mean slope perturbation results in an equation that is applied to change BFPR image from phase to elevation for SAR image pair 03 and 04.....	157
Figure 105.	Addition of BFPRL to the 10m DEM BFP results in the Snow On SAR image pair 03 and 04 DEM. The snow covered DEM assumes minimal SAR penetration. Mammoth Mountain study site, (37°37.7'N, 119°02.7'N).	158
Figure 106.	Subtracting the Snow Off DEM from the Snow On DEM generated from the SAR image pair 03 and 04 results in a snow depth image. Mammoth Mountain study site, (37°37.7'N, 119°02.7'N).	160
Figure 107.	Snow depth error for each of the 16 manual snow depth locations for each of the six SAR image pairs are indicated in the top bar graphs. The six images are the BFPs that correspond to the snow depth error bar graphs.	163
Figure 108.	Coherence varies throughout the scene. The numbered circles denote the manual snow depth validation measurement locations. Note that measurement locations 1-8 have relatively high coherence compared to locations 9-16. Mammoth Mountain study site, (37°37.7'N, 119°02.7'N)..	165
Figure 109.	Average coherence per manual snow depth location for each of the six interferometric image pairs.....	166
Figure 110.	This figure demonstrates the relationship between the normalized snow depth error for each of the six interferometric image pairs and the pattern of the BFP derived from those interferograms.	167
Figure 111.	Time series of coherence images ordered by time between image pairs. Note the decrease in coherency over time. Mammoth Mountain study site, (37°37.7'N, 119°02.7'N).	172
Figure 112.	Baseline length to interferometric phase factor relationship based on Table 14.....	184
Figure 113.	This figure demonstrates the change that the input values of the Δx , y , and z elements into the baseline calculation system of equations has on the length of the calculated baseline.	185

THIS PAGE INTENTIONALLY LEFT BLANK

LIST OF TABLES

Table 1.	Four usable Snow On and two useable Snow Off SAR images at 0.1m resolution were acquired by General Atomics during the radar collection phase of the research. These images enabled six Snow On and one Snow Off interferometric pairs to be calculated.	28
Table 1.	Four usable Snow On and two useable Snow Off SAR images at 0.1m resolution were acquired by General Atomics during the radar collection phase of the research. These images enabled six Snow On and one Snow Off interferometric pairs to be calculated.	95
Table 2.	The baseline calculation relies on the relative $\Delta(x, y, z)$ change of position from a reference point (SE(o)) to three other known locations (SW(a), NW(b), and NE(c)) and the interferometric phase ($\Delta\phi$) at those locations. The right side of the chart depicts the calculated baseline components in the x, y, z directions (B_x , B_y , and B_z).....	97
Table 3.	The baseline calculation relies on the relative $\Delta(x, y, z)$ change of position from a reference point (SE(o)) to three other known locations (SW(a), NW(b), and NE(c)) and the interferometric phase ($\Delta\phi$) at those locations. The right side of the chart depicts the calculated baseline components in the x, y, z directions (B_x , B_y , and B_z).....	101
Table 4.	The baseline calculation relies on the relative $\Delta(x, y, z)$ change of position from a reference point (SE(o)) to three other known locations (SW(a), NW(b), and NE(c)) and the interferometric phase ($\Delta\phi$) at those locations. The right side of the chart depicts the calculated baseline components in the x, y, z directions (B_x , B_y , and B_z).....	106
Table 5.	The baseline calculation relies on the relative $\Delta(x, y, z)$ change of position from a reference point (SE(o)) to three other known locations (SW(a), NW(b), and NE(c)) and the interferometric phase ($\Delta\phi$) at those locations. The right side of the chart depicts the calculated baseline components in the x, y, z directions (B_x , B_y , and B_z).....	110
Table 6.	The phase from the BFPR image was compared with the mean slope perturbation to determine the phase to elevation relationship for Snow Off SAR image pairs 21 and 22. In this particular case, only three corner reflectors were used. The fourth corner reflector phase was determined to be unreliable due to placement issues during the SAR collection	120
Table 7.	The phase from the BFPR image was compared with the mean slope perturbation to determine phase to elevation relationship for Snow Off SAR image pairs 01 and 02.	125
Table 8.	The phase from the BFPR image was compared with the mean slope perturbation to determine phase to elevation relationship for Snow Off SAR image pairs 01 and 03.	131
Table 9.	The phase from the BFPR image was compared with the mean slope perturbation to determine phase to elevation relationship for Snow Off SAR image pairs 01 and 04.	137

Table 10.	The phase from the BFPR image was compared with the mean slope perturbation to determine phase to elevation relationship for Snow Off SAR image pairs 02 and 03.	143
Table 11.	The phase from the BFPR image was compared with the mean slope perturbation to determine phase to elevation relationship for Snow Off SAR image pairs 02 and 04.	151
Table 12.	The phase from the BFPR image was compared with the mean slope perturbation to determine phase to elevation relationship for Snow Off SAR image pairs 03 and 04.	157
Table 13.	Average snow depth error by SAR image pair.	161
Table 14.	The left table demonstrates the sensitivity of the height to phase ratio in an interferogram based on the change in the baseline length. The right table demonstrates the actual change height to phase relationship from 1meter in baseline to the next.....	184
Table 15.	Calculated snow depth for each location for each of the six SAR image pairs for Best Fit Plane Removed Method.	187
Table 16.	Calculated error in the snow depth for each location for each of the six SAR image pairs for the Best Fit Plane Removed method.	189

LIST OF ACRONYMS AND ABBREVIATIONS

ADD	Algorithm Description Document
AFWA	Air Force Weather Agency
ASI	Agenzia Spaziale Italiana (Italian Space Agency)
BFP	Best Fit Plane
BFPR	Best Fit Plane Removed
BFPRL	Best Fit Plane Removed Linearized
CR	Corner Reflector
CRREL	Cold Regions Research and Engineering Laboratory
DARA	Deutsche Agentur für Raumfahrtangelegenheiten (German Space Agency)
DEM	Digital Elevation Model
DLR	Deutsche Agentur für Raumfahrtangelegenheiten (German Aerospace Center)
FFT	Fast Fourier transform
FMCW	Frequency Modulated Continuous Wave
GAA	General Atomics Aeronautical
GCP	Ground Control Point
GPR	Ground Penetrating Radar
GPS	Global Positioning System
HF	High Frequency
InSAR	Interferometric Synthetic Aperture Radar
JPL	Jet Propulsion Laboratory
LiDAR	Light Detection and Ranging
METAR	Meteorological reporting observations
medivac	Medical Evacuation
NASA	National Aeronautics and Space Administration
NPS	Naval Postgraduate School
Radar	Radio Detection and Ranging
RP	Reference Point
SAR	Synthetic Aperture Radar
SLC	Multi-pass Single Look Complex

SIR-C/X-SAR	Spaceborne Imaging Radar-C/X-Band Synthetic Aperture Radar
SNODAR	Snow Depth Airborne Radar
SNODEP	Air Force Weather Agency's Snow Depth & Sea Ice Analysis
SRP	Scene Reference Point
SSM/IS	Special Sensor Microwave Imager/Sounder
SWE	Snow Water Equivalent

ACKNOWLEDGMENTS

An intelligent heart acquires knowledge, and the ear of the wise seeks knowledge.
(Proverbs 18:15)

An incredible number of things had to come together and hurdles had to be crossed to make this research possible. There were several individuals and organizations that contributed to its success. Thanks must first go out to my advisor Prof. Fred Kruse who provided me with the guidance and mentoring so that I would emerge as a better scientist. The Remote Sensing Department here at NPS, including Prof Chris Olsen and Jean Ferreira, provided the badly needed funding for the equipment and travel. Steve Jacobs went above and beyond when the project needed to have field equipment designed and built on short notice to meet deadlines.

Dr. Ralf Dunkel and the flight crews of General Atomic Aeronautical were instrumental in this research. Without their support, this project literally would not have been able to get off the ground. I truly hope the results are beneficial to them.

Enough can't be said about the contributions made by Douglas Bickel at Sandia National Labs. His unmatched technical expertise and enthusiasm enabled me to get past more road blocks than I can count. I would like to specifically acknowledge his input and guidance in developing the baseline method equations on pages 50–52 and 70–72 of this manuscript. These were put together over the course of several face-to-face discussions and some intense phone conversations.

Alex Clayton of the Mammoth Mountain Ski Patrol played a critical role determining the best location to conduct the research and additionally made the manual labor portion of the project doable. Both Geoff Kruse and Maj Paul Homan also spent many hours on the mountain digging holes and carrying equipment to the survey site. Without their efforts, the research would not have been possible.

Thanks must also be given to my fellow PhD students; Maj Bill Ryerson, LCDR Heather Hornick, Maj Cedrick Stubblefield, and Maj Darren Murphy for their fellowship. The support and advice of Maj Paul Homan, CMD Joel Feldmeier, and Andy Penny contributed greatly to the completion of this project.

Thank you to my parents, Dan and Mary Evans. They gave me the inspiration to go after the things I wanted and taught me the perseverance to stick to my endeavors. My brother Steve enthusiastically supported me in this endeavor also, to which I am grateful.

Finally, I could not have completed this work without the unwavering support of my beautiful wife and best friend Dana. Thank you so much for your patience and taking care of me. I love you.

I. INTRODUCTION

The ability to measure snow depth over a large area is a capability that has eluded the operational and scientific communities for many years. This research is a first step towards developing methods for determining snow depth utilizing synthetic aperture radar (SAR) technology. Because the SAR hardware is already fielded, successful measurement of snow depth using remote sensing approaches will potentially lead to operational capabilities beyond what is currently available using a variety of other methods.

There are many reasons for both military and civilian agencies to have the ability to quantify snow depth. The U.S. military's need to estimate the snow depth and its effects every spring in Afghanistan in particular is the motivation for pursuing this research to develop a new and operationally relevant method for determining snow depth.

While there is a need for the military to have this capability in Afghanistan, there are a multitude of other reasons that justify the pursuit of developing an improved technique to address this issue. The amount of snow on the ground before the spring melt plays a critical role in several areas. Water management is the first and most critical of these. Urban and agricultural communities can be directly affected by the amount of stored fresh water contained in the seasonal snow fall. This is especially true in dry climates that rely on high altitude snow melt to replenish fresh water reservoirs. Central and southern California are prime examples of this. In addition to water management, the spring snow melt can be a catalyst for swollen rivers and flooding. An accurate estimate of the snow volume in a particular watershed can go a long way towards forecasting the spring flood potential. This information can be critical to local authorities for risk mitigation.

Trafficability, both on and off road, is another area impacted by the amount of snow on the ground. Snow depth can determine where and what kind of operations can be carried out and if there is a need for special equipment to conduct these operations. Additionally, this information can be used to predict an adversarial force's movement and

capability to carry out their operations. Trafficability is not restricted to just ground movement. The ability to perform insertion or extraction missions by helicopter and airborne operations are additionally impacted by snow cover. For example, the presence and amount of snow can cause potential white-out conditions, making it impossible to land rotary wing aircraft for either standard operations or medical evacuation (medivac) emergencies.

Avalanche risk assessment is yet another area that can benefit from improved snow depth estimates. One of the many factors in determining the potential for avalanches is the amount of snow on a particular slope. An estimation of the snow volume along with an estimated density can be used in conjunction, with other factors such as slope angle, seasonal history, and weather conditions to forecast snow pack stability (American Avalanche Association 2004). This generally is not as big of a problem in areas that have an active avalanche control system such as those found in many recreational ski areas. In backcountry areas and less developed areas around the world, however, snow depth can be a valuable source of intelligence for both military operations and humanitarian risk assessment.

Snow depth additionally plays a role when it comes to numerical weather and climate prediction. The high albedo of snow greatly impacts the local and global scale radiational balance. The snow decreases the absorption of solar energy received at the earth's surface, acting as a cooling mechanism (Groisman et al. 1994). Accurately predicting when and where the snow cover melts to expose bare ground benefits numerical weather and climatological model estimates of longwave and shortwave energy exchange. Having a more accurate estimate of the incoming energy will, theoretically, improve forecasts.

Current methods to estimate snow depth fall well short of our needs. While many observation sites record the amount of snowfall, few record the actual snow depth. Those that do, do not come close to providing adequate coverage. Furthermore, the few reports of snow depths that are available are not necessarily representative of the local area due to spatial variability.

Considering the relevance of this information, the objective of this research in the Snow Depth Airborne Radar (SNODAR) project is to explore the viability of a new method using remote sensing, and more specifically interferometric synthetic aperture radar (InSAR) in the Ku-band (12–18Ghz frequency range) from an airborne platform, to determine snow depth in regions that are not easily accessible. This new method should be able to provide both higher spatial resolution and accuracy for point snow depth measurements and area snow volume estimates than the current methods available. It is anticipated that existing SAR hardware could be used to develop the capability to determine both snow depth and snow volume where manual measurements are not possible.

THIS PAGE INTENTIONALLY LEFT BLANK

II. BACKGROUND

This section covers four different existing approaches that have been taken to address the snow depth issue along with their strengths and weaknesses. The primary methods that have been used to-date include Air Force Weather Agency's Snow Depth and Sea Ice Analysis (SNODEP) model, the use of NASA's SIR-C/X-SAR missions, the use of ground penetrating radar, and the use of LiDAR. The final part of this section focuses on the method investigated by this research, summarizing the theory used to derive digital elevation models (DEM) through the use of airborne or spaceborne synthetic aperture radar (SAR), and describing the science and techniques used to determine snow depth with SAR systems.

A. SNODEP

The Air Force Weather Agency's SNODEP model is the primary tool used today to provide military operational users with snow depth information. Snow depth estimates are modeled by using a combination of passive microwave imagery from the Special Sensor Microwave/Imager Sounder (SSM/IS) and surface observations to include synoptic, meteorological reporting observations (METAR) and Airways and snow depth climatology (Air Force Weather Agency [AFWA] fact sheet and AFWA Algorithm Description Document [ADD] 2012).

SNODEP takes a multiple source approach to determine snow depth. The first step makes an initial guess based on the previous model run, similar to the approach used in many numerical weather prediction models to establish an initial background field. Once the background field is established, the model incorporates any available surface depth observations. It uses an inverse linear weighting scheme to interpolate the data to the closest grid point. Then, in regions without surface reports, SSMI/S algorithms are used to detect snow. If no snow was previously detected, a value of 0.1m of snow depth is automatically assigned. If snow is detected where snow was previously detected, the snow depth estimate is trended toward climatology. If no snow is detected, the estimate for the area remains snow free (AFWA fact sheet and AFWA ADD 2012).

The main strength of SNODEP is its ability to provide a global view of snow coverage. It does, however, have several weaknesses. Due to the inherent resolution of the SSM/IS satellite; SNODEP's best resolution is 25km (Foster 2011). This spatial resolution typically is not adequate to provide the detail that operational users require. Its grid can also be too large to adequately estimate the snow depth in a smaller watershed, especially in complex terrain such as mountainous regions. In addition, the in-situ observations are extremely limited. AFWA estimates that between 100 and 150 snow depth observations across the northern hemisphere in winter are used to feed the model (T. Lewiston 2012, personal communication). This number of observations does not begin to provide a good estimate for the generation of a hemispheric-scale model. Also, the observations that we do have tend to be concentrated in more developed countries like the U.S. This makes it unlikely that these observations will have an effect on snow depth estimates for locations where military operations are taking place. Spatial variability is also a big concern. Wind, complex terrain, and variable solar radiation are the main causes of this variability (Schweizer and Kronholm 2006). Because of this high spatial variability in snow depth, the observations that are available may not be representative of the region that SNODEP is trying to describe. To make up for this poor coverage of in-situ observations the SSMIS passive microwave satellite is used to determine the snow depth everywhere else. SSMIS does this by using a correlation coefficient between the microwave brightness temperature and snow depth. This coefficient assumes snow crystal grain size, and that the snow is dry or refrozen. Failure of either of these assumptions can negatively affect the accuracy of the model. Furthermore, snow depth estimates from the SSMIS are limited to depths of 40cm or less. The snow depth algorithm becomes unreliable when the snow depth exceeds 40cm (Northrop Grumman 2010). Additionally, at first indication of snow on the ground, the model automatically assigns 0.1m of snow depth (AFWA ADD 2012). This may or may not be representative of the initial snow depth. When snow was previously detected by the algorithm it trends the current value towards climatology (AFWA ADD 2012). There are two problems with this. The first is that the current snow depth may or may not be representative of the snow on the ground at the modeled time. Changing the value is premature if the depth is

not accurate to begin with. The second problem has to do with the climatological data. As mentioned above, there are relatively few stations that actually record snow depth. Many stations record snowfall, which should not be confused with snow depth on the ground. Mechanisms such as settling, melting, sublimation, and movement of snow by wind make the snowfall measurements a poor estimate of snow depth. With so few stations recording snow depth, the accuracy of the climatology is in question, especially for areas that do not, or never have had, in-situ measurements. This potentially can have a negative impact on the accuracy of SNODEP estimates.

B. SIR-C/X-SAR

1. SIR-C/X-SAR Description

The Spaceborne Imaging Radar-C/X-band Synthetic Aperture Radar (SIR-C/X-SAR) mission was a joint National Aeronautical and Space Administration (NASA), German Space Agency (Deutsche Agentur für Raumfahrtangelegenheiten, DARA), and Italian Space Agency (Agenzia Spaziale Italiana, ASI) project designed as the next step in spaceborne imaging radar research. SIR-C/X-SAR flew two missions in 1994 imaging 57.6 million square miles, or approximately 14 percent of the Earth's surface (Stofen et al. 1995, and JPL, 2012). The space shuttle launched with three different synthetic aperture radar (SAR) antennas. These included L-band (23.5cm wavelength), C-band (5.8cm wavelength), and X-band (3cm wavelength) antennas. The L and C bands were also constructed in a way that could measure both horizontal and vertical polarizations. The use of the three different bands allowed collection of information about the Earth's surface at multiple scales, which had never been possible before with only single band SAR systems.

2. Snow Analysis Using SIR-C/X-SAR

Snow characteristics greatly affect backscattering of radar emissions. The extent of this effect is dependent on three sets of parameters (Shi and Dozier 1996):

- Sensor parameters to include frequency/wavelength, polarization, and viewing angle

- Snow pack parameters to include snow density, depth, particle size, size variation, liquid water content (stickiness), and stratification
- Ground parameters to include dielectric and roughness parameters

This difference in backscattering properties by different radar wavelengths on the snow pack can be leveraged to determine the physical characteristics of the snow pack and the underlying ground. All three of the SIR-C/X-SAR wavelengths are assumed to penetrate into the snowpack. Based on electro-magnetic scattering theory, for a given material, there is a direct relationship between the wavelength and the depth of penetration (Richards 2009). With that in mind, there should be an increase in backscattering moving from the L-band radar down to the X-band radar. This fact was used by Shi and Dozier, 2000, to retrieve snowpack properties. They first used polarized data from the L-band radar to determine snowpack density. L-band proved to be a long enough wavelength that the backscatter from the snowpack was negligible. The entire radar return therefore came from the ground below the snow pack. Despite the lack of backscatter from the snow they were able to capitalize on the fact that the snow pack caused a shift in refraction in the incidence angle of the radar pulse. The extent of the refraction was dependent on the density of the snow pack. Furthermore, there was a difference in both the magnitude and relation between the VV and HH polarizations. By modeling this interaction, they were able to derive the snowpack's density.

Due to the large variability in density in snowpacks, the density alone is not enough to estimate other characteristics of the snow pack such as snow depth or snow water equivalent (SWE). To do this Shi and Dozier used data from both the C-band and X-band radars. Both C-band and X-band radar pulses have different volume scattering properties as stated above. This fact can be used to model the particle size and expected magnitude of the scattering. Both bands are assumed to penetrate to the ground in addition to the volume scattering, which adds an additional component to the overall return. This can be accounted for, however, by using the ground roughness and dielectric properties determined from the L-band radar.

This approach of using a combination of all three SAR bands showed very positive results and has stood up well to ground validation. While this technique has

shown great potential, we do not currently have any persistent spaceborne or airborne sensors with the appropriate configuration to take advantage of this technique.

C. GROUND PENETRATING RADAR

There have also been attempts to use ground penetrating radar (GPR) to address the issue of determining snow depth and other snowpack characteristics. Frequency modulated continuous wave (FMCW) radar has proven to be the most successful of the GPRs for snow study. The FMCW radar works similarly to a standard radar system in that it times the pulse to determine range. It however uses a broad band width that results in a greater theoretical vertical resolution as compared to a standard GPR (Yankielun et al. 2004). This greater vertical resolution is quite important if you want to determine snow pack stratigraphy, which can be particularly important for avalanche prediction. Ground penetrating radars are typically deployed for snow pack analysis either by hand or by towing them behind a snowmobile. Recently they have been deployed using low flying helicopters with some success (Marshal et al. 2008).

Overall, the use of these FMCW radars has been quite successful at determining snowpack characteristics; in particular those characteristics that concern avalanche experts in focused areas. They are not, however, suited for covering larger areas. Deploying them on the ground, whether by hand or being towed behind a snowmobile or snowcat, does not provide nearly the spatial coverage provided by airborne systems. Ground deployment is also restricted by complex terrain. The use of the GPR by helicopter also has drawbacks. The systems used to-date have a fairly broad footprint. That means that as the platform that the GPR is attached to increases in altitude, the area covered by the footprint also increases dramatically. Everything in the footprint is treated as a single return per pulse. The more the terrain varies within the footprint, the less reliable the measurements. Work done by Marshal et al. (2008) has shown that altitudes greater than 100ft above the ground make the data unreliable. Performance can be worse in areas where there are steep slopes. There are plans to try to use a FMCW GPR with a narrower beam to address this issue. At the time of this writing, however, there do not

appear to be publications indicating that this has been done yet. With such restrictions, operational airborne collections in complex terrain are not currently possible.

D. LIDAR

Light Detection and Ranging (LiDAR) is another method that has been explored to estimate snow depth. LiDAR is based on measuring the time required for a pulse of light to travel to a target and then return to determine range (Hodgson et al. 2005). This can be used to build either 2-dimensional or 3-dimensional scenes. To determine snow depth, the scene is imaged with and without snow and then differenced, resulting in a snow volume and snow depth estimate at each specific point. The use of LiDAR has a lot of advantages. The first is that it can be used to cover large areas in an unobtrusive manner. It is also highly accurate, with accuracies down to the millimeter level in some cases (Osterhuber et al. 2008).

LiDAR has been deployed two different ways to determine snow depth. The most accurate way is to deploy the LiDAR system on the ground. Osterhuber et al. (2008) used a ground based unit that could either be placed on the ground or fixed to a surveyor's tripod. In a snow pack with an average depth of just over two meters the LiDAR averaged a mean difference between manual and LiDAR measurements of 5.7 cm. While the use of the ground-based system has potential, it also has some drawbacks. The system currently being used has a range limited to 1000 meters. Also, to generate a 3-D image, either multiple sensors are required or the LiDAR has to be moved to different scanning locations. Furthermore, LiDAR becomes ineffective with any obscuring weather phenomena such as clouds, fog, or precipitation. This system may prove to be a great way of measuring snow depth at fixed locations but is not a good option for large regions of land or remote areas where a ground-based unit has not been placed.

The second way to deploy LiDAR is to operate the system from either an aircraft or a spaceborne platform. Airborne LiDARs, also known as laser altimetry, are much better suited to cover large regions or remote areas than the fixed based systems (Hodgson et al. 2005). Airborne LiDAR depends on knowing the speed of light, the

location of the laser emitter, and being able to time the laser pulse transmission to reception time. These data, like the ground based systems, can be used to generate a 3-D image or terrain model with a resolution at sub-meter level (Hopkinson et al. 2004). This has the same restriction as the ground based system in the fact that the laser path has to be free of visual obscurations. Accuracy also depends on the ability to position the aircraft to a high degree of x, y, z accuracy, which can potentially be problematic. Furthermore, there are a limited number of platforms that are currently equipped to perform this task.

E. INSAR AND TOMOGRAPHIC SAR

The approaches investigated in this research are based on radar (radio detection and ranging) characteristics, principals and theory, utilizing Interferometric Synthetic Aperture Radar (InSAR). Discussion of this topic first requires a review of Synthetic Aperture Radar (SAR) basics. Radar uses radiation emitted from an antenna in the microwave region of the electromagnetic (EM) spectrum. The wavelengths most commonly used are on the order of 1.5cm to 1m, or approximately 20GHz to 300MHz (Richards 2009)(Figures 1 and 2). This frequency range is broken down into bands with L- (1.0-2.0 GHz), C- (4.0-8.0 GHz), and X-bands (8.0-12.5 GHz) as the most commonly used for remote sensing as seen in Figure 2. This emitted energy travels to a target and is then reflected back to the original, or in some cases an alternate antenna. The time it takes this radiation to travel the distance to and then back from the target is measured. Using the speed of electromagnetic propagation, this allows an estimate of the range to the target (Carrara et al. 1995). The properties of the microwave portion of the EM spectrum in particular make it a good option for transmission through the atmosphere. Microwave frequencies are able to pass freely through the atmosphere and through visible obscurations such as clouds and precipitation, allowing them to detect objects where optical wavelengths would be either absorbed or scattered. The atmospheric transmittance per frequency is annotated in Figure 1. Observe that the lower end of the microwave region used for remote sensing, or about 20GHz, has strong transmittance through the atmosphere and rapidly increases to near 100 percent as the frequency decreases.

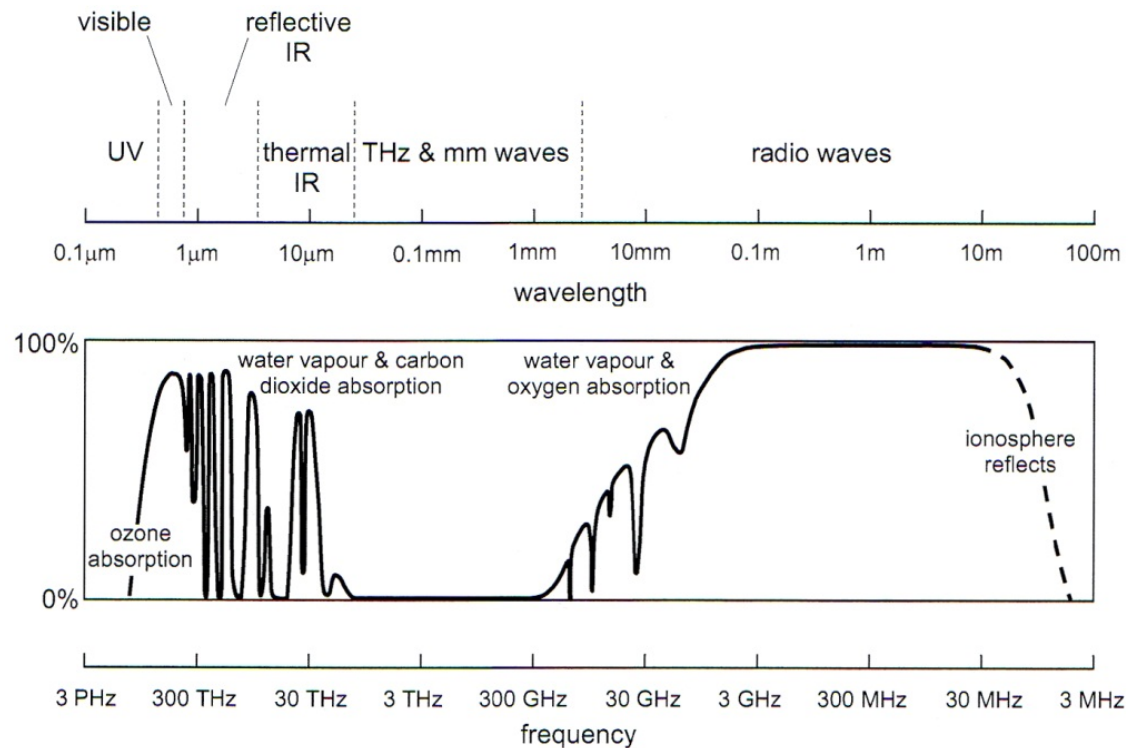


Figure 1. The electromagnetic spectrum and the indicative transmittance of the atmosphere on a path between space and the earth (Richards 2009).

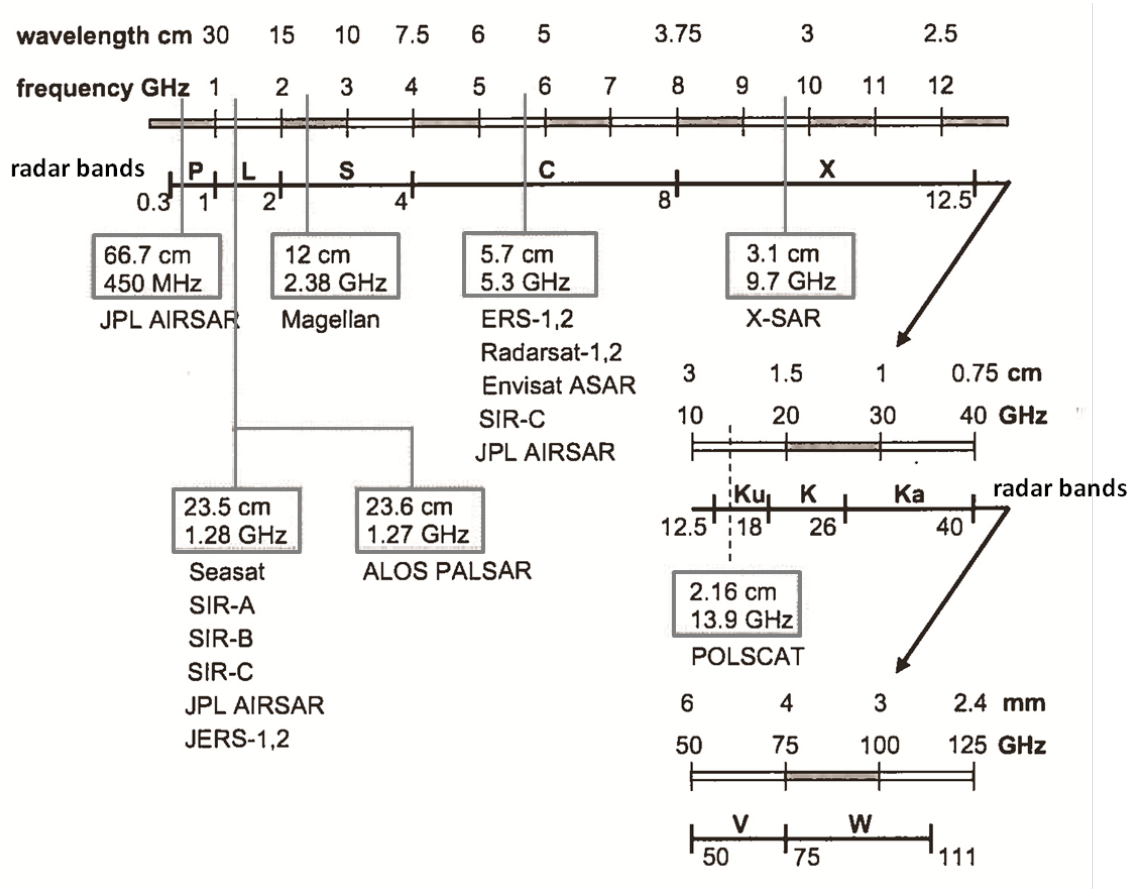


Figure 2. The microwave portion of the electromagnetic spectrum is broken down into bands with L- (1.0-2.0 GHz), C- (4.0-8.0 GHz), and X-bands (8.0-12.5 GHz) as those most commonly used for remote sensing (Richards 2009).

SAR takes the use of radar one step further. Typically SAR systems are configured in a side-looking manner. Real aperture radar (RAR) has limitations in resolution based on the beam-width “ β ” and the distance to the target. The beamwidth is dependent on the wavelength “ λ ” and the physical length of the antenna “ l_a ” and is given by equation (1) (Jakowatz, et al. 1996)

$$\beta = \frac{\lambda}{l_a} \quad (1)$$

When the radar pulse travels away from the radar it spreads out. This beam spreading can be seen in Figure 3. The radar antenna will receive a return from all objects within the footprint that are at an equal distance from the source. Because the arc

of the radar increases with increased range, the azimuthal distance required to distinguish between targets will also increase with range. In other words, the ability to resolve objects of a certain size in the azimuth direction of a side-looking radar will decrease as distance from the antenna increases. This can be a real problem when using radar for imaging rather than for detection. The azimuthal resolution, “ r_a ”, on the ground with a range R_0 and beam-width β is given by (2) (Jakowatz, 1996 and Richards, 2009).

$$r_a = R_0 \beta \quad (2)$$

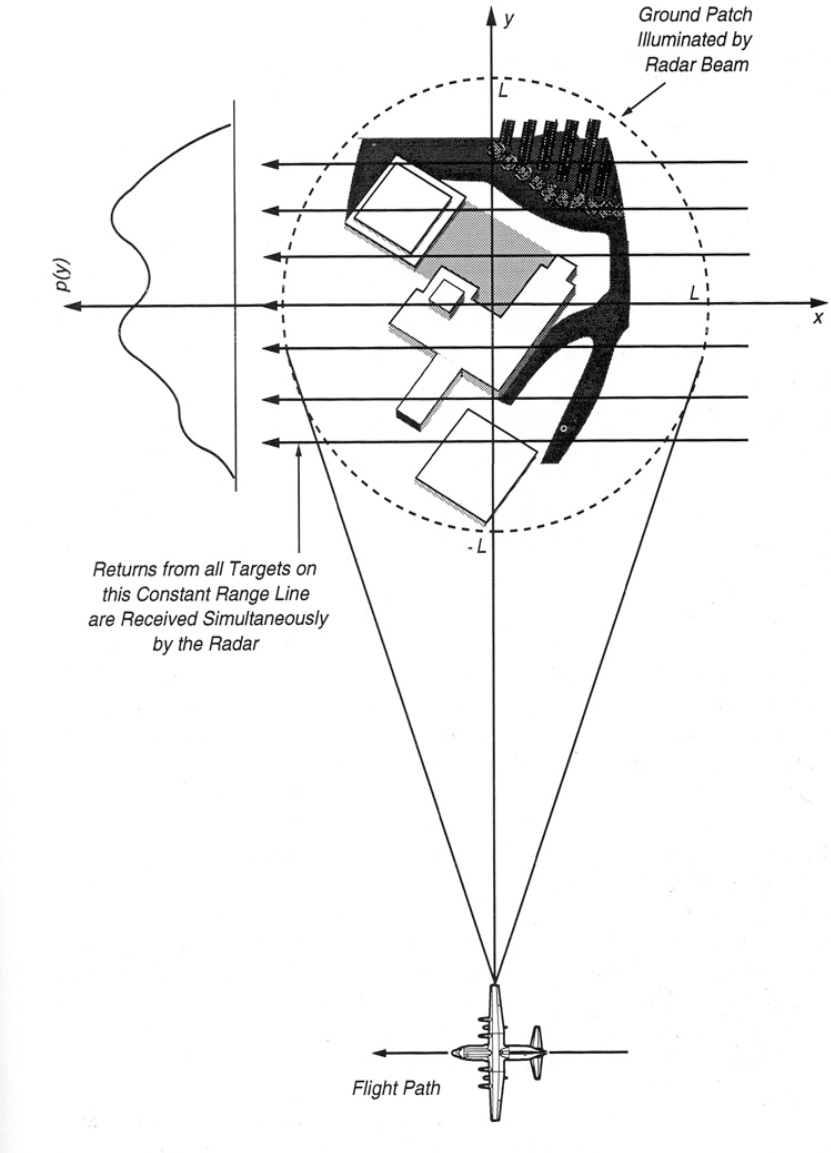


Figure 3. Imaging scenario depicting the cross-range resolvability issue. Targets lying on the same constant-range line but separated in cross range cannot be distinguished in the return of a single pulse when a broad beam is used to illuminate the entire ground patch, where L represents the patch radius and $p(y)$ represents range on the ground in the direction perpendicular to the flight path (Jakowatz, 1996).

As mentioned in the preceding paragraph, the beam width is dependent on the size of the antenna. The larger the antenna, the smaller the beam width, and the greater the resolution. Unfortunately there are limitations to the physical size of the antennas that can be used, especially for airborne and spaceborne radars. SAR solves this problem by

using the forward motion of the platform to which the radar is attached to synthesize an apparently longer antenna, as seen in Figure 4 (Richards 2009). SAR irradiates a target multiple times as it passes that target. Through processing of the multiple images, a larger antenna or narrower beam is synthesized. The SAR azimuthal resolution r_a is given by (3) where physical antenna length is “ l_a ”

$$r_a = \frac{l_a}{2} \quad (3)$$

Notice that, unlike real aperture radar, there is no dependence on the absolute range from the antenna to the target, or the wavelength used. This is what allows SAR to have improved resolution at the ground compared to RAR (Richards, 2009).

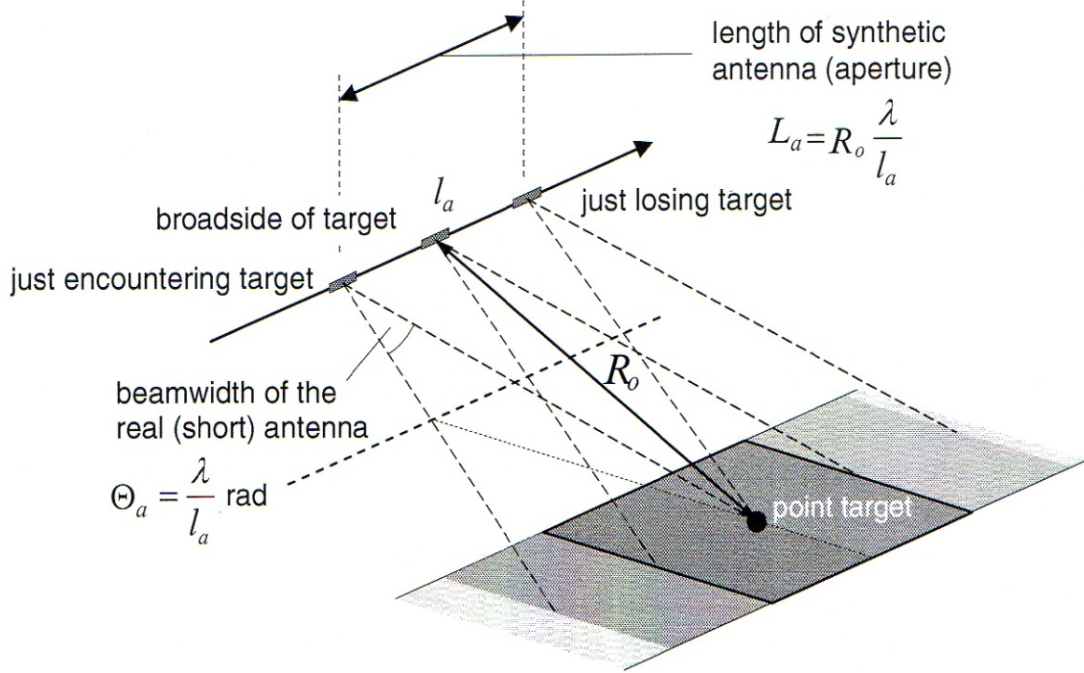


Figure 4. The concept of using the platform motion to synthesize an effectively long antenna; the footprint of the real antenna on the ground is shown as rectangular for simplicity, where “ L_a ” represents the length of the synthetic antenna, “ l_a ” represents the physical length of the antenna, “ R_0 ” represents the range, “ λ ” represents the wave length and “ θ_a ” is the beamwidth (Richards 2009).

As a side note, there is no significant distinction between SAR and RAR with respect to slant range resolution. Ground range (the range directly below the antenna to

the target) resolution is dependent on the slant range resolution. Both the slant range and ground range resolutions are dependent on the width of the radar pulse “ τ ” and the incidence angle “ θ ” (Figure 5). The slant range resolution “ r_r ” can be given by

$$r_r = \frac{c\tau}{2} \quad (4)$$

The speed of light “ c ” is treated as a constant. Correcting for the incident angle, the ground range resolution “ r_g ” can be given as

$$r_g = \frac{c\tau}{2 \sin \theta} \quad (5)$$

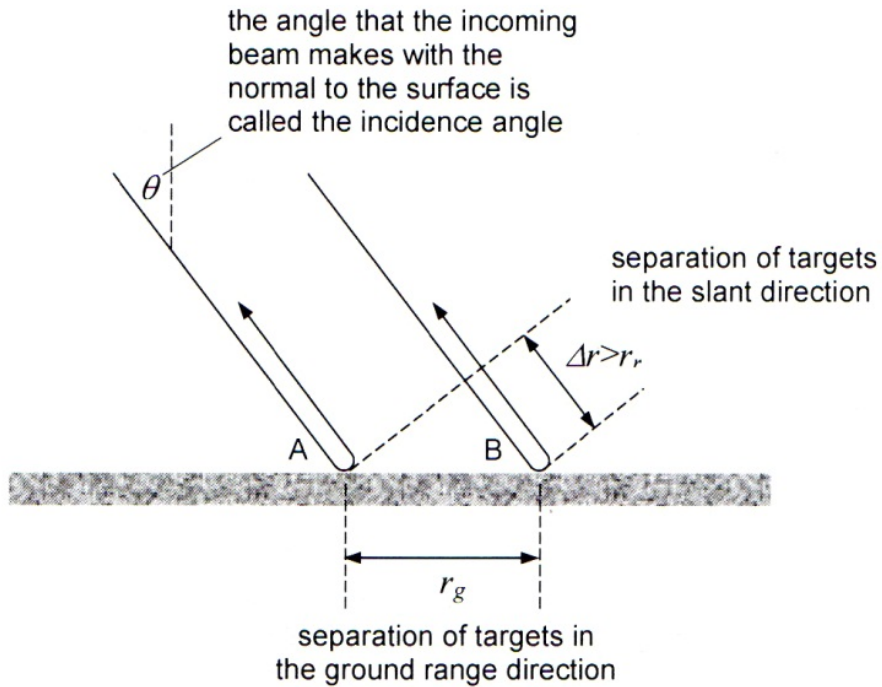


Figure 5. Geometry for computing range resolutions. “ r_g ” represents the difference in ground range with respect to the radar antenna, “ r_r ” is the slant range resolution, “ Δr ” the difference in the slant range between targets A and B, and “ θ ” is the incidence angle between the incoming beam and the normal to the surface.
(Richards 2009)

Interferometric SAR (InSAR) is a quantitative step beyond SAR imaging. InSAR capitalizes on the capability to measure the phase angle of the SAR return. The

transmitted phase is known and the return phase can be measured. This allows determination of relative distances from the sensor to the ground, and thus the determination of topography or topographic displacement. InSAR has been used for the last two decades for topographical mapping or DEM generation (Richards 2009).

The aforementioned difference between the transmitted phase and the received phase, ϕ_T , is given by (6) (Richards 2009)

$$\phi_T = \frac{4\pi R}{\lambda} \quad (6)$$

where “R” represents the one way path length and “ λ ” is the operating wavelength of the radar. Observe that the phase difference, ϕ_T , will change between two adjacent pixels as the total path distance changes. In other words the phase angle change is proportional to the difference in path lengths between targets. Therefore, since we can measure phase we should be able to directly measure the difference in the path length between targets to a very high degree of accuracy. There is however a potential ambiguity. Any change in elevation of an object that stands above or below the plane being imaged will cause a coincident return of the same phase. This can be seen in Figure 6 (a) between points “a” and “c”. This ambiguity prevents us from being able to resolve the difference between “a” and “c”.

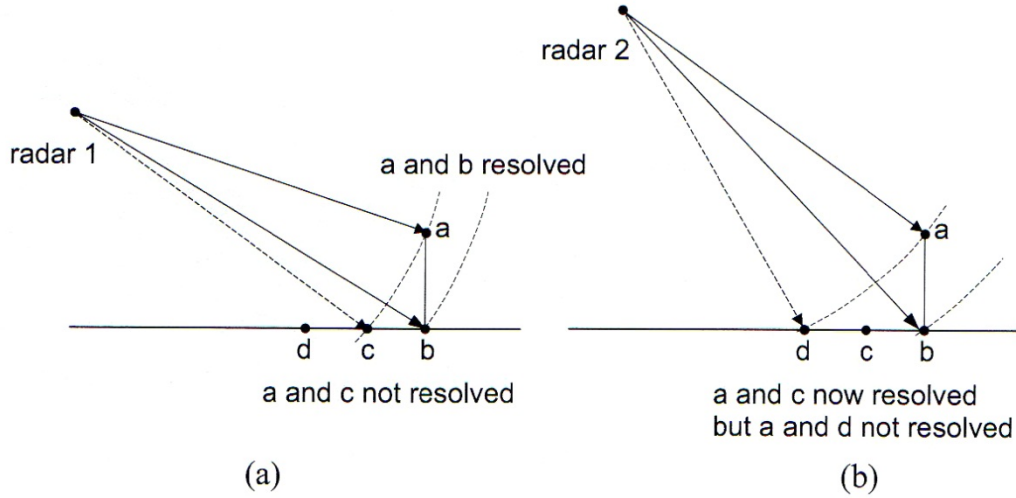


Figure 6. (a) Even though the topographic variation between a and b is resolvable, there is ambiguity between a and c (b) resolving the a and c ambiguity by changing the radar position, but causing ambiguity at a and d (Richards 2009).

This ambiguity can be overcome by changing the position of the radar as seen in (b). The change in the radar's position however causes other potential ambiguities, as can be seen between points "a" and "d". Considering both view angles at the same time, the ambiguities can be resolved. This is the basis of interferometry (Richards, 2009), (Figure 7).

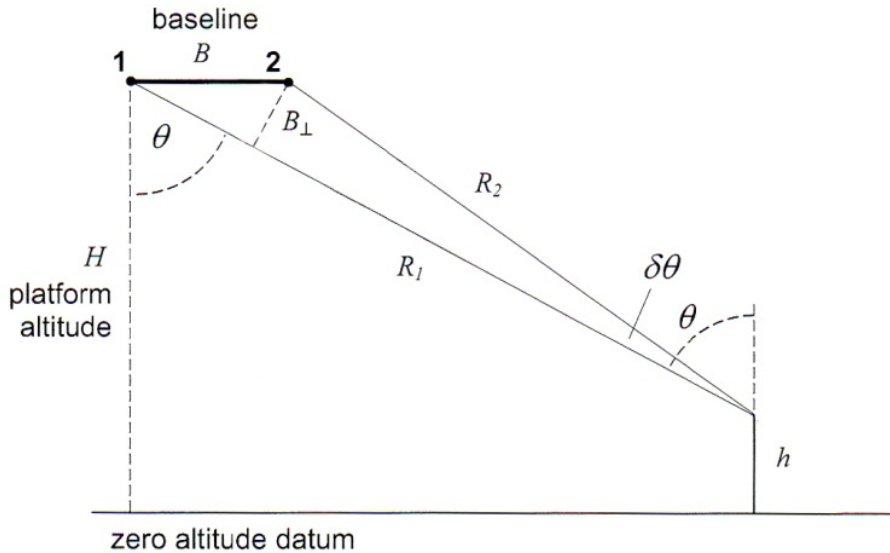


Figure 7. Geometry for single baseline SAR interferometry, in which the look and incidence angles are assumed to be the same. “ R_1 ” and “ R_2 ” are the respective ranges from antennas 1 and 2. “ B ” represents the baseline between the two antenna locations. “ B_{\perp} ” represent the orthogonal baseline between the two radar beam paths. “ θ ” and “ $\delta\theta$ ” represent the incidence angle and the change in incidence angle respectively (Richards 2009).

Figure 7 and accompanying discussion illustrates how these two view angles can be used and introduces the concept of the orthogonal baseline. Points 1 and 2 indicate the positions of the platform where the two datasets are acquired. Line “ B ” that connects these two positions indicates the *baseline*. A line is drawn perpendicular from the first slant range to position 2 and is referred to as the *orthogonal baseline*, “ B_{\perp} ”. There are limitations on the length of the orthogonal baseline known as the *critical baseline*. This is important because it allows the measurement of the difference in the length of the slant range in terms of the phase or as a percentage of the wavelength. This change in phase between the different view angles of the same target is how InSAR can be used to generate DEMs. This process is also referred to as tomographic SAR.

Using Figure 7, the difference in the path lengths “ R_1 ” and “ R_2 ” in terms of the phase and a given baseline and incidence angle of “ B ” and “ θ ” respectively as shown by (Richards 2009) can be derived.

$$R_1 = R_2 \cos \delta\theta + B \sin \theta \quad (7)$$

$\delta\theta$ is assumed to be approximately 0 using the plane wave approximation. The plane wave approximation considers the change in the incidence angle to approximate 0 when the target is infinitely far away when compared to the length of orthogonal baseline. This results in

$$R_1 = R_2 + B \sin \theta \quad (8)$$

Therefore

$$\Delta R = R_1 - R_2 = B \sin \theta \quad (9)$$

The difference in phase angle “ $\Delta\phi$ ” associated with the change in path length “ ΔR ” between the two passes can then be given as

$$\Delta\phi = \frac{4\pi B \sin \theta}{\lambda} \quad (10)$$

This difference in phase angle is referred to as *interferometric phase angle* $\Delta\phi$. $\Delta\phi$ can be obtained directly by simply imaging an area twice and taking the difference of the two recorded phases.

The next step is to determine the relationship between the topographic height “ h ” and the incidence angle in order to get the phase to height ratio (Figure 8).

From Figure 8, if “ H ” is the total height above an assumed altitude, and “ R_0 ” is the range to the target, observe that

$$h = H - R_0 \cos \theta \quad (11)$$

Taking the partial derivative of the topographic height with respect to the incidence angle results in

$$\frac{d(h)}{d\theta} = R_0 \sin \theta \quad (12)$$

Then taking the partial derivative of the interferometric phase angle $\Delta\phi$ with respect to the incidence angle also results in

$$\frac{d(\Delta\phi)}{d\theta} = \frac{4\pi B \cos \theta}{\lambda} \quad (13)$$

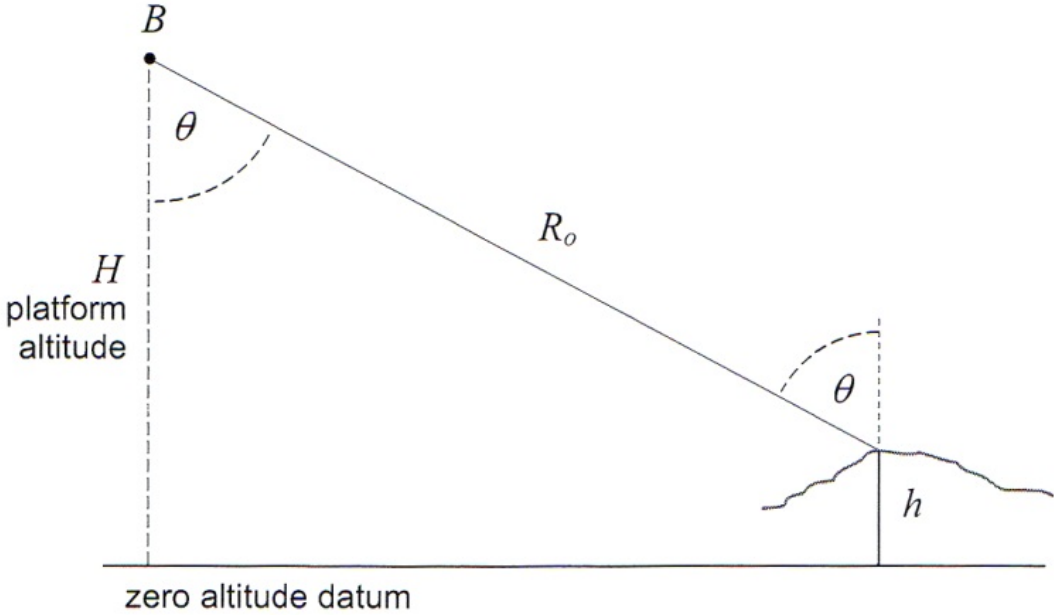


Figure 8. Determining the relationship between topographic height “ h ” and incidence angle “ θ ” with a platform altitude of “ H ” and range to the target of “ R_0 ” (Richards 2009).

Combining equations (12) and (13) results in

$$\frac{d(\Delta\phi)}{dh} = \frac{d(\Delta\phi)}{d\theta} \frac{d\theta}{d(h)} = \frac{4\pi B \cos \theta}{\lambda R_0 \sin \theta} \quad (14)$$

We now have an expression for the change in interferometric phase with respect to the change in topographic height. Taking it one step further to make it more user friendly results in

$$\frac{d(\Delta\phi)}{dh} = \frac{4\pi B_{\perp}}{\lambda R_0 \sin \theta} = \frac{4\pi B_{\perp} \cos \theta}{\lambda(H-h) \sin \theta} \quad (15)$$

So as long as the incidence angle is known, the elevation above some known reference height ($H-h$) and the orthogonal baseline, the rate of change in elevation across an interferometric phase diagram per change of radian can be predicted. An interferometric phase factor α_{IF} can be defined as

$$\alpha_{IF} = \frac{dh}{d(\Delta\phi)} \quad (16)$$

and the height of a specific pixel will be given by

$$h(x, y) = \alpha_{IF} \Delta\phi(x, y) + CONSTANT \quad (17)$$

Equation (17) enables the generation of a DEM. This ability to use InSAR to generate a DEM is ultimately the basis of this research. The use of high resolution DEMs will be used to explore a new technique to solve for the snow depth.

THIS PAGE INTENTIONALLY LEFT BLANK

III. METHODOLOGY

A. RESEARCH APPROACH

This research used SAR data in an approach similar to that taken for airborne LiDAR determination of DEMs. Interferometric (tomographic) SAR, InSAR, was used instead of laser altimetry to map both the bare ground and the snow covered ground. Snow cover effectively acts to change the elevation of the surface. Taking the difference between the two DEMs, Snow On and Snow Off, allows for determination of snow depth and snow volume over a specified area. InSAR has a couple of advantages over LiDAR. Because SAR operates in the microwave region of the electromagnetic spectrum, it can be used when there are obscurations such as clouds and precipitation. These obscurations are common during winter and can be a limiting factor for the laser based systems. From an operational standpoint, InSAR has another advantage. There are numerous platforms currently carrying SAR for other purposes, most notably the MQ-1 Predator and MQ-9 Reaper (General Atomic Aeronautical 2012). These can potentially be adapted for operational InSAR snow depth determination.

Two different SAR approaches were explored. The first approach, referred to as the “Baseline Method”, attempted to calculate the baseline between two different data sets’ locations. The second method, referred to as the “Best Fit Plane Removed Method” (BFPR), circumvents the need to calculate the baseline and determines the difference in the Snow On and Snow Off terrain by removing a best fit plane (BFP).

The proposed approaches have not previously been taken before for snow depth measurement for a couple of reasons. Generally speaking, active airborne and spaceborne radar tend to penetrate the snowpack, making it impossible to infer the snow-air interface. This is primarily due to the frequency (wavelengths) used. Most SAR systems tend to use L- (1.0-2.0 GHz), C- (4.0-8.0 GHz), and X-band (8.0-12.5 GHz) radars. All of these bands significantly penetrate the snow pack (Ulaby, 1982). In these bands, with the exception of using a radar with a relatively high power output located at close range to a target such as that used with ground penetrating radar, there is not

enough backscatter from the snow pack to identify the snow-air interface. The longer wavelengths primarily show volume scattering, which varies depending on the condition of the snow. It has been demonstrated by Ulaby, 1982, however, that shorter wavelength (higher frequency) SAR systems such as Ku- and Ka-band do not penetrate the snow pack as far as other longer wavelength systems, Figure 9. This research takes advantage of the fact that the SAR used on the MQ-1 Predator and MQ-9 Reaper platforms uses a shorter wavelength or higher frequency (Ku-band) radar. This higher frequency should penetrate less into the snow pack, resulting in a greater interaction at the snow-air interface and leading to successful snow depth determination.

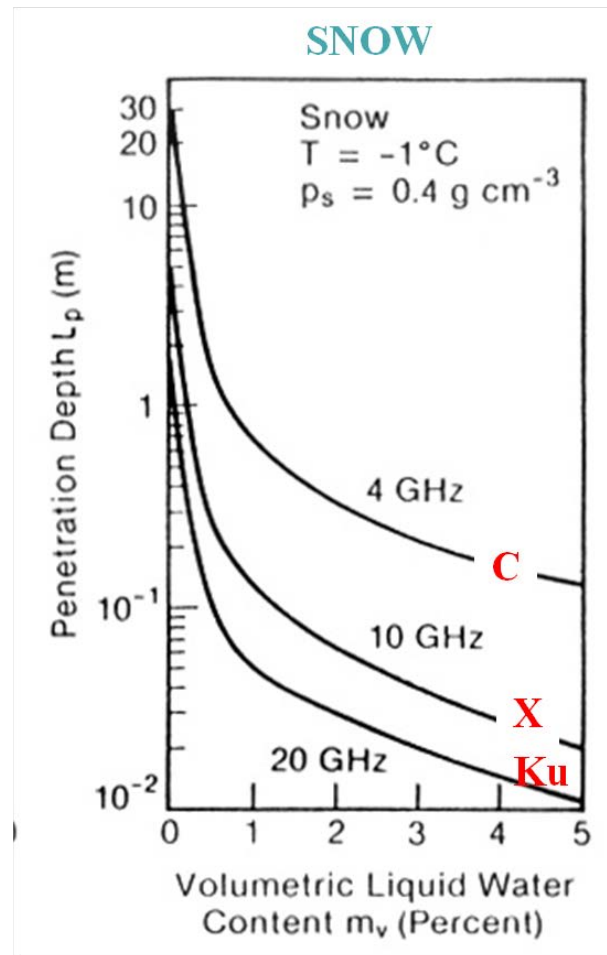


Figure 9. Penetration depth as a function of frequency. Ulaby et al. 1982 demonstrates that as frequency increase, the penetration into the snowpack decreases. In contrast, lower frequencies will penetrate further into the snowpack.

B. SAR DATA COLLECTION AND FIELD WORK

Unfortunately, no archived data sets were available at the start of this research that would allow exploration of the InSAR snow depth mapping concept using short-wavelength SAR. Therefore, in order to explore this approach, a new SAR data set was collected and processed. Furthermore, direct measurements of snow depth were made to validate and determine the accuracy of the results. The field work and data collection consisted of four parts; (1) aircraft SAR data collection, (2) site selection and preparation, (3) site survey, and (4) validation.

1. Aircraft SAR Collection

The first portion of the field work and the ultimate tool used in this approach was the airborne SAR collection. General Atomics Aeronautical (GAA), the manufacturer of the Lynx Ku-band radar (Tsunoda et al. 1999), agreed to fly collection missions to generate the raw radar datasets necessary for the technique. The collection for this research was done using a Lynx II SAR mounted to a King Air aircraft. As stated earlier this is the same ground imaging radar that is used on many military aircraft. The radar itself is a Ku-band radar that operates at a 15.2-18.2GHz frequency with a wavelength of 1.8cm. The maximum slant range of this system is 30km. There are multiple ground resolution options, to include 0.1, 0.3, 1.0, and 3.0m. Table 1 indicates the SAR images used in this study. The radar can be operated in different modes to include spotlight, strip-map, and coherent change detection (Tsunoda et al. 1999). For the purposes of this research, multiple passes were made at both the 0.1 and 0.3m resolutions using the spotlight mode. Both Snow On and Snow Off collections were flown on 3 April 2012 and 13 July 2012 respectively. The actual flights were flown at a flight level of 5330m and approximately 10km to the south of the collection area with the radar looking north.

SAR Image number	Date	Time	Surface Condition
01	3 April 2012	18:47 Z, 10:47 L	snow covered
02	3 April 2012	18:55 Z, 10:55 L	snow covered
03	3 April 2012	19:04 Z, 11:04 L	snow covered
04	3 April 2012	19:00 Z, 11:00 L	snow covered
21	13 July 2012	17:58 Z, 10:58 L	bare
22	13 July 2012	18:05 Z, 11:05 L	bare

Table 1. Four usable Snow On and two useable Snow Off SAR images at 0.1m resolution were acquired by General Atomics during the radar collection phase of the research. These images enabled six Snow On and one Snow Off interferometric pairs to be calculated.

2. Site Selection and Preparation

The second aspect of the field work revolved around the site preparation. First an appropriate site had to be chosen. There were several requirements to consider in the site selection. They were: sufficient snow depth, relatively obstacle free, clear view of sky, relatively flat i.e. no steep slopes relative to the resolution, accessibility, and within the General Atomics flight radius centered in San Diego, California. It must be noted here that the first criterion of sufficient snow depth played a major role in site selection. Due to the low snow fall in the 2011–2012 winter and dissertation time restrictions there were not many viable options. Mammoth Mountain, California (Figure 10) ultimately met the requirements better than any other location.

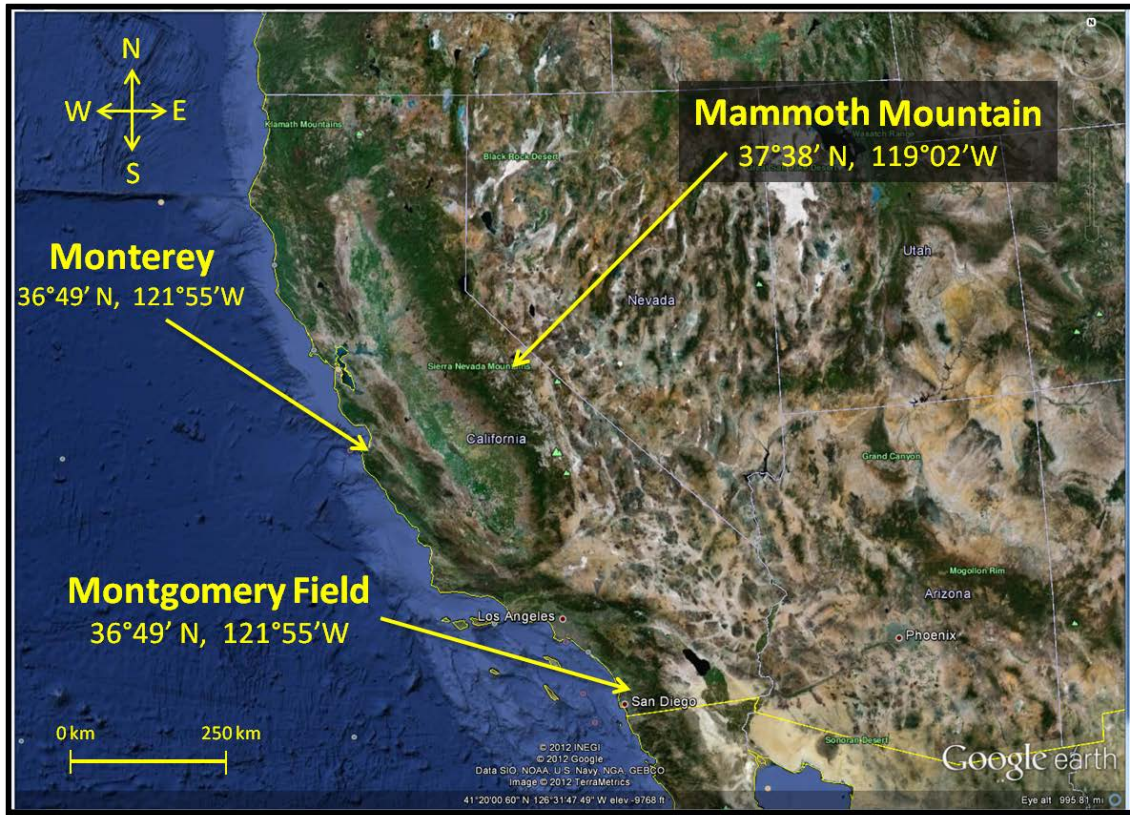


Figure 10. Map depicting relationship between General Atomics home airfield and Snow study site at Mammoth Mountain, CA (Google Earth 2012).

Mammoth's higher elevation with respect to other sites provided a greater and longer lasting snowpack. Ski lifts made many of the higher elevation areas accessible. It was also within the GAA flight radius. In addition, it also a Cold Regions Research and Engineering Laboratory (CRREL) snow study site situated there and the Mammoth Mountain Ski Patrol was both willing and interested in participating. This ultimately made a big difference. Their local knowledge of the mountain and surrounding areas were key to identifying good locations in the time allotted. With their help, eight possible collection locations were identified. SAR data were ultimately only collected for one site, "Elysian Fields," shown in Figure 11.

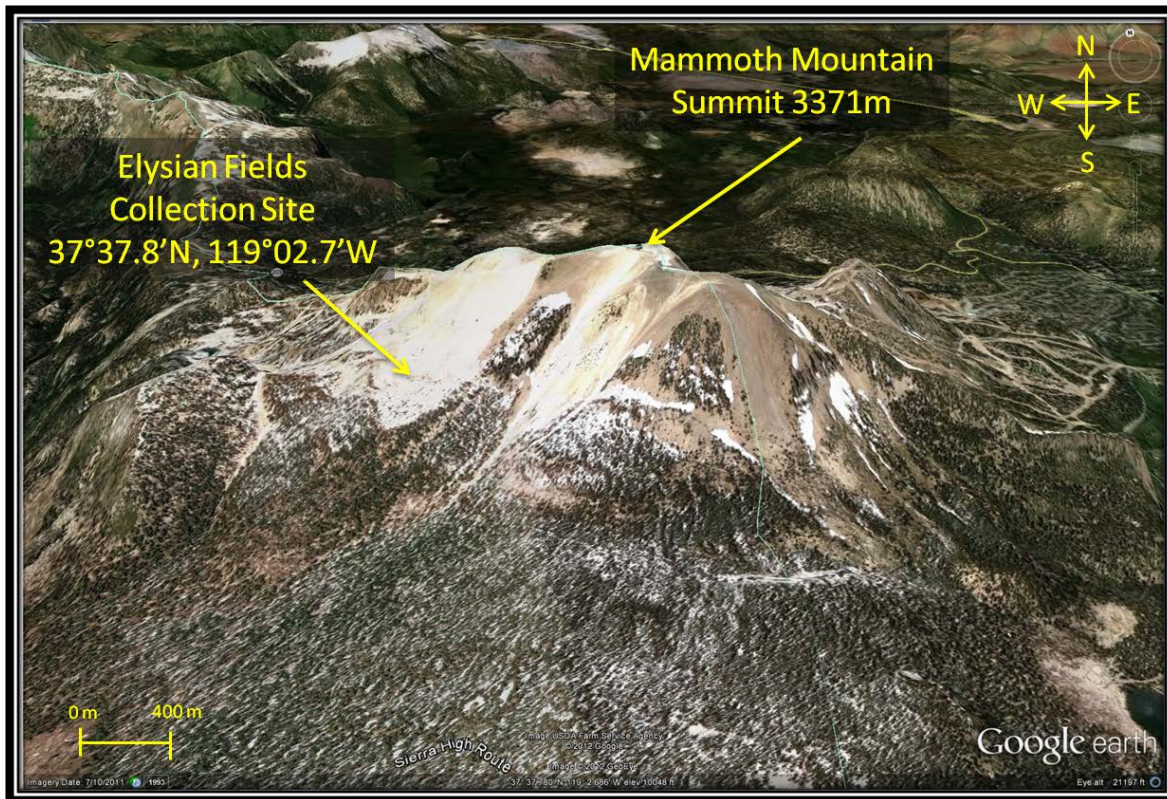


Figure 11. Google Earth 3D perspective view of Elysian Fields collection area looking northward towards Mammoth Mountain, CA (Google Earth 2012).

The generation of InSAR images and production of DEMs from airborne radar data is not a straightforward process. One of the things that can be done to increase the accuracy is the use of ground control points (GCP), also commonly referred to as tie points. This can be done using natural features or manmade features or equipment. Manmade GCPs, specifically corner reflectors (CR), however, provide several orders of magnitude greater radar return than that of the surrounding terrain. Highly reflective CRs make it much easier to identify specific locations in each image. Their use removes much of the ambiguity in the DEM generation process. In addition to the generation of the InSAR images and DEMs, the CRs/GCPs can be used to warp the Snow On and Snow Off DEMs for the differencing phase of the processing. Furthermore, they can be used to extract information that can be used to determine the baseline between the two flight paths used in the generation of an interferometric image. There are several

different configurations that can be used in the construction of corner reflectors. Examples of these are shown Figure 12.

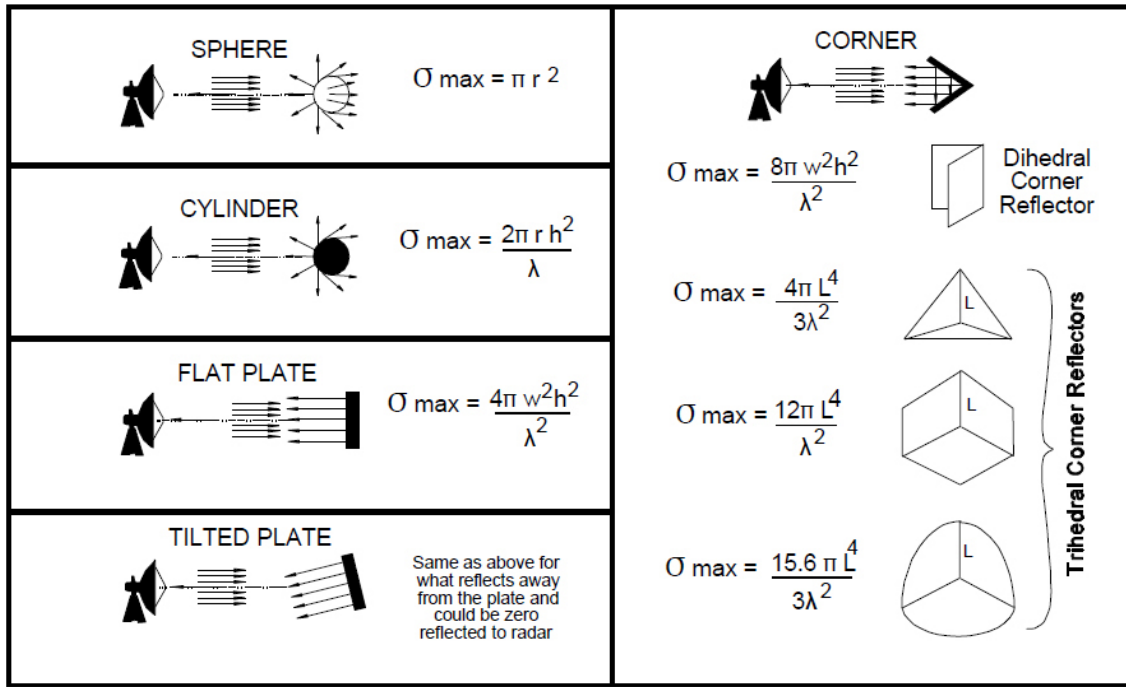


Figure 12. Backscatter from various shapes and corresponding radar cross section equations (Granit Island Group, 2013).

With this in mind, trihedral radar reflectors were chosen to be deployed at selected ground locations in the collection area. Through coordination with Douglas Bickel at Sandia National Laboratory, the laboratory that designed the Lynx II radar, the optimum radar cross section required for best radar response was determined to be 25dBsm and field-portable trihedral reflectors were designed and fabricated, Figure 13. These field portable corner reflectors facilitated the ability to transport a total of five reflectors and tripods in a single backpack to the collection sites.



Figure 13. Lightweight portable corner reflectors were designed to be broken down for use in the field. Five of these along with their stands could easily be put in to a backpack and either skied or hiked in to the SAR collection areas.

Two of the eight identified sites were chosen for SAR collection. These sites will be referred to as “Elysian Fields” and the “CRREL snow study site.” Ultimately, while both sites were prepared for the collection, due to flight time restrictions, SAR data were collected only on Elysian Fields. Site preparation for the Snow On collection took place on the first and second of April 2012. The first step in preparing the sites was to identify the center of the SAR collection areas. These coordinates were taken on the earlier performed site survey. With these coordinates in mind, locations for the corner reflectors

were chosen. The initial plan for the Elysian Fields collection area was to place the corner reflectors 100 meters apart in the shape of a square centered on the target location coordinates. This had to be adjusted during site preparation because a 100m square encroached into the tree line on the south side and up against the ski area boundaries on the north side. Therefore, the reflectors were adjusted to be approximately 80 meters apart in the north-south direction while the east-west direction remained at 100 meters (Figure 14). The snow was excavated to the ground at each corner reflector location to emplace the tripods. The GPS locations were recorded and a stake was placed to mark the location. The stake was critical to allow for return of the reflectors to the same location during the Snow Off SAR collection. The snow pits dug for the corner reflectors varied between 1.5 to 2.3 meters in snow depth at this collection site. Three of the four tripods were positioned directly on the bare ground and allowed the reflector to be at or above the snow line, making them visible to the radar (Figure 15). The fourth tripod, in the deepest pit, was positioned with its legs placed into the side walls of the pit at a height that allowed the reflector to be visible to the aircraft. All the reflector stands were then staked and tied down. The reflectors were attached to the heads of the tripods on the day of the collection with a clear view of the sky towards the flight track. They were pointed due south or 167° magnetic and with an elevation angle of -13° to correspond with GAA SAR parameters and planned flight-lines. The direction was determined with a magnetic compass and verified with a GPS compass. The elevation angle was accomplished with a carpenter's protractor. This proved to provide a very well pointed reflector and the aircrew could clearly identify the reflectors; thus no additional adjustments were required.

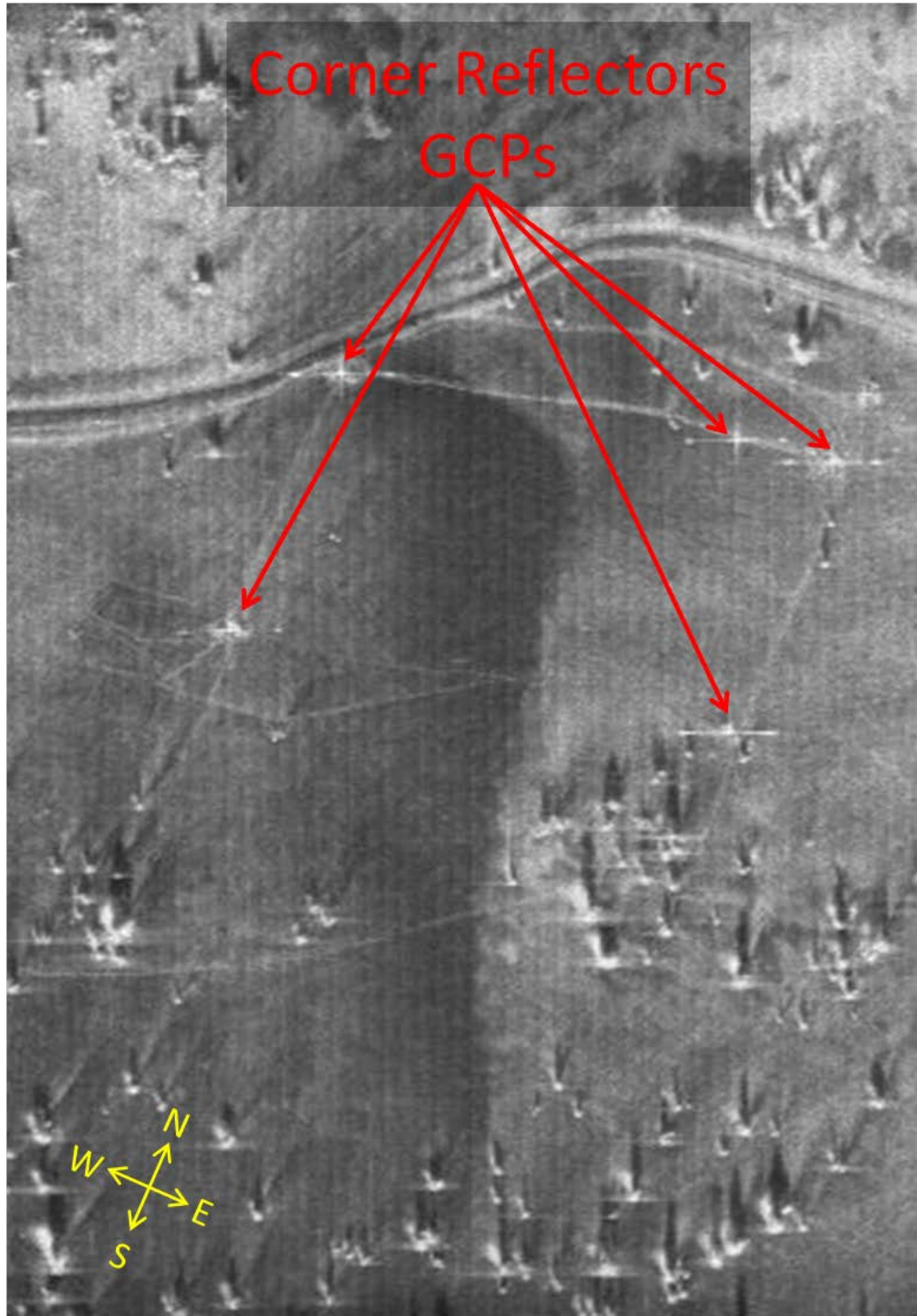


Figure 14. Corner reflector orientation at Elysian Fields collection site during Snow On SAR collection ($37^{\circ}37.7'N$, $119^{\circ}02.7'N$). The image area is 312 x 176m with the N-S corner reflectors 80m apart and the E-W corner reflectors 100m apart. Magnitude image provided by General Atomics Aeronautical.



Figure 15. Deployment of corner reflectors used as ground control points at Elysian Fields collection site.

The Snow Off collection was similar to the Snow On collect. The majority of the site preparation was done the day of the collection, Friday 13 July 2012. Initially, the trihedral reflectors were set up at the same four locations as during the Snow On collection. They were mounted on tripods as before and raised to the same recorded elevation above the bare ground as the initial collection. One tripod, the northwest corner, had to be modified. This location is where the tripod could not be placed on the ground due to snow depth. For this collection, an extension was manufactured for the tripod legs out of three-sided channel aluminum. This proved to be stable and strong enough to meet the requirements. Once the tripods were positioned and brought to the correct elevation above the ground, the reflectors were attached and pointed as before.

Five additional reflectors were put in place during the Snow Off collect to help assess SAR accuracy (Figure 17). They were positioned directly on the ground and pointed in accordance with the previous mentioned procedures. Four of the reflectors were placed approximate 35 meters out in a diagonal direction from the four already established reflectors. The fifth one was placed in the center of the square formed by the already established reflectors. The resulting shape was an “X” pattern. It should be mentioned that the additional reflectors were intended to help improve the accuracy of the interferogram processing and the subsequent DEM. They were not however directly used as control points when comparing the Snow On and Snow Off images since they were not present during the Snow On collection.



Figure 16. Corner reflector deployment for Snow Off SAR collection.

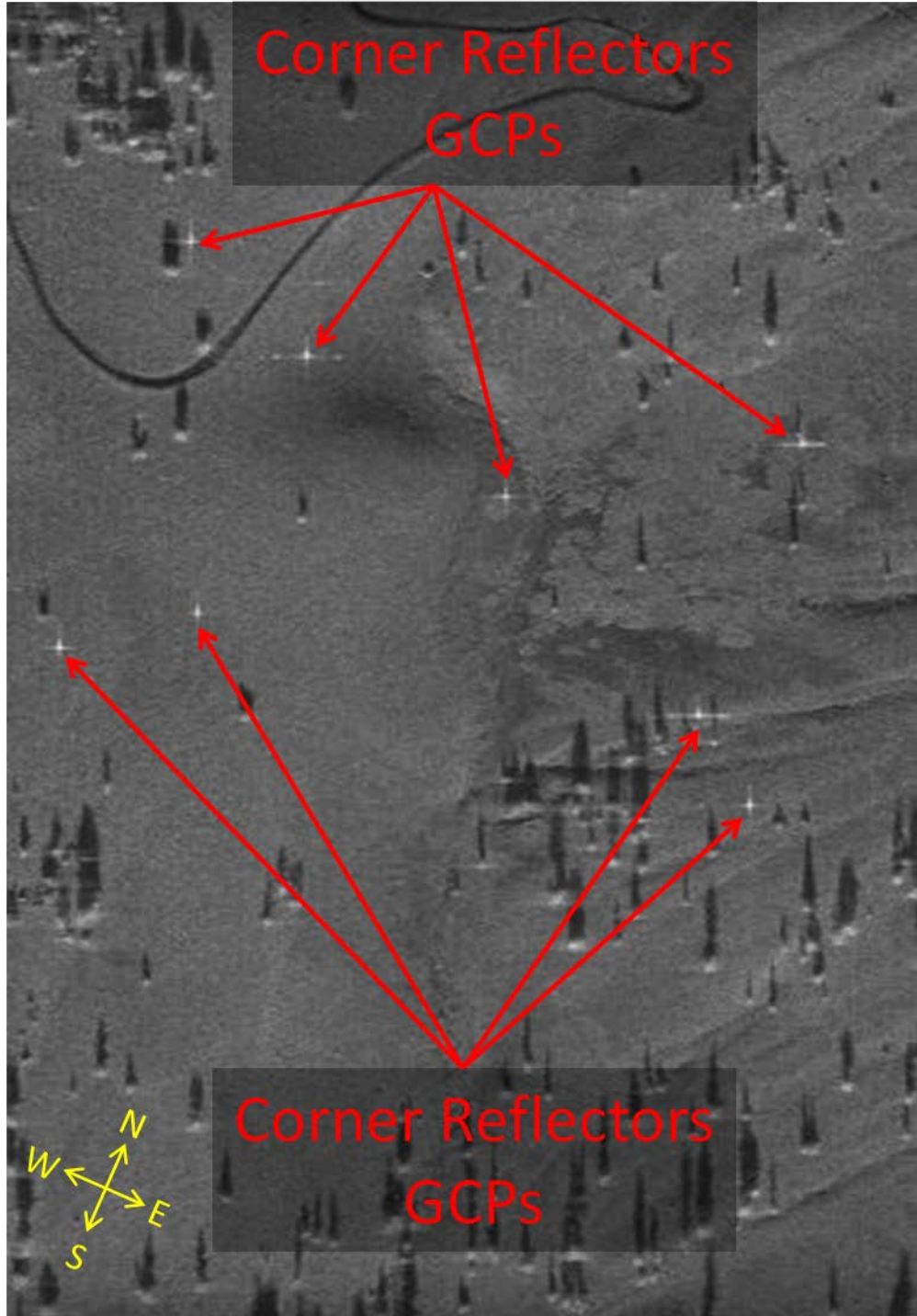


Figure 17. Corner reflector orientation at Elysian Fields (312 x 176m) collection site during Snow Off SAR collection ($37^{\circ}37.7'N$, $119^{\circ}02.7'N$). The ninth corner reflector is outside the image area. Magnitude image provided by General Atomics Aeronautical.

3. Site Survey

The process of performing the calculations to determine the baseline in the Baseline method and the linear regression in the BFPR method required as much precision as possible for the corner reflector locations. According to GPS.Gov 2013, an accuracy of three meters can be expected when using standard GPS units. This is under optimal conditions and errors can easily be greater. To improve on this, a survey grade GPS was used to determine CR locations. The Trimble GeoExplorer 6000 (centimeter) was the specific unit used. Through post processing this unit is advertised to have an accuracy of 1cm in the horizontal and 1.5cm vertical (Trimble 2013). The corner reflector locations were surveyed with this unit multiple times at different times of the day for Snow Off conditions. Post processing on the surveys showed positioning consistency within a centimeter or two. Due to the limited availability of this equipment, it was only used in the surveying of the corner reflector locations.

4. Validation

The fourth aspect of the field work was the validation. To ensure that the SAR snow depth retrieval techniques' accuracy could be tested, in-situ snow depth measurements were taken concurrently with the Snow On data collection on 3 April 2012. These measurements were taken using a 1cm graduated avalanche probe immediately after the General Atomics aircrew finished collecting the datasets of the Elysian Fields area during the Snow On collection. Due to the disturbed snow directly between the corner reflectors, the measurements were taken approximately every 20 meters within the box outlined by the reflectors. A total of 16 measurements were taken in a roughly 80x80m grid. Due to the shortening of the box outlined by the corner reflectors, the in-situ snow depth grid extended outside of the planned analysis area marked by the corner reflectors to the south. In addition to these measurements, random measurements were taken further south of the planned verification area. These measurements extended into the tree-line and may provide some insight to the impacts of foliage on this method. All the snow depth measurement locations were recorded with a GPS along with calculated GPS error. In addition to these snow depth measurements, a

snow pit was dug concurrently with the SAR collection for snow analysis near the northeast CR. It included temperature readings, crystal size and type, and density measurements throughout the column.



Figure 18. An avalanche snow analysis pit was dug during the SAR collection. A vertical profile of the snowpack's temperature, crystal size, crystal type, and snow density was recorded.

C. DATA PROCESSING (BASELINE METHOD)

The Baseline InSAR data processing method is made up of several well documented steps. The path used for this method modifies the path that is described by M. A. Richards 2007 and J. A. Richards 2009 and was carried out using the MATLAB programming language. The following steps were used in the process:

- Data preparation
- Complex image generation
- Image registration

- Interferogram generation
- Phase unwrapping
- Base line determination
- Flat Earth removal
- Height to phase scaling
- DEM generation
- Snow On/Snow Off differencing
- Verification

1. Data Preparation

The SAR data, as mentioned earlier, were collected by General Atomics. The data are recorded in proprietary “.limg” files that can only be read through the General Atomics CLAW III imaging software (D. Bickel, 2012, personal communication) . The software was not directly available for this research so Sandia National Labs and General Atomics pulled the relevant data out from the Snow On and Snow Off collections respectively and shipped it to NPS as MATLAB files. The data consisted of three pieces of information for each pass. These were the raw magnitude of the reflectivity, the recorded phase, and the header data consisting of the specific flight and radar pointing information.

2. Complex Image Generation

Once the data were available in a form that could be used in MATLAB, the magnitude and phase arrays were combined to create a complex image for each pass. These complex images are required for the complex coherence calculations and are the basis for the generation of the interferogram (Richards 2009). The complex image array can be calculated as shown in (18), “j” represents the imaginary number square root of “-1”.

$$\text{Complex_image} = \text{magnitude} \times e^{\left[\frac{(j \times \text{phase}) \times 2\pi}{2^{16}} \right]} \quad (18)$$

It should be noted here that the $2\pi/2^{16}$ is a conversion factor to account for the fact that the raw phase is encoded as a 16-bit integer during the SAR collection (D. Bickel, 2012, personal communication).

3. Registration

As described in the background section, the generation of DEMs from SAR data requires two different viewing angles. For this research, this was accomplished with SAR acquisitions from two separate individual passes. The arrays or images from the first pass will be referred to as the “master” array/image and the data from the second pass will be referred to as the “slave” array/image. Because the two images are viewed from different viewing angles they have different perspectives. They therefore must go through a registration process that lines up the pixels from the slave image with those of the master image so that the proper calculations can be made.

The first step in the registration of these arrays begins with identifying control points in each of the images. Because the control points are common between the images, they can be used to help align those images. As stated earlier, control points were marked on the ground using trihedral corner reflectors. Locating these control points in the images was therefore a fairly straightforward process. The magnitude array was displayed as an image showing the collection area. Once this image was displayed, the corner reflectors were clearly visible. The values of the pixels associated with the center of the reflectors were several orders of magnitude greater than those of the surrounding pixels. Being able to clearly identify the location of the reflector center allowed for the identification of the exact X-Y location in the array. These identified locations were ultimately used in the processing that warped the slave image to the master image, which ensures that the pixel locations between the master and slave images line up correctly. This is necessary for the interferometric phase generation and any other direct comparisons made between images. The corner reflectors can be seen the “bright stars” in the zoomed in image Figure 19.

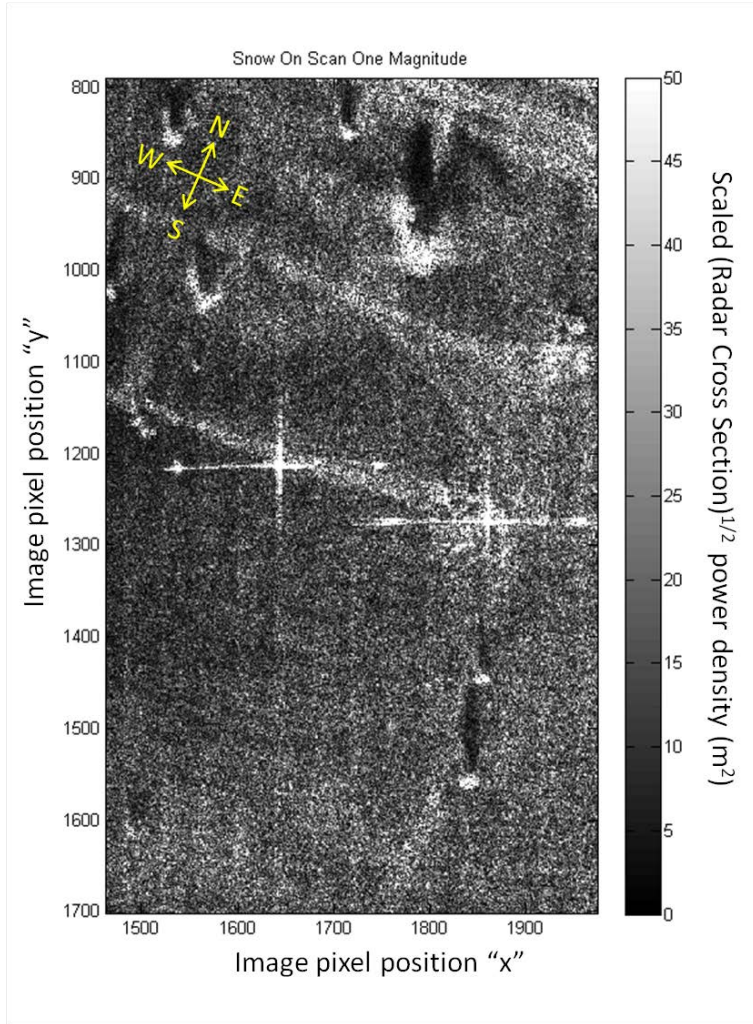


Figure 19. Magnified Snow On SAR magnitude image showing two corner reflectors. In addition to the reflectors, the walking paths can be seen in the snow as bright linear tracks. Image size 45x77m, Mammoth Mountain study site, (37°37.7'N, 119°02.7'N).

The warping process itself consists of four steps and is achieved using several specialized functions in the MATLAB image toolbox (Mathworks, 2013). Using the identified control points in both the master and slave image along with the image toolbox “cporr” function which uses normalized cross-correlation to adjust each pair of control points, the slave control points are tuned to the master control points. This provides an output that is used to generate a spatial transform that is used to warp the rest of the image. The image toolbox “cp2form” function uses the above output to create this spatial transform.

The spatial transform of the slave image unfortunately, as would be expected, causes a change in the array size. This change in array size prevents any further array calculations. Therefore it is necessary that the proper array size is maintained for performing calculations. This is easily enough circumvented using the “size” function to match the array sizes.

With the arrays the same size and the spatial transformation generated, the last step is to perform the final warping of the slave image. This is accomplished using the MATLAB image toolbox “imtransform” function, which takes the previously calculated spatial transform and applies it to the entire image.

4. Interferogram Generation

Once the slave image is properly warped to the master image, the next step is to generate the interferogram and complex coherence. The interferogram “ i ” can be calculated according to (19) (Richards 2009)

$$i(x, y) = e_1(x, y)e_2^*(x, y) \quad (19)$$

The complex master array and complex conjugate slave array are represented by “ e_1 ” and “ e_2^* ” respectively. Again, this calculation is straightforward in MATLAB. An example of an interferogram can be seen if Figure 20.

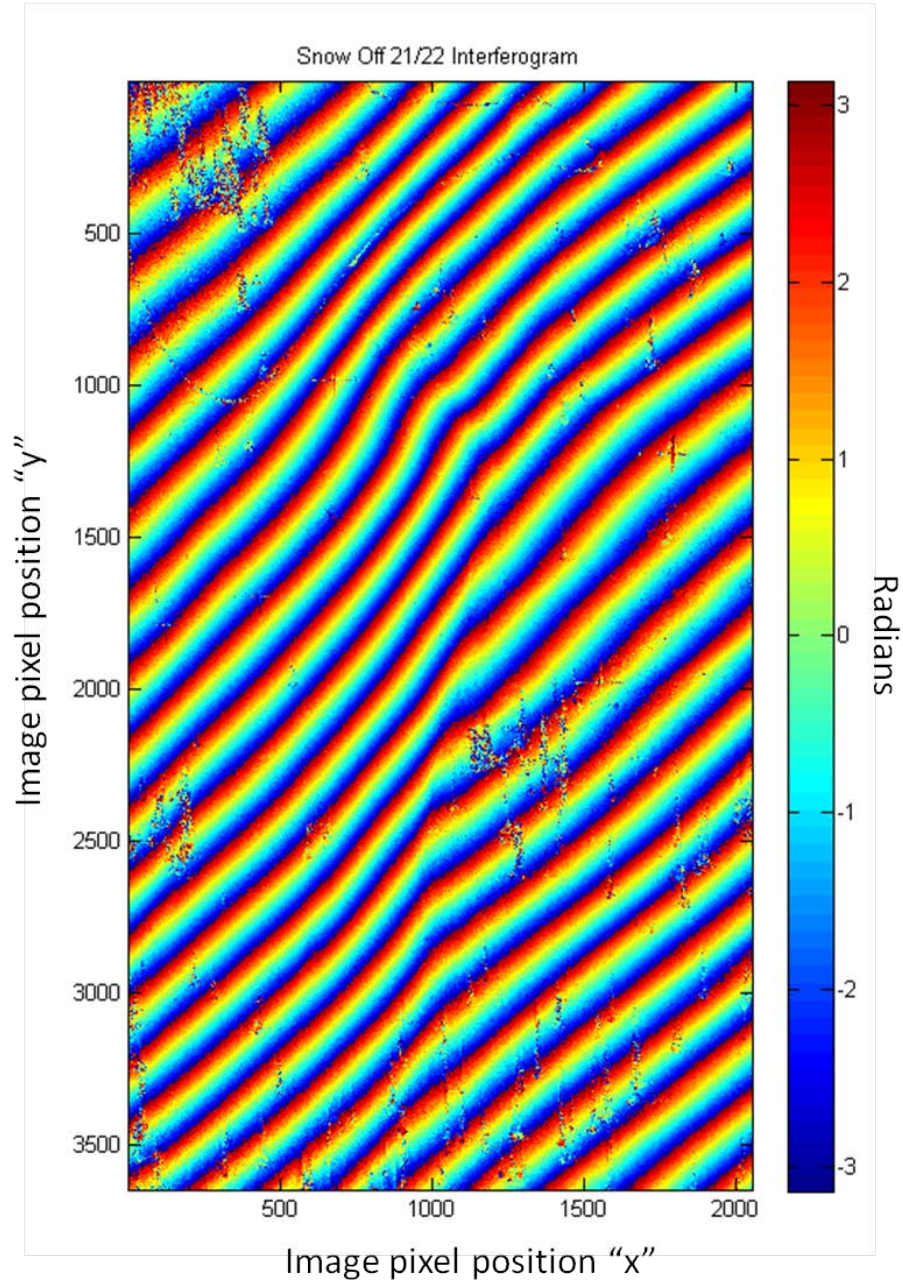


Figure 20. Example of interferogram generated during the Snow Off SAR collection. The repeating fringe pattern is derived from the subtraction of the phases of the two interferometric datasets. Both datasets record values between $-\pi$ and π . Therefore the phase difference between the fringes can never be greater than 2π . Mammoth Mountain study site, (37°37.7'N, 119°02.7'N).

Displaying the interferogram demonstrates how the terrain changes based on the measured change of phase from one pixel to the next. Because phase difference is being

measured, only values between $-\pi$ to π radians are recorded. The resulting “wrapped” phase image displays repeating values between $-\pi$ to π as was seen in Figure 20.

In addition to the interferogram, the complex coherence is a useful parameter to calculate as it provides information about the quality of the radar returns and their suitability for generating DEMs. The complex coherence represented by “ γ ” can be calculated as seen in (20) (Richards 2009).

$$\gamma = \frac{|\langle e_1 e_2^* \rangle|}{\sqrt{\langle |e_1|^2 \rangle \langle |e_2|^2 \rangle}} \quad (20)$$

An example of complex coherence can be seen in Figure 21.

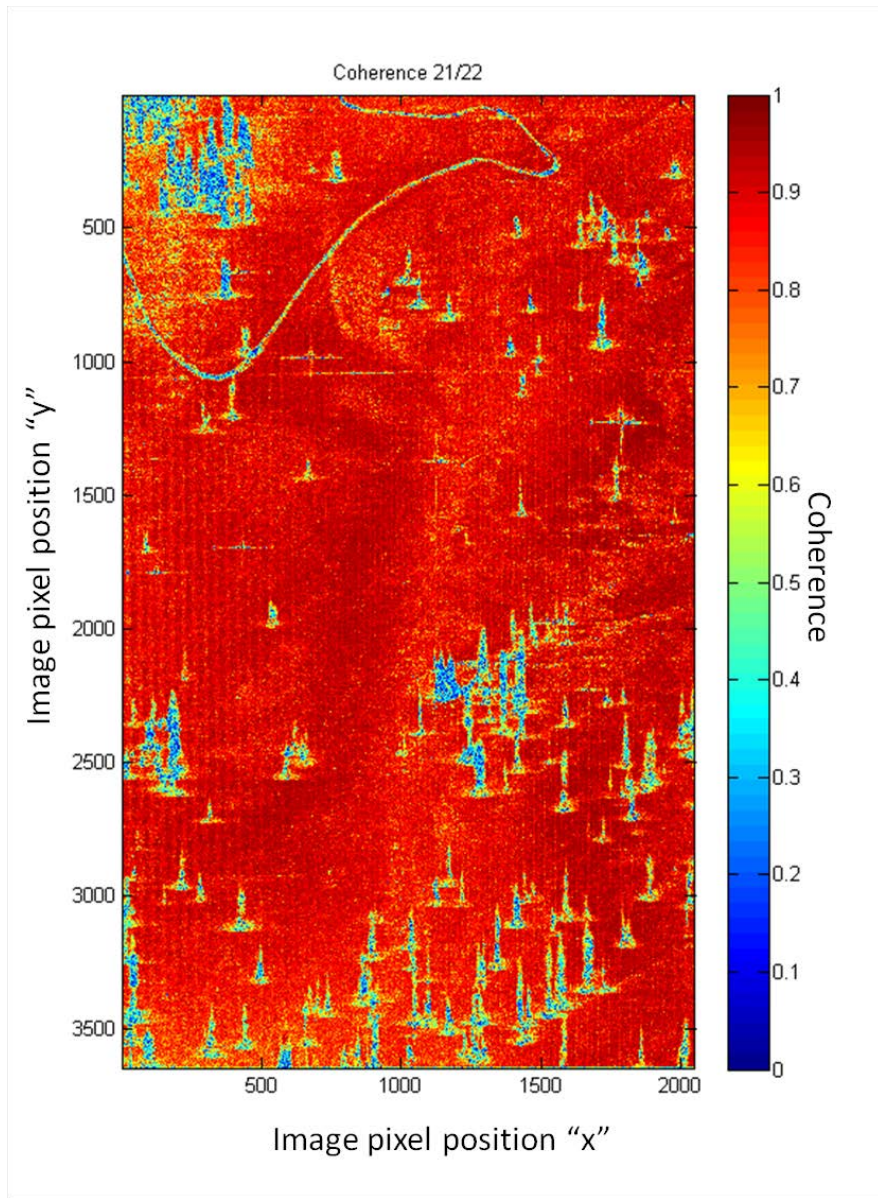


Figure 21. Example of coherence image generated from the Snow Off SAR collection.
Mammoth Mountain study site, (37°37.7'N, 119°02.7'N).

5. Phase Unwrapping

The “wrapped” interferometric phase image needs to be “unwrapped” to determine the overall phase difference between the two SAR images and to generate an image displaying constant change in phase. The phase unwrapping process consists of changing the 2π cyclical variations in phase to a constant change in phase that will eventually be used to determine elevation change across the scene (Richards 2009).

Unwrapping the interferogram generated from the SAR image pair produces a single array or image showing the change in phase attributable to terrain. It is important to note that because this array is measured in phase, that the units being used to describe the change in the terrain are radians. The branch cut method developed by R.M. Goldstein et al. 1988 was used to unwrap the Mammoth Mountain interferograms. The MATLAB unwrapping algorithms implementing this approach were written by Bruce Spottiswoode and latter modified by Carey Smith (Mathworks 2013) to increase processing efficiency. An example of the unwrapped phase from Figure 20 can be seen in Figure 22.

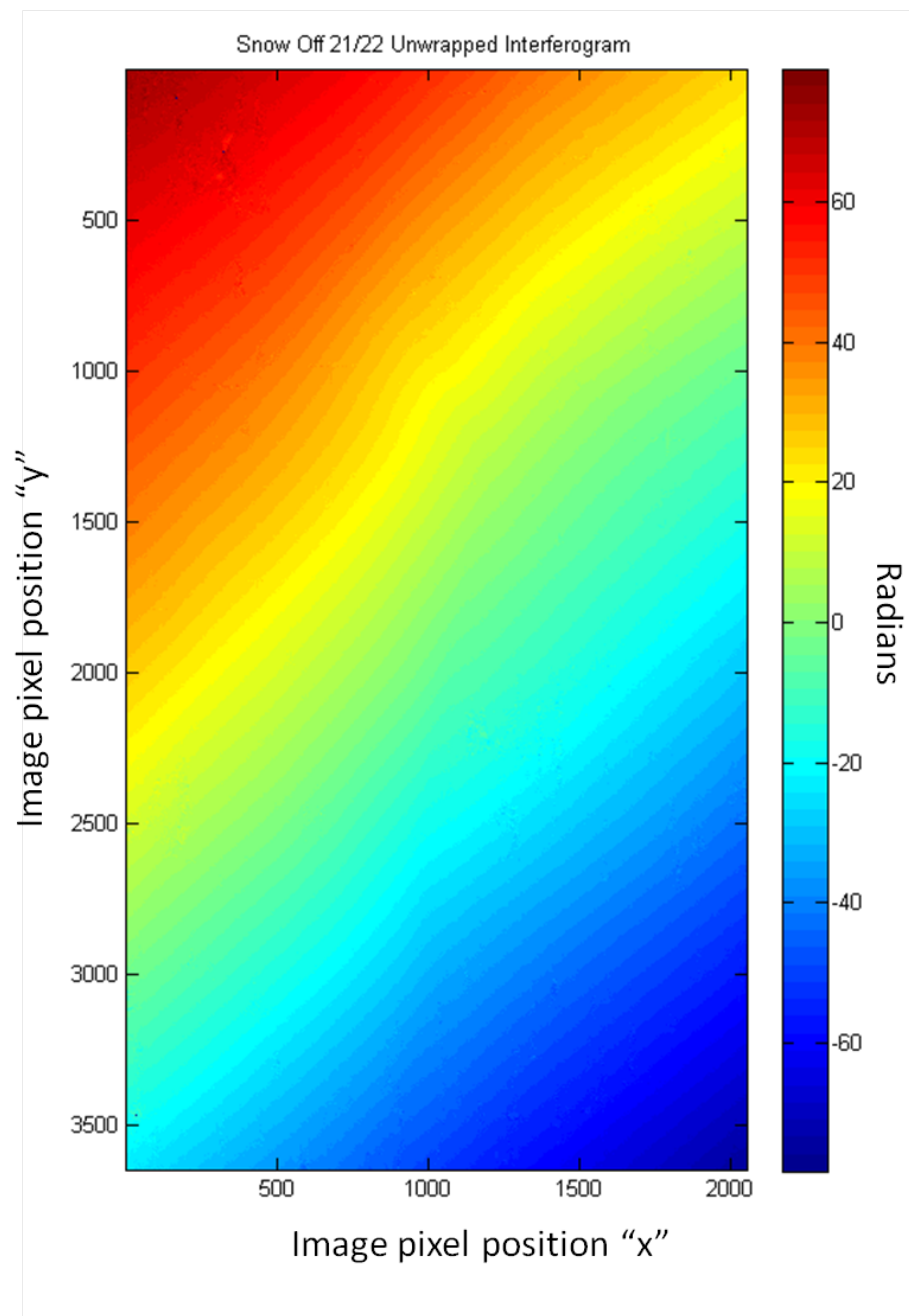


Figure 22. Unwrapped total phase generated from interferometric image collected during Snow On SAR collection. The repeating 2π pattern has been removed and the full range of phase difference can be seen. Mammoth Mountain study site, $(37^{\circ}37.7'N, 119^{\circ}02.7'N)$.

The above interferometric image is not yet ready to be converted to elevation. It consists of phase that is due to changes in the x, y, and z directions. The changes in the

phase due to changes in the x and y direction is often referred to as the “Flat Earth Phase”. The total phase, which is represented by the unwrapped phase in Figure 20, is a combination of the phase change from the elevation change that we are trying to derive and the flat earth phase, which can be shown in (21), where “ $\Delta\phi_{total}$ ” is the total phase seen in Figure 22. “ $\Delta\phi_z$ ” is the phase change associated with the change in the elevation, and “ $\Delta\phi_{flat_earth}$ ” is the flat earth phase change (Richards 2009). For simplicity, atmospheric, noise, and baseline uncertainty effects on phase are not considered at this time.

$$\Delta\phi_{total} = \Delta\phi_z + \Delta\phi_{flat_earth} \quad (21)$$

Therefore, to get at the elevation at each pixel, the flat earth phase must be removed. To do this, the flat earth phase, which requires precise knowledge of the base line, must first be calculated, and is the subject of the next sub-section.

6. Baseline Determination

Considering the interferometric phase equation (equation 10, repeated below), it can be seen that the interferometric phase is highly sensitive to the baseline length “B”. The baseline is used in the calculation of the flat earth phase that will be removed from the total phase and the height to phase ratio to get to the finale DEM. According to Richards 2007, the baseline length needs to be known to an accuracy of a factor of 10^{-4} to 10^{-6} of the absolute slant range to the target.

$$\Delta\phi = \frac{4\pi B \sin \theta}{\lambda} \quad (10)$$

The level of accuracy required for the baseline can be a bit problematic. If the SAR images are being collected from ranges on the order of 10,000 meters, the baseline accuracy needs to be sub-meter at a minimum with cm accuracy preferred. Aircraft positioning is generally handled by GPS. Recall that standard GPS accuracy does not approach the level of precision that is needed for the baseline determination. Consider the fact that the aircraft’s position is being determined for both passes at an accuracy of around three meters, it is possible that the GPS error can be on the order of six meters under optimal conditions. Because of this, there needs to be a better way to estimate the

baseline between the flights. It may be possible to use the SAR data themselves to determine the baseline if there is information about the three dimensional change available for multiple locations in the target area.

To begin solving for the baseline, go back to the interferometric phase equation which can be seen in expanded form in (22).

$$\Delta\phi = \frac{4\pi}{\lambda}(r_2 - r_1) = \frac{4\pi}{\lambda}\Delta r = \frac{4\pi B \sin \theta}{\lambda} \quad (22)$$

Recall that the goal in the derivation of the interferometric phase angle is to determine the difference in the length between the two ranges as it is measured in radians. The earlier simplified derivation must be expanded to consider the fact that in airborne SAR collections, there is no way to insure that the two collections are taken in a flat plane relative to the earth as was shown in the earlier example. The two flight paths orientation is more likely to be something along the lines seen in Figure 23.

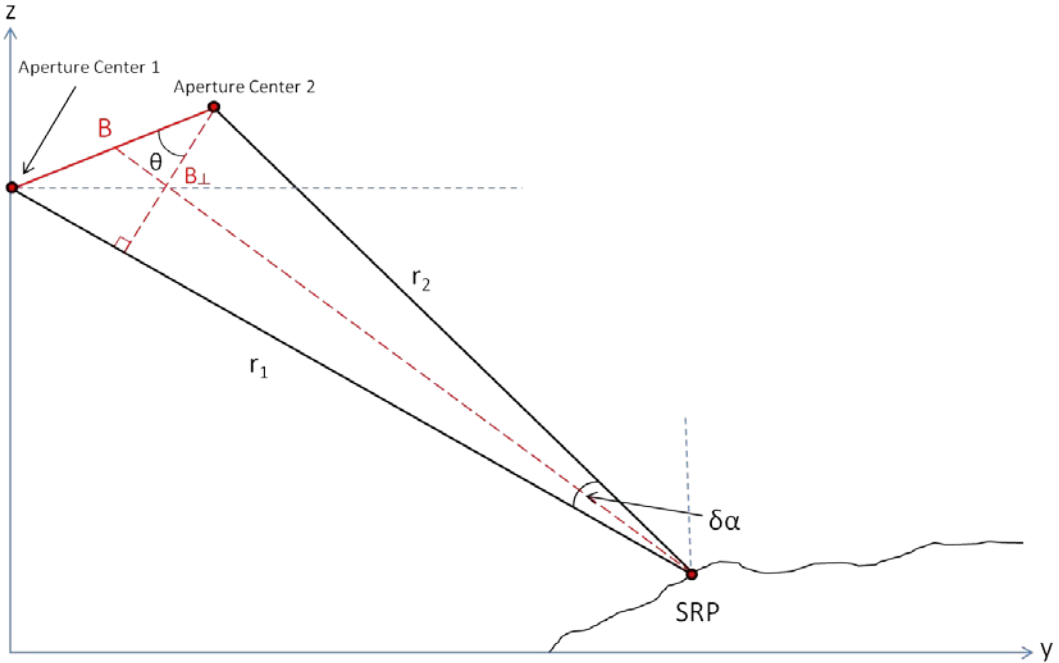


Figure 23. Geometry for Multi-pass Single Look Complex interferometric SAR collection. “ r_1 ” and “ r_2 ” are the respective ranges from antennas 1 and 2. “ B ” represents the baseline between the two antenna locations. “ B_{\perp} ” represents the orthogonal baseline between the two radar beam paths. SRP is the scene reference point. “ θ ” represent the angle between the baseline and the orthogonal baseline. “ $\delta\alpha$ ” represents the angle between the two range vectors. (After Richards 2009; with input from Douglas Bickel personal communication, 2013).

Due to the SAR geometry; there are multiple components of the phase that need to be considered. Keep in mind that phase in the above figure is merely a rendition of the difference in range between the two different collections. The radar range from one pixel to the next is determined by three different aspects. It is determined by the difference in the change in the range in the x, y, and z directions. The previous phase image consists of phase that is made up of changes in these three directions and the change in the overall range in 3-dimensional space will be different between the two aperture centers from one pixel to the next. That is good because it allows for the generation of a 3-dimensional image. That also means though, that if extraction of elevation information is the goal, the impact that the change in the x and y directions will have on the interferometric phase, which is the aforementioned flat earth phase will need to be considered. Looking at

Figure 8 again, notice the changes in either the y and z direction on the ground affect the ranges to the two aperture centers which ultimately affect the interferometric phase.

Recall from equations 7 through 9 that

$$r_1 = r_2 \cos \delta\theta + B \sin \theta \quad (23)$$

Using the small angle approximation

$$r_1 = r_2 + B \sin \theta \quad (24)$$

Therefore

$$\Delta r = r_1 - r_2 = B \sin \theta \quad (25)$$

Also, recall From Figure 23 that $B \sin(\theta)$ is merely the length of the portion of “ r_1 ” that goes from the intersection of the perpendicular baseline to “Aperture Center 1”. Notice that this length can also be characterized as the projection of vector \vec{B} onto vector \vec{r}_1 . This can be calculated by taking the dot product of vector \vec{B} onto the unit vector of \vec{r}_1 or \vec{U}_{r_1} .

$$B \sin \theta = \vec{B} \cdot \vec{U}_{r_1} \quad (26)$$

Where

$$\vec{B} = \langle \vec{B}_x, \vec{B}_y, \vec{B}_z \rangle \quad (27)$$

And

$$\vec{r}_1 = \langle \vec{r}_{1x}, \vec{r}_{1y}, \vec{r}_{1z} \rangle \quad (28)$$

The magnitude of \vec{r}_1 can be given by

$$r = \sqrt{r_x^2 + r_y^2 + r_z^2} \quad (29)$$

Resulting in

$$\vec{U}_{r_1} = \left\langle \frac{\vec{r}_x}{r}, \frac{\vec{r}_y}{r}, \frac{\vec{r}_z}{r} \right\rangle \quad (30)$$

Which means that

$$\vec{B} \cdot \vec{U}_{r_1} = \frac{B_x r_x + B_y r_y + B_z r_z}{r} \quad (31)$$

Making a substitution, the interferometric phase angle can now be defined as:

$$\Delta\phi = \frac{4\pi}{\lambda} \frac{B_x r_x + B_y r_y + B_z r_z}{r} \quad (32)$$

The equation for the interferometric phase angle at a given location (x , y , z) in terms of that location and the components of the baseline has now been defined. Unfortunately there is still a lot of information needed. $\Delta\phi$, λ , and r are known but B_x , B_y , and B_z are unknowns.

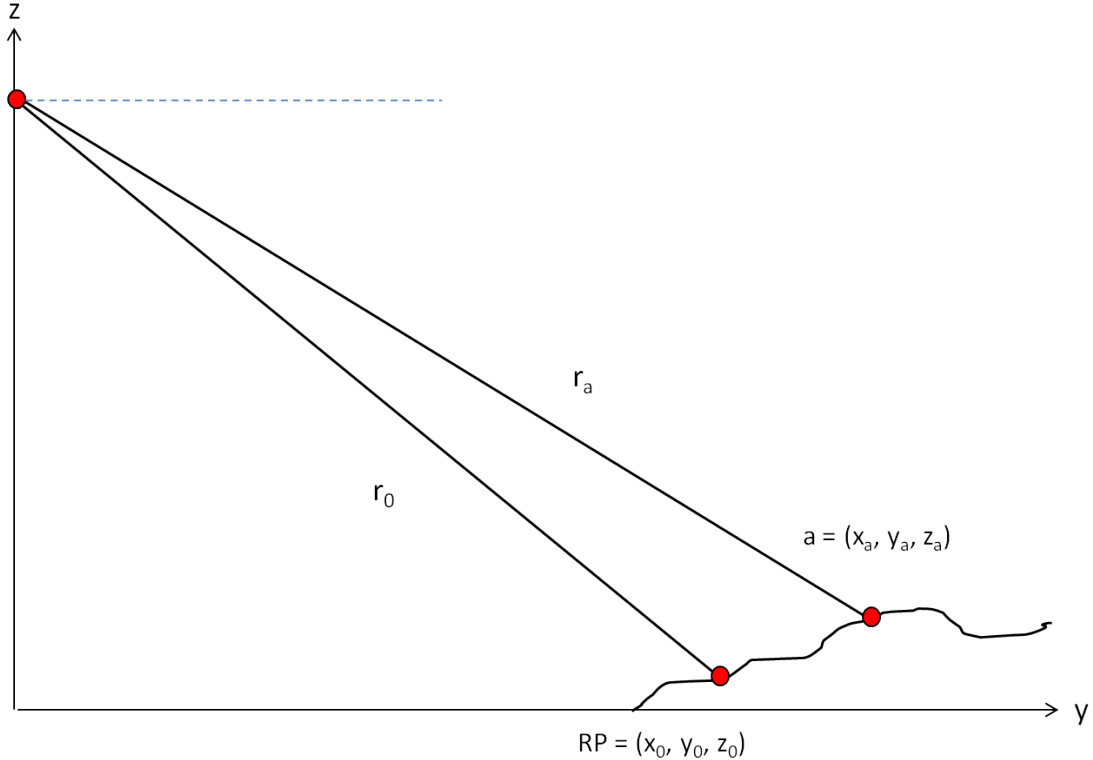


Figure 24. Comparing the physical change in location and phase of multiple points to a reference point “RP” enables the construction of a system of equations to solve for the baseline. The given ranges to the reference point “ r_0 ” and the other points “ r_a ”, is also required for the solving the system of equations. (After Douglas Bickel, personal communication, 2013).

If a second point “ a ” is chosen at location (x_a, y_a, z_a) as seen in Figure 24, “ a ” can be written as

$$a(x, y, z) = (x_0 + \Delta x_a, y_0 + \Delta y_a, z_0 + \Delta z_a) \quad (33)$$

Therefore, when B_x , B_y , B_z , represent the components of the baseline; x_0 , y_0 , z_0 , are the coordinates of the reference point; Δx_a , Δy_a , Δz_a , are the x , y , z distance to point “ a ”; and “ r ” in the range to target; $\Delta\phi$ at point “ a ” becomes

$$\Delta\phi_a = \frac{4\pi}{\lambda} \frac{B_x(x_0 + \Delta x_a) + B_y(y_0 + \Delta y_a) + B_z(z_0 + \Delta z_a)}{r} \quad \square \quad (34)$$

Separating the components of (34) results in

$$\Delta\phi_a \frac{\lambda}{4\pi} = \frac{B_x x_0 + B_y y_0 + B_z z_0}{r} + \frac{B_x \Delta x_a + B_y \Delta y_a + B_z \Delta z_a}{r} \quad \square \quad (35)$$

Focusing on the first component of the right hand side of (35), notice that the variables are unknown, but it is known that this is a constant and that it is equal to the value of $\Delta\phi \frac{\lambda}{4\pi}$ at the reference point (RP) (x_0, y_0, z_0) since $\Delta(x, y, z)$ is 0. The second component of the right hand side of (35) is responsible for all of the change in the phase relative to the RP. Therefore if $\Delta\phi$ is known at the RP and three different points along with their relative $\Delta(x, y, z)$, there would be three equations and three unknown variables that allow for a system of equations to solve for those variables. This approach to solving for the baseline was developed in cooperation with Douglas Bickel of Sandia National labs. Figure 25 depicts the four locations being used in the system of equations. MATLAB algorithms designed to solve multiple simultaneous equations were used to make these calculations.

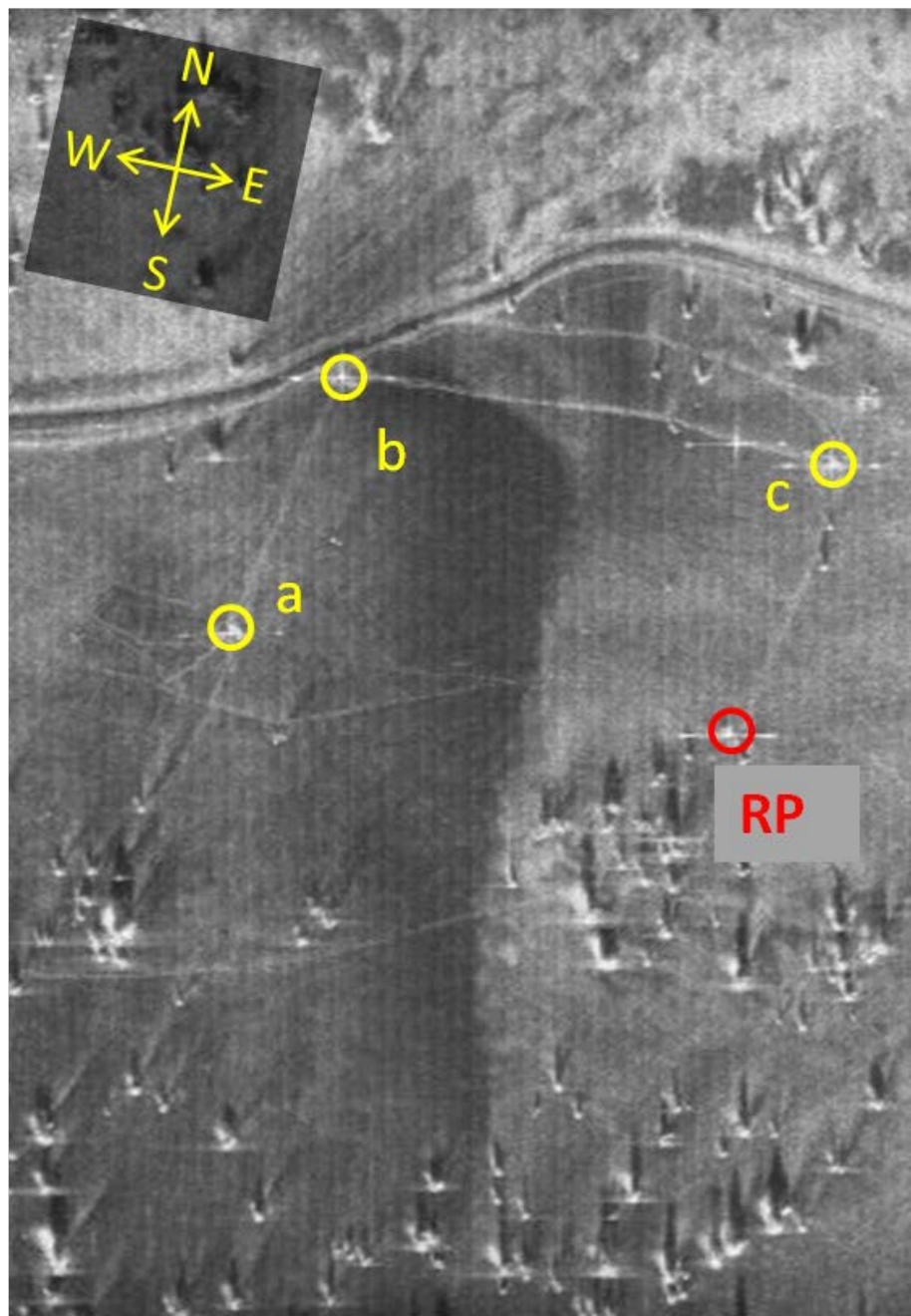


Figure 25. This approximately 200x300m scene depicts a reference point "RP" defined by the SE corner reflector and the relative positions of the other three known positional points defined by the other three emplaced corner reflectors at positions "a", "b", and "c". Mammoth Mountain study site (312 x 176m), (37°37.7'N, 119°02.7'N).

Before the system of equations can be solved, the data used to solve these equations needs to be addressed. The interferometric phase angle is straightforward. $\Delta\phi$ has already been calculated as discussed in previous sections. The real world $\Delta(x,y,z)$ also needs to be determined. As discussed earlier, standard GPS does not provide the level of accuracy needed to make these calculations. Therefore the survey grade GPS was used to determine the $\Delta(x,y,z)$.

Knowing the real world $\Delta(x,y,z)$, is not enough though. The real world “y” coordinate orientation is true north/south and the real world “x” coordinate orientation true east/west. Despite best efforts and potential other collection scenarios; the SAR image coordinate system does not match the real world coordinate system. This can be seen in Figure 26. Because all calculations are being performed in a SAR image centric coordinate system, the real world $\Delta(x,y)$ needs to have its coordinate system rotated to match that of the SAR acquisition. When this is done, the Δx and Δy values will change and will therefore need to be recalculated based on the coordinate system rotation.

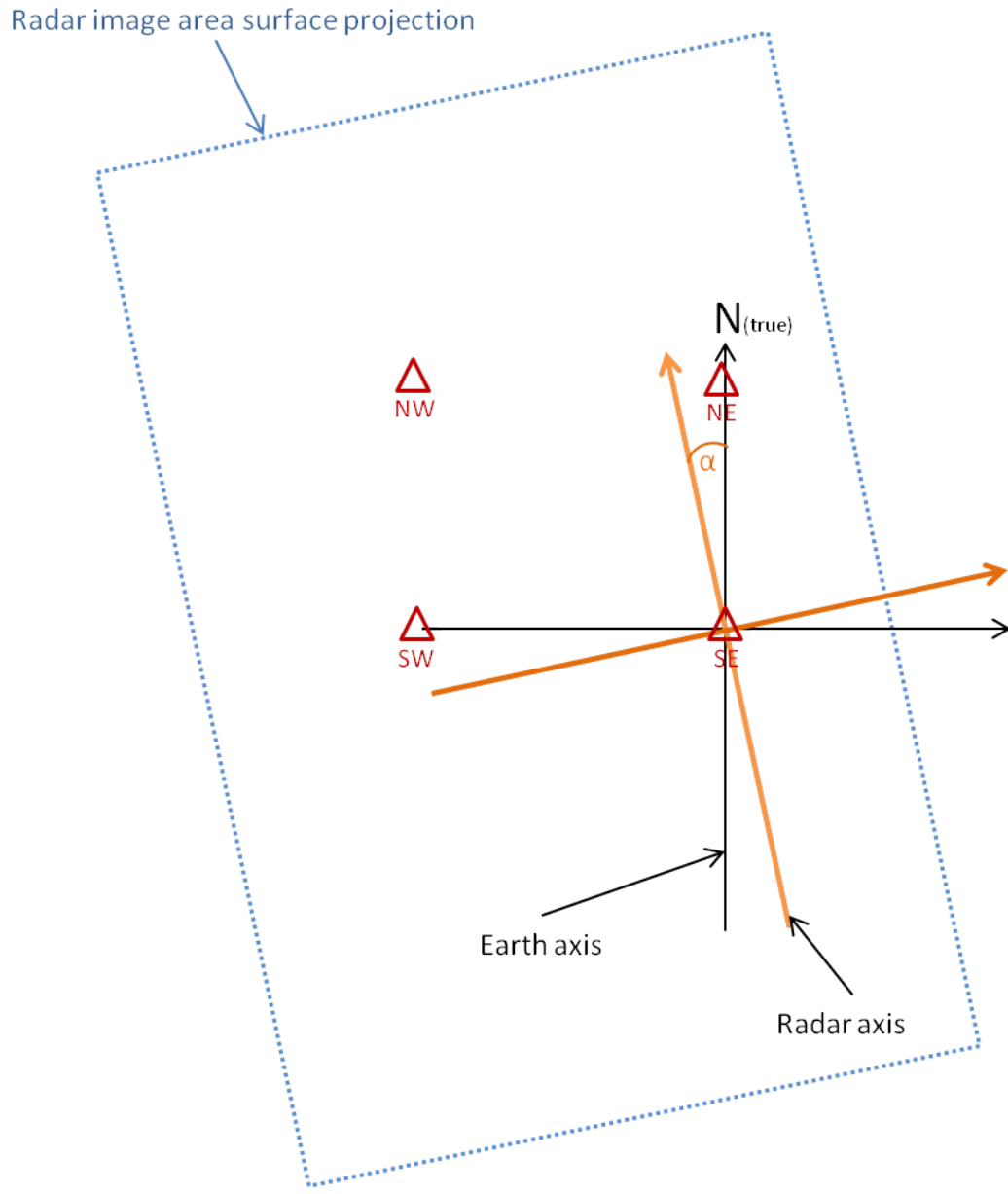
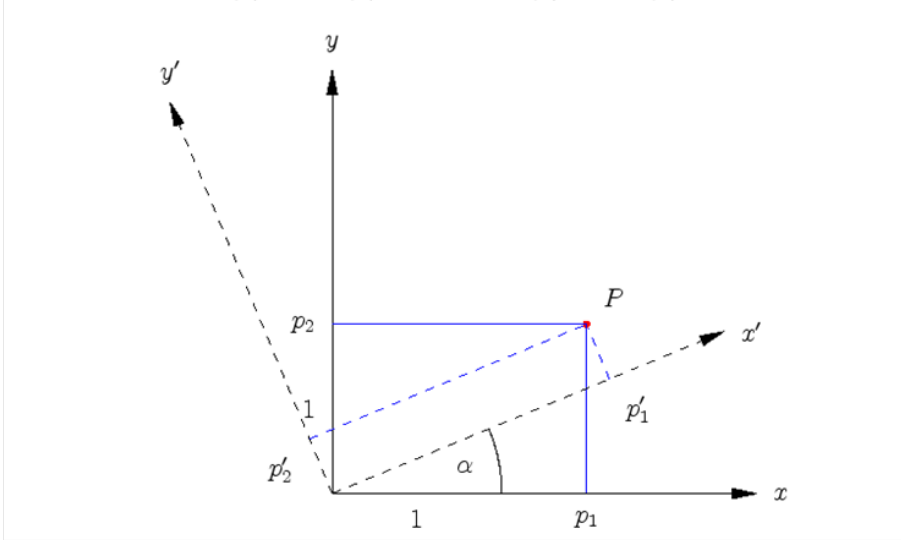


Figure 26. In order to correctly determine the baseline, an accurate representation of the x, y, and z changes must be known. Those changes were computed in a reference frame where the x axis was east/west and the y axis was north/south. The radar reference frame does not line up, thereby requiring an adjustment to the x and y components in the baseline calculation equations.

Reorientation from the real world coordinate system to the SAR coordinate system is a matter of geometry/trigonometry and can be seen in Figure 27.



$$p'_1 = p_1 \cos(\alpha) + p_2 \sin(\alpha) \quad p'_2 = -p_1 \sin(\alpha) + p_2 \cos(\alpha)$$

Figure 27. Demonstration of the correction required for a given rotation of α° rotation in reference frames (From Mathematics-Online Lexicon, 2013).

To determine the proper rotation to calculate the new $\Delta(x,y)$, “ α ” must first be determined in the above equations. That is where the third piece of SAR data provided by Sandia and General Atomics comes in. Recall that third data set for each SAR acquisition was the “Header Data” that provides both flight information and radar pointing information. An example of the header data can be seen in Figure 28.

Header data: Scan 21 0.1m

Field	Value	Min	Max
version	513	513	513
submode	7	7	7
bytes_per_pixel	4	4	4
navtime	4.9672e+05	4.9672...	4.9672...
r_b	1.0293e+04	1.0293...	1.0293...
x_dist	1.1531e+03	1.1531...	1.1531...
y_dist	-9.9595e+03	-9.959...	-9.959...
z_dist	-2.3295e+03	-2.329...	-2.329...
v_x	90.1654	90.1654	90.1654
v_y	0.7233	0.7233	0.7233
v_z	0.0956	0.0956	0.0956
vlos	10.8226	10.8226	10.8226
phi	13.0802	13.0802	13.0802
cos_phi	0.9741	0.9741	0.9741
theta	82.9342	82.9342	82.9342
lat	37.5398	37.5398	37.5398
long	-119.0328	-119.0...	-119.0...
hgt	5.4263e+03	5.4263...	5.4263...
heading	-89.1830	-89.18...	-89.18...
ground_speed	90.1904	90.1904	90.1904
v_north	1.2860	1.2860	1.2860
v_east	-90.1812	-90.18...	-90.18...
v_down	0.1013	0.1013	0.1013
week	1696	1696	1696
azpixels	2048	2048	2048
rngpixels	3642	3642	3642
azpixspace	0.0858	0.0858	0.0858
rngpixspace	0.0858	0.0858	0.0858
rhoa	0.1016	0.1016	0.1016
rhor	0.1016	0.1016	0.1016
calparm	4.8928e-04	4.8928...	4.8928...
sig0_eff_db	-35.7972	-35.79...	-35.79...
scla	263.7491	263.74...	263.74...
range_nom	1.0302e+04	1.0302...	1.0302...
phi_nom	13.1147	13.1147	13.1147
theta_nom	83.3976	83.3976	83.3976
ap_count	0	0	0
srp	<1x1 struct>		

Figure 28. Header data provided with each SAR acquisition provides specifics on the aircraft flight path orientation and the orientation of the radar with respect to the flight information. In addition to the flight data, the header provides the calculated pixel size for the given image or the ground resolution.

There are two key pieces of information with respect to determining “ α ”. The first number of interest is the “scla” which represents the flight path of the aircraft relative to true north. In the above header data, “scla” can be seen to be 263.7491° . The “scla” can be visualized in Figure 29.

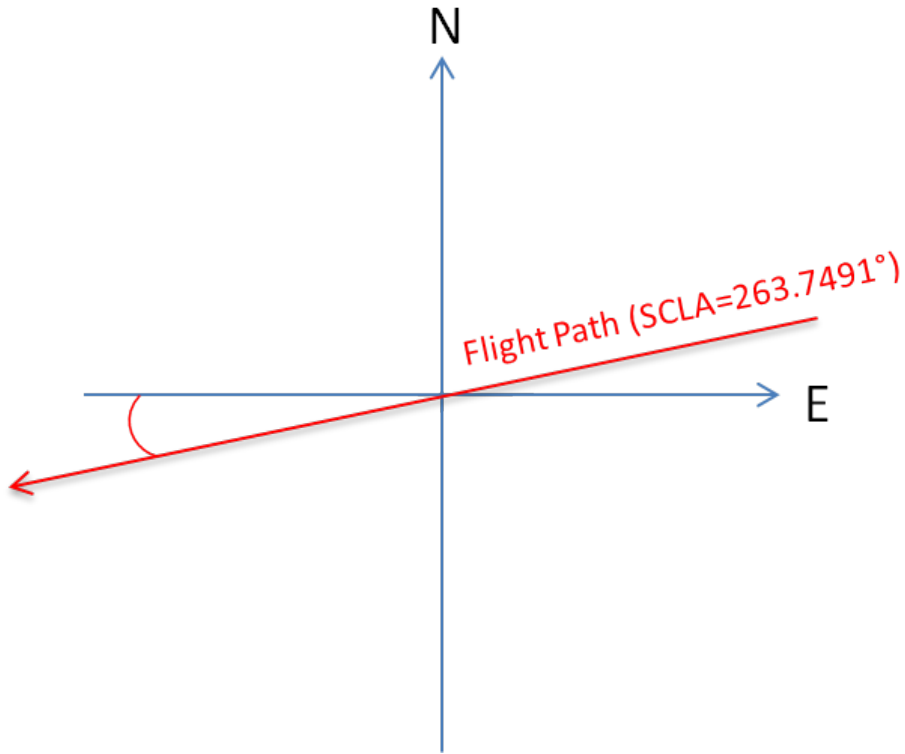


Figure 29. SCLA represents the flight path relative to true north.

The second piece of information that is required is “theta.” “Theta” represents the squint angle or the pointing direction of the radar relative to the flight path. In the above header data “theta” can be seen to be 82.9342° . This particular theta should not be confused with the use of θ in other portions of this method. Due to use of it in the header data by General Atomics it will simply be referred to as “theta” rather than the symbol in the text and will not be renamed. Theta can be visualized in Figure 30.

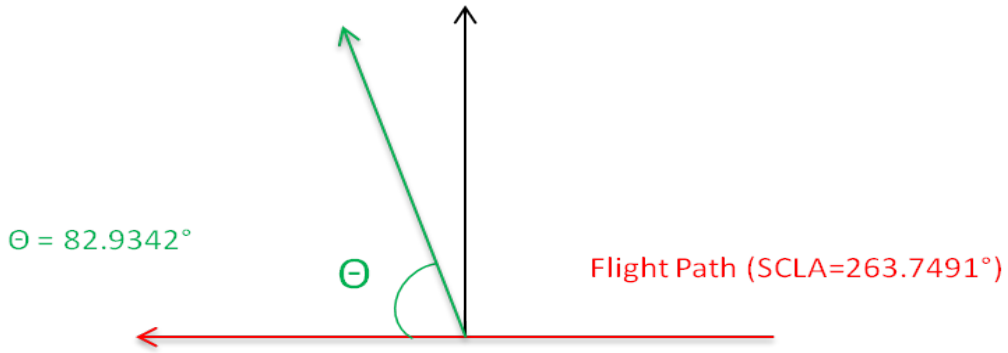


Figure 30. Theta in the header data represents the squint angle or the angle that the radar is looking relative to the flight path. In this case theta is 82.9342° .

The next step is to combine the “scla” and “theta” data to determine how the SAR pointing direction deviates from true north. This deviation will be the “ α ” used to determine the change in $\Delta(x,y)$. The final geometry can be seen in Figure 31 and the equation used can be seen in (36) resulting in a calculated α of 13.3167 in this example. If the flight path is in the opposite direction and the radar is pointed to the left of the direction of flight, “theta” will be a negative number and (36) will have to be adjusted accordingly for the differing geometry.

$$\alpha = 360 - (scla + theta) \quad (36)$$

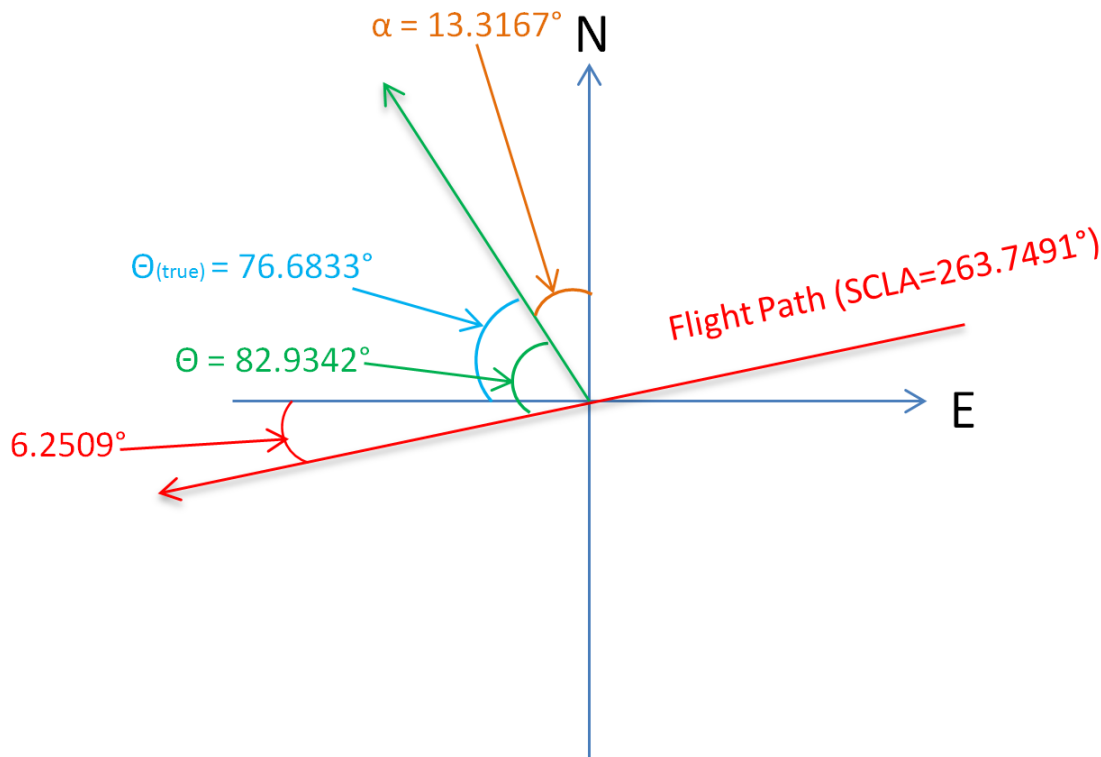


Figure 31. This figure shows all the relevant angles required to determine the rotation angle “ α ” used in calculating the change in x and y for the rotation of the reference frame. “ Θ ” represents the squint angle. “ $\Theta_{(true)}$ ” represents the squint angle adjust for true north. SCLA represents the flight heading.

Now that the correct “ α ” has been determined, $\Delta(x,y)$ can be adjusted so that it can be used to calculate the components of the baseline in the system of equations that was discussed above.

7. Flat Earth Removal

Once the components of the baseline have been determined, all the information is available to determine the flat earth interferometric phase. Recall that the total phase generated in the interferogram is a combination of phase due to the change in topography and the change in the phase due to the change in range from the two acquisitions in the x and y directions. The flat earth phase needs to be removed before the terrain phase can be addressed.

To determine the flat earth phase, refer back to the interferometric phase equation.

$$\Delta\phi = \frac{4\pi B \sin \theta}{\lambda} \quad (10)$$

The flat earth phase is simply a representation of what the interferometric phase would be if the ground was a flat plane. It can be seen from (10) that this phase depends on the baseline B which is determined by the flight geometry in 3-dimensional space. The flat earth phase itself is made up of two aspects, to include the range direction and the azimuth direction. The range aspect of the flat earth is determined by the height of the platform above the flat plane and the ground distance in the y direction. The azimuth component is composed of strictly the x direction, the along the flight path direction.

Starting with the range portion of the flat earth, equation 10 shows that the interferometric phase is dependent on three variables. The wavelength λ is a constant and is known. The baseline “B” was calculated in the previous section and is also constant throughout the scene. The third variable is the incidence angle θ . Figure 32 shows that when moving along the established flat plane in the y direction, that the height remains constant while θ changes with the change in y. Therefore, the knowledge of the change in θ is required to determine the change in the interferometric phase angle throughout the scene.

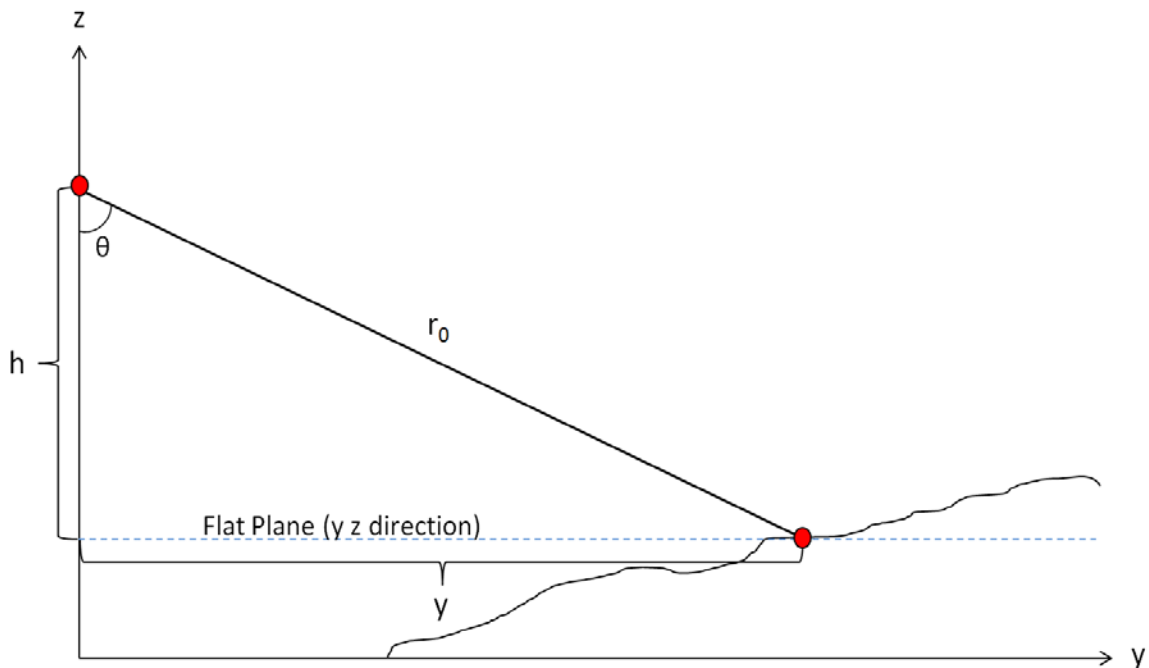


Figure 32. Geometry shows that θ changes as the distance from the antenna “ r_0 ” changes. This change in θ is required to determine the interferometric phase angle and is calculated using the known altitude “ h ” above the scene reference point (SRP) and the ground distance “ y ”.

The first step in this process is to establish an array the same size as that of the interferometric images being analyzed. In order to calculate θ ; both the height and ground range “ y ” must be known. It should be mentioned at this point that the SAR system is very good at determining range to the reference point. This allows accurate determination of the platform height and the ground distance to the center pixel in the target image. The center pixel in a SAR image represents that target and is referred to as the scene reference point (SRP). All other pixels in the image are at known ranges but the y and z coordinates are not known because both y and z changes in the terrain contribute to the range at each individual pixel. The radar system calculates the size of the pixels in the image, or the resolution, and provides it in the header data. With this in mind, an imaginary flat plane is established through the SRP ensuring that the height “ h ” is known. In addition to the height, the ground distance is known to the reference point. Using the ground distance to the SRP and the processed ground resolution, the ground

distance to every pixel can be determined in an imaginary plane. This allows calculation of θ for every point on the flat earth plane. With the calculation of θ for all of the positions in the array, the calculation of the interferometric phase with respect to the y-z direction is not difficult. Simply apply the interferometric phase equation with λ , the B_{yz} baseline component, and the newly calculated θ . An example of this phase can be seen in Figure 33 fully unwrapped and Figure 34 wrapped.

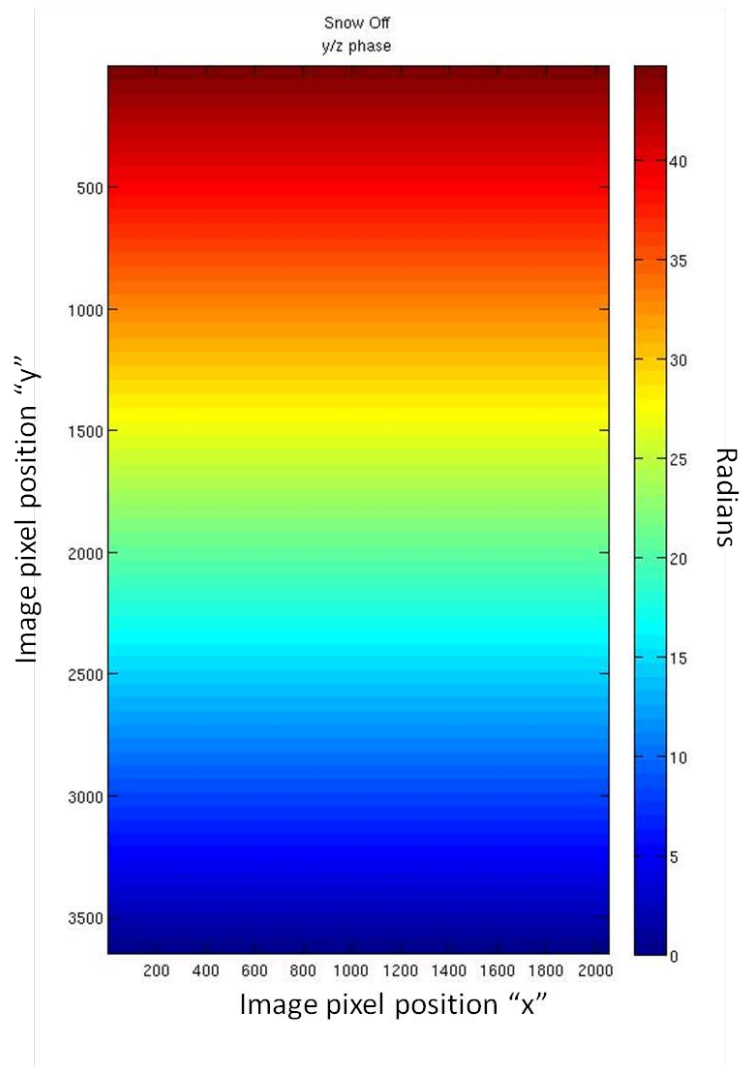


Figure 33. This notional figure demonstrates the unwrapped change in phase in the “y” direction due to the change in range (range aspect of the flat earth phase).

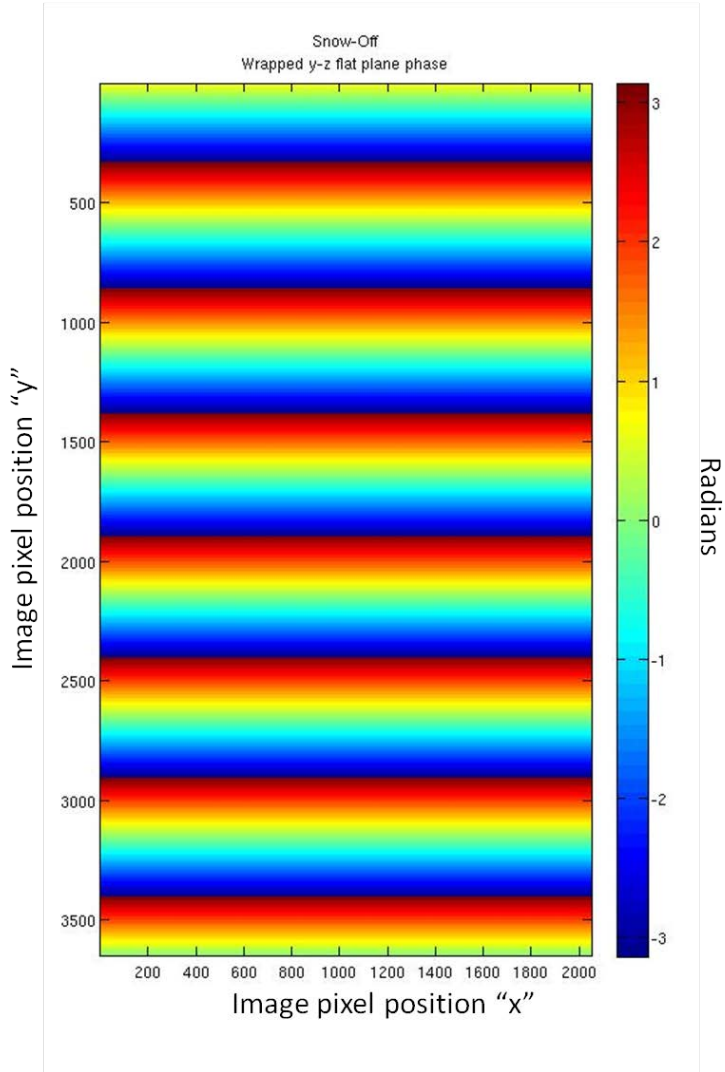


Figure 34. This notional figure demonstrates the wrapped change in phase in increments of 2π radians in the “y” direction due to the change in range (range aspect of the flat earth phase). .

The second step in determining the flat earth phase is to determine the azimuthal phase change. The azimuthal flat earth change “ $\Delta\phi_{bx_flat}$ ” can be given by (37) where “ B_x ” is the x component of the baseline and “X” is the azimuthal distance from the SRP.

$$\Delta\phi_{bx_flat} = \frac{4\pi B_x}{\lambda} \frac{X}{r} \quad (37)$$

The resulting unwrapped image can be seen in Figure 35 and the wrapped image can be seen in Figure 36.

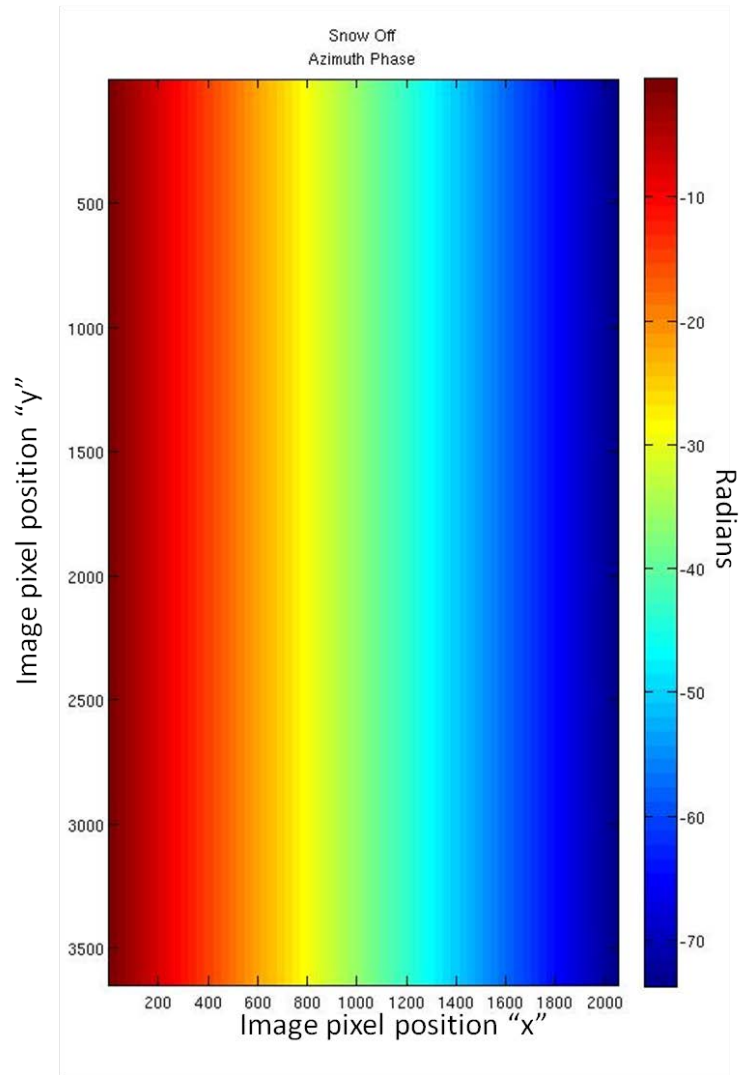


Figure 35. This notional figure demonstrates the unwrapped change in phase in the “x” or azimuth aspect of the flat earth phase.

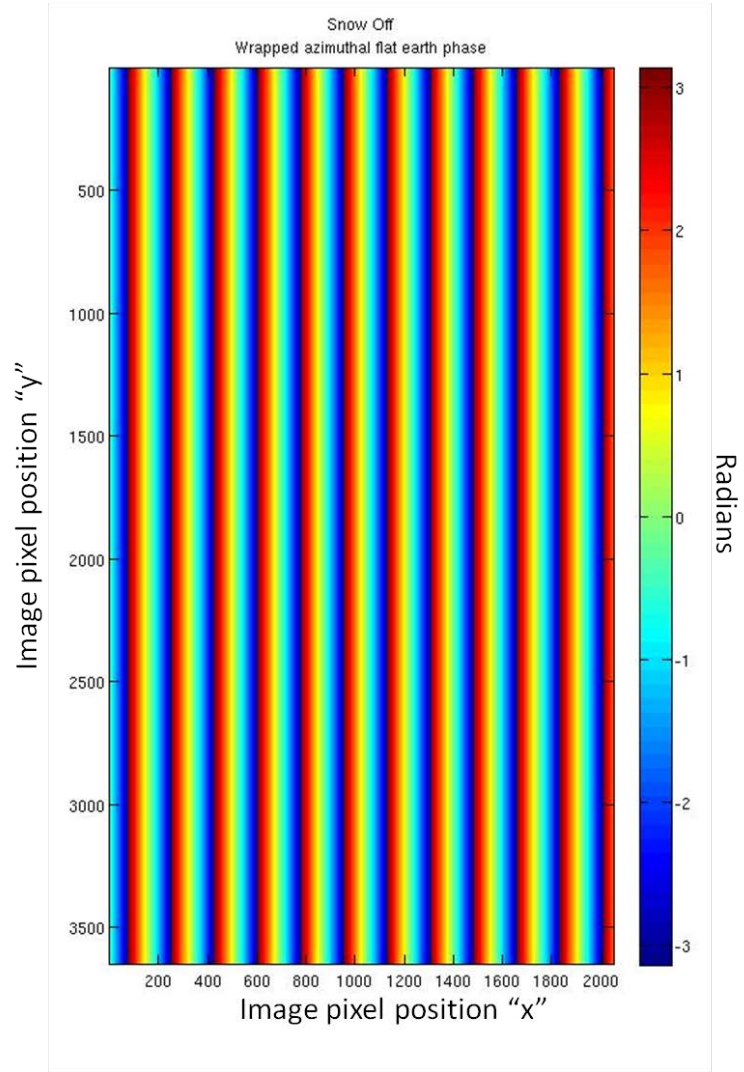


Figure 36. This figure demonstrates the unwrapped change in phase in increments of 2π radians in the “x” or azimuth aspect of the flat earth phase.

Once the flat earth phase in the range (y-z direction) and the azimuth direction are determined, they can be added together to get the total phase correction or the flat earth correction. This can be seen in Figure 37.

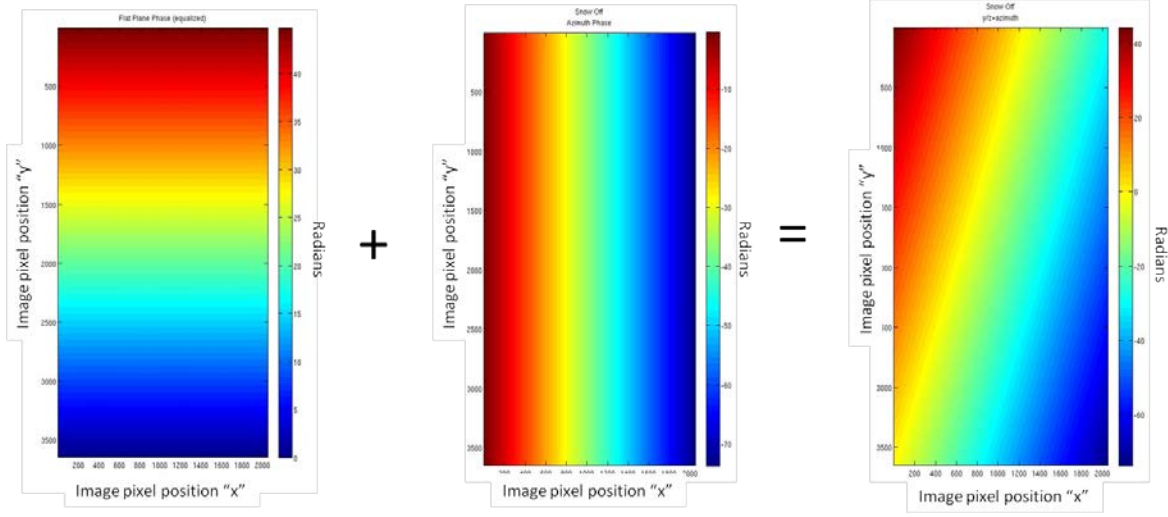


Figure 37. The flat earth phase is sum of the range and azimuth phases. Subtracting the flat earth phase from the total unwrapped phase results in the terrain phase.

The final step is to remove the total flat earth phase from the total interferometric phase. Figure 38 (right) represents the interferometric phase that is due to elevation change or the topography alone. This is also known as the flattened phase.

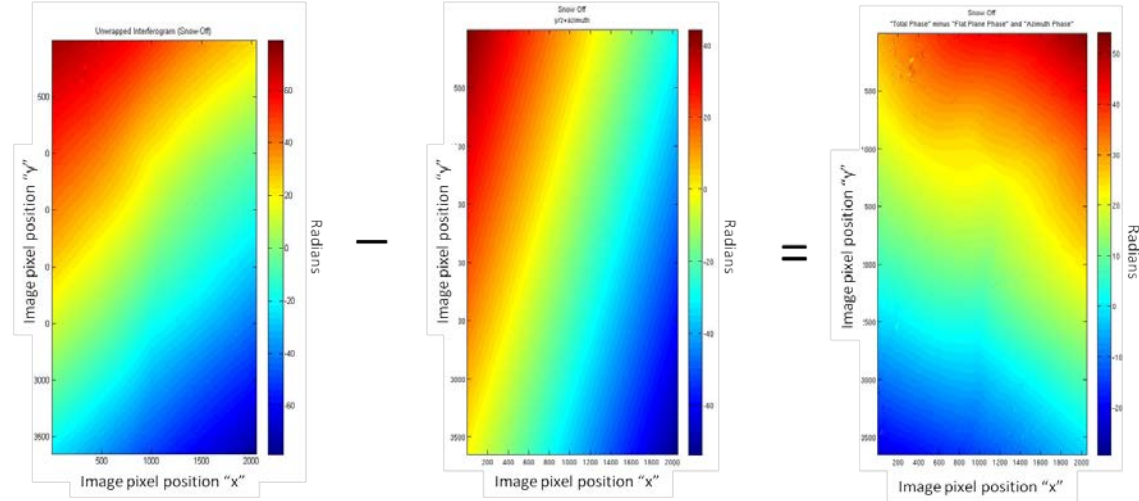


Figure 38. Subtracting the flat earth phase from the total unwrapped interferometric phase results in a phase array or flattened phase that represents terrain phase only (right image).

8. Height to Phase Scaling

The interferometric phase due to the terrain is the only phase left once the total phase has been flattened. The next step is to convert this flattened phase into elevation or a DEM (Figure 39) (Rosen 2009).

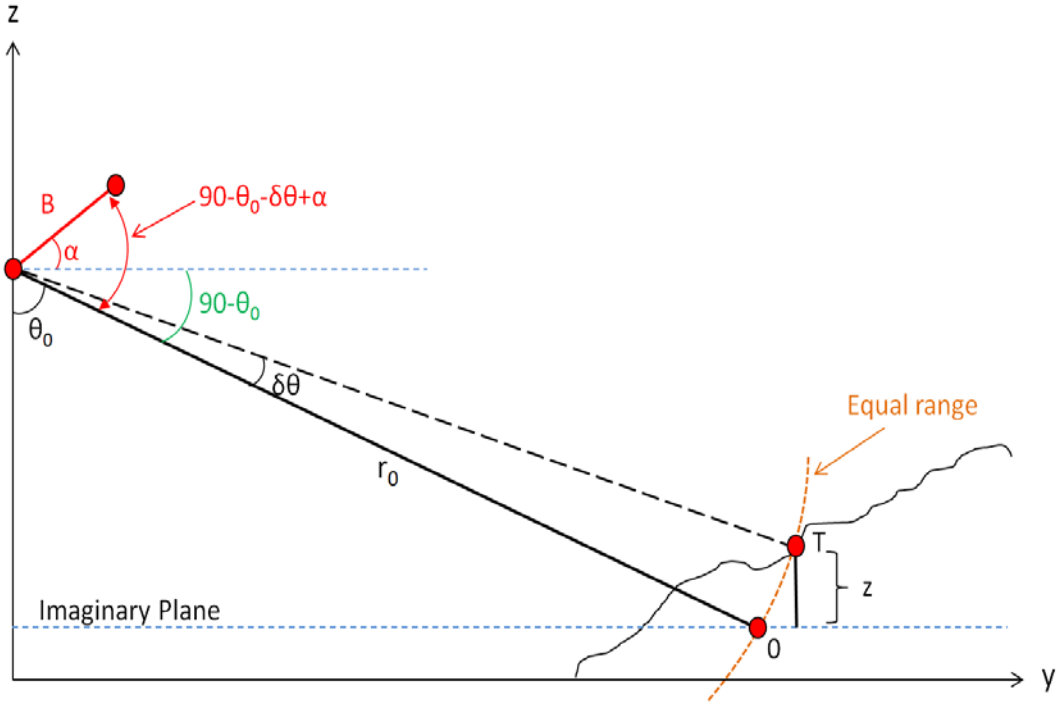


Figure 39. Geometry involved in determining phase to elevation scaling where “ r_0 ” represents the radar range to an imaginary plane, “T” represents a point on the terrain that is at the same range as r_0 but at a height of “ z ” above the imaginary plane. “ θ_0 ” represent the incidence angle to a given point “0” on the imaginary plane that is at the same range as that of point T. “ $\delta\theta$ ” is the angle between the vectors to point O and T. “ α ” is the angle between the baseline in the y-z plane and the horizontal (After Rosen 2009; with input from Douglas Bickel, personal communication, 2013).

To start the phase to elevation conversion process (Rosen 2009), Figure 39, establishes the equations of the imaginary plane’s interferometric phase, “ $\Delta\phi_0$ ”, and the total interferometric phase equation, “ $\Delta\phi_T$ ”, given by (38) and (39)

$$\Delta\phi_0 = \frac{4\pi}{\lambda} B \sin(\theta_0 - \alpha) \quad (38)$$

$$\Delta\phi_T = \frac{4\pi}{\lambda} B \cos(90 - \theta_0 - \delta\theta + \alpha) \quad (39)$$

Expanding (39) and using the small angle approximation results in,

$$\Delta\phi_T = \frac{4\pi}{\lambda} B \sin(\theta_0 + \delta\theta - \alpha) \quad (40)$$

Two things should be noted from the above equations. The first is that α can be determined from the previously calculated baseline components. The second is that “ $\theta_0 + \delta\theta$ ” on the right hand side of (40), is equal to θ .

Expanding (40) becomes,

$$\Delta\phi_T = \frac{4\pi}{\lambda} B \sin(\theta_0 - \alpha) + \frac{4\pi}{\lambda} B \cos(\theta_0 - \alpha) \delta\theta \quad (41)$$

Notice that the first term in (40), is the same as “ $\Delta\phi_0$ ”. Therefore, (41) can be rewritten as,

$$\Delta\phi_T = \Delta\phi_0 + \frac{4\pi}{\lambda} B \cos(\theta_0 - \alpha) \delta\theta \quad (42)$$

Rearranging (42) results in,

$$\Delta\phi_T - \Delta\phi_0 = \frac{4\pi}{\lambda} B \cos(\theta_0 - \alpha) \delta\theta = \Delta\phi_{FE} \quad (43)$$

Equation (43) represents the phase that has had the non-terrain phase removed or the same phase that has been previously shown in Figure 38.

To summarize, “ $\Delta\phi_T$ ” is known; it is the total interferometric phase calculated in Figure 22. Likewise “ $\Delta\phi_0$ ” is the interferometric phase calculated from the imaginary plane seen in Figure 37. θ_0 is known from the recorded header data. The baseline “B” has been calculated and “ α ” can be determined from the components of “B”. The wavelength “ λ ” is also known. The only variable not known in (43) is $\delta\theta$. $\delta\theta$ can therefore be calculated as seen in (44) and (45).

$$\delta\theta = \frac{\lambda}{4\pi B} \frac{\Delta\phi_T - \Delta\phi_0}{\cos(\theta_0 - \alpha)} \quad (44)$$

or

$$\delta\theta = \frac{\lambda}{4\pi B} \frac{\Delta\phi_{FE}}{\cos(\theta_0 - \alpha)} \quad (45)$$

The final step in deriving the phase to height ratio can be seen in Figure 40.

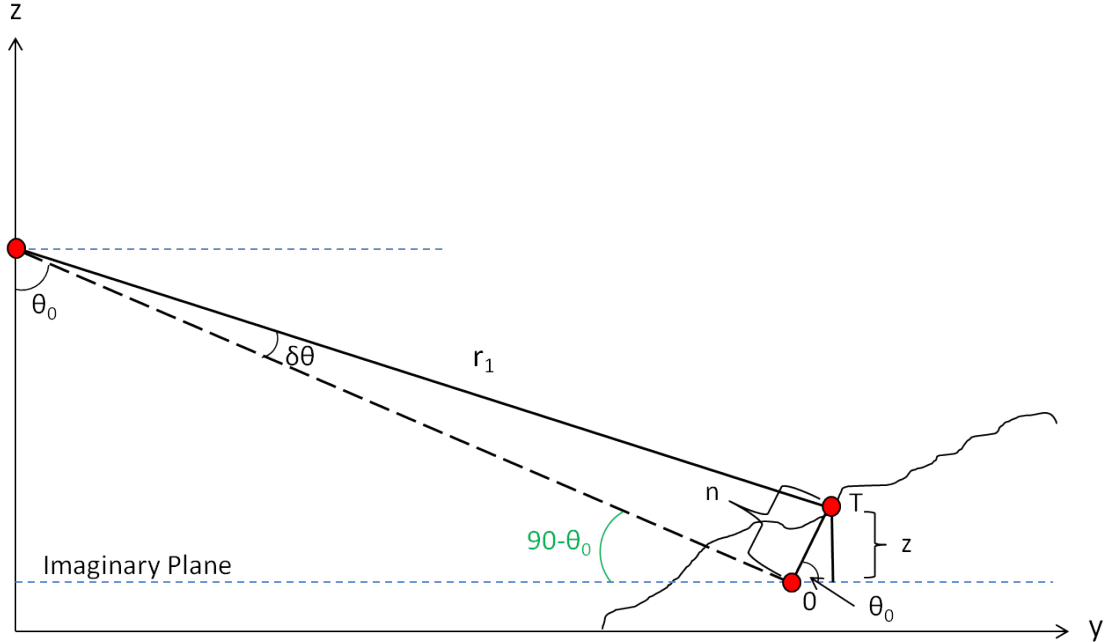


Figure 40. “ $\delta\theta$ ” or the angle between the vectors that point toward points “O” and “T” is required to determine the phase to height relationship. An equation can be derived by introducing “n” for the distance between “O” and “T” and recognizing that “ θ_0 ”, incidence angle, is the same as the angle between “n” and the imaginary plane. (After Rosen 2009; with input from Douglas Bickel, personal communication, 2013)

It can clearly be seen that,

$$\sin \delta\theta = \frac{n}{r_1} \quad (46)$$

Applying the small angle approximation, (46) becomes,

$$\delta\theta = \frac{n}{r_1} \quad (47)$$

which can be rearranged to be,

$$n = r_1 \delta\theta \quad (48)$$

It can also clearly be seen that,

$$\sin \theta_0 = \frac{z}{n} \quad (49)$$

which can be rearranged to be,

$$z = n \sin \theta_0 \quad (50)$$

Combining (49) and (50) results in the equation that provides the elevation,

$$z = r_i \delta \theta \sin \theta_0 \quad (51)$$

(51) is the final calculation needed to generate the DEM. Applying these calculations to the previously interferometric phase fields results in Figure 41. The mathematical path to determine the phase to height ratio was developed in cooperation with and primarily by Douglas Bickel from Sandia National Labs.

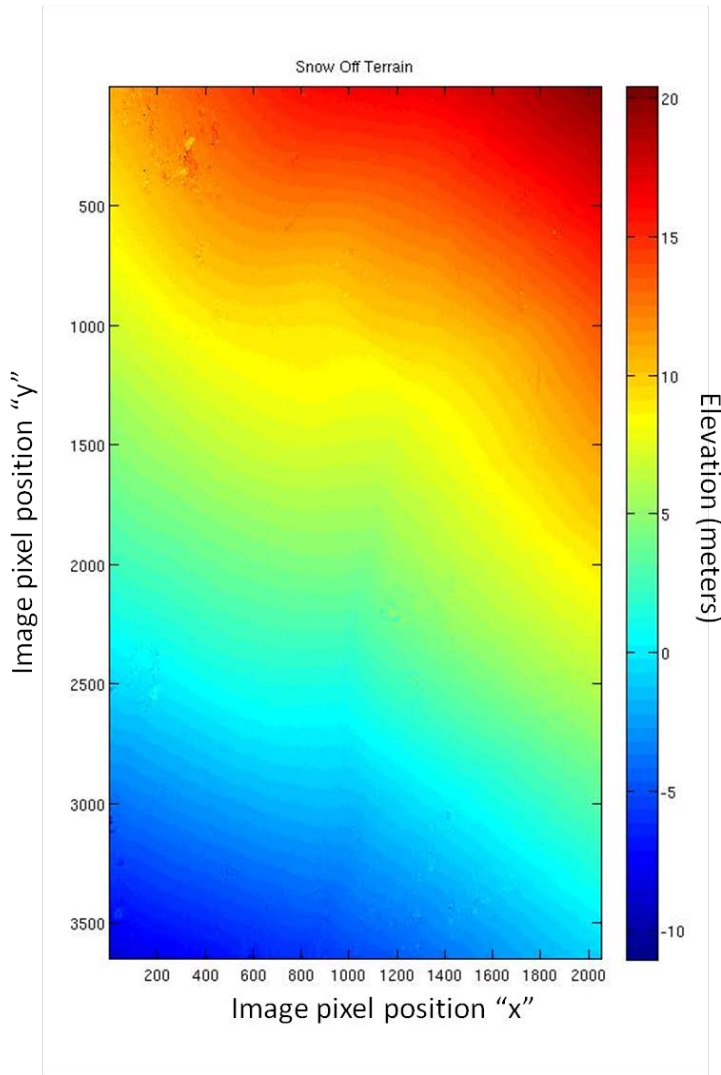


Figure 41. Snow Off DEM. Mammoth Mountain study site ($37^{\circ}37.7'N$, $119^{\circ}02.7'N$).

9. Snow On Snow Off Differencing

The last step in deriving the snow depth is to subtract a DEM generated from a Snow Off scene from a DEM generated from a Snow On scene. The resulting image is the result of the change in elevation strictly due to the addition of snow.

10. Baseline Method Summary

Figure 42 is a flow chart that summarizes the steps and processing order of the Baseline method.

Baseline Method

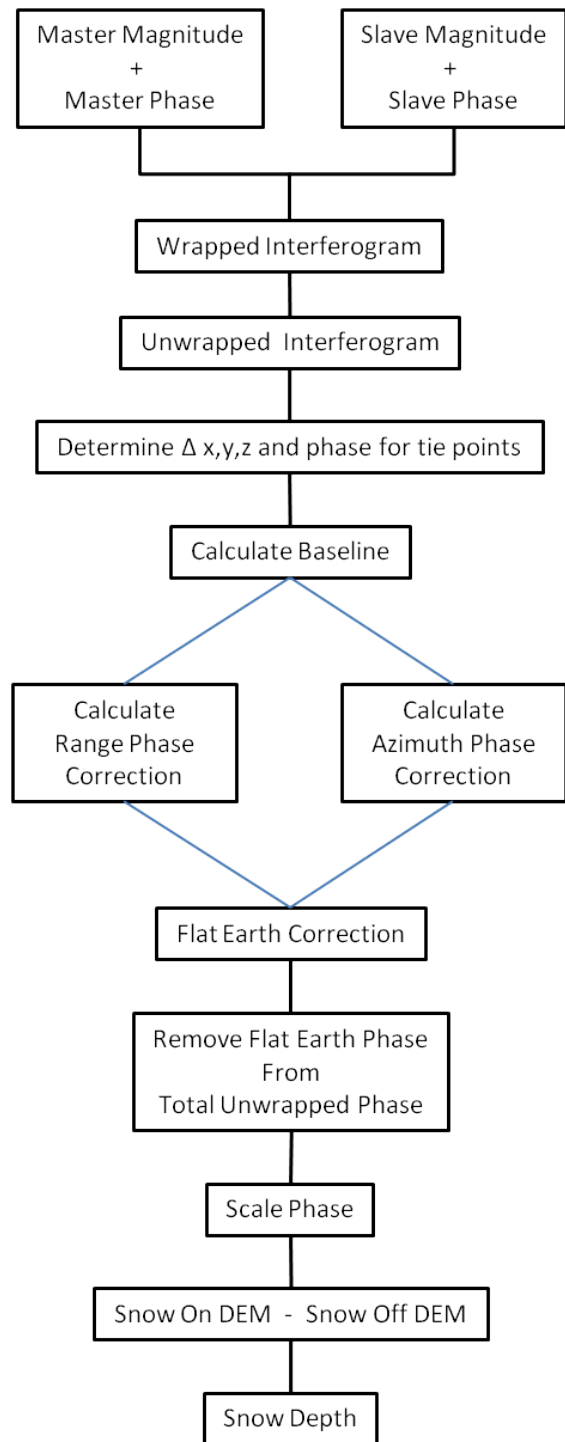


Figure 42. Baseline method flow chart.

D. DATA PROCESSING (BEST FIT PLANE REMOVAL METHOD)

The “Best Fit Plane Removal (BFPR) Method” takes a different approach to calculating the DEM than the Baseline method. The BFPR approach does, however, share some of the same steps that were performed in the Baseline method. The Baseline method takes a direct route to calculating and removing the flat earth phase “ $\Delta\phi_{\text{flat_earth}}$ ”, and the phase to elevation ratio. These calculations require knowledge of the baseline. The BFPR method bypasses the baseline knowledge requirement, thus removing some steps and adding several others. The BFPR processing steps, accomplished in MATLAB are as follows (shared steps italicized):

- *Data preparation*
- *Complex image generation*
- *Image registration*
- *Interferogram generation*
- *Phase unwrapping*
- Best Fit Plane generation
- Best Fit Plane Removal
- Terrain slope generation from low resolution DEM
- Control point elevation difference from average slope
- Phase to elevation linear regression
- Application of linear regression equation to BFPR image
- Add linearized field to average slope
- *Snow On/Snow Off differencing*
- *Verification*

BFPR is best described from a perturbation or decomposition perspective. Variables with an over-bar represent the mean of that variable while the “prime” symbol or accent mark represents the deviation of the value from a particular mean. In the following equations “ $\Delta\phi_{\text{total}}$ ” represents the total phase or the unwrapped interferometric phase, “ $\Delta\phi_{\text{flat_earth}}$ ” represents the flat earth phase, “ $\Delta\phi_z$ ” represents the phase associated with the terrain.

Recall from equation (21) that unwrapped interferogram is made up of both flat earth and terrain phase as is reiterated in (52) (Richards 2009).

$$\Delta\phi_{total} = \Delta\phi_{flat_earth} + \Delta\phi_z \quad (52)$$

From a perturbation perspective the flat earth phase is

$$\Delta\phi_{flat_earth} = \Delta\bar{\phi}_{flat_earth} + \Delta\phi'_{flat_earth} \quad (53)$$

The flat earth phase, however, is a plane and has no perturbation. Therefore it reduces down to

$$\Delta\phi_{flat_earth} = \Delta\bar{\phi}_{flat_earth} \quad (54)$$

The terrain phase from a perturbation perspective is

$$\Delta\phi_z = \Delta\bar{\phi}_z + \Delta\phi'_z \quad (55)$$

Unlike the flat earth phase, there are variations throughout the image. “ $\bar{\Delta\phi}_z$ ” represents the average slope of the terrain and “ $\Delta\phi'_z$ ” is the variation or perturbation from that average slope.

By replacing (54) and (55) into (53), the total phase can now be given as

$$\begin{aligned} \Delta\phi_{total} &= \Delta\bar{\phi}_{flat_earth} + \Delta\bar{\phi}_z + \Delta\phi'_z \\ &\text{or} \\ \Delta\phi_{total} &= \Delta\phi_{flat_earth} + \Delta\bar{\phi}_z + \Delta\phi'_z \end{aligned} \quad (56)$$

Taking the best fit plane of the total phase is the same as finding the average slope of the phase image and is now given by

$$\Delta\bar{\phi}_{total} = \Delta\bar{\phi}_{flat_earth} + \Delta\bar{\phi}_z \quad (57)$$

Subtracting the BFP or (57) from the total phase yields

$$\Delta\phi_{total} - \Delta\bar{\phi}_{total} = \Delta\phi_{flat_earth} + \Delta\bar{\phi}_z + \Delta\phi'_z - \Delta\phi_{flat_earth} - \Delta\bar{\phi}_z = \Delta\phi'_z \quad (58)$$

(58) represents the BFPR and demonstrates that subtracting the BFP from the total phase results in only the terrain perturbations or terrain that deviates from the mean slope (Figure 43).

The BFPR is in phase space and needs to be converted to elevation to be of any use in snow depth estimation. Converting it to elevation requires determination of the phase to elevation relationship. Recall that highly accurate elevations were recorded using a survey grade GPS at the corner reflector locations for the Mammoth Mountain site. If the difference in the elevations at those locations to the average slope can be determined, a direct comparison can be made to the phase in the BFPR image at those same locations. Calculating a best fit plane (BFP) of a lower resolution DEM provides that average terrain slope. After the differences between the GPS elevations and BFP of the DEM are determined, a linear regression can be performed, which results in the phase to elevation relationship.

The next step is to apply the above relationship to the BFPR image. This results in an image that represents the perturbation of the terrain from the average slope. This will be referred to as the “Best Fit Plane Removed and Linearized” (BFPL) image. Adding the BFPL image to the previously calculated mean slope from the low resolution DEM results in a DEM at the same resolution as the SAR image.

The last step is to subtract a Snow Off DEM from a Snow On DEM to obtain the snow depth on a per-pixel-basis.

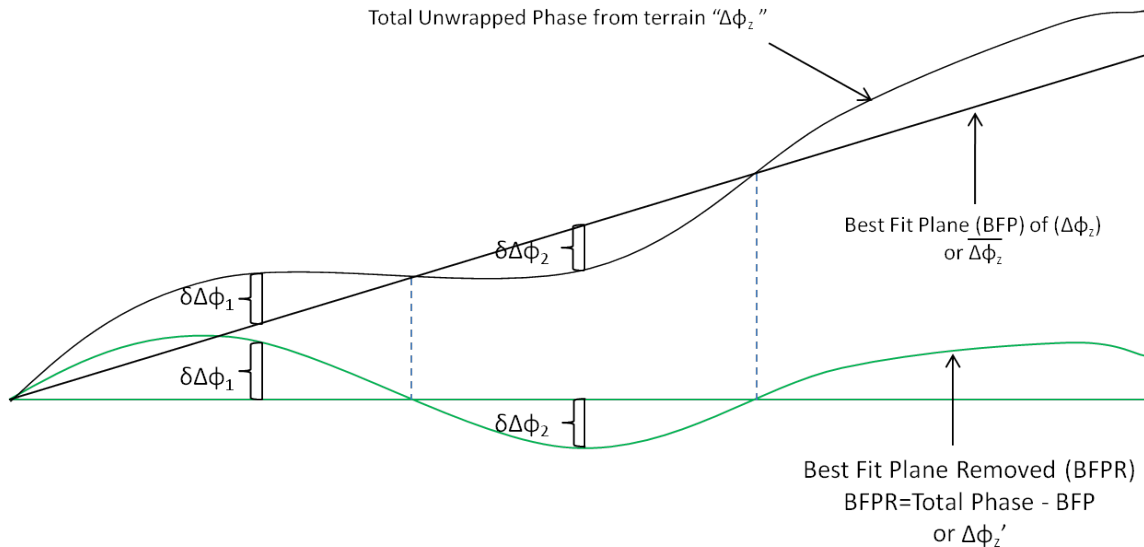


Figure 43. The Best Fit Plane Removed (BFPR) method subtracts the best fit plane (BFP) from the total unwrapped phase. The BFPR isolates the portion of the total unwrapped phase that is due to the deviation of the terrain from the average slope of the terrain and is signified as “ $\delta\Delta\phi$ ”. This can then be compared to ground data to establish a relationship between this phase and elevation.

1. Best Fit Plane Generation

As mentioned previously, this method is applied to an unwrapped interferogram. From a data processing and methodology stand point, the steps that were used in the Baseline method starting at “data preparation” through “phase unwrapping” are the same and will not be reiterated here and further discussion will simple carry on from that point.

Once the unwrapped interferogram is available, the BFP can be generated from the unwrapped phase. This was done using MATLAB. Standard code to accomplish orthogonal regression fitting available through Mathworks 2013 was used to generate the best fit plane.

Before the script could be used, the 2052x3646 phase array had to be converted to a three column matrix. Once that was done, the data were fed into the regression script. The script itself uses principal component analysis to fit a linear regression that minimizes the perpendicular distance of a data set to a fitted model, which is the BFP. The output is in the form of two vectors. One consists of two principle components that

form the basis of a plane. The other vector consists of a principle component that is orthogonal to the first two components and defines the normal to the plane. In simple terms, the code generates the components of the equation of a plane that represents the average of the unwrapped total phase by minimizing the distance of that plane to the phase field.

With these outputs, the equation of the BFP can be defined. After defining the equation it can be used to generate an array that represents all the values on that plane at every pixel location. Once that array is established it can be used in subsequent steps. Figure 44 is an example of the best fit plane from the Snow Off unwrapped interferogram generated from SAR images 21 and 22.

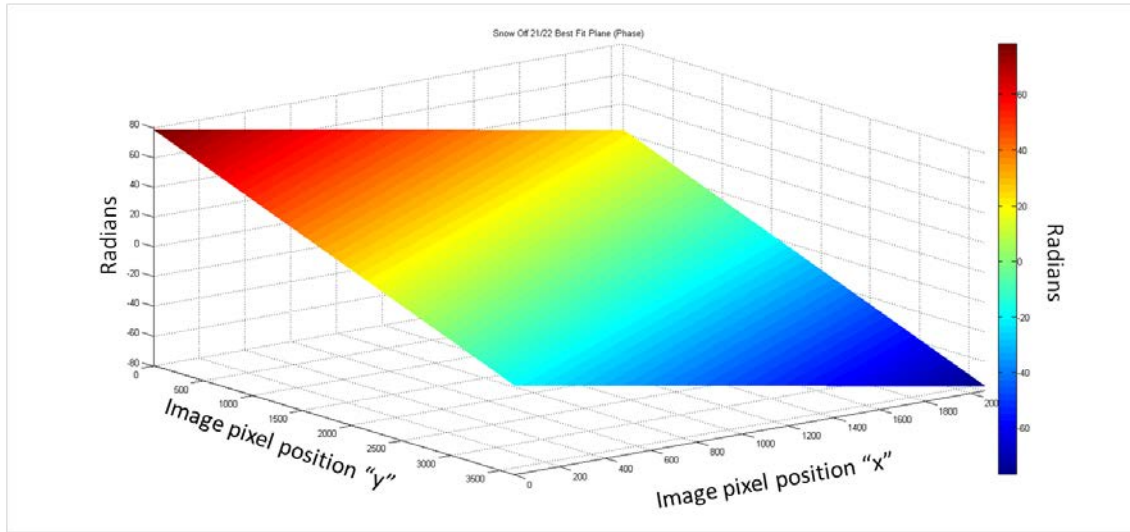


Figure 44. Best fit plane generated from an unwrapped interferogram showing the average slope of the phase image. Mammoth Mountain study site, ($37^{\circ}37.7'N$, $119^{\circ}02.7'N$).

2. Best Fit Plane Removal

Being able to generate a best fit plane from the unwrapped interferogram is important because it facilitates the isolation of the phase produced by high frequency terrain. As mentioned earlier, this is accomplished by subtracting the BFP from the total

phase. This effectively removes the flat earth phase and the average slope phase. Looking back at (58) this can be seen.

$$\Delta\phi_{total} - \Delta\bar{\phi}_{total} = \Delta\phi_{flat_earth} + \Delta\bar{\phi}_z + \Delta\phi'_z - \Delta\phi_{flat_earth} - \Delta\bar{\phi}_z = \Delta\phi'_z \quad (58)$$

The actual subtraction of the best fit plane is fairly straightforward and can be seen in Figures 45 through 48. Figure 45 is a representation of the Snow On unwrapped interferogram or the total unwrapped phase. Figure 46 is a representation of the best fit plane generated from that interferogram and Figure 47 is the result of subtracting 46 from 45.

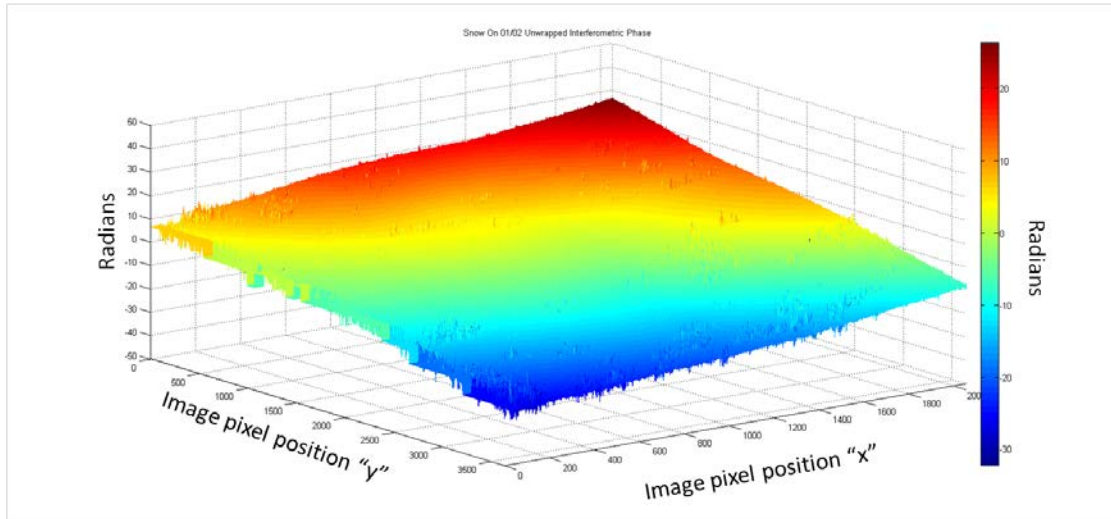


Figure 45. Unwrapped interferogram. Mammoth Mountain study site, ($37^{\circ}37.7'N$, $119^{\circ}02.7'N$).

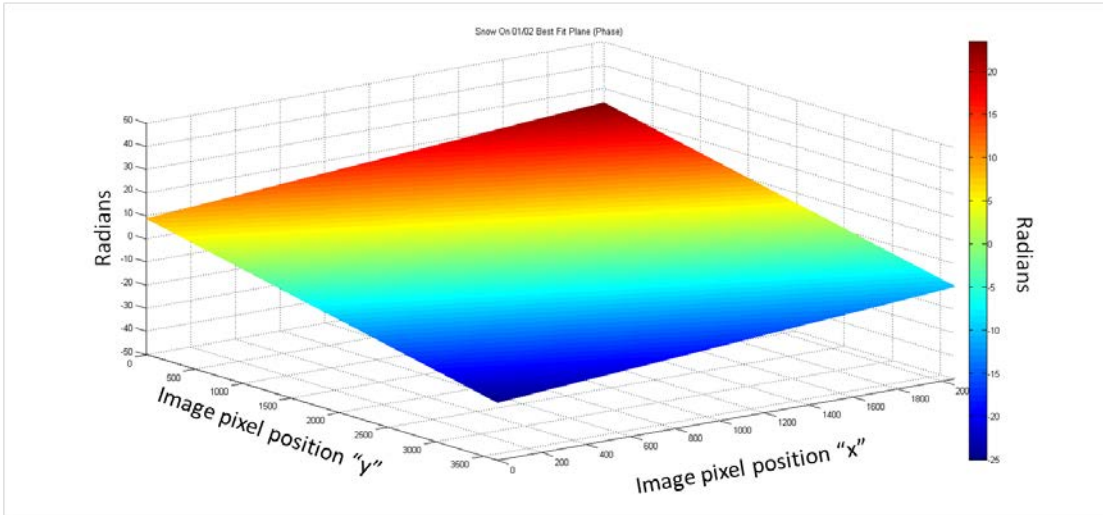


Figure 46. Best Fit Plane generated from the unwrapped interferogram. Mammoth Mountain study site, ($37^{\circ}37.7'N$, $119^{\circ}02.7'N$).

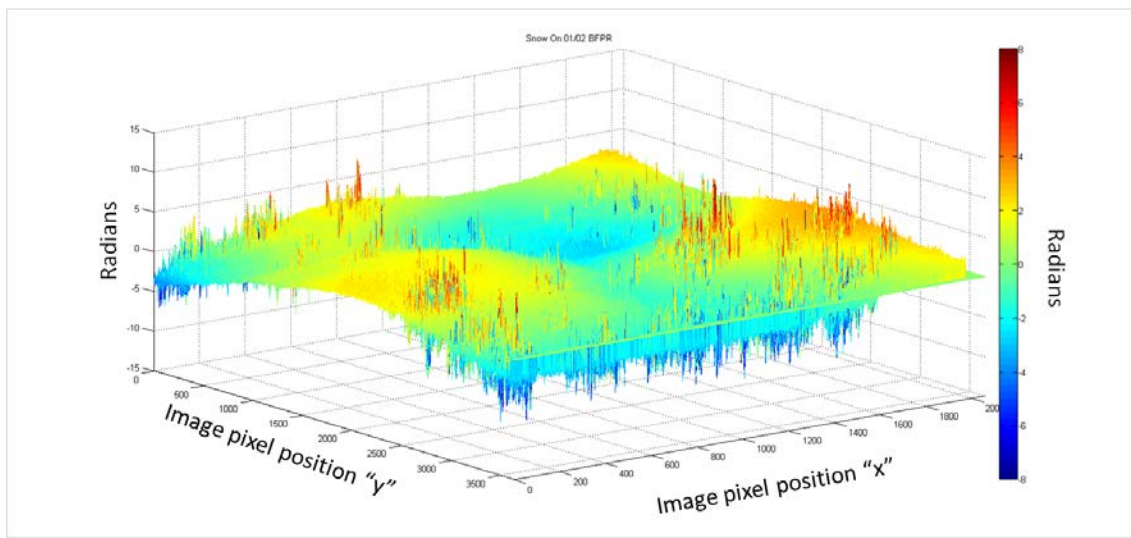


Figure 47. This figure represents the phase that is left after subtracting the BFP from the unwrapped interferogram and is referred to as Best Fit Plane Removed (BFPR). Mammoth Mountain study site, ($37^{\circ}37.7'N$, $119^{\circ}02.7'N$).

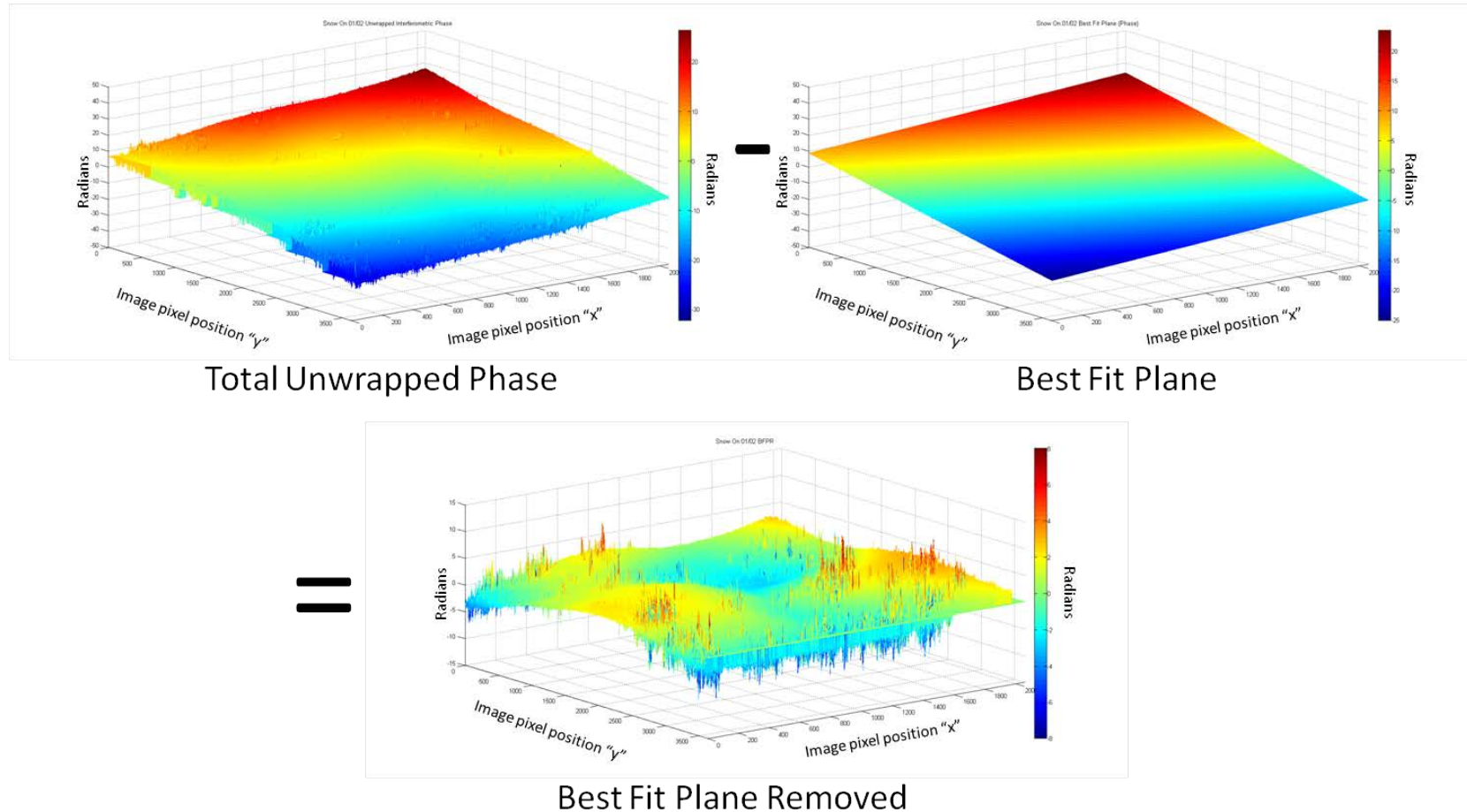


Figure 48. Path to the BFPR. Mammoth Mountain study site, ($37^{\circ}37.7'N$, $119^{\circ}02.7'N$).

3. Mean Slope Generation from Low Resolution DEM

The next step after the BFPR image (in phase space) was established was to determine the relationship between the phase and elevation. The first step in that process was to generate the elevation slope. This was accomplished by calculating the BFP of a relatively low resolution DEM of the same image area. To meet this requirement a 10m resolution DEM was downloaded from the United States Department of Agriculture (USDA) (National Agriculture Imagery Program (NAIP) 2013). The low resolution image was geocorrected using the four corner reflector locations and using a rotation, scaling translation (RST) transformation to WGS84 at 0.0858m resolution using nearest neighbor resampling. Then, one of the SAR Snow Off images was geocorrected using the corner reflector locations as previously described and the DEM was subset to match the SAR data extent. The DEM was then transformed into the SAR geometry and converted to a flat binary file for ingest into MATLAB for the best fit plane processing. The resulting DEM can be seen in Figure 49.

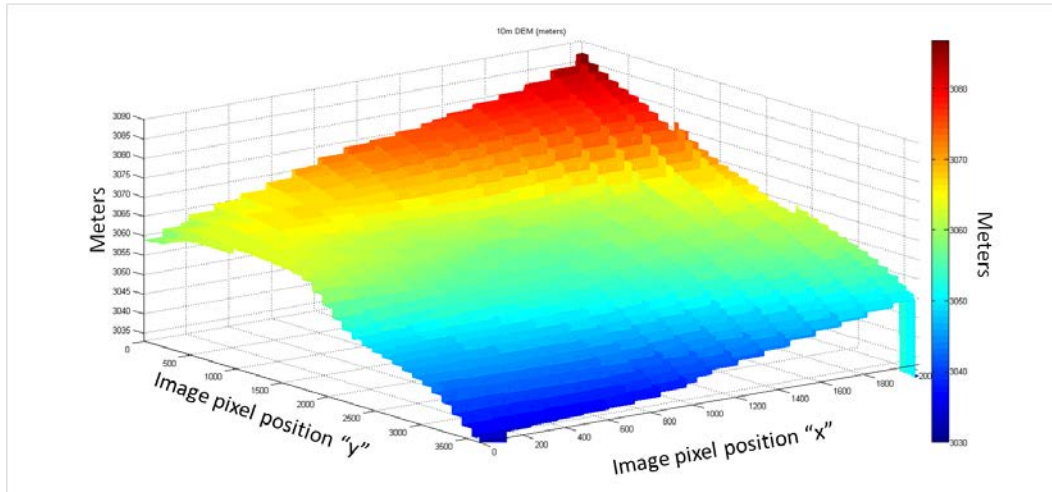


Figure 49. 3D representation of a 10 meter resolution DEM used to determine average slope of the terrain. Mammoth Mountain study site, (37°37.7'N, 119°02.7'N).

The BFP, or average terrain slope, of the low resolution DEM can now be calculated. The same process that was used to calculate the BFP of the unwrapped interferogram was used in this case also. The resulting plane can be seen in Figures 50.

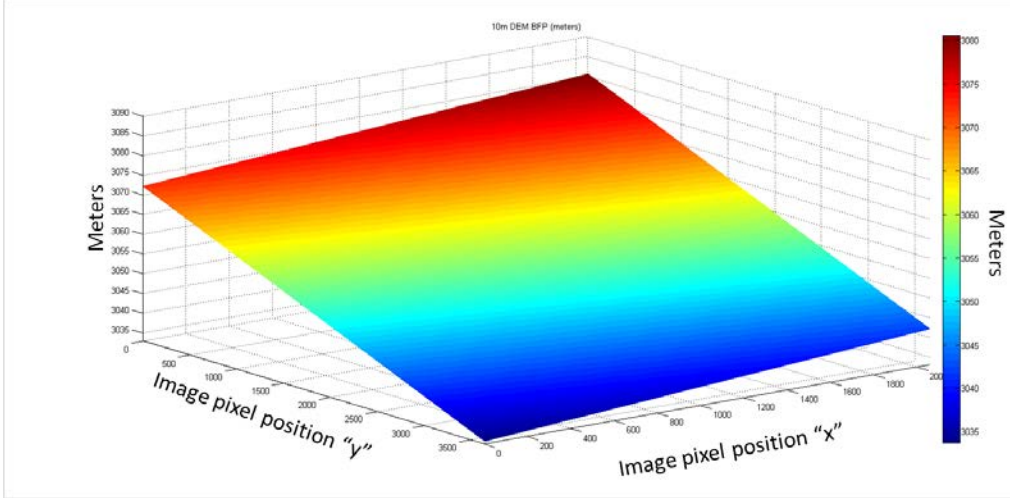


Figure 50. 3D representation of 10m DEM BFP (average terrain slope in meters). Mammoth Mountain study site, ($37^{\circ}37.7'N$, $119^{\circ}02.7'N$).

4. Control Point Elevation Difference from Average Slope

Recall that the BFPR image from the unwrapped interferogram resulted in an image that represents the deviation from the average terrain slope in phase space. To get at the phase to height relationship, the phase perturbation needs to be compared to the elevation perturbation. The GPS-derived elevations allow for a direct comparison between the known elevations at defined points such as the corner reflectors and the calculated mean elevation slope (Figure 51).

The pixel coordinate for each GCP was determined in the 10m DEM BFP image, the elevation value was recorded, and then compared to the elevation value determined by the GPS. This difference was used to compare the elevation deviation to the phase deviation in the next step.

5. Phase to Elevation Linear Regression

Richards, 2009 showed that the phase to elevation relationship is linear. Therefore, direct comparison between phase slope perturbations and elevation slope perturbations should be viable. Figure 51 shows the locations of the known elevations with respect to a BFPR image. A linear regression between the phase and elevation is

demonstrated in Figure 52. The linear regression results in an equation that can now be applied to the entire scene.

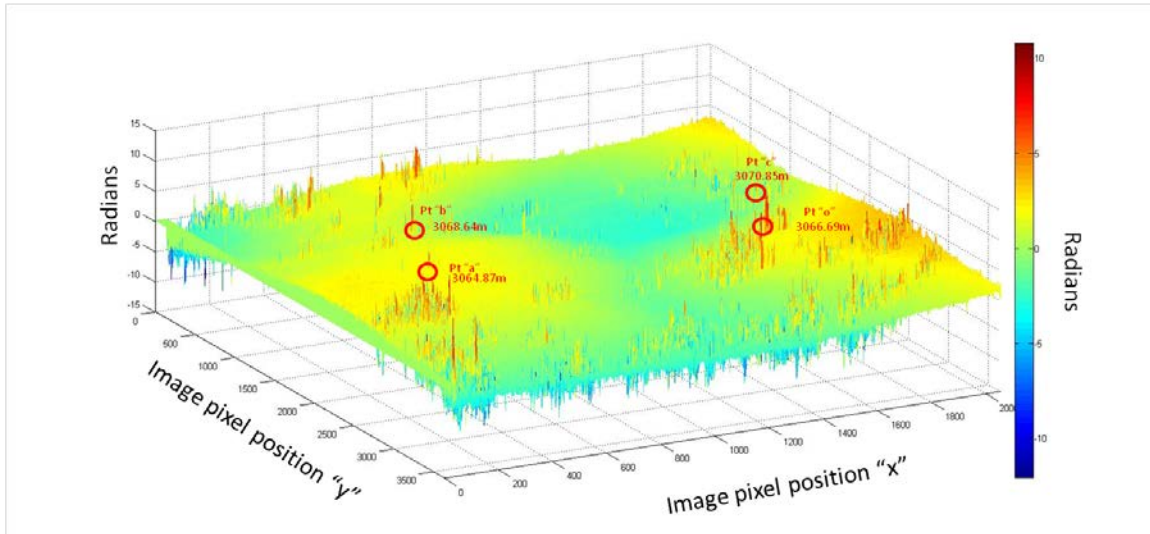


Figure 51. Perspective view of BFPR with tie points and accompanying elevations depicted.
Mammoth Mountain study site, ($37^{\circ}37.7'N$, $119^{\circ}02.7'N$).

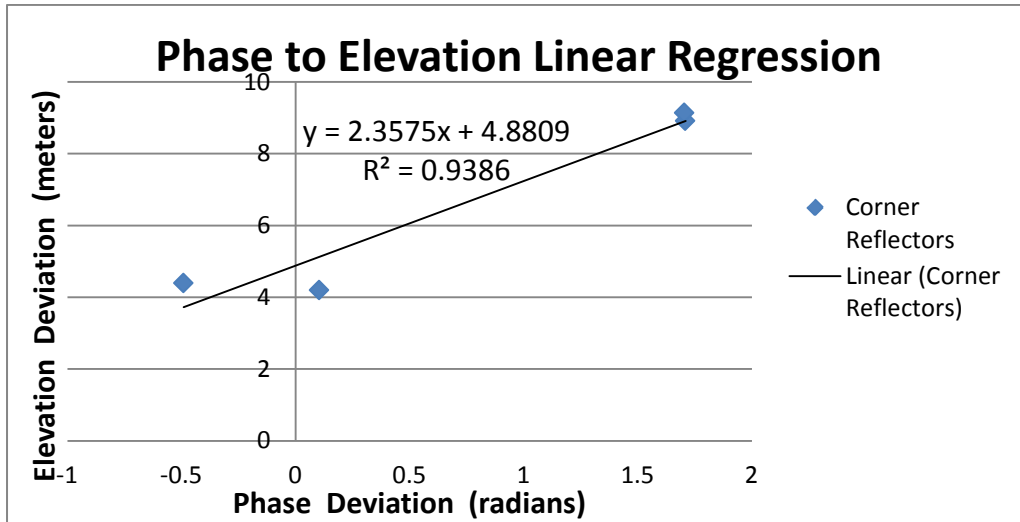


Figure 52. Linear regression for Snow On 01/02 SAR image pair shows the relationship between the phase and elevation.

6. Apply Linear Regression Equation to BFPR Image

The second to last step in making the DEM is to apply the linear regression equation to the BFPR (phase) image seen in Figure 52. The “x” in the linear regression equation represents the phase array to which the equation is applied. The image will not visually change but the values will be converted from phase (radians) to elevation (meters). Recall that this new image now represents the perturbation of the terrain from the slope in elevation or meters.

7. Add Linearized Image to Average Slope

The final step in generating the DEM is to add the above generated terrain perturbation to the 10m DEM BFP (average slope (m)). The resulting image is a DEM at the SAR resolution and can be seen in Figure 53.

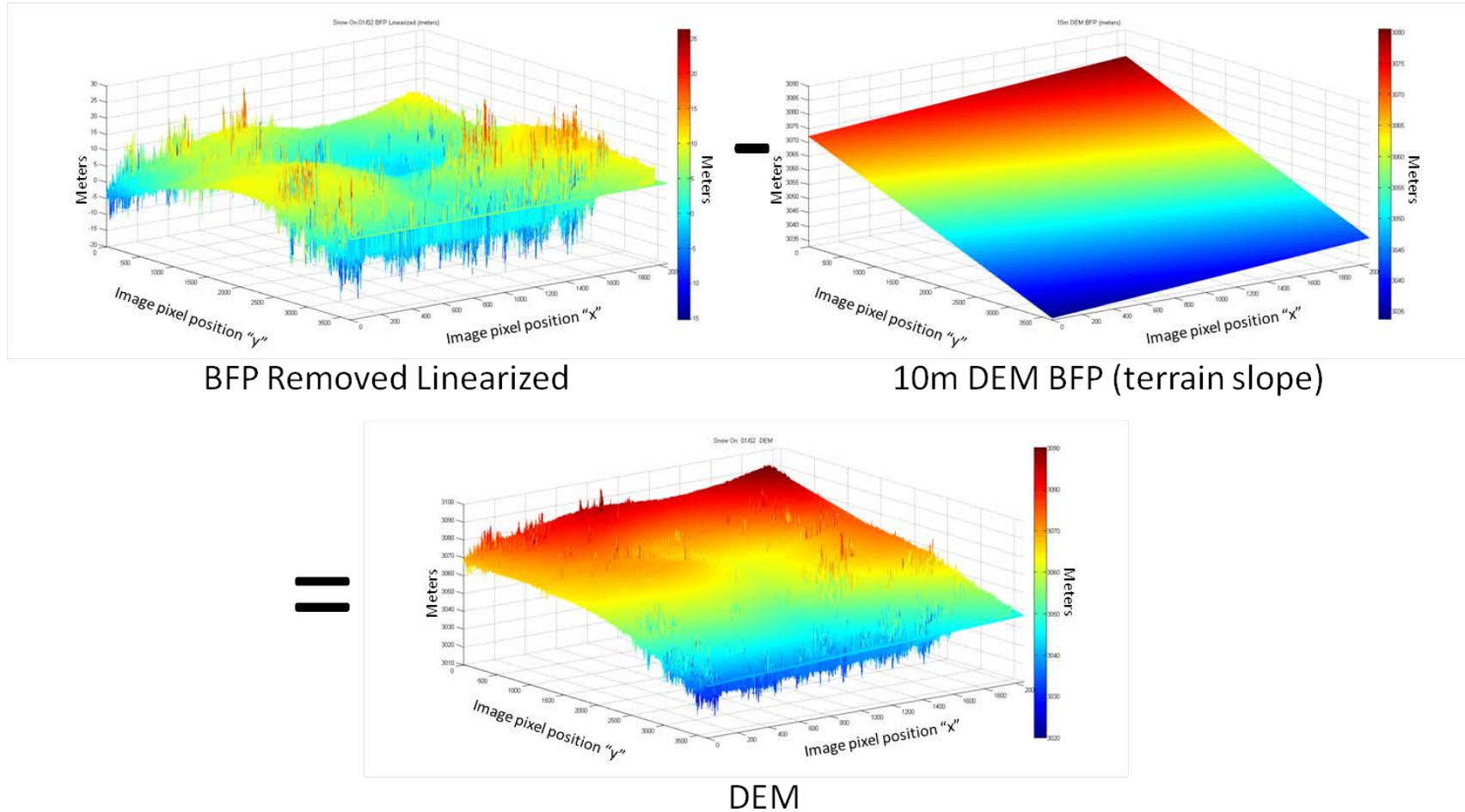


Figure 53. Adding the BFPR after it has had the linear regression equation applied to the low resolution DEM BFP (terrain slope in meters) results in a DEM that is measured in meters. Mammoth Mountain study site, ($37^{\circ}37.7'N$, $119^{\circ}02.7'N$).

8. Snow On/Off Differencing

The final step in calculating the snow depth was to subtract a Snow Off DEM from a Snow On DEM. The resulting image is the difference in elevation between the two images, the snow depth, and can be seen in Figure 54.

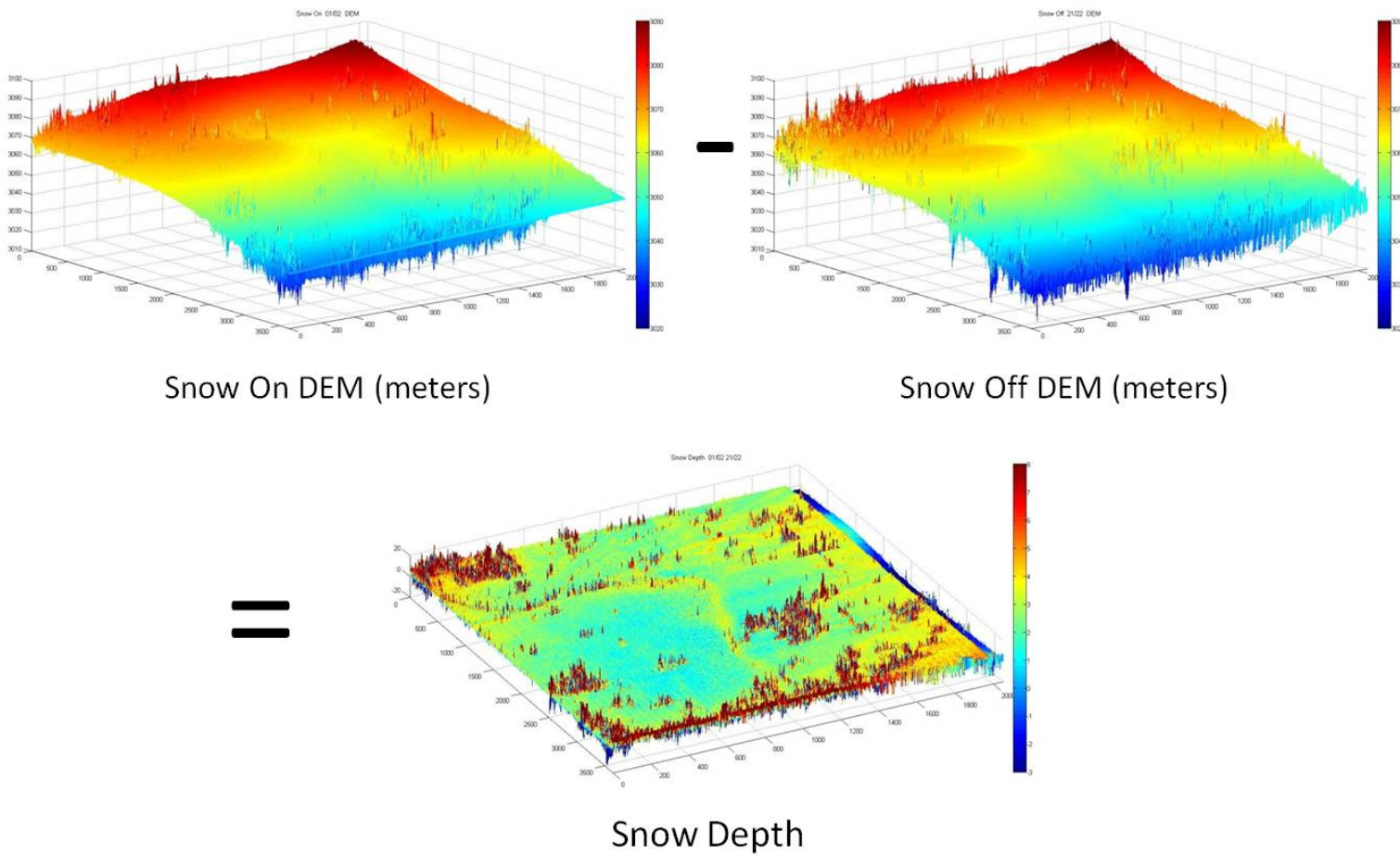


Figure 54. Subtracting the Snow Off DEM from the Snow On DEM results in a snow depth image. Mammoth Mountain study site, (37°37.7'N, 119°02.7'N).

9. Best Fit Plan Removed Summary

Figure 55 summarizes the BFPR method.

Best Fit Plane Removed Method

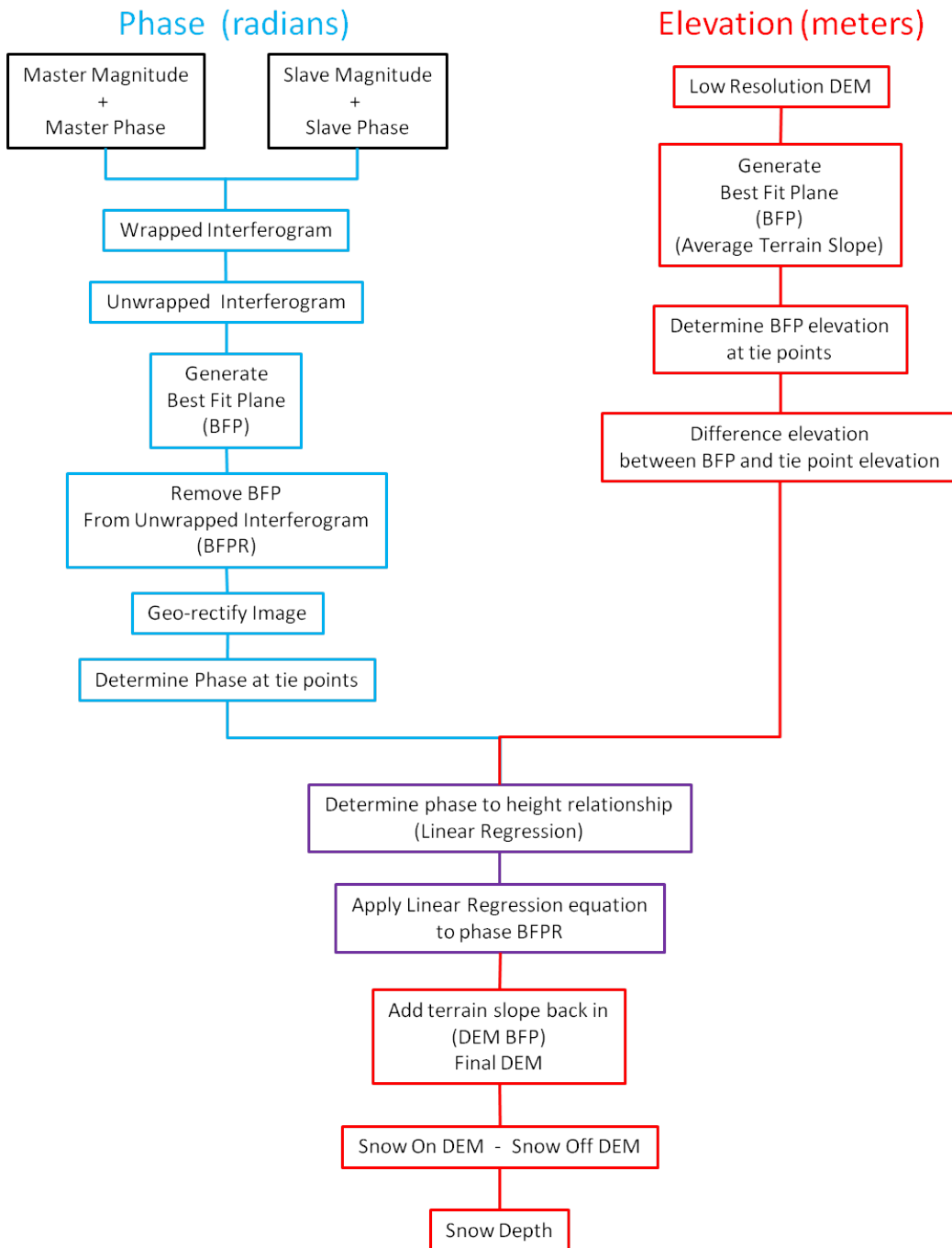


Figure 55. Best fit plane removed method flow chart.

E. VERIFICATION

In order to determine the accuracy of the SAR-determined snow depths, manual snow depth measurements were taken during the field deployment. As mentioned in the field work section, measurements were taken in a grid within the box formed by the corner reflectors. Those measurement locations were recorded with a GPS. Unfortunately a post processing survey grade GPS was not available at the time. This meant that the location accuracy was not the same as that of the corner reflector survey. The estimated accuracy of the snow depth locations was recorded to be on the order of four meters in the horizontal.

The first step in verifying the snow depth was to geo-correct the snow depth image using the previously calculated image-to-map transformation. Once this was done, the specific locations where the snow depth measurements were taken could be located on the imagery and analyzed.

Due to the limitations of accuracy of the GPS locations for the snow measurements, an average snow depth was calculated for a radius of five meters around the recorded locations. Figure 56 shows a recorded snow depth image along with the locations of the manual measurements and the five meter radius circles used.

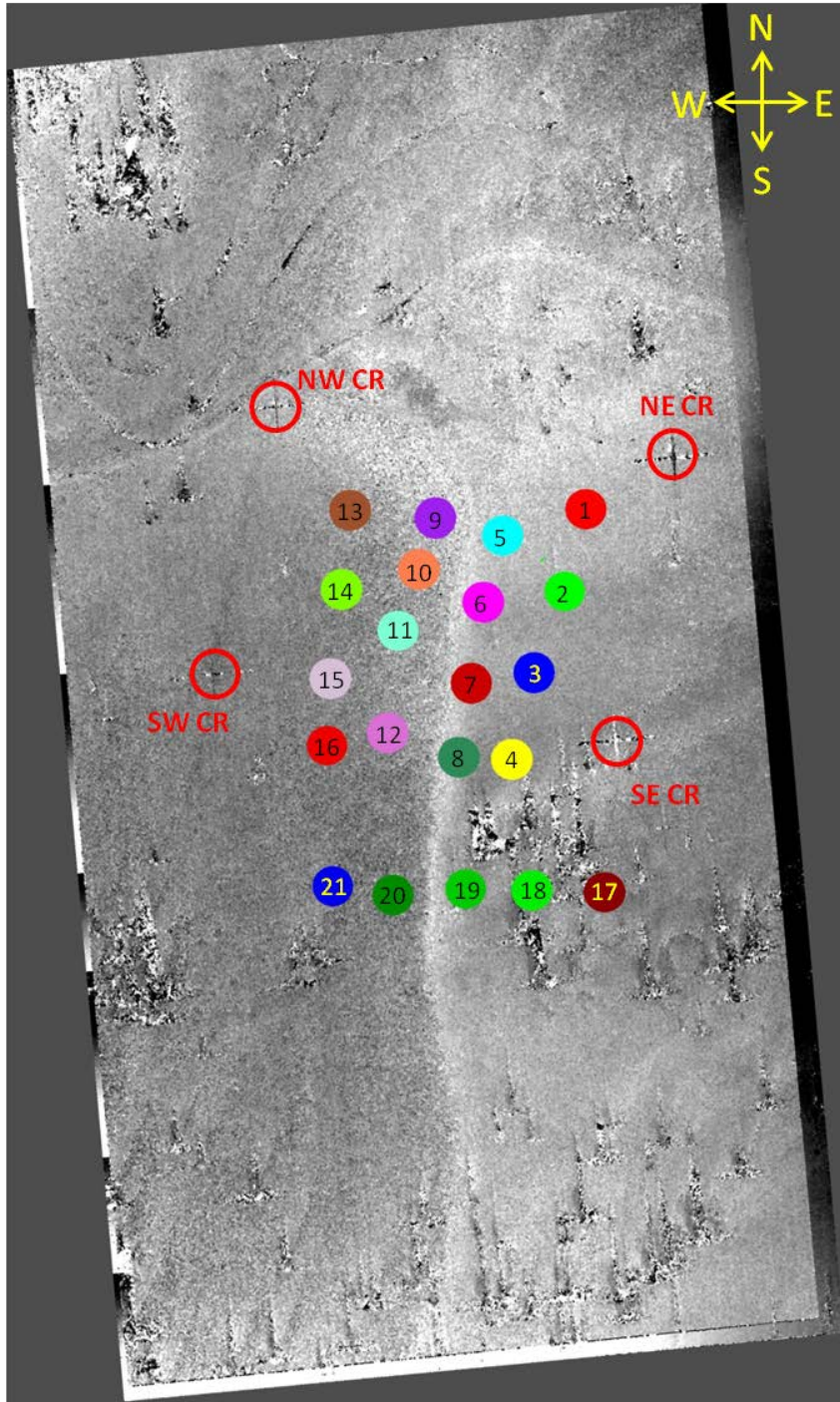


Figure 56. Manual snow depth measurements were taken throughout the scene and are represented by the circles in the above snow depth image. The circle size also demonstrates the 5m radius area that was used to average the snow depth in that location. Corner reflector locations are also shown and labeled (red outlined circles). Mammoth Mountain study site (312 x 176m), (37°37.7'N, 119°02.7'N).

IV. BASELINE METHOD RESULTS

A. PROCESSED IMAGERY

The Baseline Method results/imagery will be displayed in the same order as shown in the processing flow chart. The Snow Off case will be shown first and the DEM produced from it will be applied to the subsequent Snow On charts for the calculated snow depth. Table 1 is provided again for reference.

SAR Image number	Date	Time	Surface Condition
01	3 April 2012	18:47 Z, 10:47 L	snow covered
02	3 April 2012	18:55 Z, 10:55 L	snow covered
03	3 April 2012	19:04 Z, 11:04 L	snow covered
04	3 April 2012	19:00 Z, 11:00 L	snow covered
21	13 July 2012	17:58 Z, 10:58 L	bare
22	13 July 2012	18:05 Z, 11:05 L	bare

Table 1. Four usable Snow On and two useable Snow Off SAR images at 0.1m resolution were acquired by General Atomics during the radar collection phase of the research. These images enabled six Snow On and one Snow Off interferometric pairs to be calculated.

1. Snow Off Pair 21/22

This Snow Off SAR pair processing started by first generating the interferogram image using image pairs 21 and 22. After the interferogram was calculated the image was then unwrapped (Figure 57). The baseline was then calculated using both ground data and phase values at the GCPs (Table 2). Both the range and azimuth corrections were calculated and combined resulting in the flat earth correction (Figure 58). The flat earth correction was subtracted from the total phase resulting in the flattened image (Figures 59). The scaling factor was then applied resulting in the final DEM (Figure 60).

(1) Interferogram

Snow Off 21/22 BL

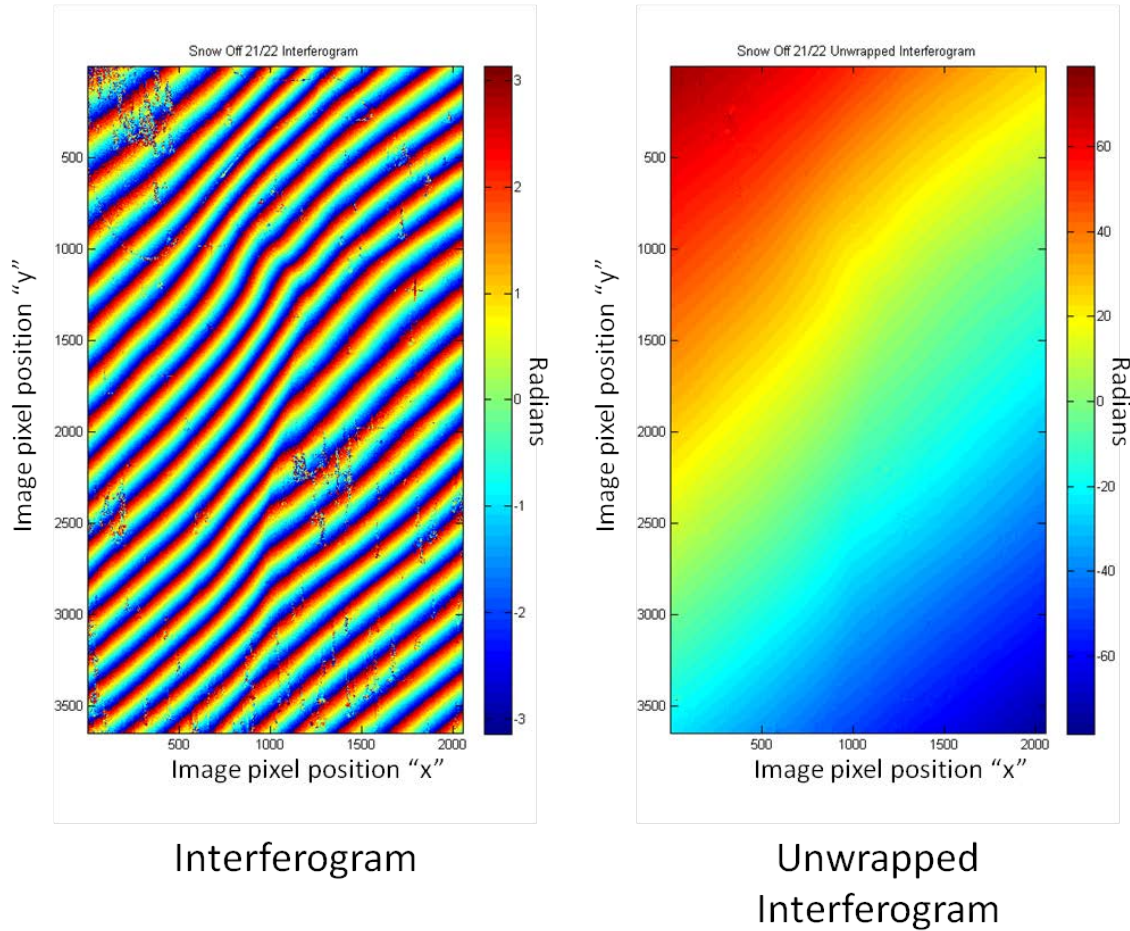


Figure 57. Snow Off SAR image pair 21 and 22 interferogram and the resulting unwrapped interferogram. Mammoth Mountain study site, (37°37.7'N, 119°02.7'N).

(2) Calculated Baseline. The system of equations to calculate the baseline between the two flight paths requires inputs that include the change in the x, y, and z in meters relative to the reference tie point or corner reflector and the interferometric phase at those tie points. Those inputs along with the calculated baseline can be seen in the following table.

Baseline input Data 21/22 (meters)						Baseline (meters)	
	SE (o)	SW (a)	NW (b)	NE (c)			
phase $\Delta\phi$	-17.7481	23.2551	33.6268	-3.6191		Bx	-9.23
adjusted Δx	NA	-92.522	-63.6515	28.36108		By	-0.7
adjusted Δy	NA	36.16798	96.75298	64.08585		Bz	123.59
Δz	NA	-1.813	1.949	4.158		Total BL	123.9362

Table 2. The baseline calculation relies on the relative $\Delta(x, y, z)$ change of position from a reference point (SE(o)) to three other known locations (SW(a), NW(b), and NE(c)) and the interferometric phase ($\Delta\phi$) at those locations. The right side of the chart depicts the calculated baseline components in the x, y, z directions (B_x , B_y , and B_z)

(3) Flat Earth Correction

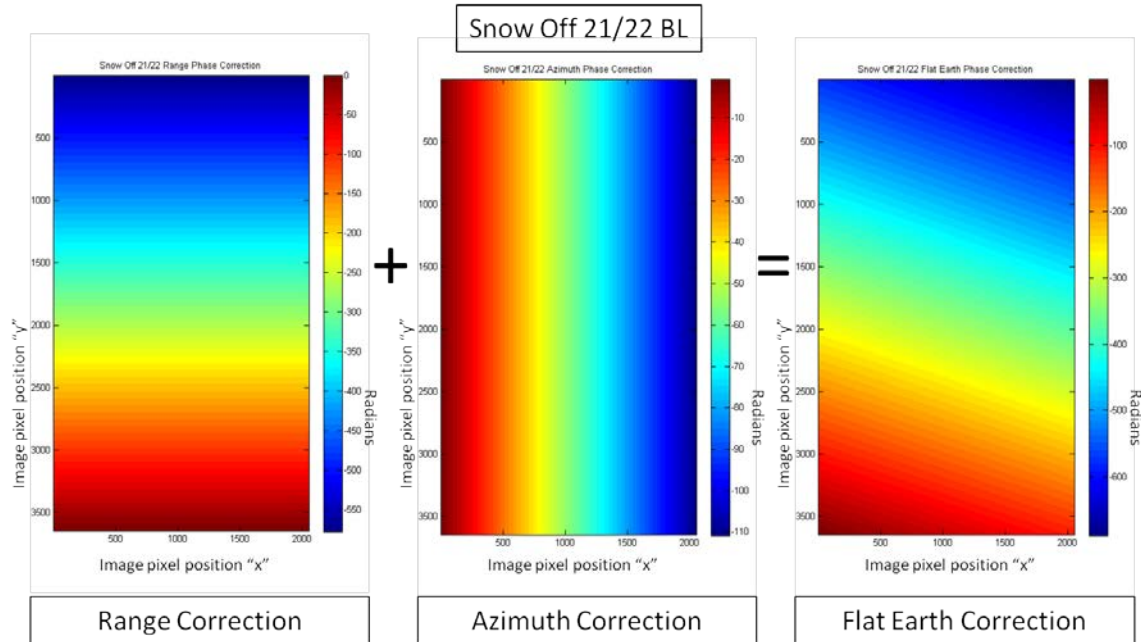


Figure 58. The summation of the range phase correction and azimuth phase correction results in the total flat earth phase correction that will be applied to the unwrapped interferogram. Mammoth Mountain study site, (37°37.7'N, 119°02.7'N).

(4) Flattened Phase Calculation

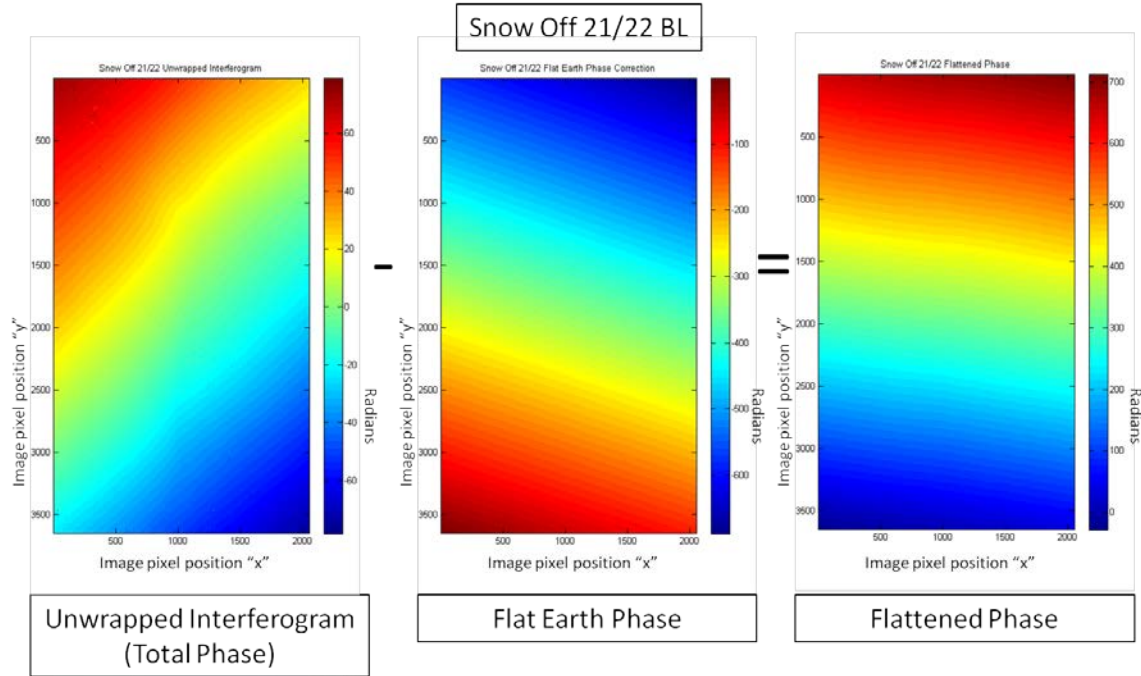


Figure 59. Subtracting the flat earth correction from the unwrapped phase results in a phase that is entirely due to the snow covered terrain and is known as the flattened phase. Mammoth Mountain study site, ($37^{\circ}37.7'N$, $119^{\circ}02.7'W$).

(5) Scaling and DEM Generation.

The scaling equation (51) that converts the flattened phase to elevation was applied to generate the DEM.

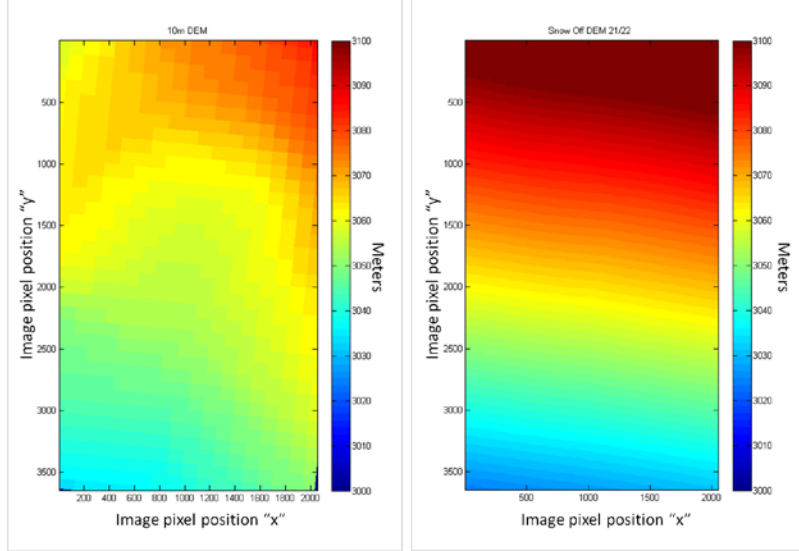


Figure 60. Once the scaling factor is applied to the flattened phase, the resulting image is a DEM of the area being sampled. The image on the right is the SAR-calculated DEM while the image on the left is the low resolution DEM for comparison.
Mammoth Mountain study site, (37°37.7'N, 119°02.7'N).

2. Snow On Pair 01/02

The Snow On SAR pair processing started by first generating the interferogram image using image pairs 01 and 02. After the interferogram was calculated the image was then unwrapped (Figure 61). The baseline was then calculated using both ground data and phase values at the GCPs (Table 3). Both the range and azimuth corrections were calculated and combined resulting in the flat earth correction (Figure 62). The flat earth correction was subtracted from the total phase resulting in the flattened image (Figures 63). The scaling factor was then applied resulting in the final DEM (Figure 64). The Snow Off DEM was then subtracted from this DEM resulting in the final snow depth image (Figure 65).

(1) Interferogram

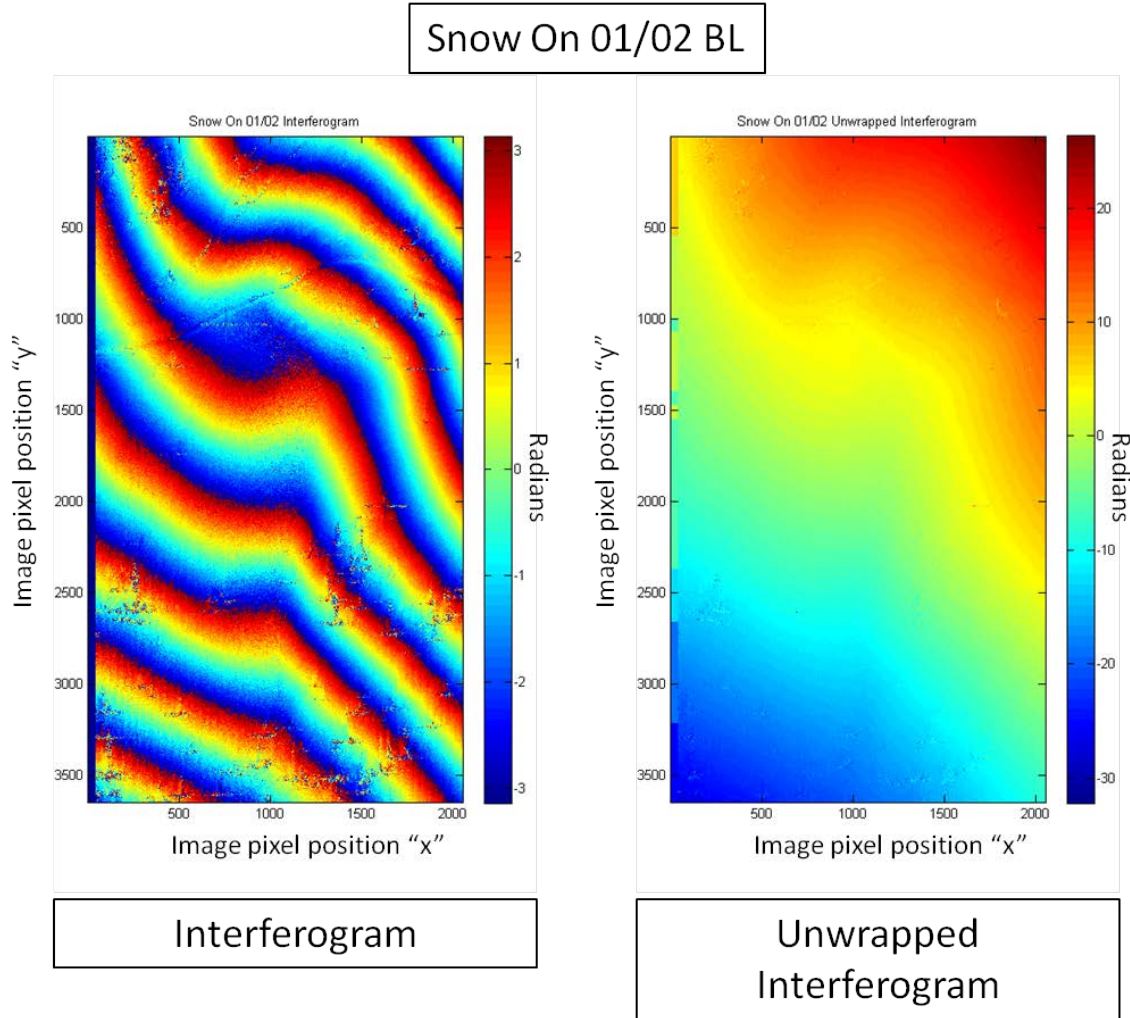


Figure 61. Snow On SAR image pair 01 and 02 interferogram and the resulting unwrapped interferogram. Mammoth Mountain study site, (37°37.7'N, 119°02.7'N).

(2) Calculated Baseline. The system of equations to calculate the baseline between the two flight paths requires inputs that include the change in the x, y, and z in meters relative to the reference tie point or corner reflector and the interferometric phase at those tie points. Those inputs along with the calculated baseline can be seen in Table 3.

Baseline input Data 01/02 (meters)						Baseline (meters)	
	SE (o)	SW (a)	NW (b)	NE (c)		Bx	2.27
phase $\Delta\phi$	3.369	-2.1338	4.5911	9.7968		By	2.24
adjusted Δx	NA	-92.6249	-63.9277	28.17786		Bz	-26.99
adjusted Δy	NA	35.90349	96.57073	64.16662		Total BL	27.17776
Δz	NA	-1.813	1.949	4.158			

Table 3. The baseline calculation relies on the relative $\Delta(x, y, z)$ change of position from a reference point (SE(o)) to three other known locations (SW(a), NW(b), and NE(c)) and the interferometric phase ($\Delta\phi$) at those locations. The right side of the chart depicts the calculated baseline components in the x, y, z directions (B_x , B_y , and B_z)

(3) Flat Earth Correction

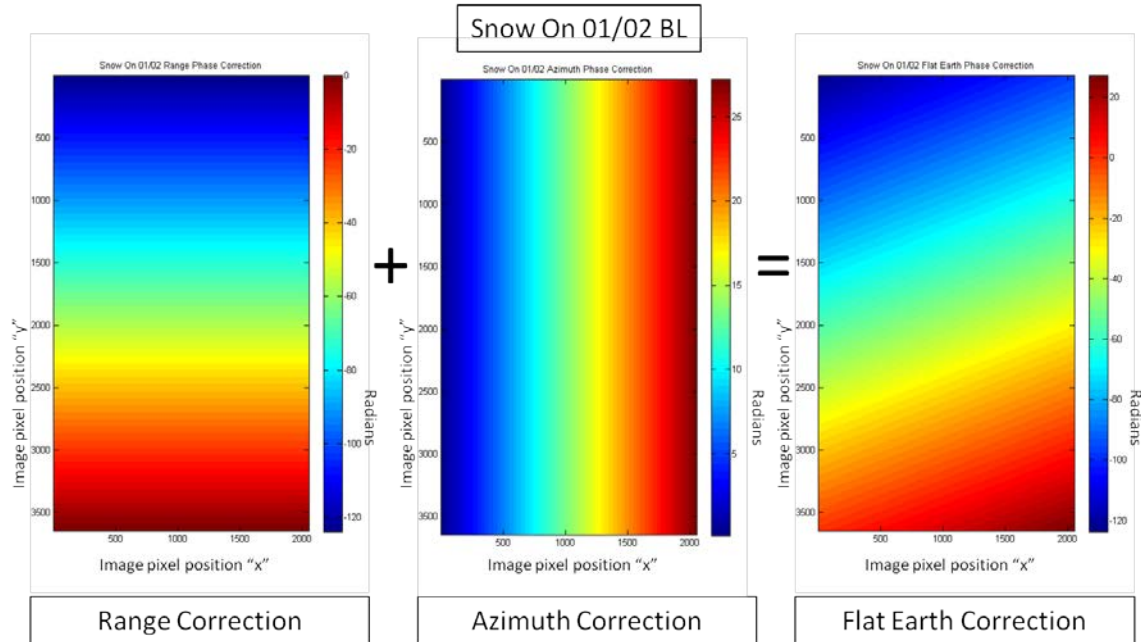


Figure 62. The summation of the range phase correction and azimuth phase correction results in the total flat earth phase correction that will be applied to the unwrapped interferogram. Mammoth Mountain study site, (37°37.7'N, 119°02.7'N).

(4) Flattened Phase Calculation

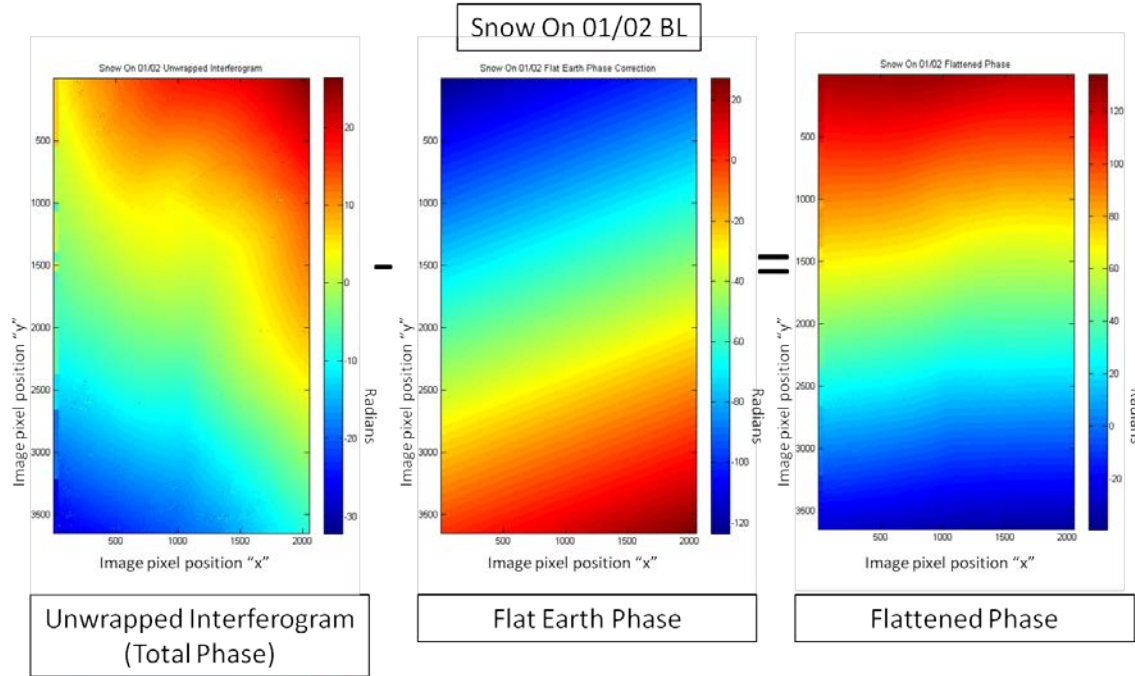


Figure 63. Subtracting the flat earth correction from the unwrapped phase results in a phase that is entirely due to the snow covered terrain and is known as the flattened phase. Mammoth Mountain study site, ($37^{\circ}37.7'N$, $119^{\circ}02.7'W$).

(5) Scaling and DEM Generation.

The scaling equation was applied to generate the DEM.

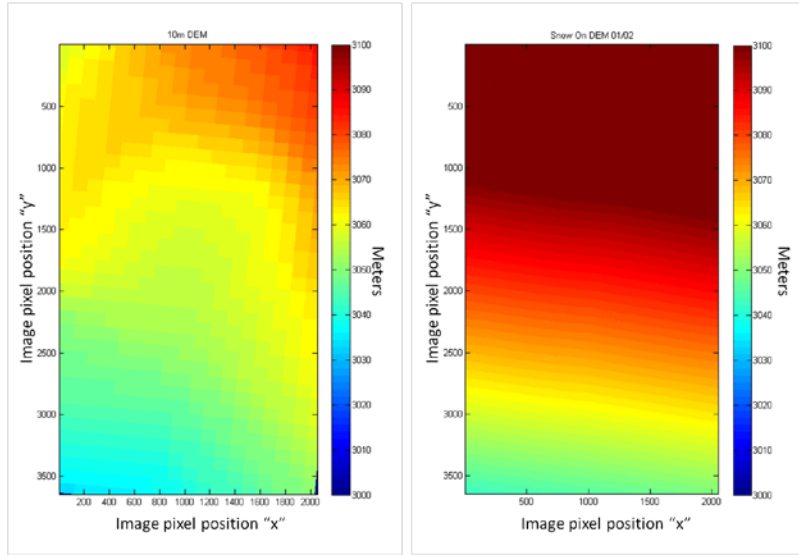


Figure 64. Once the scaling factor is applied to the flattened phase, the resulting image is a DEM of the area being sampled. The image on the right is the SAR-calculated DEM while the image on the left is the low resolution DEM for comparison.
Mammoth Mountain study site, ($37^{\circ}37.7'N$, $119^{\circ}02.7'N$).

(6) Snow Depth

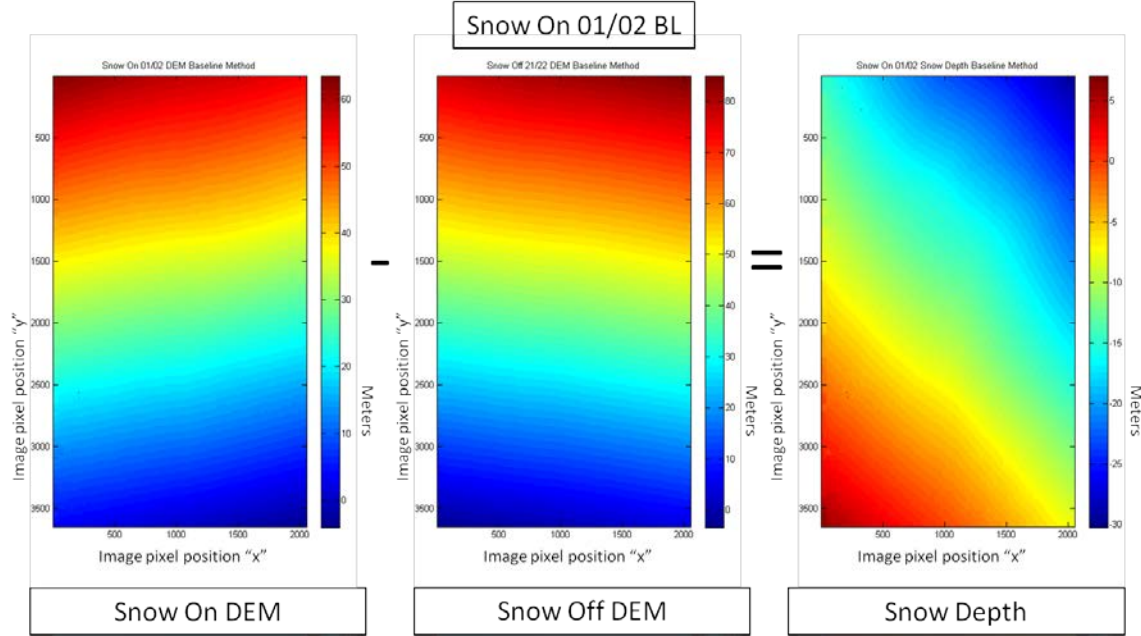


Figure 65. Subtracting the Snow Off DEM from the Snow On DEM should result in an image representing the snow depth. Mammoth Mountain study site, (37°37.7'N, 119°02.7'N).

3. Snow On Pair 01/03

This Snow On SAR pair processing started by first generating the interferogram image using image pairs 01 and 03. After the interferogram was calculated the image was then unwrapped (Figure 66). The baseline was then calculated using both ground data and phase values at the GCPs (Table 4). Both the range and azimuth corrections were calculated and combined resulting in the flat earth correction (Figure 67). The flat earth correction was subtracted from the total phase resulting in the flattened image (Figures 68). The scaling factor was then applied resulting in the final DEM (Figure 69). The Snow Off DEM was then subtracted from this DEM resulting in the final snow depth image (Figure 70).

(1) Interferogram

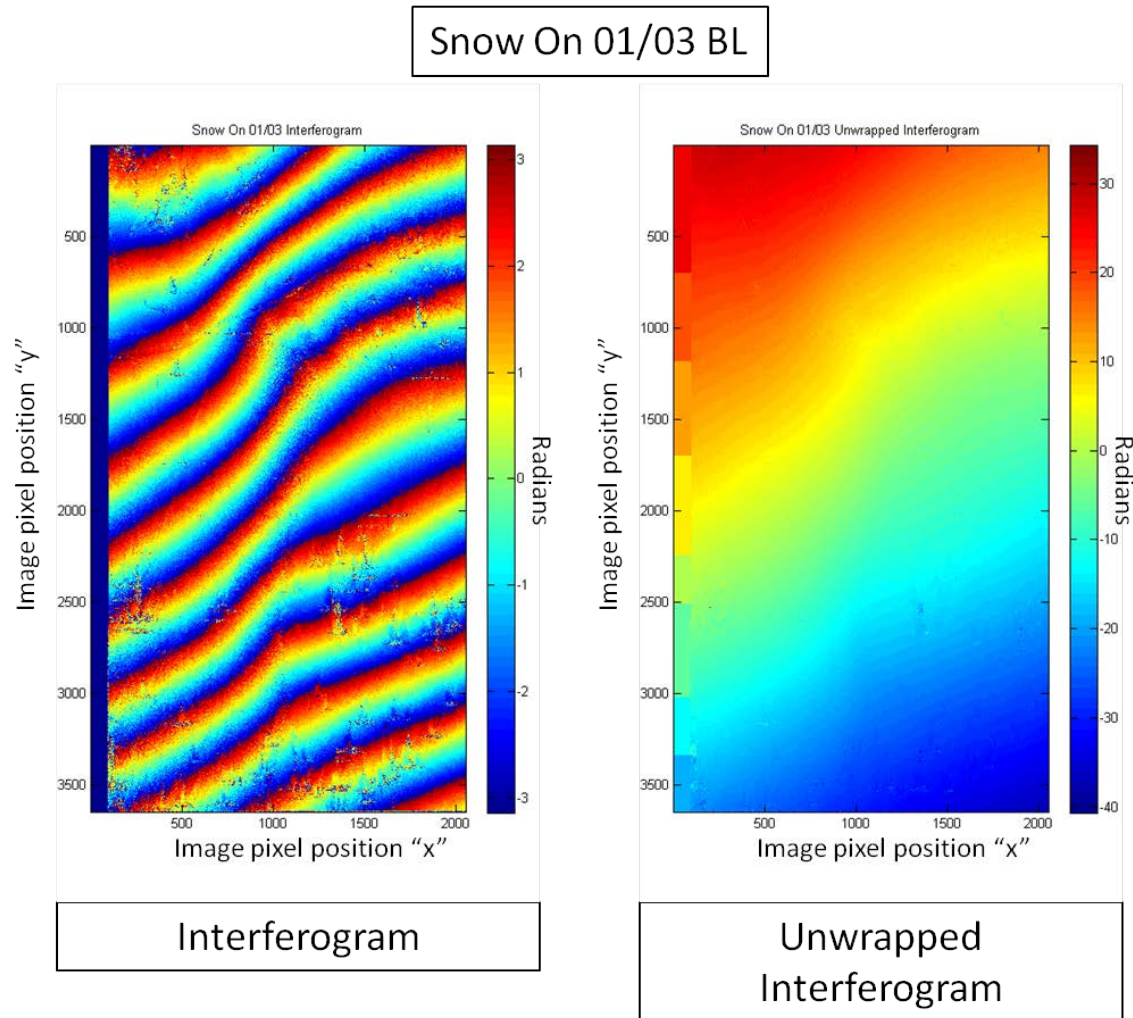


Figure 66. Snow On SAR image pair 01 and 03 interferogram and the resulting unwrapped interferogram. Mammoth Mountain study site, ($37^{\circ}37.7'N$, $119^{\circ}02.7'N$).

(2) Calculated Baseline. The system of equations to calculate the baseline between the two flight paths requires inputs that include the change in the x, y, and z in meters relative to the reference tie point or corner reflector and the interferometric phase at those tie points. Those inputs along with the calculated baseline can be seen in Table 4.

Baseline input Data 01/03 (meters)						Baseline (meters)	
	SE (o)	SW (a)	NW (b)	NE (c)			
phase $\Delta\phi$	-	3.2806	11.5804	17.7238	2.7155	Bx 0.2141	
adjusted Δx	NA	-92.6249	-63.9277	28.17786	By 4.3107		
adjusted Δy	NA	35.90349	96.57073	64.16662	Bz -46.6489		
Δz	NA	-1.813	1.949	4.158	Total BL 46.84814		

Table 4. The baseline calculation relies on the relative $\Delta(x, y, z)$ change of position from a reference point (SE(o)) to three other known locations (SW(a), NW(b), and NE(c)) and the interferometric phase ($\Delta\phi$) at those locations. The right side of the chart depicts the calculated baseline components in the x, y, z directions (B_x , B_y , and B_z)

(3) Flat Earth Correction

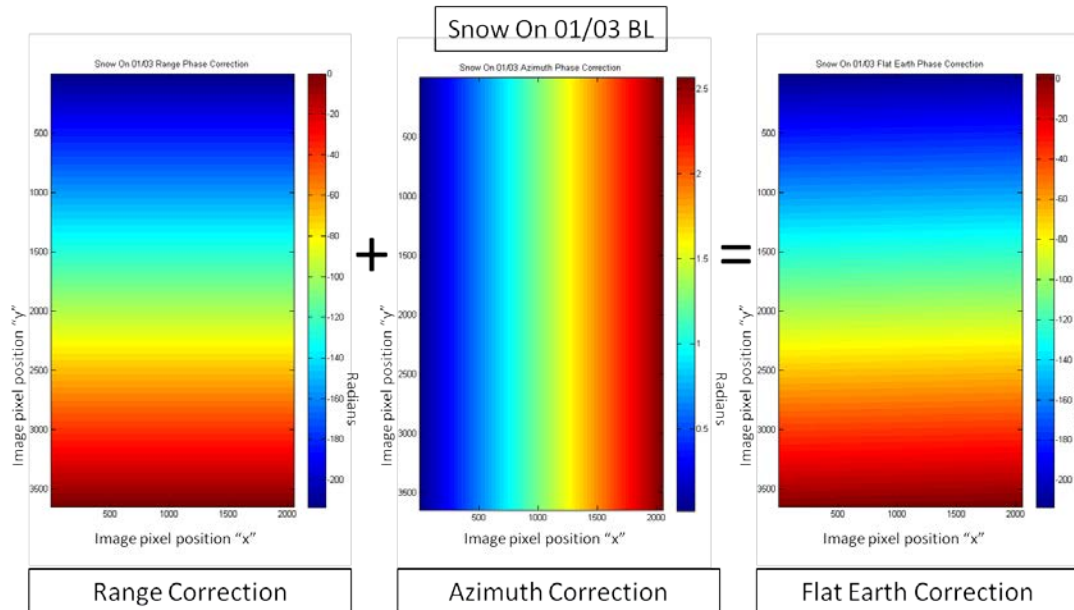


Figure 67. The summation of the range phase correction and azimuth phase correction results in the total flat earth phase correction that will be applied to the unwrapped interferogram. Mammoth Mountain study site, (37°37.7'N, 119°02.7'N).

(4) Flattened Phase Calculation

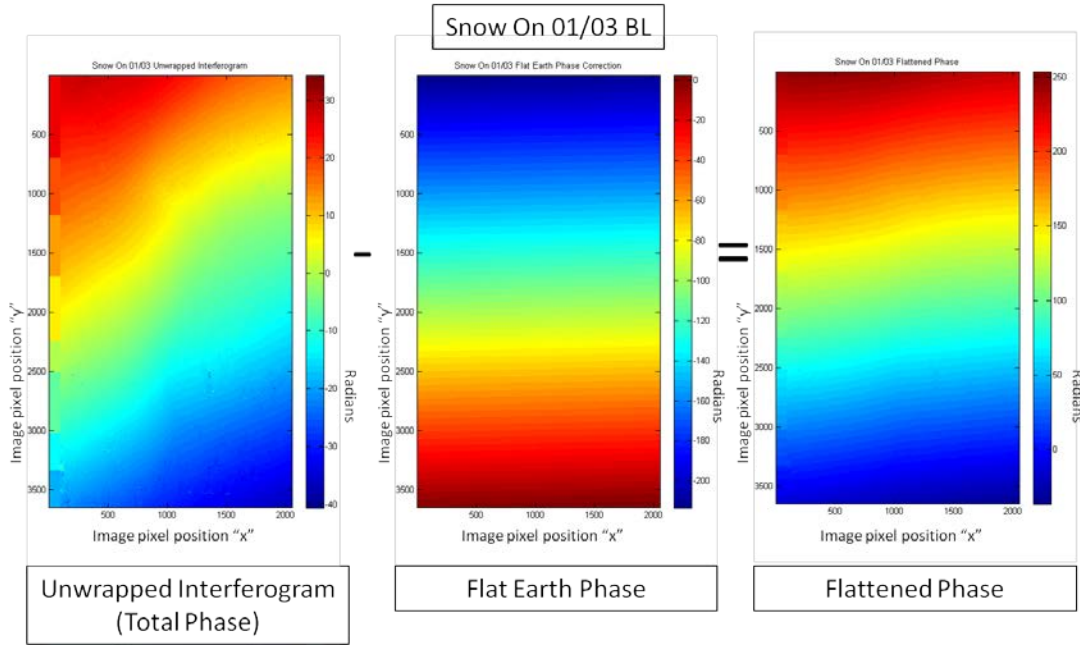


Figure 68. Subtracting the flat earth correction from the unwrapped phase results in a phase that is entirely due to the snow covered terrain and is known as the flattened phase. Mammoth Mountain study site, ($37^{\circ}37.7'N$, $119^{\circ}02.7'N$).

(5) Scaling and DEM Generation. The scaling equation was applied to generate the DEM.

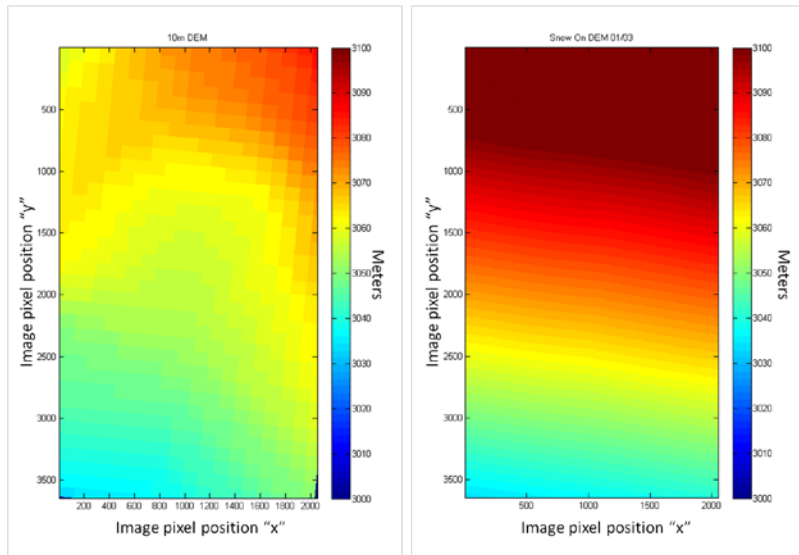


Figure 69. Once the scaling factor is applied to the flattened phase, the resulting image is a DEM of the area being sampled. The image on the right is the SAR-calculated

DEM while the image on the left is the low resolution DEM for comparison.
 Mammoth Mountain study site, ($37^{\circ}37.7'N$, $119^{\circ}02.7'N$).

(6) Snow Depth

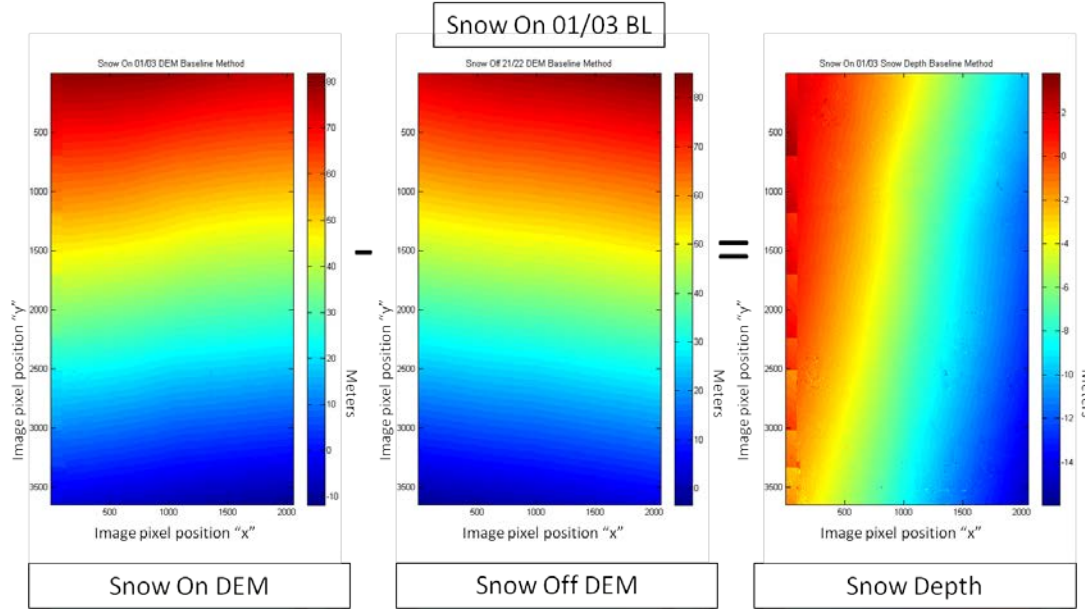


Figure 70. Subtracting the Snow Off DEM from the Snow On DEM should result in an image representing or the snow depth. Mammoth Mountain study site, ($37^{\circ}37.7'N$, $119^{\circ}02.7'N$).

4. Snow On Pair 01/04

This Snow On SAR pair processing started by first generating the interferogram image using image pairs 01 and 04. After the interferogram was calculated the image was then unwrapped (Figure 71). The baseline was then calculated using both ground data and phase values at the GCPs (Table 5). Both the range and azimuth corrections were calculated and combined resulting in the flat earth correction (Figure 72). The flat earth correction was subtracted from the total phase resulting in the flattened image (Figures 73). The scaling factor was then applied resulting in the final DEM (Figure 74). The Snow Off DEM was then subtracted from this DEM resulting in the final snow depth image (Figure 75).

(1) Interferogram

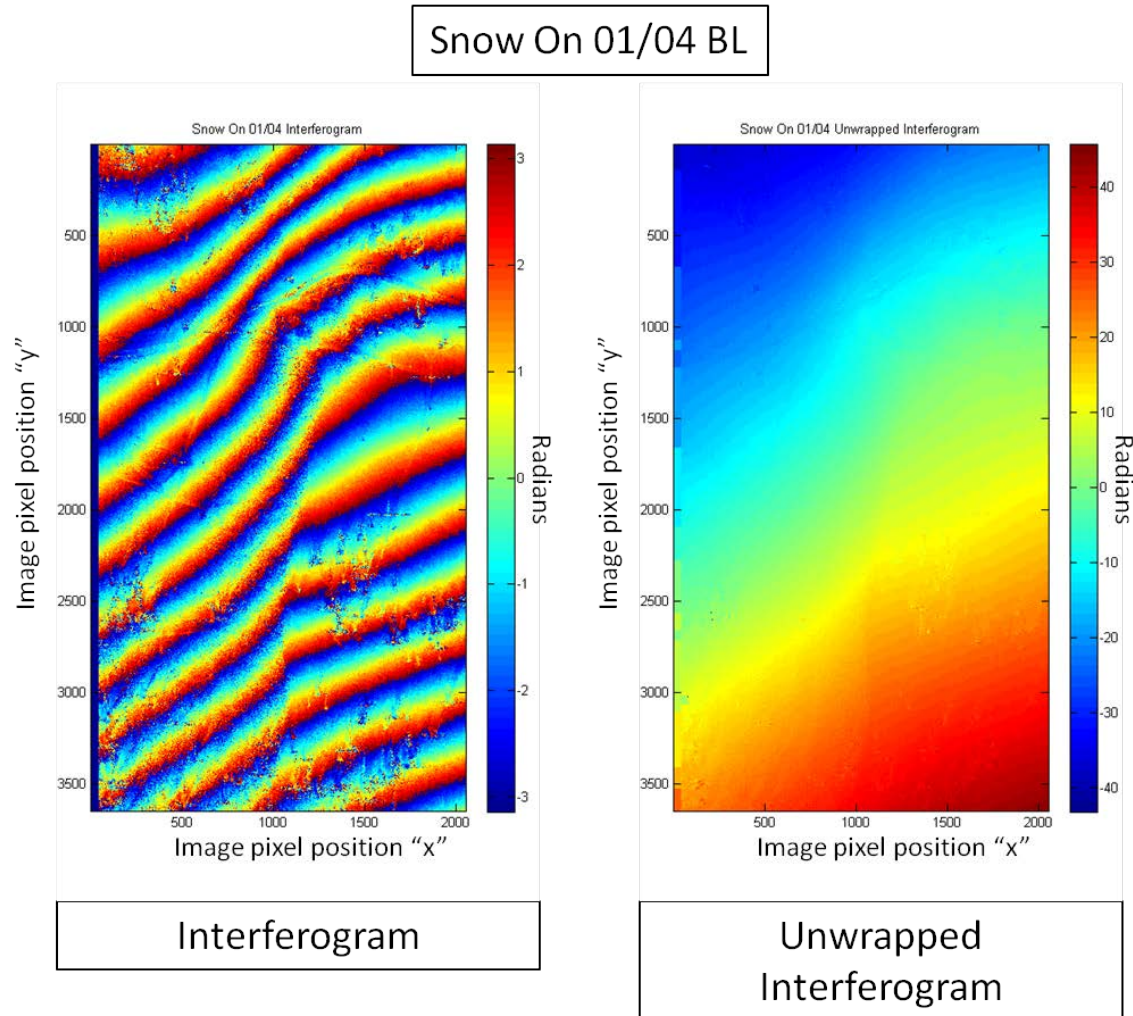


Figure 71. Snow On SAR image pair 01 and 04 interferogram and the resulting unwrapped interferogram. Mammoth Mountain study site, (37°37.7'N, 119°02.7'N).

(2) Calculated Baseline. The system of equations to calculate the baseline between the two flight paths requires inputs that include the change in the x, y, and z in meters relative to the reference tie point or corner reflector and the interferometric phase at those tie points. Those inputs along with the calculated baseline can be seen in Table 5.

Baseline input Data 01/04 (meters)						Baseline (meters)	
	SE (o)	SW (a)	NW (b)	NE (c)		Bx	5.68
phase $\Delta\phi$	5.2711	-15.1552	-22.2503	-4.3794		By	1.45
adjusted Δx	NA	-92.6249	-63.9277	28.17786		Bz	-95.12
adjusted Δy	NA	35.90349	96.57073	64.16662		Total BL	95.30047
Δz	NA	-1.813	1.949	4.158			

Table 5. The baseline calculation relies on the relative $\Delta(x, y, z)$ change of position from a reference point (SE(o)) to three other known locations (SW(a), NW(b), and NE(c)) and the interferometric phase ($\Delta\phi$) at those locations. The right side of the chart depicts the calculated baseline components in the x, y, z directions (B_x , B_y , and B_z)

(3) Flat Earth Correction

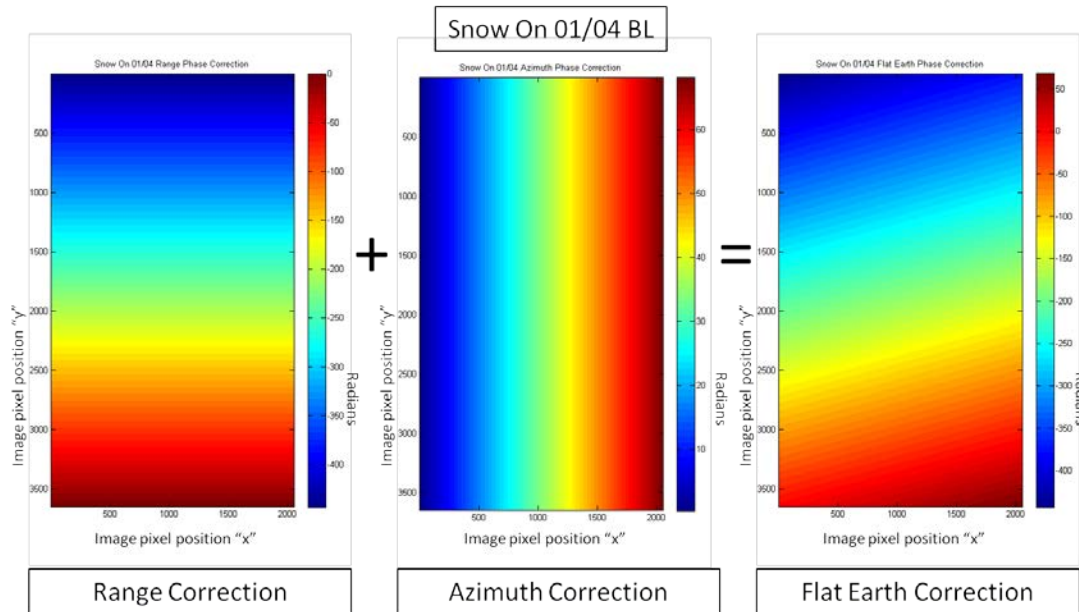


Figure 72. The summation of the range phase correction and azimuth phase correction results in the total flat earth phase correction that will be applied to the unwrapped interferogram. Mammoth Mountain study site, (37°37.7'N, 119°02.7'N).

(4) Flattened Phase Calculation

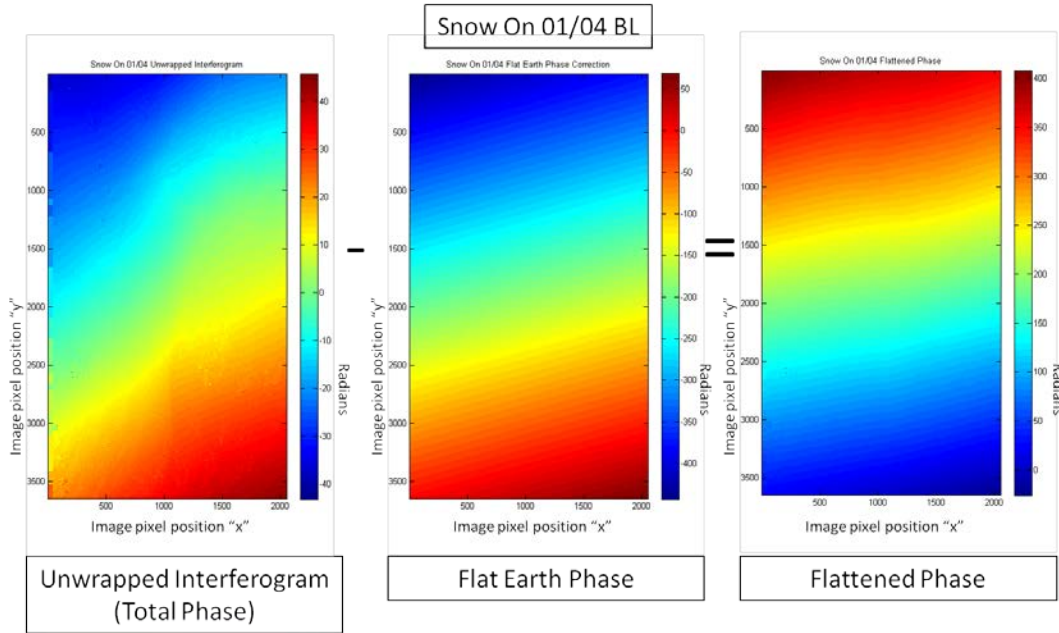


Figure 73. Subtracting the flat earth correction from the unwrapped phase results in a phase that is entirely due to the snow covered terrain and is known as the flattened phase. Mammoth Mountain study site, ($37^{\circ}37.7'N$, $119^{\circ}02.7'N$).

(5) Scaling and DEM Generation. The scaling equation was applied to generate the DEM.

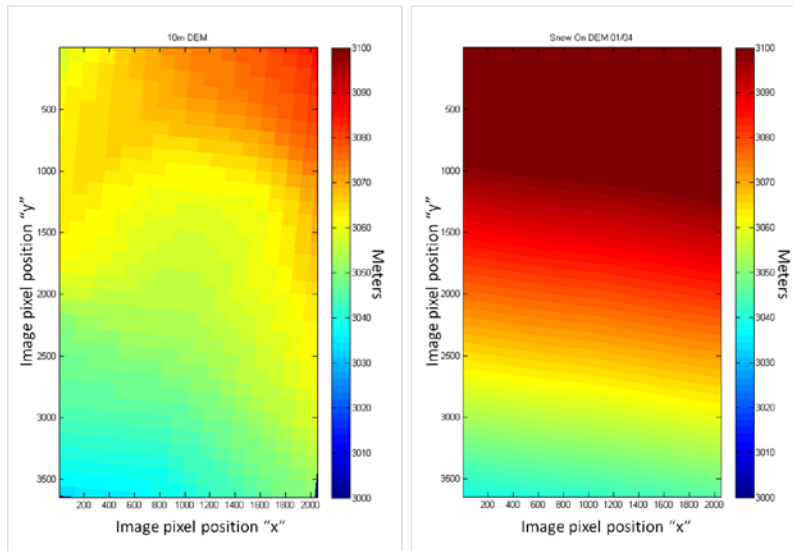


Figure 74. Once the scaling factor is applied to the flattened phase, the resulting image is a DEM of the area being sampled. The image on the right is the SAR-calculated

DEM while the image on the left is the low resolution DEM for comparison.
 Mammoth Mountain study site, (37°37.7'N, 119°02.7'N).

(6) Snow Depth

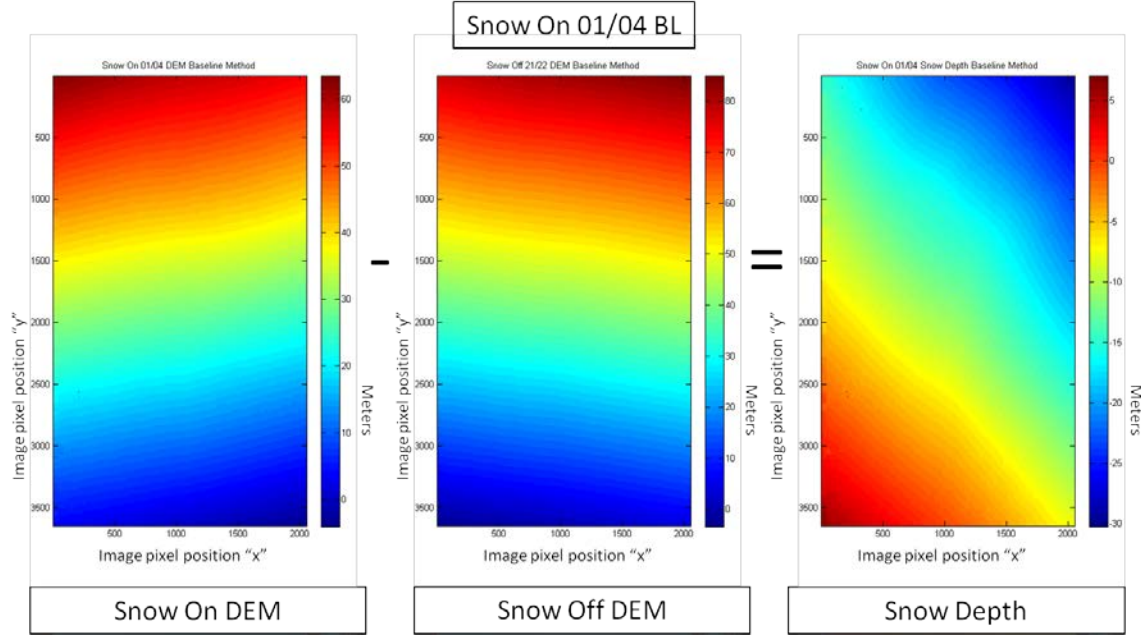


Figure 75. Subtracting the Snow Off DEM from the Snow On DEM results in an image representing or the snow depth. Mammoth Mountain study site, (37°37.7'N, 119°02.7'N).

B. BASELINE METHOD ANALYSIS

Ultimately the baseline method proved to be quite problematic. Based on comparison of the images above, following the prescribed steps did not result in representative DEMs that could be used for either the Snow Off or any of the Snow On image pairs (Figures 61, 65, 70, and 75). The problem is clearly evident when the flat earth correction is applied. The resulting image in phase space should clearly represent the terrain even if it has not been converted from phase to elevation.

There are a couple of potential areas where the problem could reside. Confidence is high that the problem does not reside in the processing chain above the unwrapping of the interferogram. Problems in those areas would have resulted in a failure to produce the fringe images or a uniform unwrapped interferogram. With the problem first being

evident in the flat earth removal, the attention was focused there. Flat earth removal uses well established interferometric theory. It is therefore unlikely that the problem is a result of any issues involving the fundamental equations being used. Therefore the problem is most likely in the calculations or the data that were used in the calculations. The code that was used was scrutinized by both the author and outside sources at Sandia National labs with no errors observed. Due to the level of complexity involved in the calculations, however, errors in the coding to perform the calculations cannot be entirely ruled out. If it is assumed that the calculations were performed correctly, the most likely source for the failure of the method would be in the data themselves.

The flat earth phase calculation is composed of three input sources. They are the incident angle, wavelength, and baseline information. The incident angle is straightforward to calculate and the wavelength is fixed. The baseline is expected to be the most likely source of error. The baseline is the primary determinate of the phase pattern in an interferometric image. An inability to get an accurate baseline prevents the generation of the flat earth phase along with the inability to derive the proper phase to height ratio. Recall that the baseline was determined using a system of equations that used the phase at four GCPs and the relative Δx , y , and z distances between those positions. Errors in the phase are not probable but are possible. It is also possible that the 5 pixel boxcar averaging that was used for the corner reflector position may have affected the phase at that specific location. This is not, however, believed to be the case. It also needs to be stated that during the Snow Off data collection, the southeast corner reflector orientation was affected by the wind. It was not pointed in the same manner as the other reflectors. There is strong potential that this could have affected the phase at that particular pixel in the unwrapped phase image. This only occurred in the Snow Off SAR collection and would not account for the inability to generate reasonable DEMs in the Snow On cases as seen when comparisons were made to an independent low resolution DEM image.

It is believed that if the baseline is in error, it is more likely that the error came from the $\Delta(x,y,z)$ inputs between the tie points. One potential source of error is the GPS coordinates. Two measurements were taken of the tie point locations at different times

using the survey grade GPS. After post processing the GPS data, the results were remarkably consistent with the locations being within a few centimeters from each other. This seems to rule out tie point GPS locations as a source of error. Another potential source of error with respect to the $\Delta(x,y,z)$ inputs may involve the coordinate rotation performed to adjust the real world $\Delta(x,y,z)$ into the SAR image orientation. The inputs to these adjustments were based on the aircraft's flight headings and pointing data of the radar. The limitations of the accuracy of those inputs are not well known and it is difficult to know how potential errors in the recorded flight data may affect the calculations used to rotate the coordinate system and thereby cause changes in the $\Delta(x,y,z)$ inputs for the baseline calculations.

To explore this potential problem, sensitivity analyses were performed to determine the impact of errors of $\Delta(x,y,z)$ inputs on both the calculation of the baseline components and the impact of baseline error on interferometric phase to height ratio. Recall that the calculation of the baseline has phase inputs from the four different GCPs along with the x, y, and z change between the reference GCP and the three other GCPs. Analysis shows that the overall sensitivity depends on the length of the baseline and can be seen in the table in Appendix A. This table was generated using the interferometric phase to height equation (Richards, 2009), and reasonable aircraft height, incident angle, and wavelength numbers for the flights performed for this research. The analysis indicates that the shorter the baseline, the greater the sensitivity of the phase to height relationship. This is important because the flight paths are designed to keep the baseline as short as possible to increase coherence. Lynx radar flight paths typically are designed to have a baselines on the order of meters (D. Bickel, 2013, personal communication). Appendix B demonstrates the sensitivity of measurement error in $\Delta(x,y,z)$ measurements between the GCPs on the baseline calculation. For demonstration purposes a baseline with components of $B_x = -6.14$, $B_y = 23.54$ and $B_z = 40.89$ were used. This baseline is not particularly short but it does demonstrate the sensitivity of small errors in $\Delta(x,y,z)$ inputs. Additionally these charts show sensitivity for only one of the GCPs. Remember each GCP's Δx , y , and z affects all three of the baseline components, B_x , B_y , and B_z differently. Δz measurements tend to be the most sensitive. Note that measurement

errors on the order of one centimeter in Δz can result in a baseline B_z error of a quarter of a meter. If one has an error of 5cm the error becomes 1.3 meters. That can have a tremendous impact on the calculated flat earth. It in effect adds an incorrect tilt or gradient to the phase field.

The true sensitivity to potential measurement error is difficult to quantify with 13 ground measurements (9 $\Delta x, y, z$'s and 4 $\Delta\phi$'s) determining 3 different components of the baseline (B_x, B_y , and B_z) differently. Potential errors ultimately determine the flat earth phase that is subtracted from total phase and phase to height ratio. Due to this complexity, a quantified sensitivity was not explored at this time. Despite this, it is clear from the examples provided that these potential errors make the task of determining the baseline at the necessary accuracy difficult.

Without the necessary accuracy and precision in the ground measurements it was impossible to calculate a baseline that allowed determination of a representative flat earth image to be subtracted from the unwrapped interferogram. Thus it was not possible to generate a good DEM using the Baseline method.

THIS PAGE INTENTIONALLY LEFT BLANK

V. BEST FIT PLANE REMOVAL METHOD RESULTS

A. PROCESSED IMAGERY

The BFPR processed results will be broken down into three parts. The first two parts will show the low resolution DEM processing and the Snow Off DEM generation respectively. Due to available data, only one Snow Off DEM could be generated. Both the low resolution DEM processing and Snow Off DEM were combined with the Snow On DEM processed images to calculate the snow depth. The Snow On DEM generation will be the third section discussed in the processed imagery portion of the results.

1. Low Resolution DEM Processing

The low resolution DEM processing was straightforward. A 10m resolution DEM was obtained and geocorrected to match the observation area being processed using the methods previously described. Figure 76 is a 3D perspective representation of this DEM. Figure 77 is a 3D representation of the Best Fit Plane to the DEM. This BFP was used in the processing of all of the higher resolution DEMs for both the Snow On and Snow Off cases.

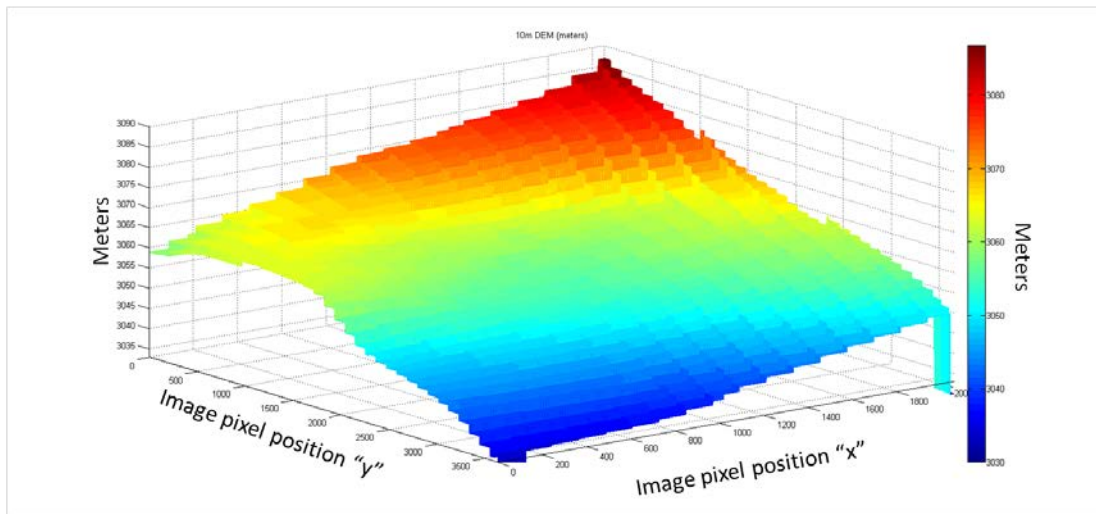


Figure 76. A relatively low resolution 10m DEM of the survey area was obtained from the USDA NAIP and then geocorrected to match the SAR image area. Centered on Mammoth Mountain study site, ($37^{\circ}37.7'N$, $119^{\circ}02.7'W$).

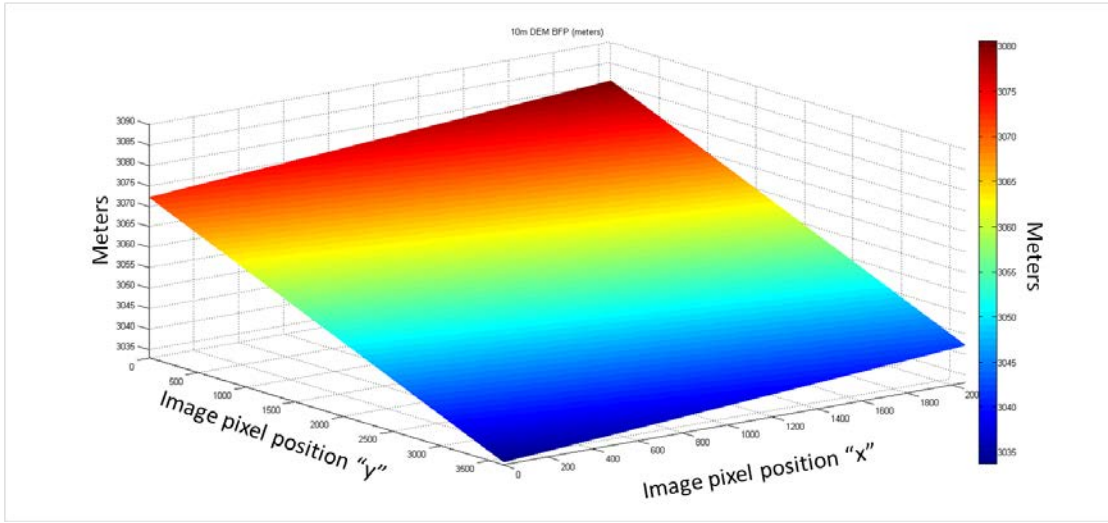


Figure 77. Best fit Plane of low resolution 10m DEM of survey area. This represents the generalized terrain slope for the Elysian Fields site. Centered on Mammoth Mountain study site, ($37^{\circ}37.7'N$, $119^{\circ}02.7'W$).

2. Snow Off DEM Generation

(1) Best Fit Plane Generation

The BFP was generated for the SAR image pair 21/22 by fitting a plane to the total unwrapped phase image and then removing it via subtraction as previously described (Figure 78). Linear regression was then used to convert the BFPR phase to the difference between the mean slope elevation and corner reflector location elevations (Table 6, Figure 79). Finally, the 10m DEM BFP or mean elevation slope was added back in to get the DEM (Figure 80).

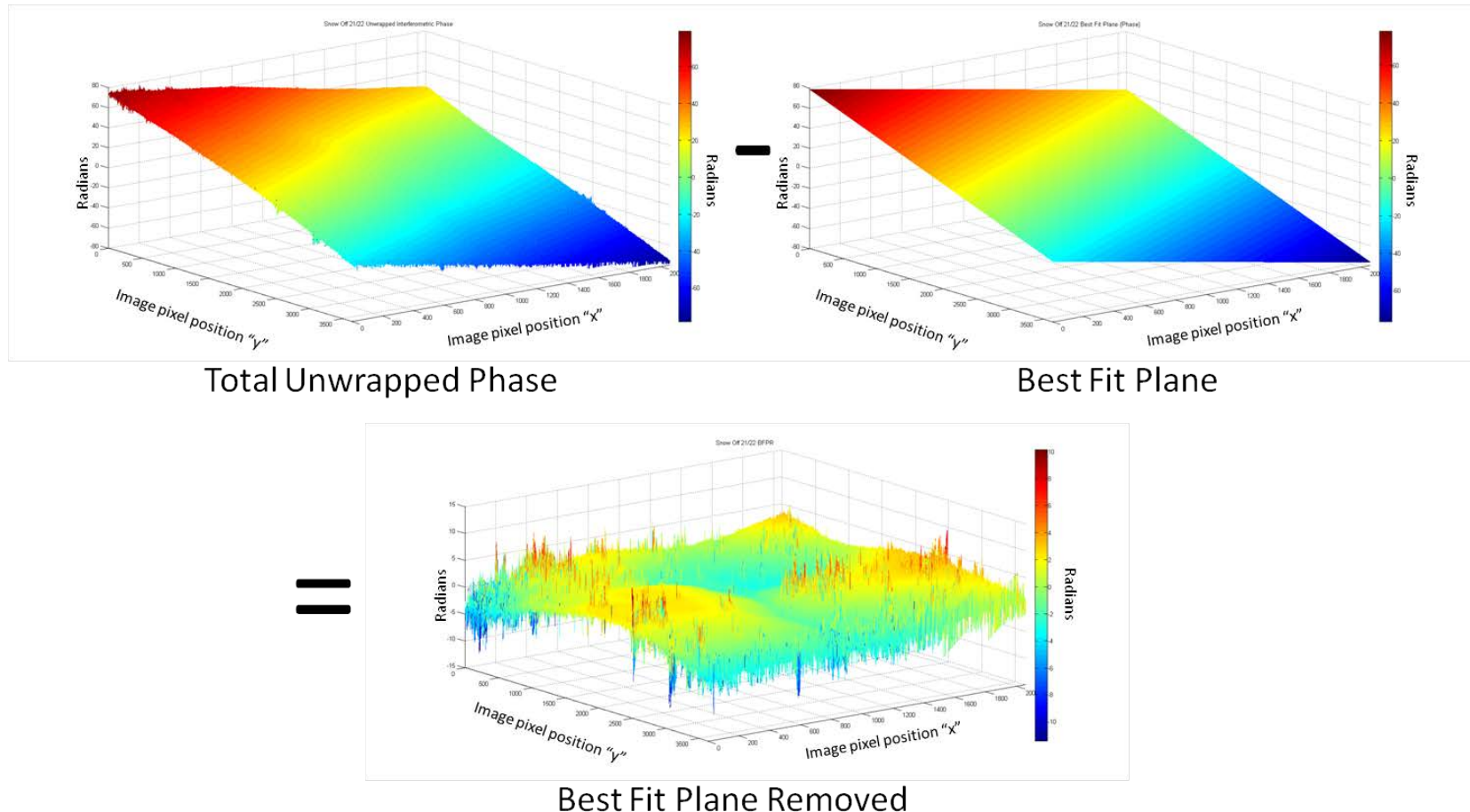


Figure 78. A Best Fit Plane (BFP) was generated from the interferometric SAR image pair (total unwrapped phase) 21 and 22. After generating the BFP, it was subtracted from the total phase resulting in a Best Fit Plane Removed (BFPR) image. Mammoth Mountain study site, ($37^{\circ}37.7'N$, $119^{\circ}02.7'N$).

(2) Phase Statistics

BFPR Statistics Snow Off 21/22						
	x	y	BFP (10m DEM) (meters)	Real (GPS) (meters)	Phase	Difference (meters)
SW (a)	432	1696	3055.95	3064.87	2.653742	8.92
NW (b)	678	985	3064.44	3068.64	0.662982	4.2
NE (c)	1790	1227	3066.45	3070.85	0.641027	4.4
Problem with SE CR during collection						

Table 6. The phase from the BFPR image was compared with the mean slope perturbation to determine the phase to elevation relationship for Snow Off SAR image pairs 21 and 22. In this particular case, only three corner reflectors were used. The fourth corner reflector phase was determined to be unreliable due to placement issues during the SAR collection

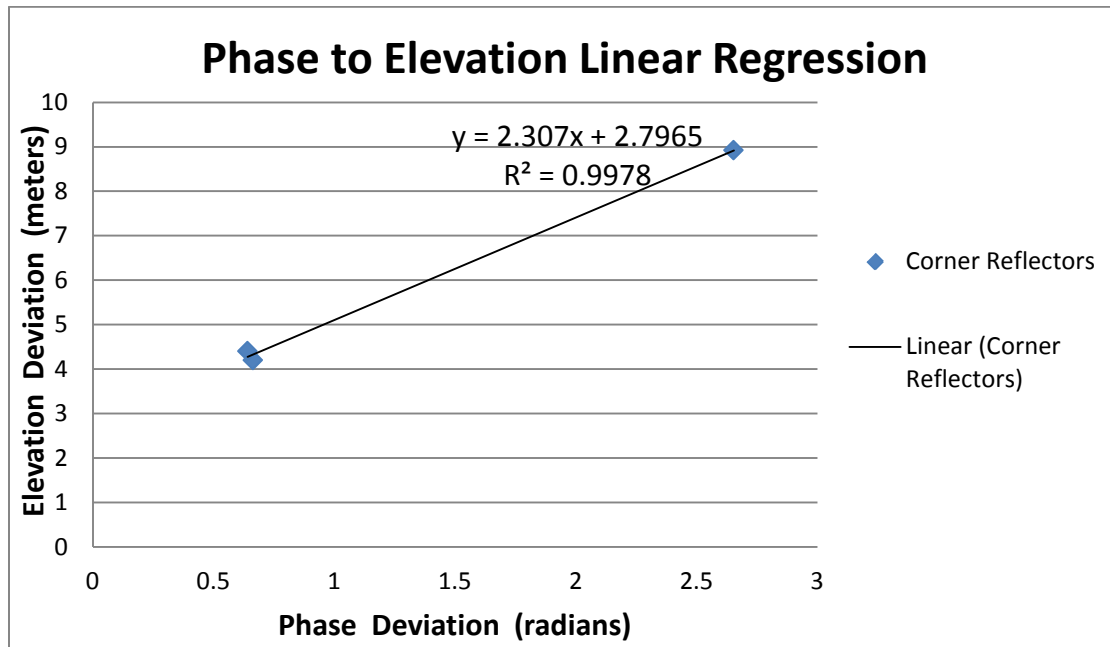


Figure 79. Linear regression of the BFPR phase and mean slope perturbation results in an equation that is applied to change BFPR image from phase to elevation for SAR image pair 21 and 22.

(3) DEM Generation

At this point the linear regression formula was applied to the BFPR phase image, resulting in a BFPRL image. The average slope was then added back in to generate the DEM.

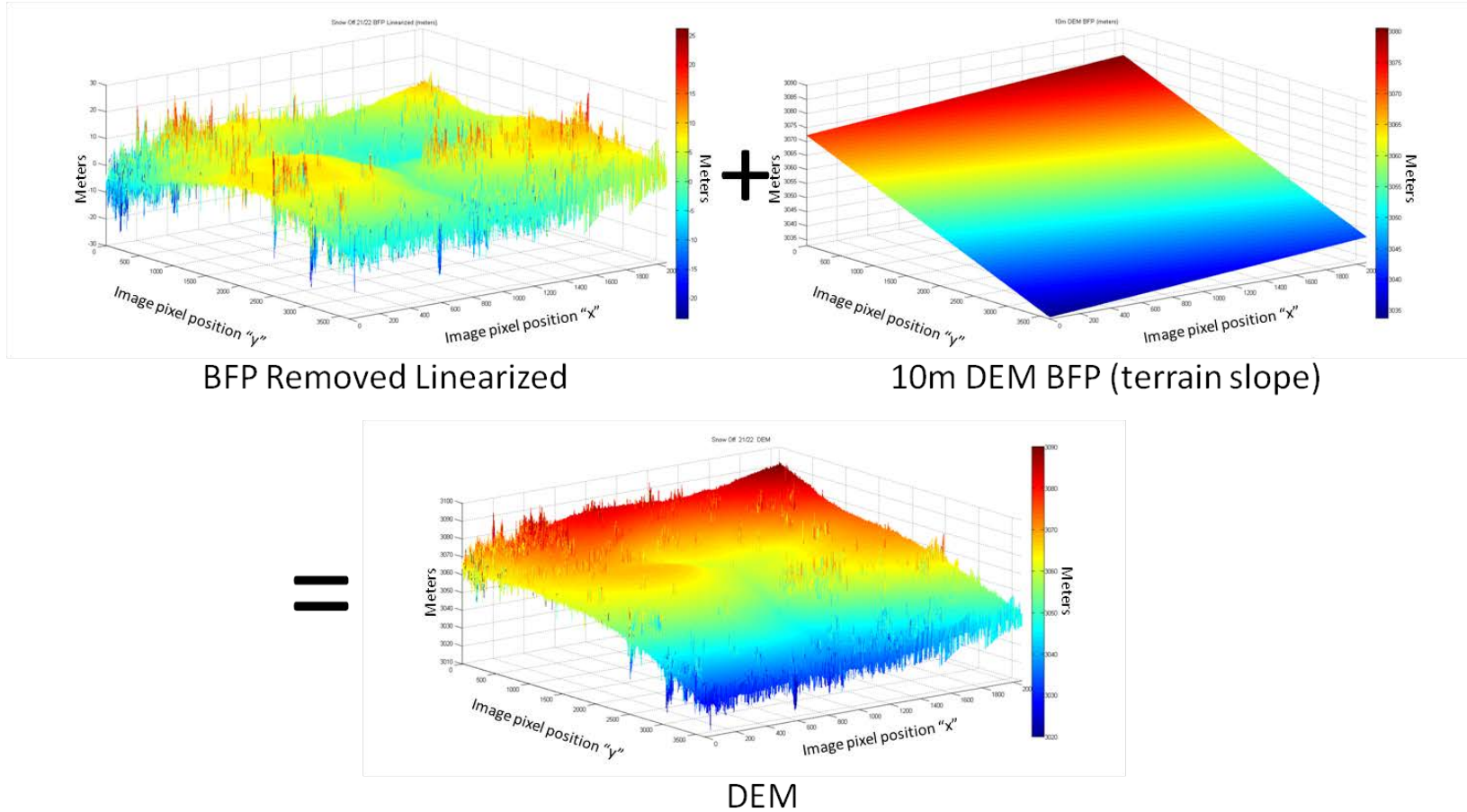


Figure 80. Addition of BFPRL to the 10m DEM BFP results in the Snow Off SAR image pair 21 and 22 DEM. Mammoth Mountain study site, ($37^{\circ}37.7'N$, $119^{\circ}02.7'N$).

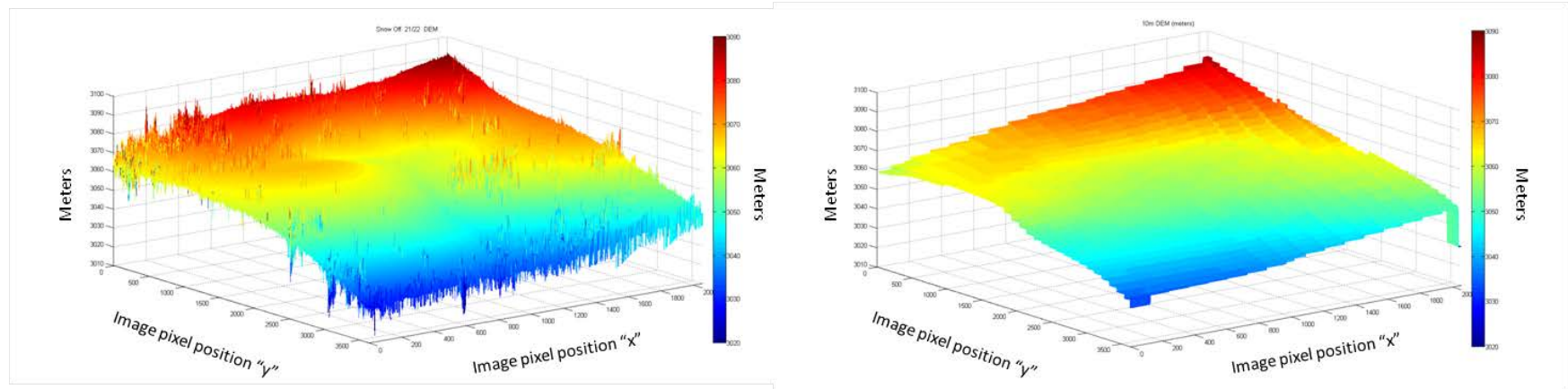


Figure 81. The BFPR derived DEM (left) generally resembles the low resolution DEM (right), however, it exhibits higher detail and fine terrain variability.

The calculated DEM compared well to the 10m DEM as seen in Figure 81. No further comparisons of the calculated DEM to the low resolution will be made unless there is a specific exception.

3. Snow On 01/02 DEM Generation and Snow Depth Calculation

(1) Best Fit Plane Generation

The BFP was generated for the SAR image pair 01/02 by fitting a plane to the total unwrapped phase image and then removing it via subtraction as previously described (Figure 82). Linear regression was then used to convert the BFPR phase to the difference between the mean slope elevation and corner reflector location elevations (Table 7, Figure 83). Next, the 10m DEM BFP or mean elevation slope was added back in to get the Snow On DEM (Figure 84). The last step was to subtract the Snow Off DEM from the Snow On DEM to get the snow depth (Figure 85).

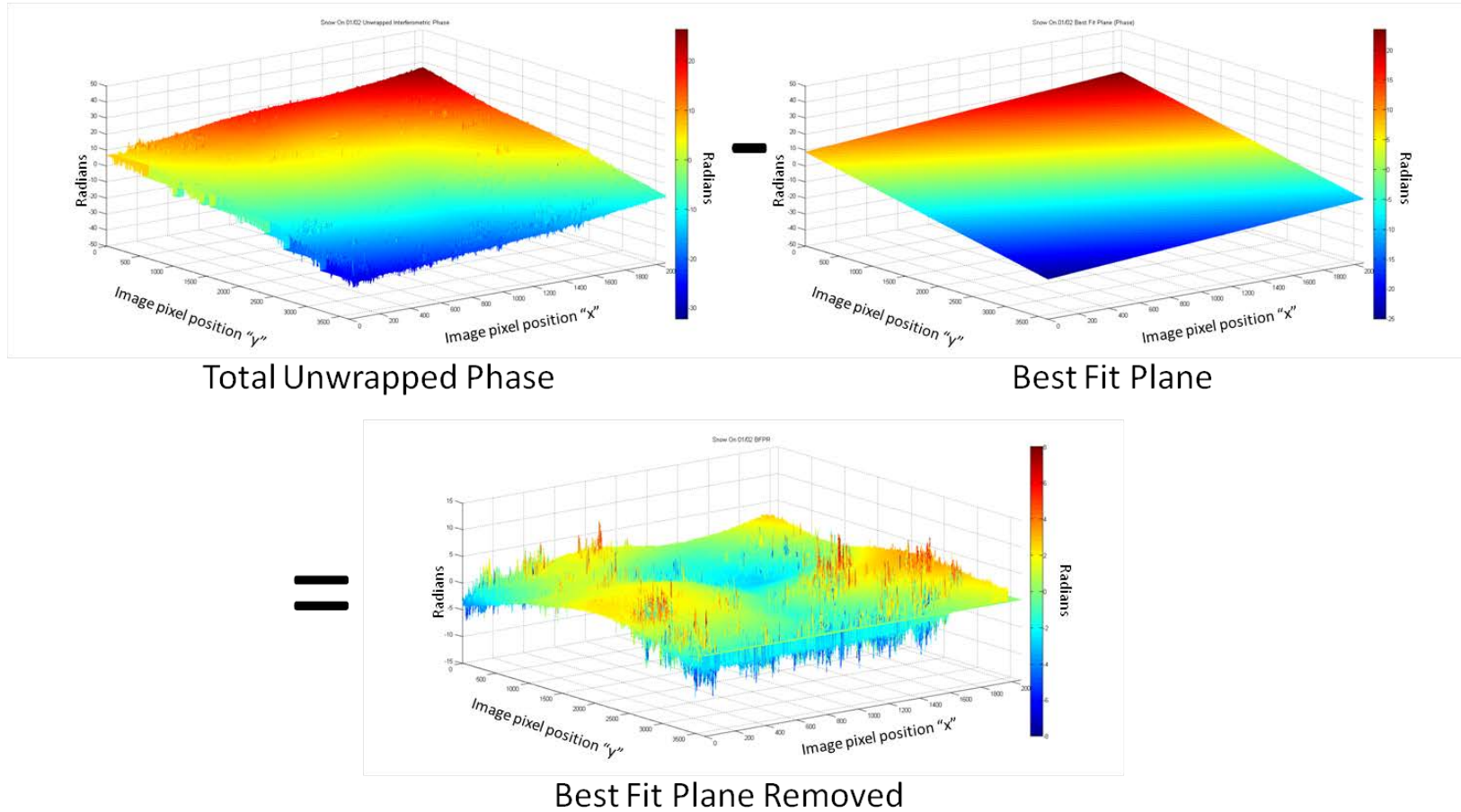


Figure 82. A Best Fit Plane (BFP) was generated from the interferometric SAR image pair (total unwrapped phase) 01 and 02 . After generating the BFP, it was subtracted from the total phase resulting in a Best Fit Plane Removed (BFPR) image. Mammoth Mountain study site, ($37^{\circ}37.7'N$, $119^{\circ}02.7'N$).

(2) Phase Statistics

BFPR Statistics Snow On 01/02						
	x	y	BFP (10m DEM) (meters)	Real (GPS) (meters)	Phase	Difference (meters)
SW (a)	432	1696	3055.95	3064.87	1.709228	8.92
NW (b)	678	985	3064.44	3068.64	0.104561	4.2
NE (c)	1790	1227	3066.45	3070.85	-0.49067	4.4
SE	1554	1980	3057.55	3066.69	1.704008	9.14

Table 7. The phase from the BFPR image was compared with the mean slope perturbation to determine phase to elevation relationship for Snow Off SAR image pairs 01 and 02.

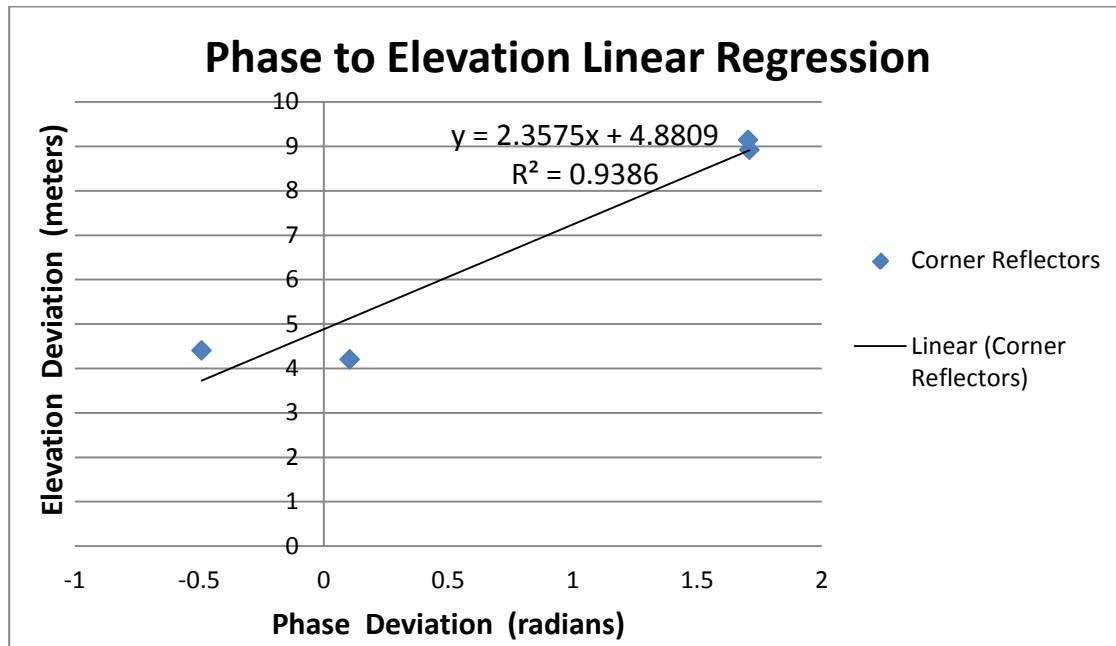


Figure 83. Linear regression of the BFPR phase and mean slope perturbation results in an equation that is applied to change BFPR image from phase to elevation for SAR image pair 01 and 02.

(3) DEM Generation

At this point the linear regression formula was applied to the BFPR phase image, resulting in a BFPRL image. The average slope was then added back in to generate the DEM.

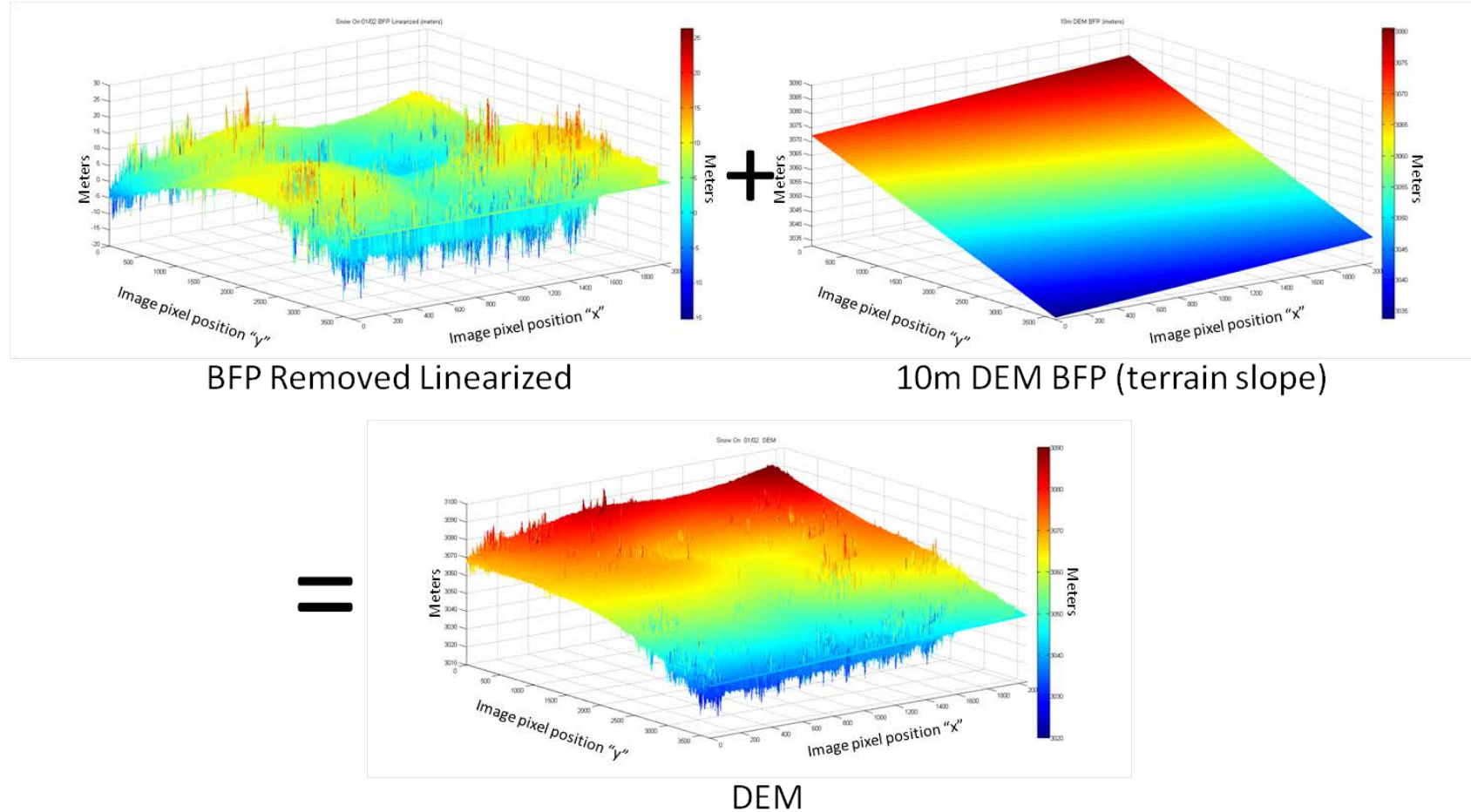


Figure 84. Addition of BFPRL to the 10m DEM BFP results in the Snow On SAR image pair 01 and 02 DEM. The snow covered DEM assumes minimal SAR penetration. Mammoth Mountain study site, (37°37.7'N, 119°02.7'N).

(4) Snow Depth Calculation

The last step in the process was to subtract the Snow Off DEM from the Snow On DEM to get the snow depth.

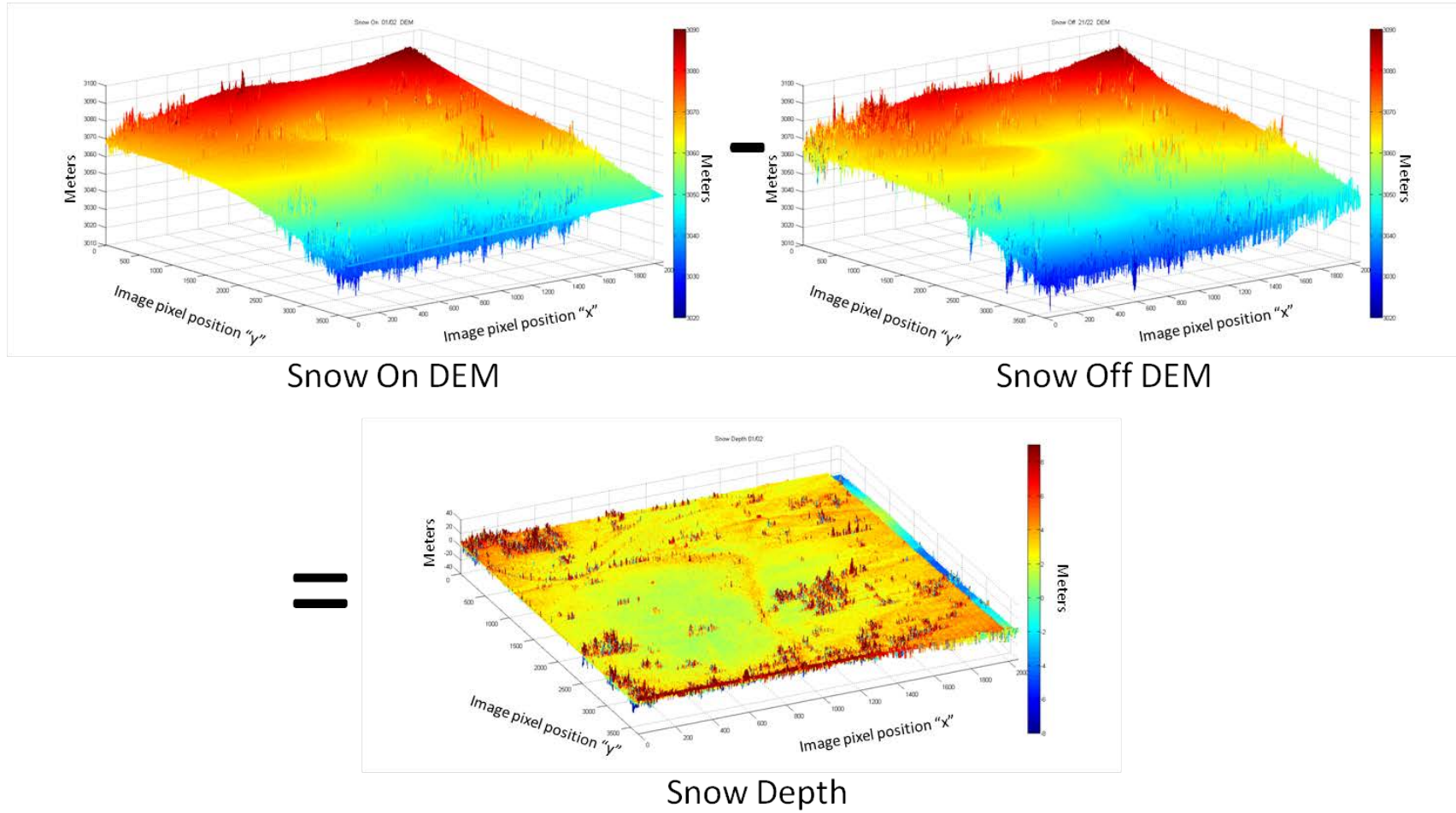


Figure 85. Subtracting the Snow Off DEM from the Snow On DEM generated from the SAR image pair 01 and 02 results in a snow depth image. Mammoth Mountain study site, (37°37.7'N, 119°02.7'N).

4. Snow On 01/03 DEM Generation and Snow Depth Calculation

(1) Best Fit Plane Generation

The BFP was generated for the SAR image pair 01/03 by fitting a plane to the total unwrapped phase image and then removing it via subtraction as previously described (Figure 86). Linear regression was then used to convert the BFPR phase to the difference between the mean slope elevation and corner reflector location elevations (Table 8, Figure 87). Next, the 10m DEM BFP or mean elevation slope was added back in to get the Snow On DEM (Figure 88). The last step was to subtract the Snow Off DEM from the Snow On DEM to get the snow depth (Figure 89).

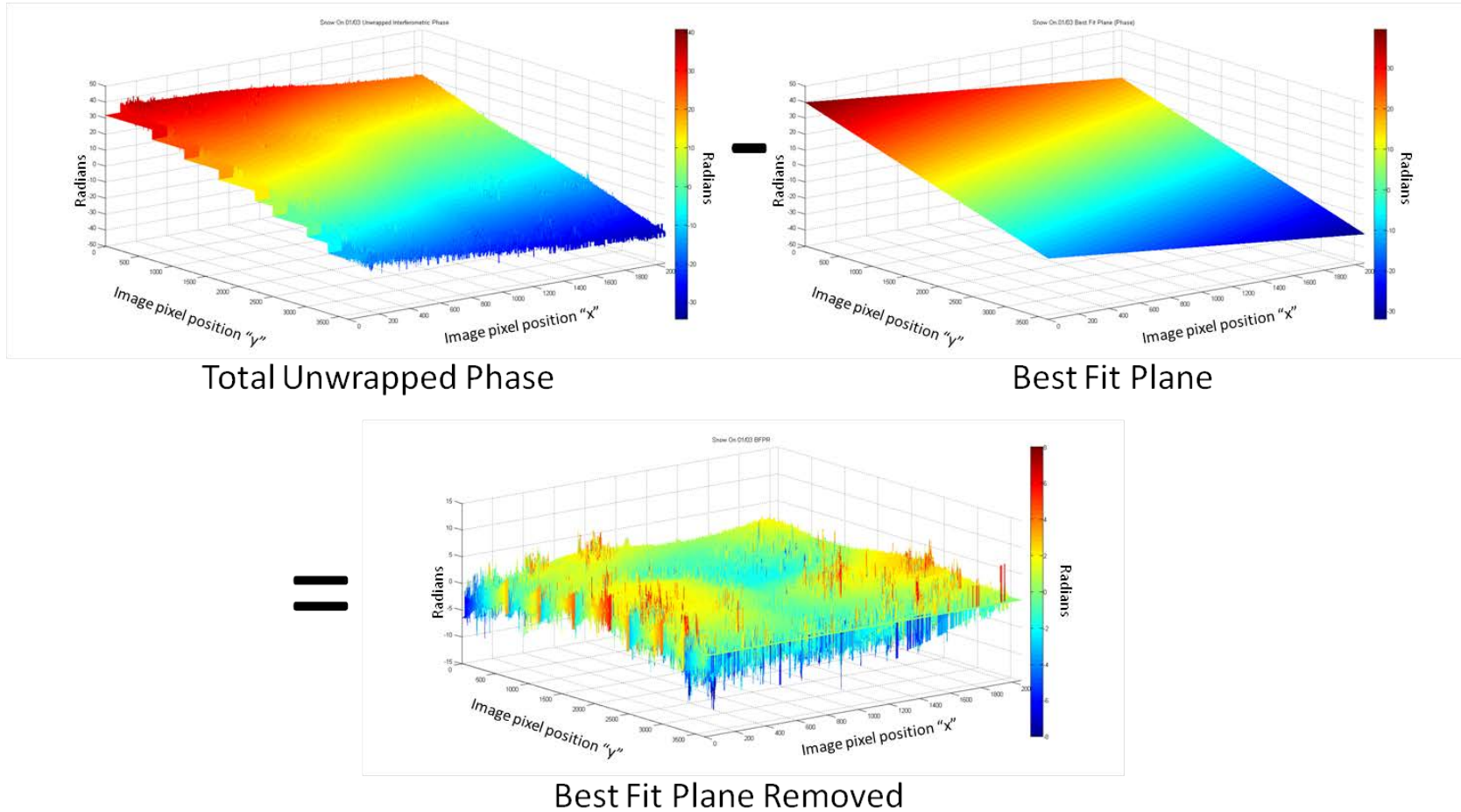


Figure 86. A Best Fit Plane (BFP) was generated from the interferometric SAR image pair (total unwrapped phase) 11 and 03 . After generating the BFP, it was subtracted from the total phase resulting in a Best Fit Plane Removed (BFPR) image. Mammoth Mountain study site, (37°37.7'N, 119°02.7'N).

(2) Phase Statistics

BFPR Statistics Snow On 01/03						
	x	y	BFP (10m DEM) (meters)	Real (GPS) (meters)	Phase	Difference (meters)
SW (a)	432	1696	3055.95	3064.87	1.594771	8.92
NW (b)	678	985	3064.44	3068.64	0.035803	4.2
NE (c)	1790	1227	3066.45	3070.85	-0.62206	4.4
SE	1554	1980	3057.55	3066.69	1.589361	9.14

Table 8. The phase from the BFPR image was compared with the mean slope perturbation to determine phase to elevation relationship for Snow Off SAR image pairs 01 and 03.

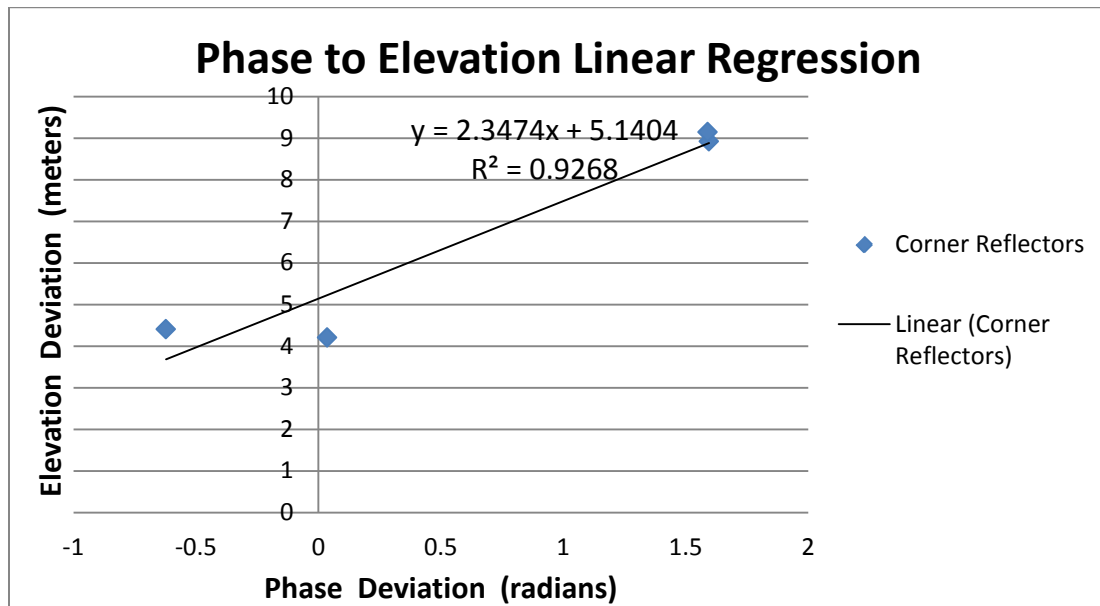


Figure 87. Linear regression of the BFPR phase and mean slope perturbation results in an equation that is applied to change BFPR image from phase to elevation for SAR image pair 01 and 03.

(3) DEM Generation

At this point the linear regression formula was applied to the BFPR phase image, resulting in a BFPRL image. The average slope was then added back in to generate the DEM.

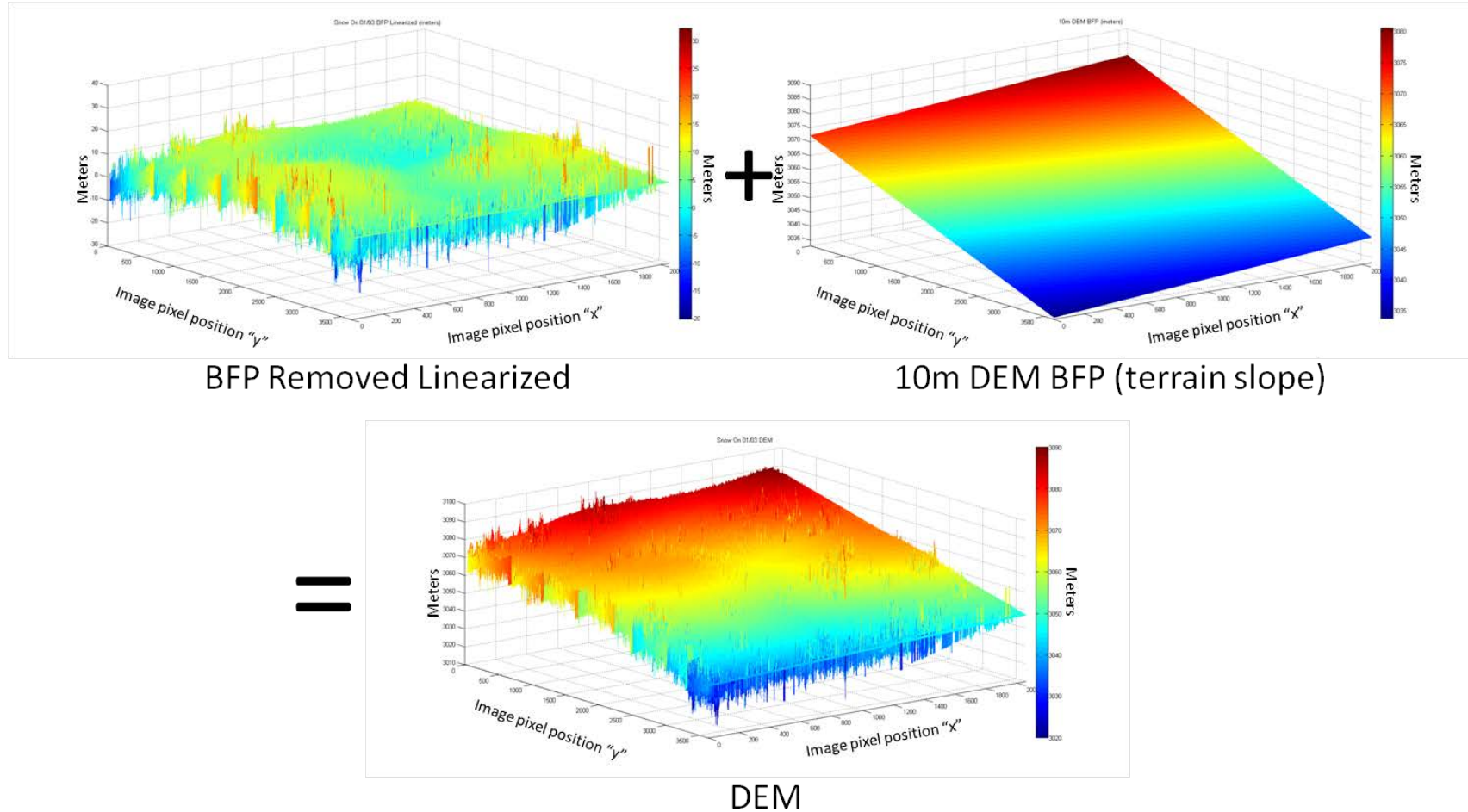


Figure 88. Addition of BFPRL to the 10m DEM BFP results in the Snow On SAR image pair 01 and 03 DEM. The snow covered DEM assumes minimal SAR penetration. Mammoth Mountain study site, (37°37.7'N, 119°02.7'N).

(4) Snow Depth Calculation

The last step in the process was to subtract the Snow Off DEM from the Snow On DEM to get the snow depth.

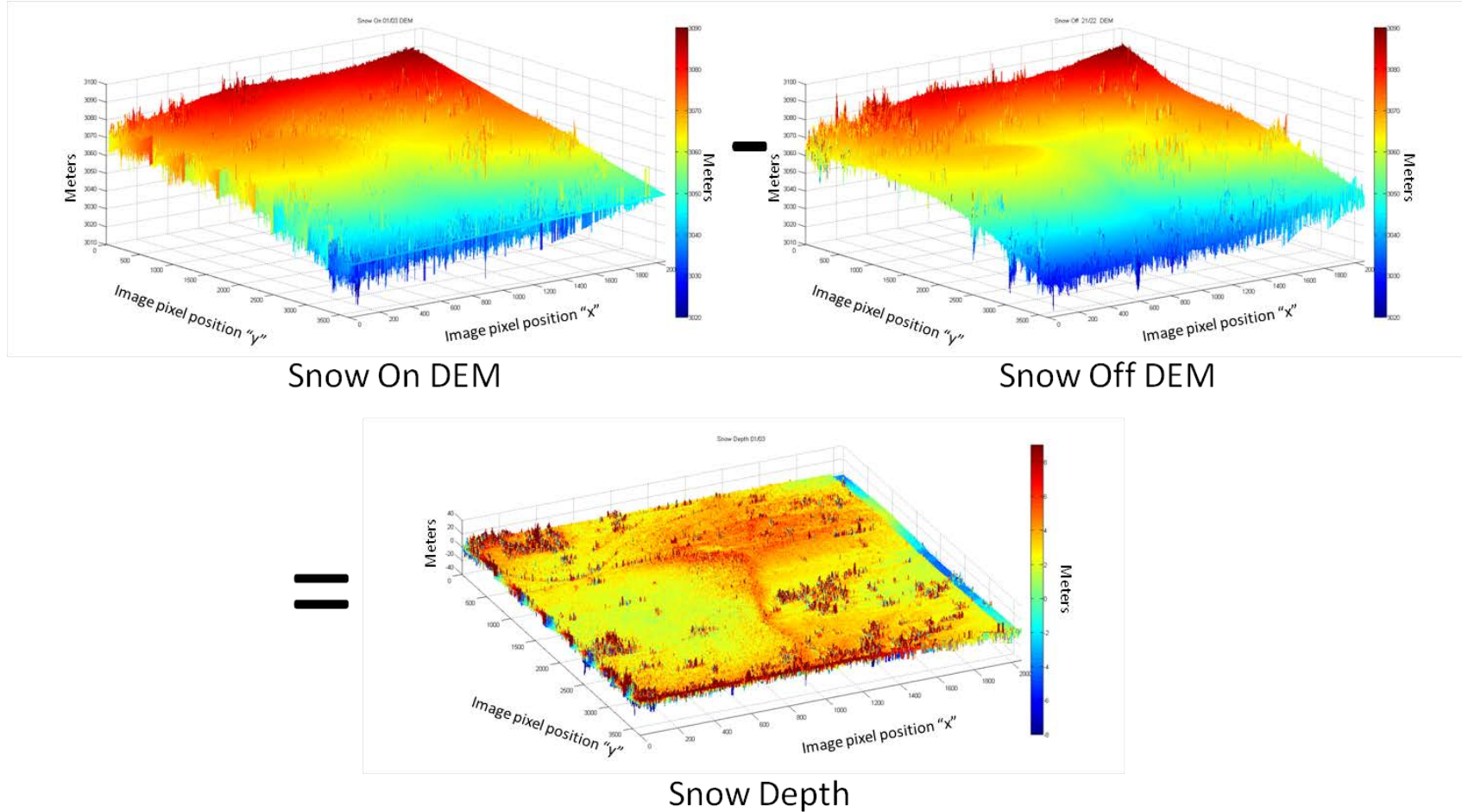


Figure 89. Subtracting the Snow Off DEM from the Snow On DEM generated from the SAR image pair 01 and 03 results in a snow depth image. Mammoth Mountain study site, (37°37.7'N, 119°02.7'N).

5. Snow On 01/04 DEM Generation and Snow Depth Calculation

(1) Best Fit Plan Generation

The BFP was generated for the SAR image pair 01/04 by fitting a plane to the total unwrapped phase image and then removing it via subtraction as previously described (Figure 90). Linear regression was then used to convert the BFPR phase to the difference between the mean slope elevation and corner reflector location elevations (Table 9, Figure 91). Next, the 10m DEM BFP or mean elevation slope was added back in to get the Snow On DEM (Figure 92). The last step was to subtract the Snow Off DEM from the Snow On DEM to get the snow depth (Figure 93).

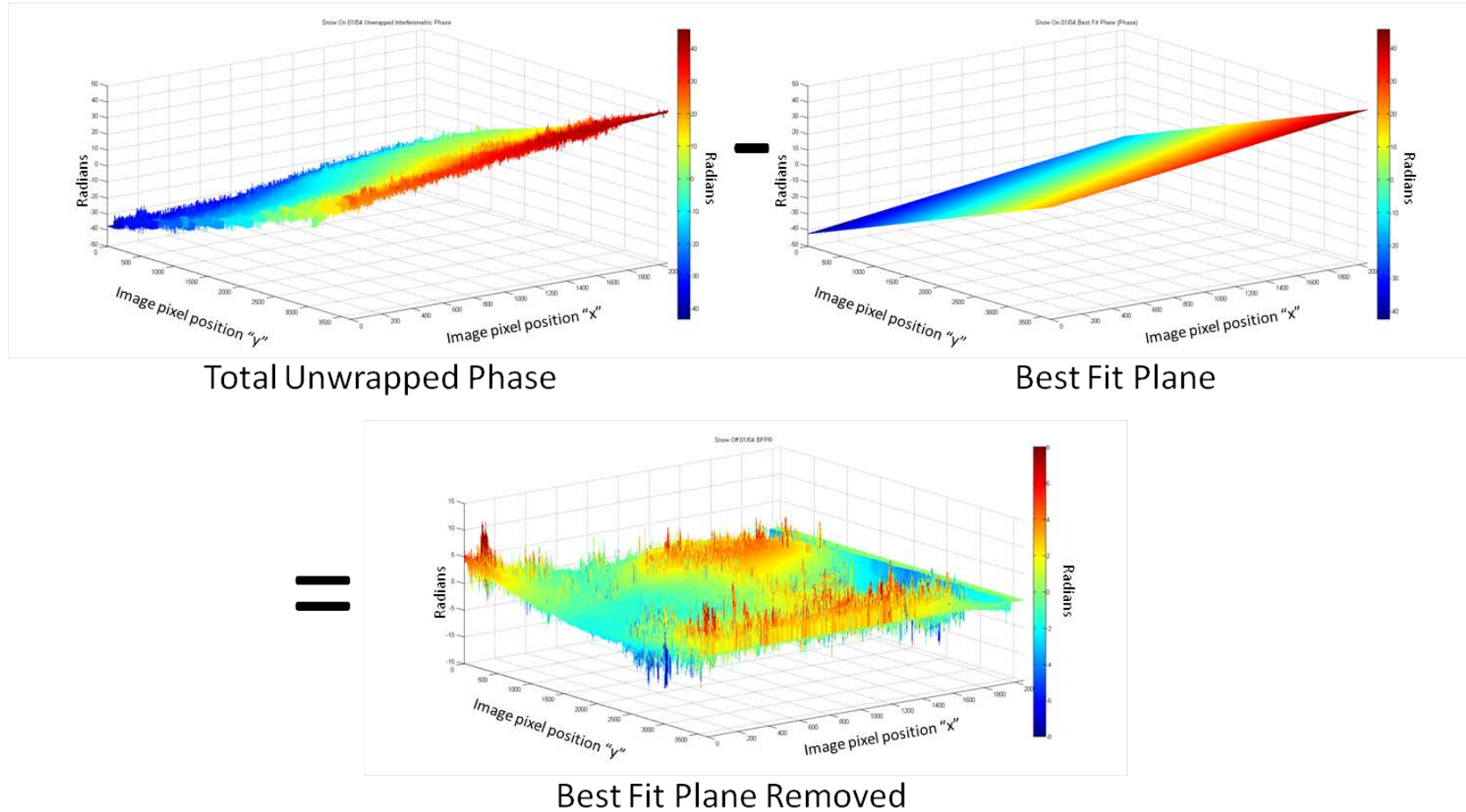


Figure 90. A Best Fit Plane (BFP) was generated from the interferometric SAR image pair (total unwrapped phase) 01 and 04. After generating the BFP, it was subtracted from the total phase resulting in a Best Fit Plane Removed (BFPR) image. Mammoth Mountain study site, (37°37.7'N, 119°02.7'N).

(2) Phase Statistics

BFPR Statistics Snow On 01/04						
	x	y	BFP (10m DEM) (meters)	Real (GPS) (meters)	Phase	Difference (meters)
SW (a)	432	1696	3055.95	3064.87	-2.56739	8.92
NW (b)	678	985	3064.44	3068.64	-0.5732	4.2
NE (c)	1790	1227	3066.45	3070.85	-0.78525	4.4
SE	1554	1980	3057.55	3066.69	-1.01204	9.14

Table 9. The phase from the BFPR image was compared with the mean slope perturbation to determine phase to elevation relationship for Snow Off SAR image pairs 01 and 04.

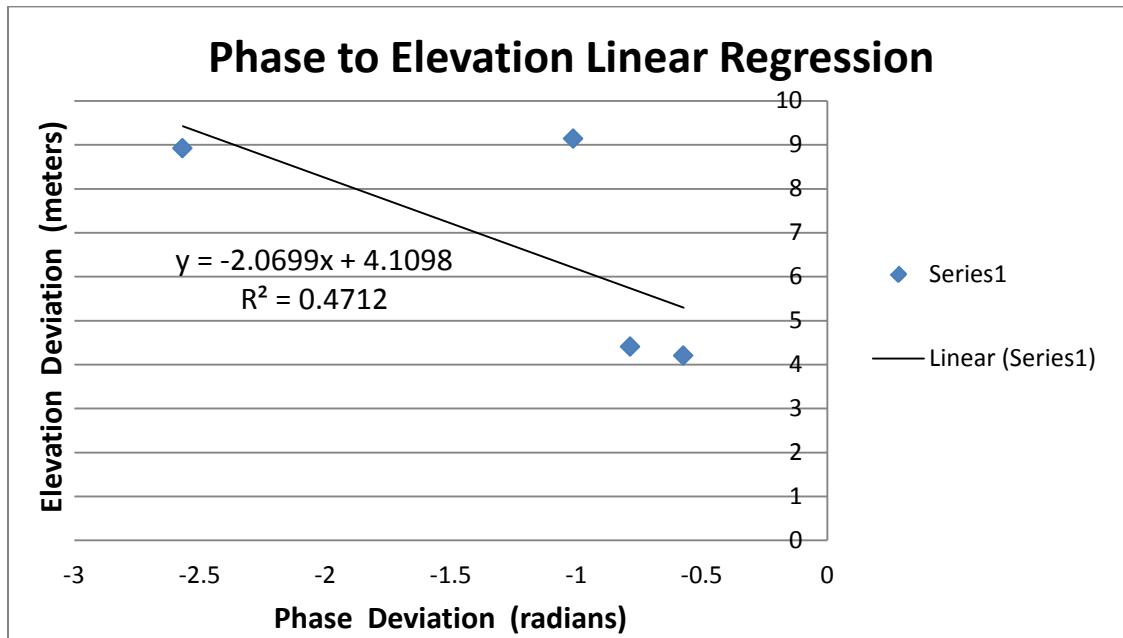


Figure 91. Linear regression of the BFPR phase and mean slope perturbation results in an equation that is applied to change BFPR image from phase to elevation for SAR image pair 01 and 04.

(3) DEM Generation

At this point the linear regression formula was applied to the BFPR phase image, resulting in a BFPRL image. The average slope was then added back in to generate the DEM.

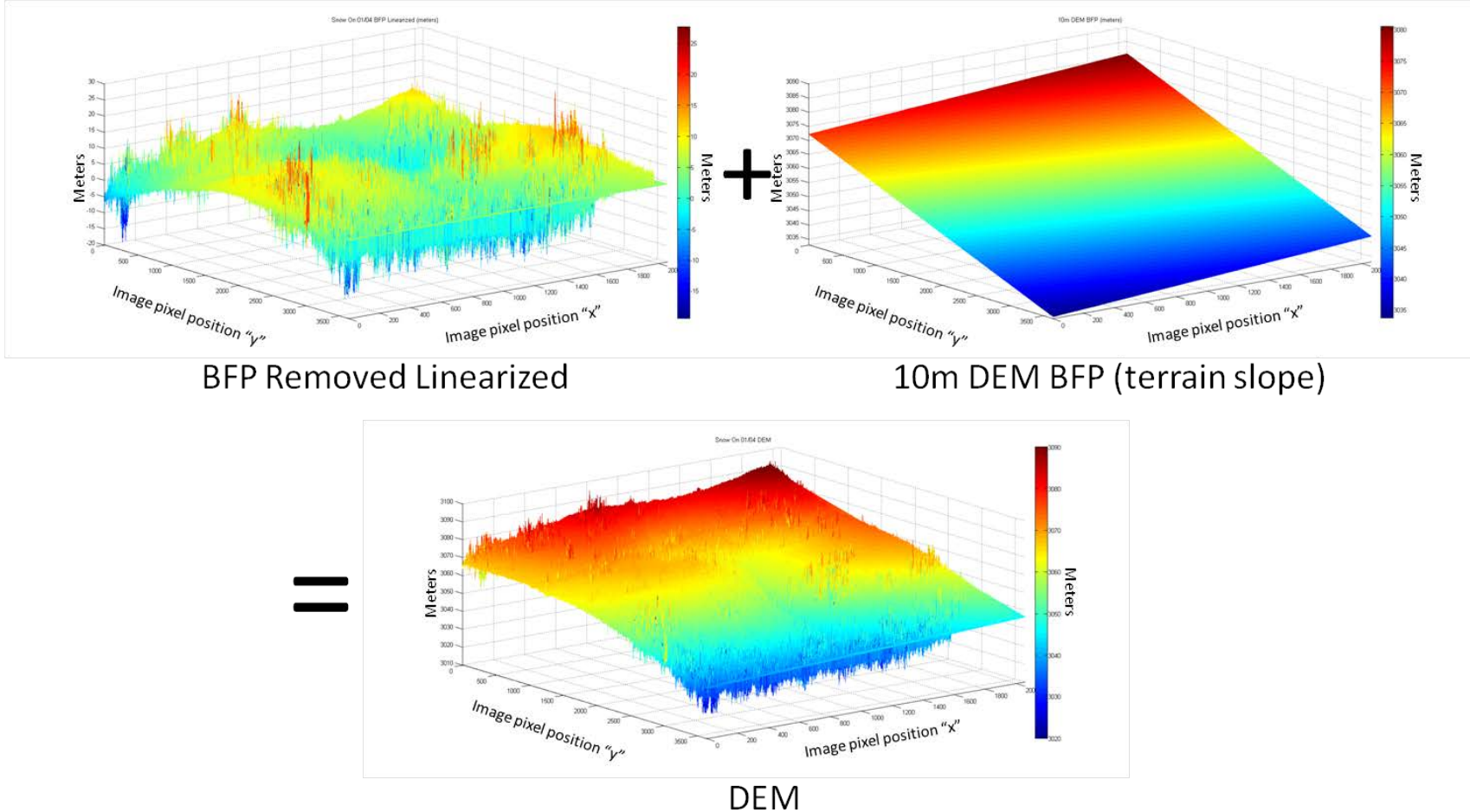


Figure 92. Addition of BFPRL to the 10m DEM BFP results in the Snow On SAR image pair 01 and 04 DEM. The snow covered DEM assumes minimal SAR penetration. Mammoth Mountain study site, (37°37.7'N, 119°02.7'N).

(4) Snow Depth Calculation

The last step in the process was to subtract the Snow Off DEM from the Snow On DEM to get the snow depth.

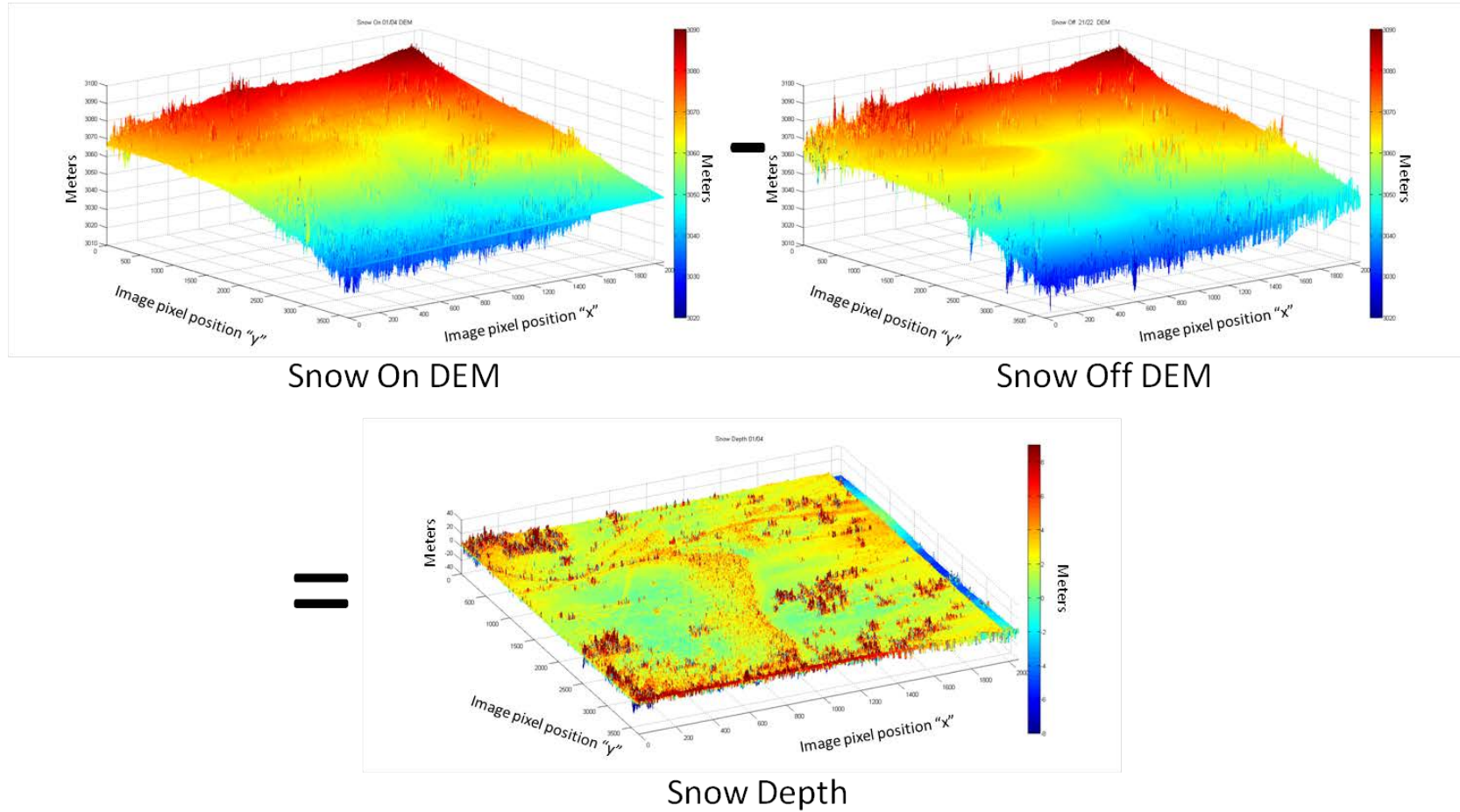


Figure 93. Subtracting the Snow Off DEM from the Snow On DEM generated from the SAR image pair 01 and 04 results in a snow depth image. Mammoth Mountain study site, (37°37.7'N, 119°02.7'N).

6. Snow On 02/03 DEM Generation and Snow Depth Calculation

(1) Best Fit Plane Generation

The BFP was generated for the SAR image pair 02/03 by fitting a plane to the total unwrapped phase image and then removing it via subtraction as previously described (Figure 94). Linear regression was then used to convert the BFPR phase to the difference between the mean slope elevation and corner reflector location elevations (Table 10, Figure 95). Next, the 10m DEM BFP or mean elevation slope was added back in to get the Snow On DEM (Figure 96). The last step was to subtract the Snow Off DEM from the Snow On DEM to get the snow depth (Figure 98).

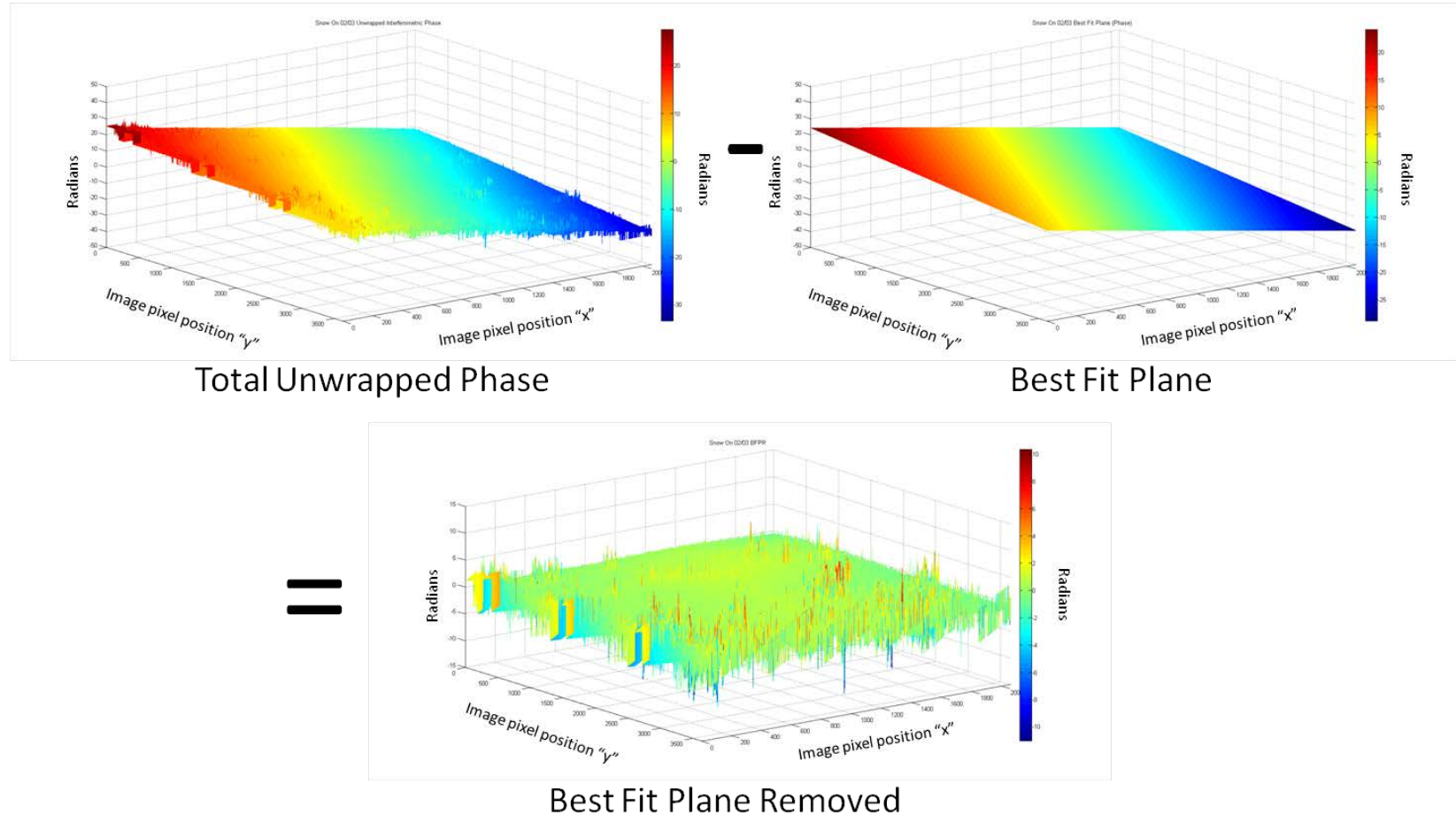


Figure 94. A Best Fit Plane (BFP) was generated from the interferometric SAR image pair (total unwrapped phase) 02 and 03. After generating the BFP, it was subtracted from the total phase resulting in a Best Fit Plane Removed (BFPR) image. Mammoth Mountain study site, ($37^{\circ}37.7'N$, $119^{\circ}02.7'W$).

(2) Phase Statistics

BFPR Statistics Snow On 02/03						
	x	y	BFP (10m DEM) (meters)	Real (GPS) (meters)	Phase	Difference (meters)
SW (a)	432	1696	3055.95	3064.87	0.15168	8.92
NW (b)	678	985	3064.44	3068.64	0.04424	4.2
NE (c)	1790	1227	3066.45	3070.85	0.09059	4.4
SE	1554	1980	3057.55	3066.69	0.00938	9.14

Table 10. The phase from the BFPR image was compared with the mean slope perturbation to determine phase to elevation relationship for Snow Off SAR image pairs 02 and 03.

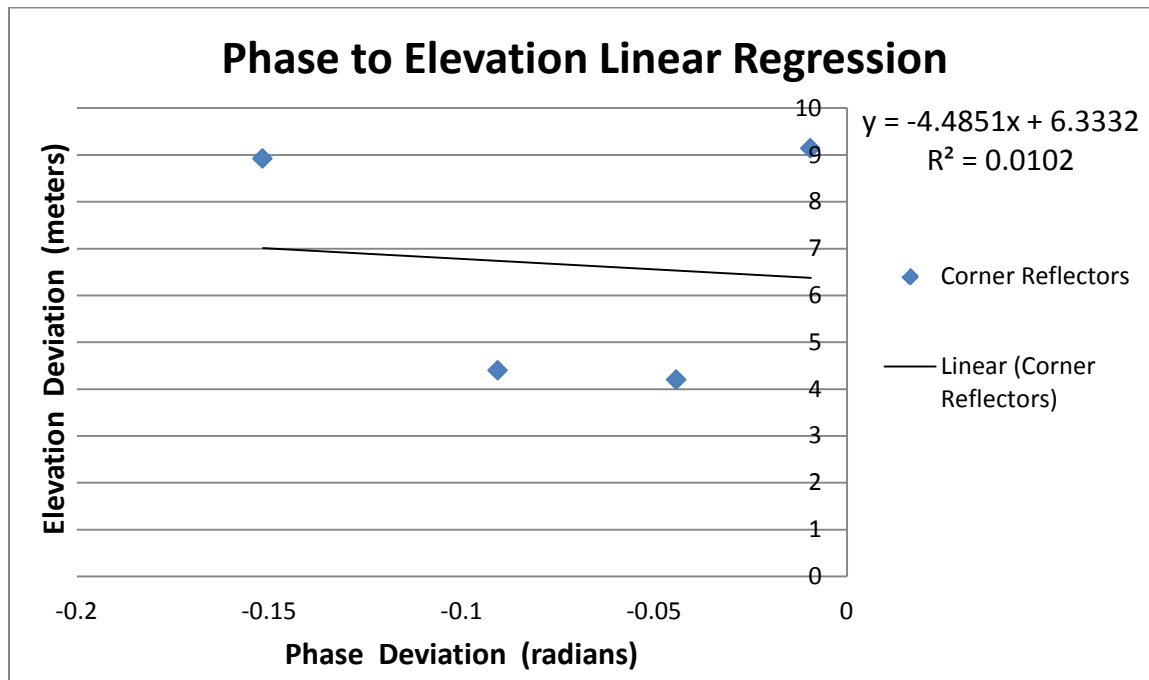


Figure 95. Linear regression of the BFPR phase and mean slope perturbation results in an equation that is applied to change BFPR image from phase to elevation for SAR image pair 02 and 03. This SAR pair has a particularly low R^2 value of .0102 resulting in a poorly defined DEM.

(3). DEM Generation

At this point the linear regression formula was applied to the BFPR phase image, resulting in a BFPRL image. The average slope was then added back in to generate the DEM.

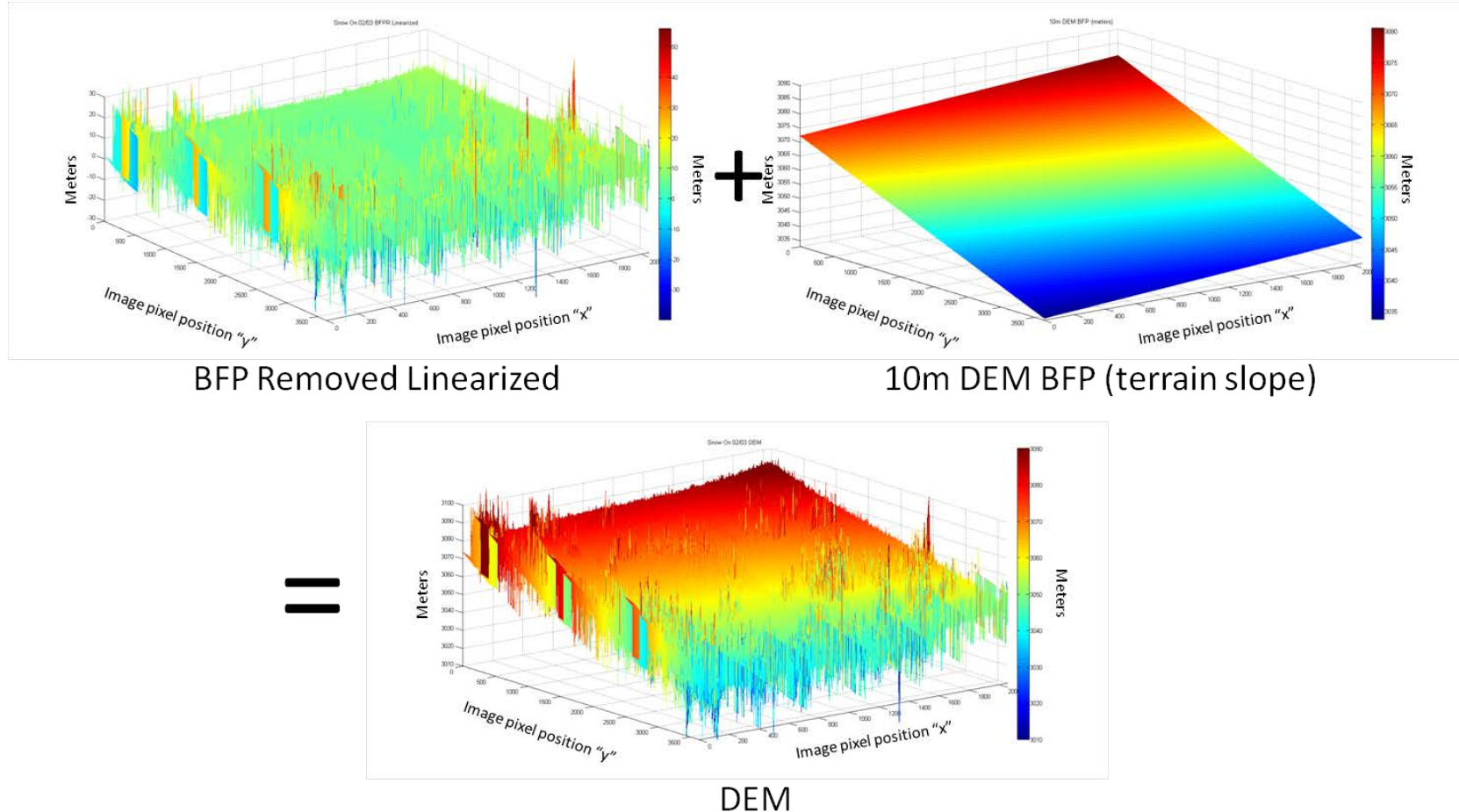


Figure 96. Addition of BFPRL to the 10m DEM BFP results in the Snow On SAR image pair 02 and 03 DEM. The snow covered DEM assumes minimal SAR penetration. Mammoth Mountain study site, ($37^{\circ}37.7'N$, $119^{\circ}02.7'W$).

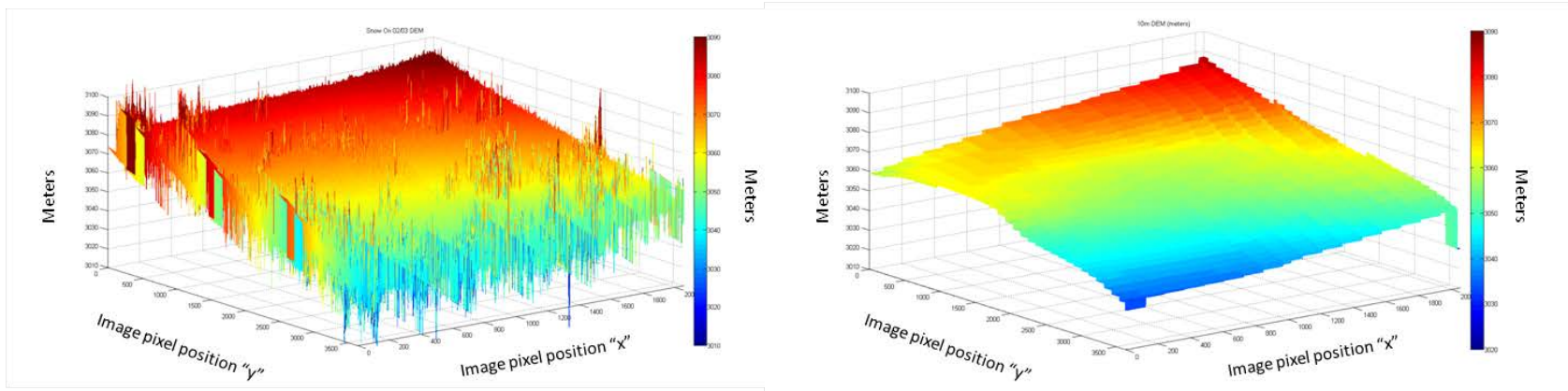


Figure 97. The BFPR derived DEM (left) only partially resemble the low resolution DEM (right)

In this particular case the generated DEM did not compare well with the low resolution DEM. The linear regression showed a very poor correlation between the phase perturbation and the elevation perturbation. The BFPR showed very little terrain definition in the phase field. This is most likely a result of the baseline between this SAR image pair.

(4) Snow Depth Calculation

The last step in the process was to subtract the Snow Off DEM from the Snow On DEM to get the snow depth.

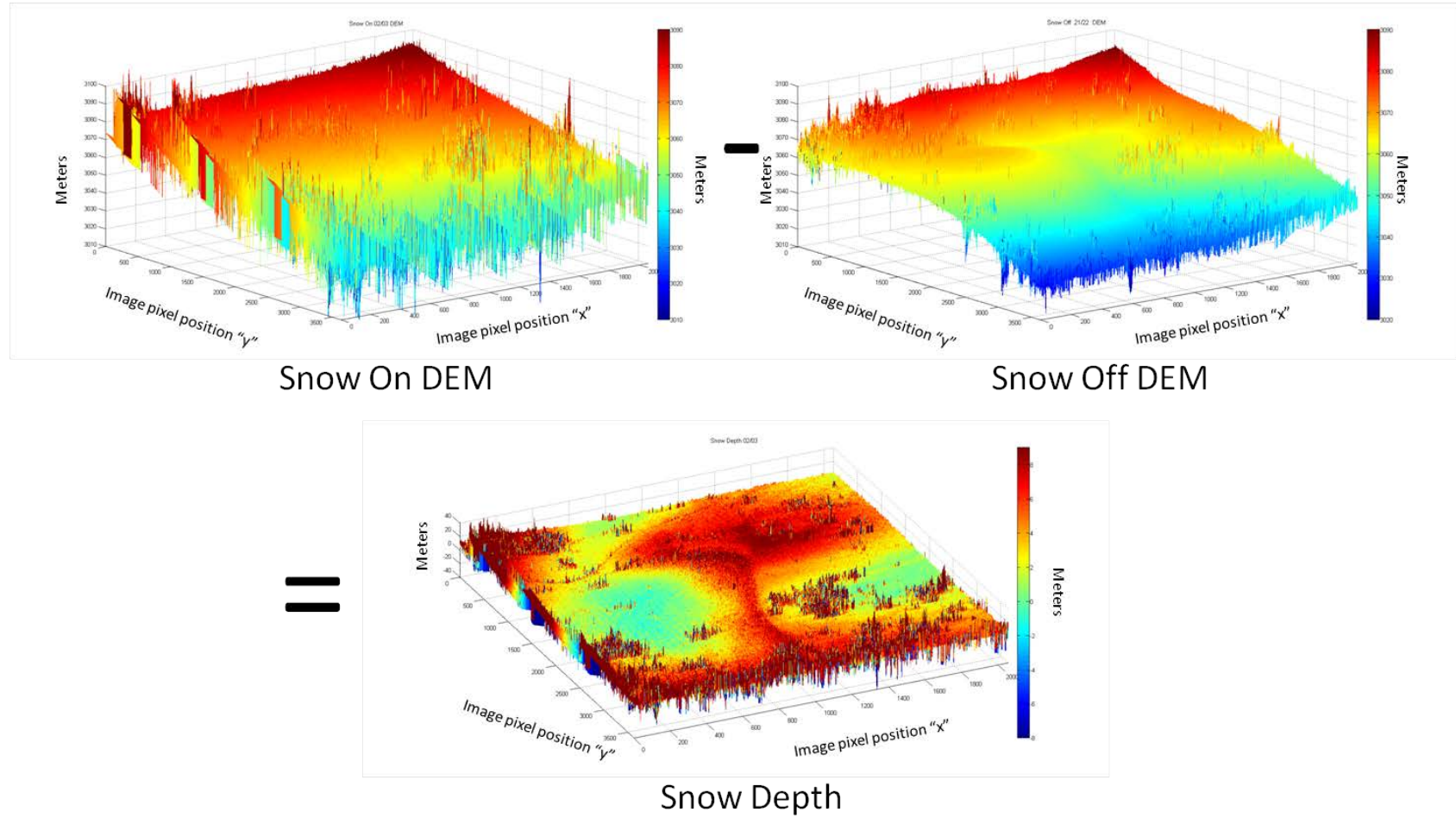


Figure 98. Subtracting the Snow Off DEM from the Snow On DEM generated from the SAR image pair 02 and 03 results in a snow depth image. Mammoth Mountain study site, (37°37.7'N, 119°02.7'N).

7. Snow On 02/04 DEM Generation and Snow Depth Calculation

(1) Best Fit Plane Generation

The BFP was generated for the SAR image pair 01/02 by fitting a plane to the total unwrapped phase image and then removing it via subtraction as previously described (Figure 99). Linear regression was then used to convert the BFPR phase to the difference between the mean slope elevation and corner reflector location elevations (Table 11, Figure 100). Next, the 10m DEM BFP or mean elevation slope was added back in to get the Snow On DEM (Figure 101). The last step was to subtract the Snow Off DEM from the Snow On DEM to get the snow depth (Figure 102).

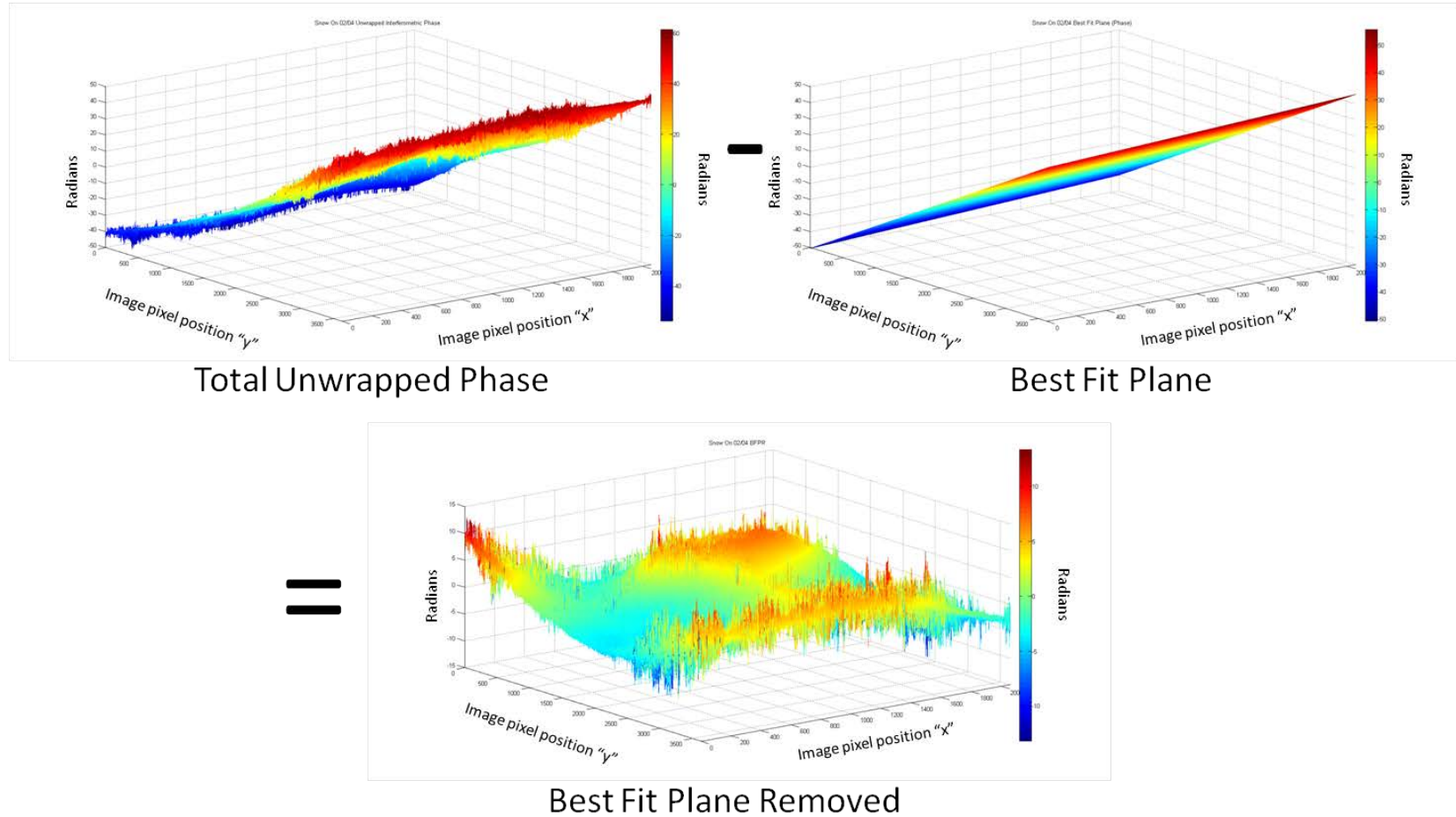


Figure 99. A Best Fit Plane (BFP) was generated from the interferometric SAR image pair (total unwrapped phase) 02 and 04. After generating the BFP, it was subtracted from the total phase resulting in a Best Fit Plane Removed (BFPR) image. Mammoth Mountain study site, ($37^{\circ}37.7'N$, $119^{\circ}02.7'N$).

(2) Phase Statistics

BFPR Statistics Snow On 02/04						
	X	Y	BFP (10m DEM) (meters)	Real (GPS) (meters)	Phase	Difference (meters)
SW (a)	432	1696	3055.95	3064.87	4.21036	8.92
NW (b)	678	985	3064.44	3068.64	0.59179	4.2
NE (c)	1790	1227	3066.45	3070.85	0.09139	4.4
SE	1554	1980	3057.55	3066.69	2.43061	9.14

Table 11. The phase from the BFPR image was compared with the mean slope perturbation to determine phase to elevation relationship for Snow Off SAR image pairs 02 and 04.

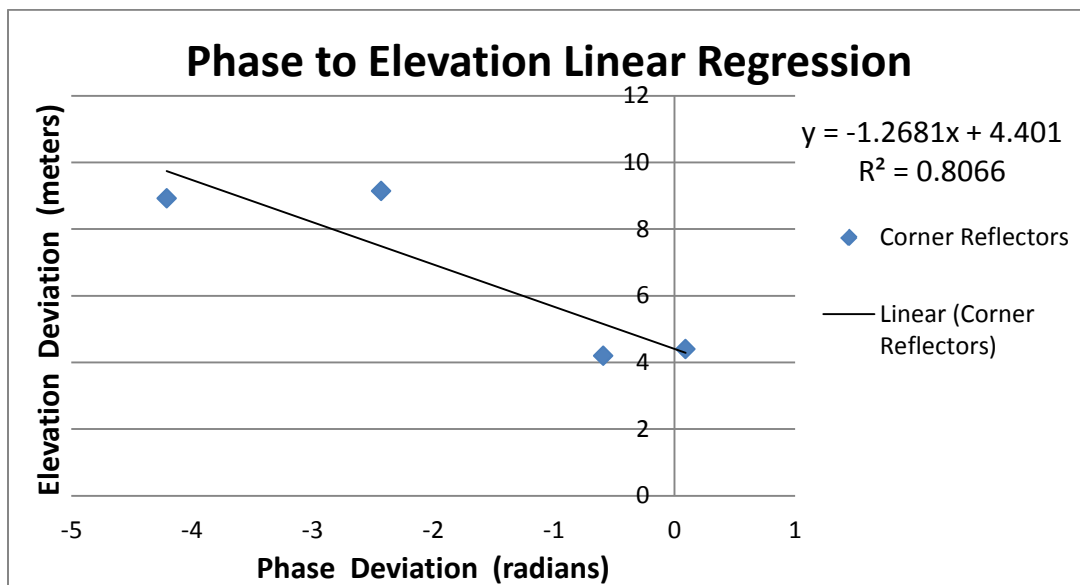


Figure 100. Linear regression of the BFPR phase and mean slope perturbation results in an equation that is applied to change BFPR image from phase to elevation for SAR image pair 02 and 04.

(3) DEM Generation

At this point the linear regression formula was applied to the BFPR phase image, resulting in a BFPRL image. The average slope was then added back in to generate the DEM.

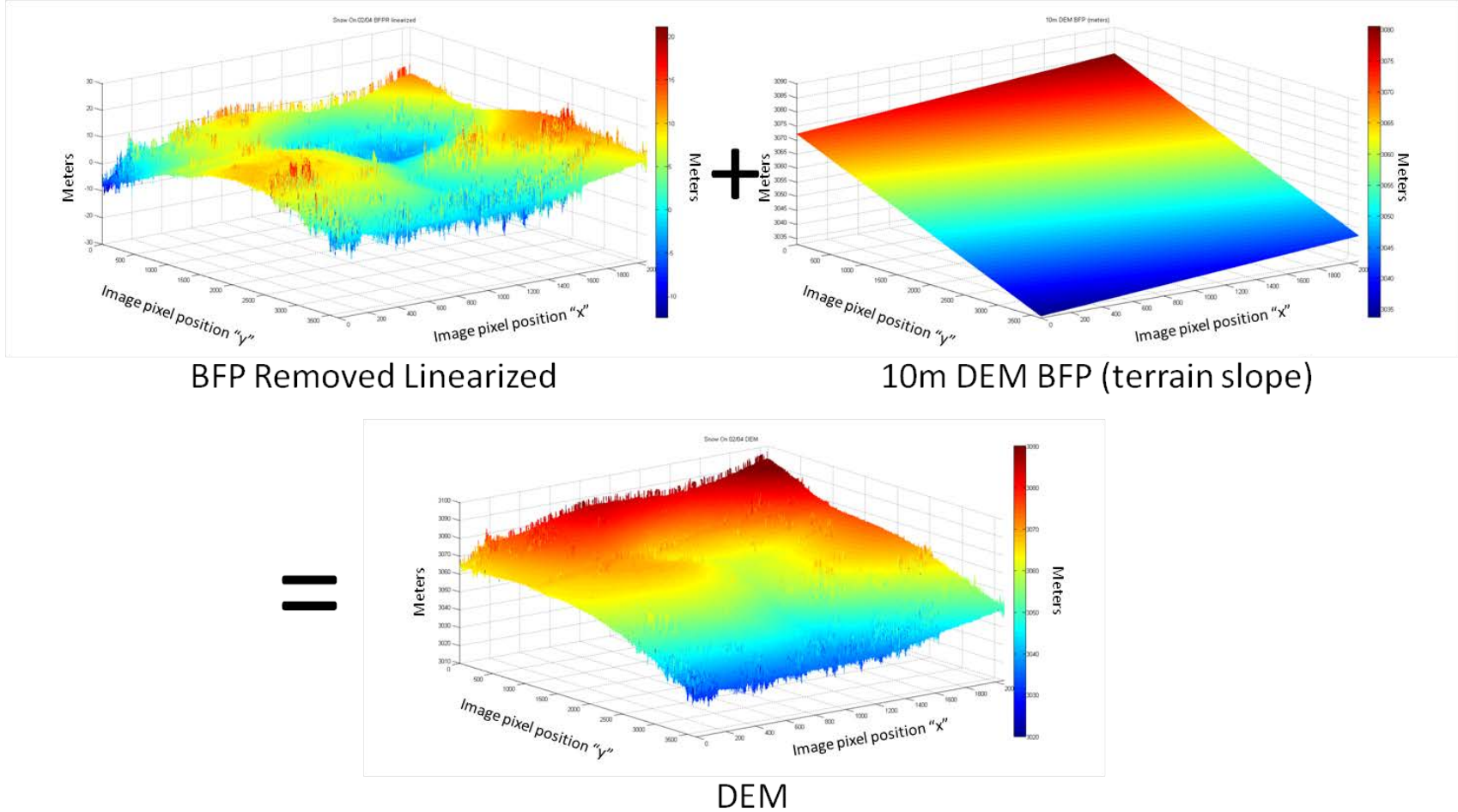


Figure 101. Addition of BFPRL to the 10m DEM BFP results in the Snow On SAR image pair 02 and 04 DEM. The snow covered DEM assumes minimal SAR penetration. Mammoth Mountain study site, (37°37.7'N, 119°02.7'N).

(4) Snow Depth Calculation

The last step in the process was to subtract the Snow Off DEM from the Snow On DEM to get the snow depth.

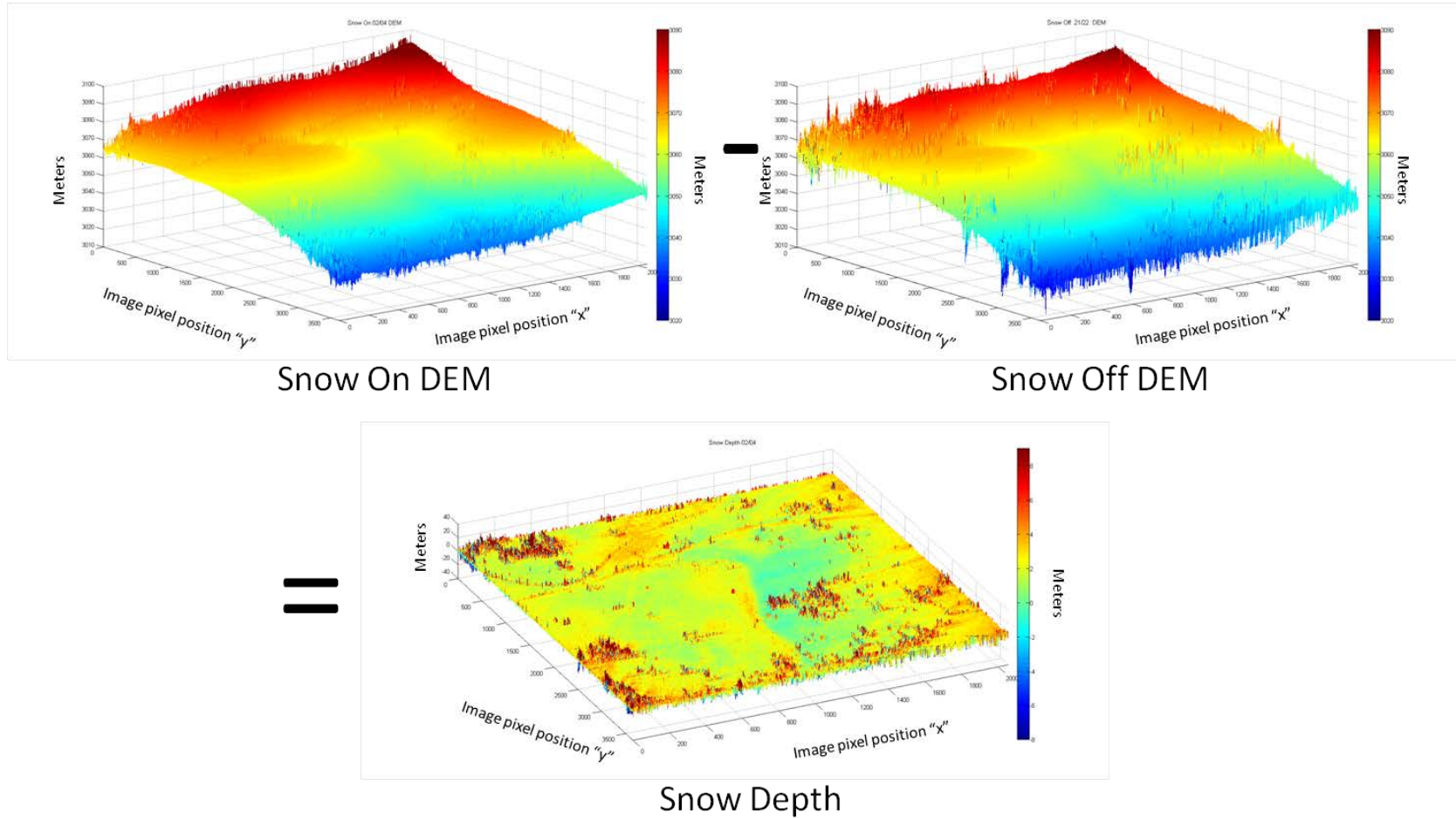


Figure 102. Subtracting the Snow Off DEM from the Snow On DEM generated from the SAR image pair 02 and 04 results in a snow depth image. Mammoth Mountain study site, ($37^{\circ}37.7'N$, $119^{\circ}02.7'N$).

8. Snow On 03/04 DEM Generation and Snow Depth Calculation

(1) Best Fit Plane Generation

The BFP was generated for the SAR image pair 03/04 by fitting a plane to the total unwrapped phase image and then removing it via subtraction as previously described (Figure 103). Linear regression was then used to convert the BFPR phase to the difference between the mean slope elevation and corner reflector location elevations (Table 12, Figure 104). Next, the 10m DEM BFP or mean elevation slope was added back in to get the Snow On DEM (Figure 105). The last step was to subtract the Snow Off DEM from the Snow On DEM to get the snow depth (Figure 106).

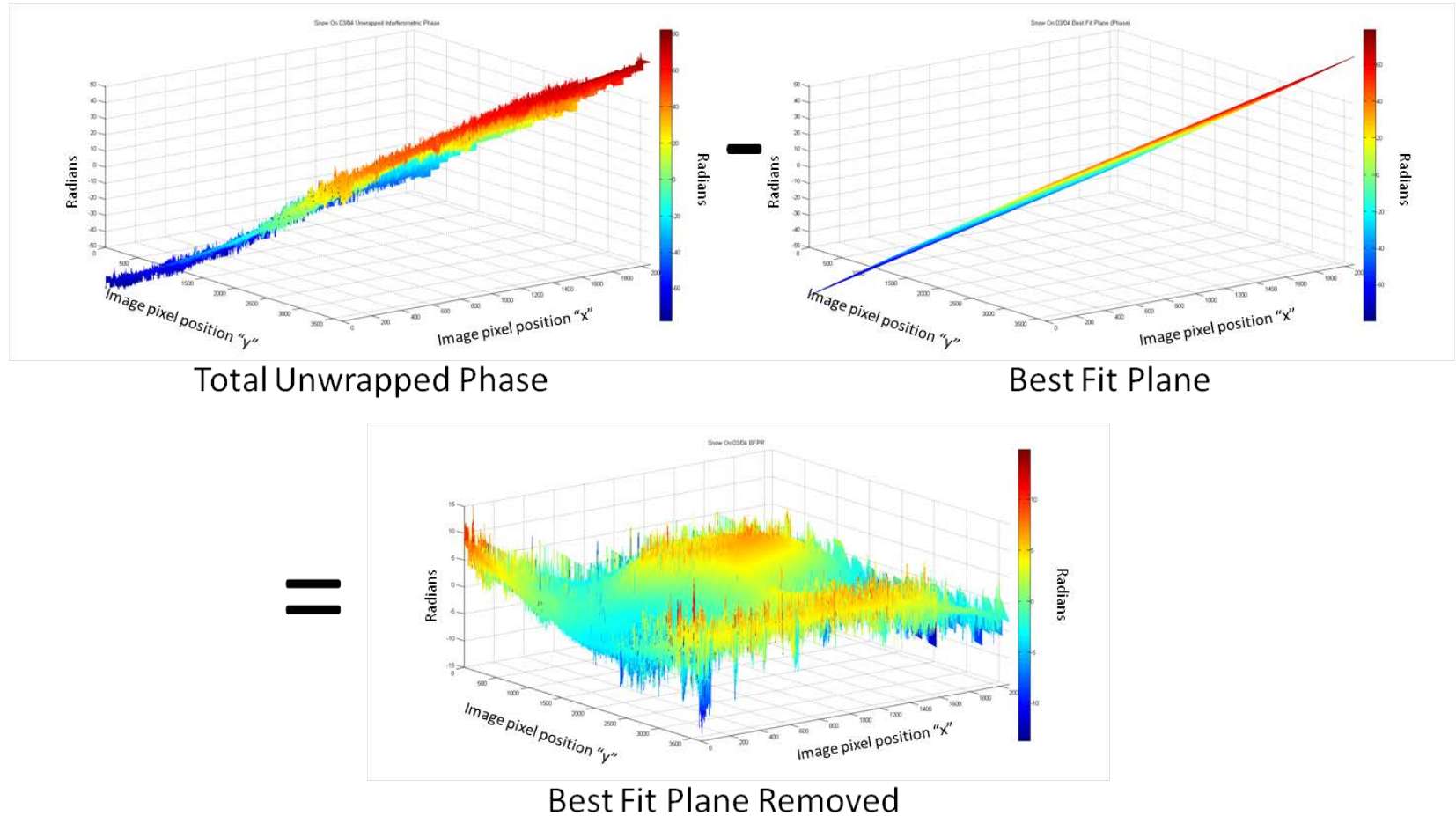


Figure 103. A Best Fit Plane (BFP) was generated from the interferometric SAR image pair (total unwrapped phase) 03 and 04. After generating the BFP, it was subtracted from the total phase resulting in a Best Fit Plane Removed (BFPR) image. Mammoth Mountain study site, ($37^{\circ}37.7'N$, $119^{\circ}02.7'N$).

(2) Phase Statistics

BFPR Statistics Snow On 03/04						
	x	y	BFP (10m DEM) (meters)	Real (GPS) (meters)	Phase	Difference (meters)
SW (a)	432	1696	3055.95	3064.87	-4.0578	8.92
NW (b)	678	985	3064.44	3068.64	-0.53533	4.2
NE (c)	1790	1227	3066.45	3070.85	0.552876	4.4
SE	1554	1980	3057.55	3066.69	-2.09339	9.14

Table 12. The phase from the BFPR image was compared with the mean slope perturbation to determine phase to elevation relationship for Snow Off SAR image pairs 03 and 04.

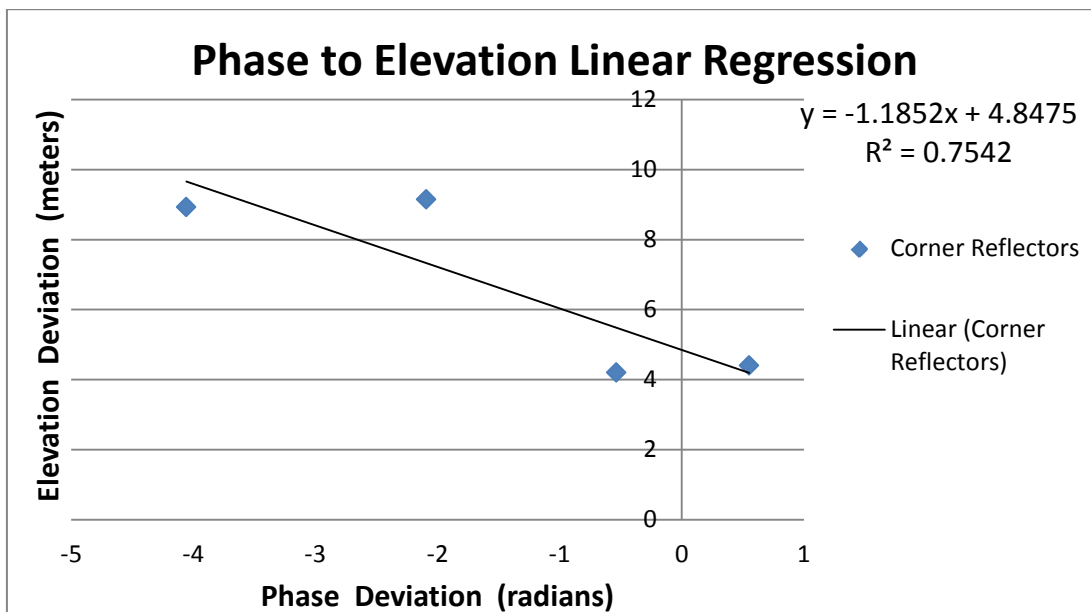


Figure 104. Linear regression of the BFPR phase and mean slope perturbation results in an equation that is applied to change BFPR image from phase to elevation for SAR image pair 03 and 04.

(3) DEM Generation

At this point the linear regression formula was applied to the BFPR phase image, resulting in a BFPRL image. The average slope was then added back in to generate the DEM.

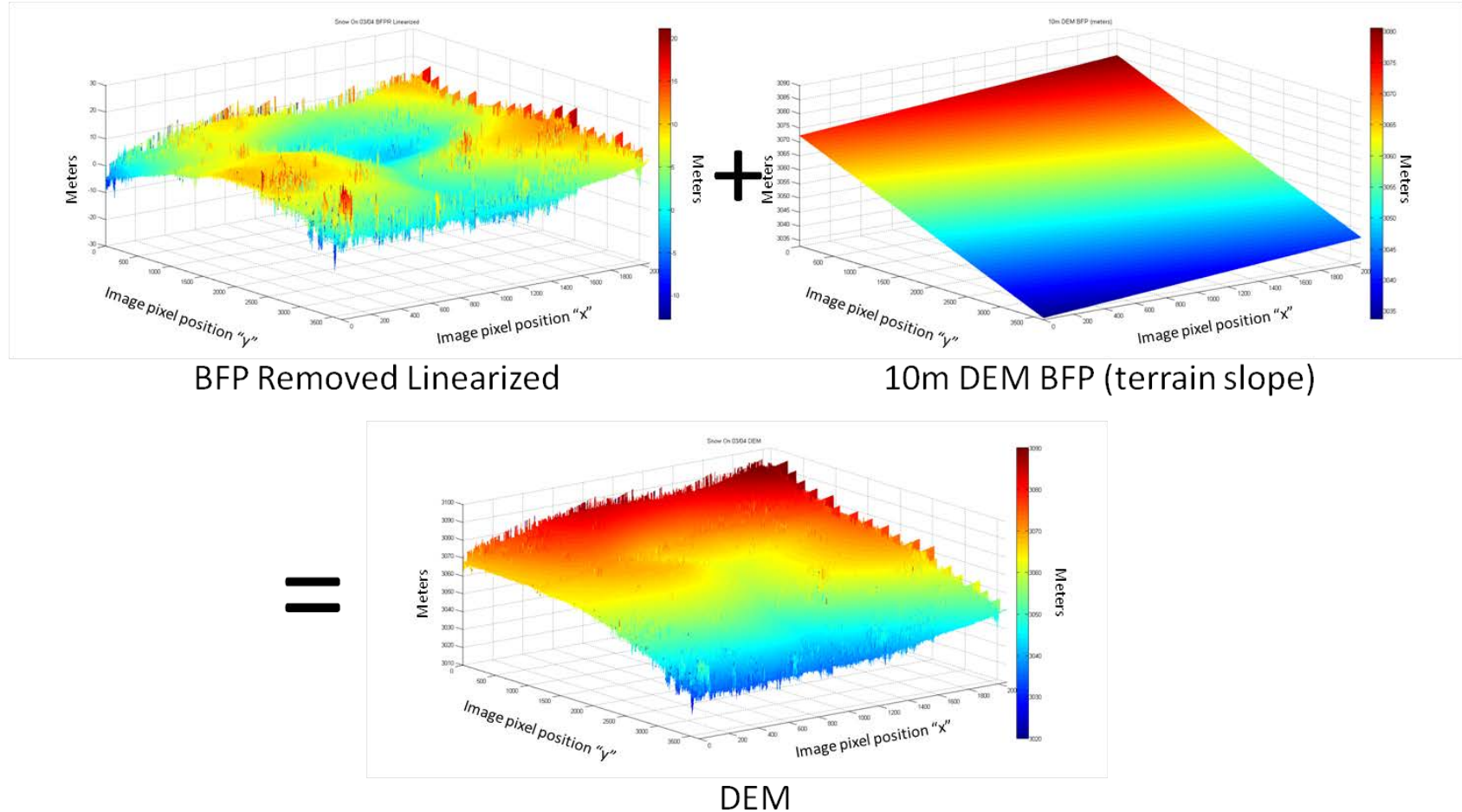


Figure 105. Addition of BFPRL to the 10m DEM BFP results in the Snow On SAR image pair 03 and 04 DEM. The snow covered DEM assumes minimal SAR penetration. Mammoth Mountain study site, (37°37.7'N, 119°02.7'N).

(4) Snow Depth Calculation

The last step in the process was to subtract the Snow Off DEM from the Snow On DEM to get the snow depth.

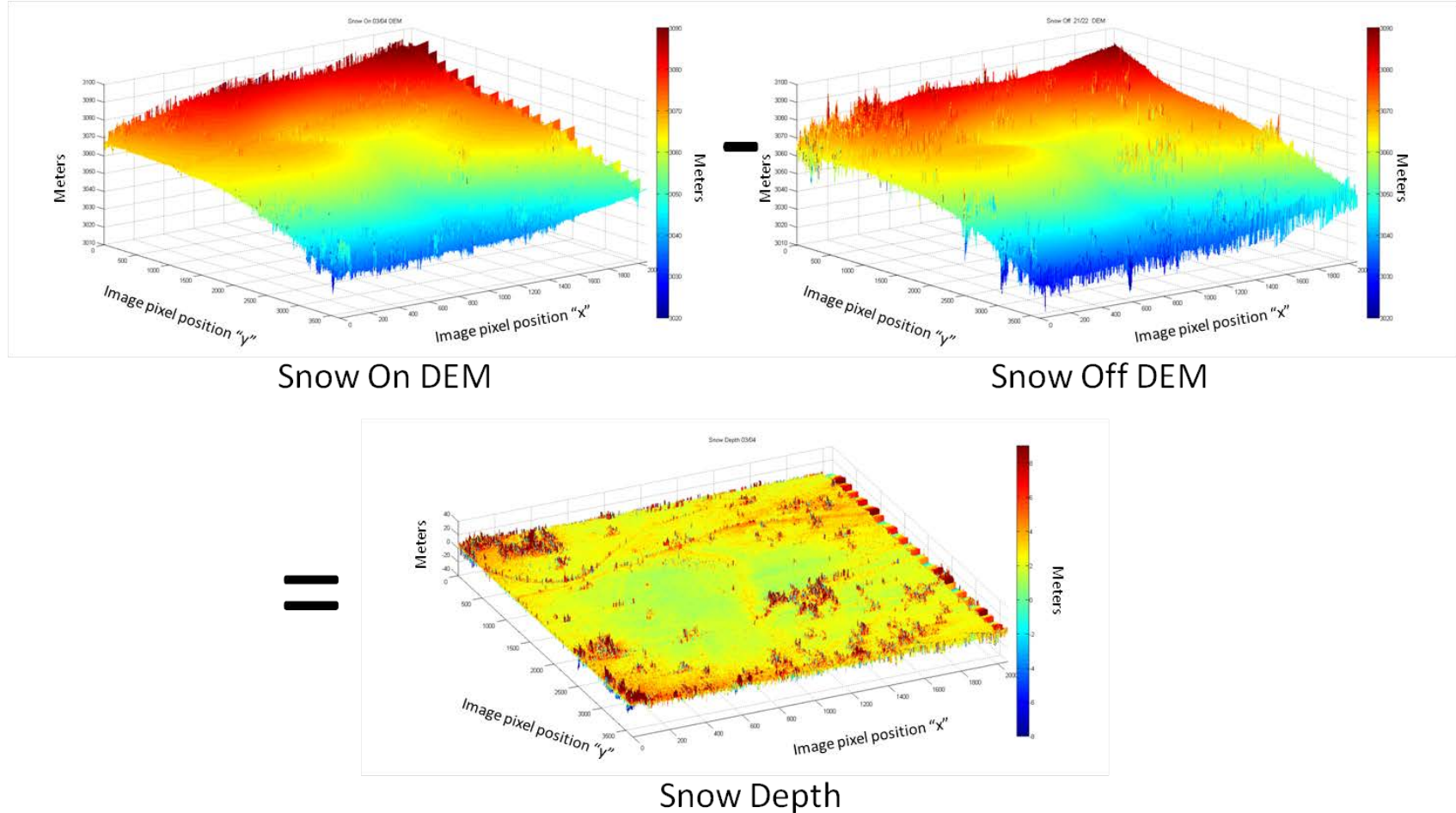


Figure 106. Subtracting the Snow Off DEM from the Snow On DEM generated from the SAR image pair 03 and 04 results in a snow depth image. Mammoth Mountain study site, (37°37.7'N, 119°02.7'N).

B. BEST FIT PLANE REMOVED ANALYSIS

The Best Fit Plane Removed method showed substantially better results than the baseline method with respect to generating viable DEMs. A total of six SAR image pairs were calculated with varying results and can be seen in Table 13. The snow depth calculation for every manual measurement location and its associated error can be seen in Appendix C. The errors were calculated using two different data sets. The first set compared the calculated positions against the 16 manually determined snow depths in the area roughly contained by the corner reflectors. The second included the 16 mentioned spots along with the five other measured locations to the south of the box formed by the GCPs. The other five locations fell within the edge of the tree line. A percentage of those calculated snow depths had radar shadows from trees in some of their averaged areas. For that reason, those locations were not considered in the current analysis and will be left for further consideration at a future date.

Snow Depth Error by SAR image pair						
SAR Image Pair	01/02	01/03	01/04	02/03	02/04	03/04
Average Snow Depth error (cm)	-8.00	95.00	-49.06	175.69	-86.56	-41.69

Table 13. Average snow depth error by SAR image pair.

Examination of the summary results in Table 13 and Appendix B shows widely varying snow depth errors. Table 13 averages all 16 snow depth locations for each of the six SAR image pairs. It is important to note that in some cases, image pair 01/02 in particular, positive and negative error values average to give a lower average error. Furthermore, high and low coherence locations are mixed in these averages. Appendix B lists the error values for each individual snow depth location for each of the SAR image pairs.

The varying snow depth error results seen in table 13 do not tell the whole story. Each of the different SAR image pairs tend to show either a high or low average error rather than all the pairs having a bias in the same direction. While it is not quite clear where these biases are coming from, it is believed that they are either related to the BFP

or potentially indicated by certain characteristics that can be found in the BFP calculations. There are two noted biases. The first is the overall high/low bias. In the pairs that have been computed, two pairs have a high bias for snow depth (01/03, 02/03), and the other four have a low bias (01/02, 01/04, 02/04, 03/04). One of those with a low bias, pair 01/02, has only a slight bias.

Recall that the flat earth phase is made up of both range phase and azimuth phase. It has also been observed, at least in the cases for this research, that the flat earth phase tends to be the dominant phase in the unwrapped interferograms or the total phase images. This observation suggests that the BFPs calculated tend to be dominated by the flat earth phase as opposed to the terrain. Recall also that it is the flight pair geometry or the baseline that determines the flat earth phase pattern. A quick look at the unwrapped interferograms or total phase (Figures 78, 82, 87, 92, 97, 102, 103) show this to be true. Very little of the terrain phase can be seen in the total phase images. Often it is impossible to get even a sense of the underlying terrain.

Both the range tilt and azimuth tilt, determined by the baseline, can be observed in each BFP. For example, in SAR Image pair 01/02, in Figure 107 below, the range phase tilts up toward the north or away from the radar platform. In addition to that observation, the azimuth phase also tilts toward the east or the right side of the image area. Focusing on the azimuth phase and comparing it to the high and low average errors seem to indicate a pattern where the images with an eastward tilting azimuth phase demonstrate a low average error. Likewise, for those with a westward tilting phase there is a high average error. The mechanism behind this is not understood at this time. The noted correlation does not prove causality; however it cannot be ignored and warrants further exploration.

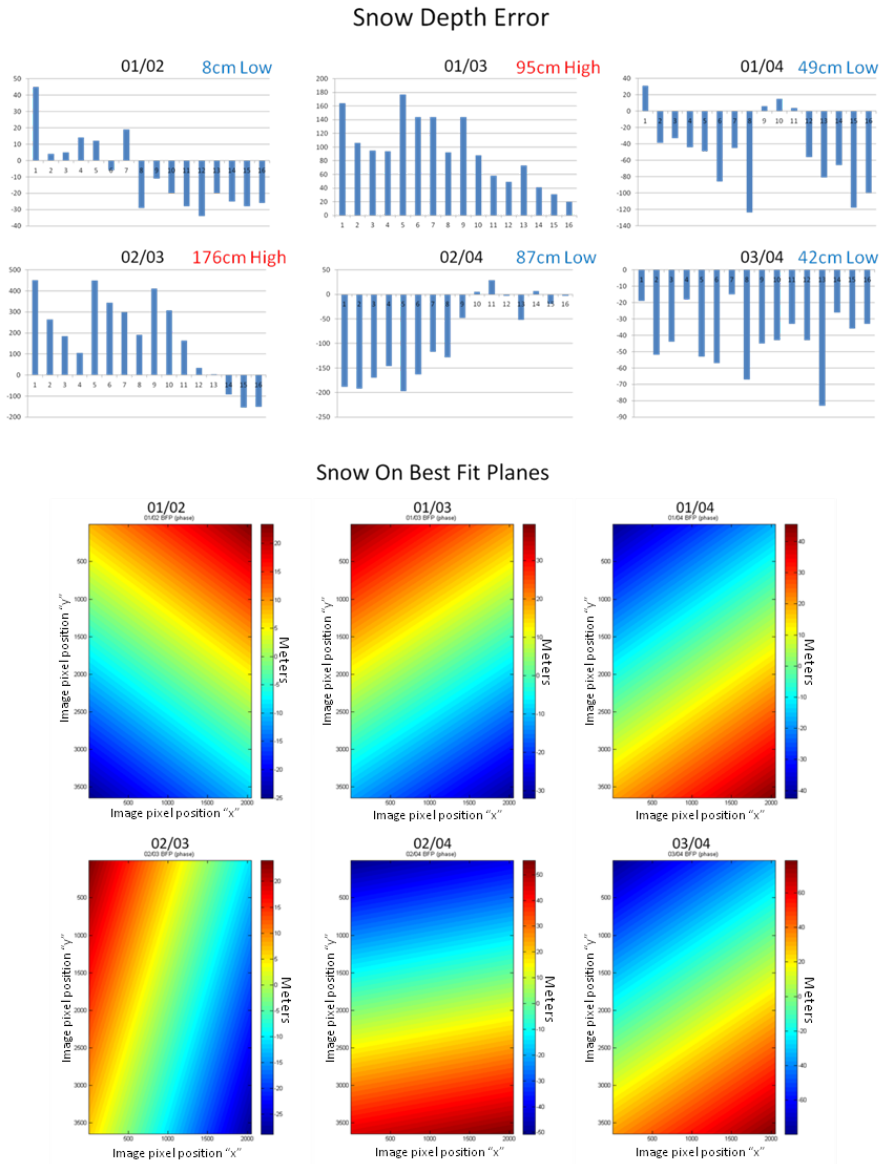


Figure 107. Snow depth error for each of the 16 manual snow depth locations for each of the six SAR image pairs are indicated in the top bar graphs. The six images are the BFPs that correspond to the snow depth error bar graphs.

The second bias noted involves both the coherence of the area in the image being looked at and the range phase tilt. Note that there is a distinct difference between the first eight snow depth locations and the second eight with respect to coherence. That can clearly be seen in Figure 108. The first 8 locations have high coherence, ranging typically above 0.85 throughout the SAR image pairs. The second eight have lower

coherence, typically averaging below 0.7, with the majority between 0.5 and 0.65, and some of the SAR image pairs as low as the mid-0.3 range. The exact reason for the low coherence in some of the SAR image pairs cannot be absolutely determined. It is however likely that this is due to low values in the magnitude of the returns at those particular locations. A quick comparison against the magnitude images seems to corroborate this. Because magnitude is part of the coherence calculation, this is the most likely cause. The reason for the low return magnitude is difficult to define absolutely. The strength of the magnitude of the radar return is typically due the surface properties and the incidence angle of the incoming radar emission. Snow radar reflectivity was observed to be significantly less than that of the solid ground. In addition to that, it appears that there are portions of the varying terrain that may be affected by a shallow incidence angle. A shallow incidence angle could be responsible for a decrease in the magnitude, and therefore be responsible for a decrease in the coherence. One other possibility is a difference in the liquid water content of the snow surface as opposed to the frozen content. Generally, the higher the liquid content, the higher the expected reflectivity. This scenario seems unlikely though because east facing slopes should have a greater potential for melting than west facing slopes in the late morning hours when this area was imaged. The image area has a ravine running from the north to the south through the scene. The magnitude pattern seen is the opposite of what would be expected if there was disproportionate melting occurring. In other words, it is the west facing slope that has the greater magnitudes and the east facing slope has weaker magnitudes. Ultimately, the important take away is that there is a distinct difference between the SAR coherency of the first and the second eight snow depth locations.

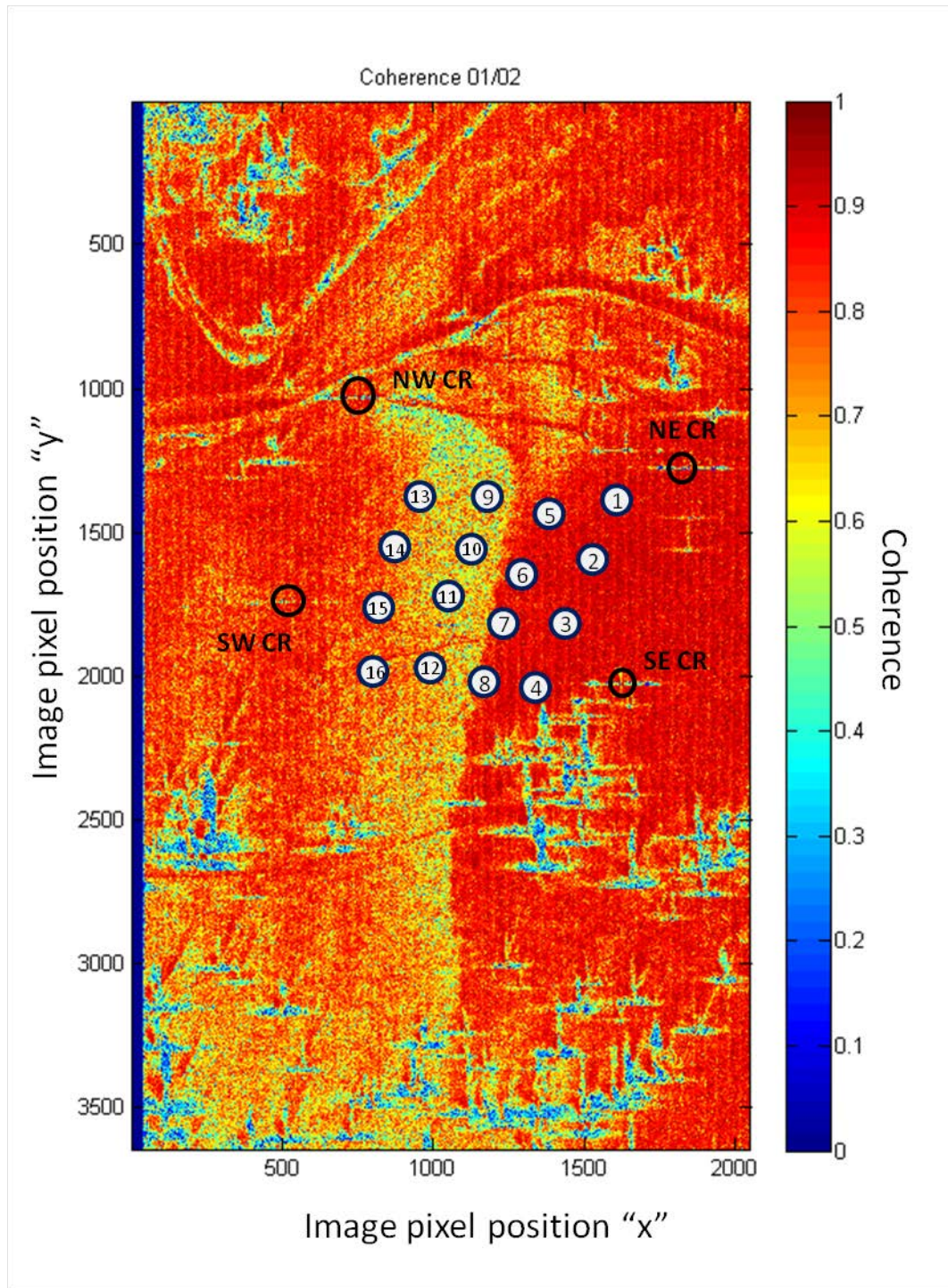


Figure 108. Coherence varies throughout the scene. The numbered circles denote the manual snow depth validation measurement locations. Note that measurement locations 1-8 have relatively high coherence compared to locations 9-16. Mammoth Mountain study site, ($37^{\circ}37.7'N$, $119^{\circ}02.7'N$).

Two approaches were taken to explore this potential bias. The first was to take a look at the relative coherence of the 16 sites in all 6 SAR image pairs. These were plotted along the “0.7” coherence line that delineated the two coherence regimes (Figure 108). Note the pattern that differentiates the first eight snow depth locations from the second eight relative to coherence. Normalizing the snow depth errors for each of the six pairs was the second action taken. New tables were made with the average snow depth errors subtracted from each of the measurement locations. This indicated how each individual location varied with respect to the average error. The results can be seen in Figure 109.

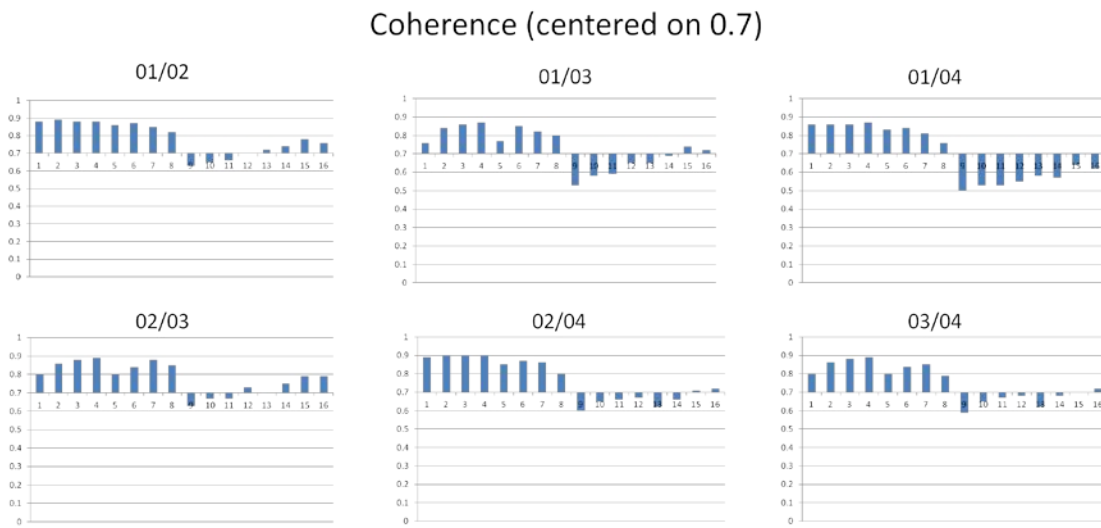
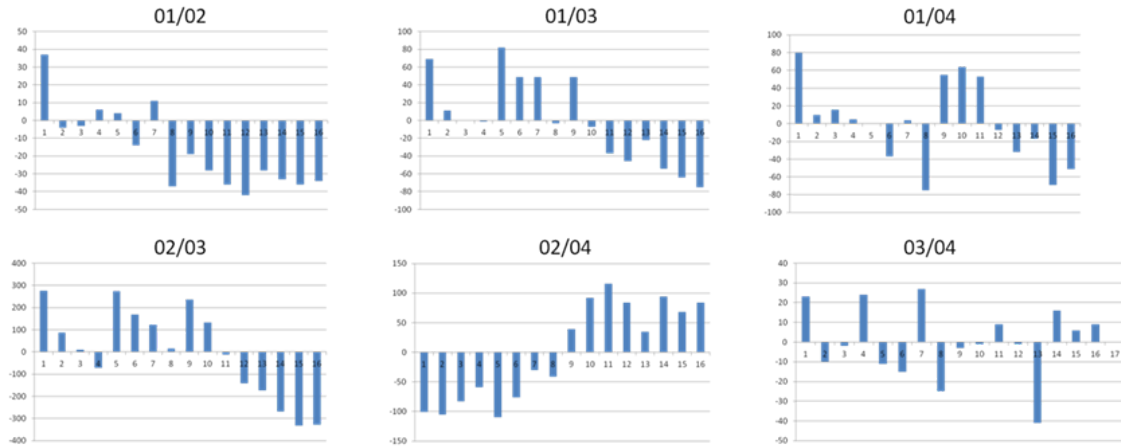


Figure 109. Average coherence per manual snow depth location for each of the six interferometric image pairs.

Snow Depth Error (normalized for bias)



Snow On Best Fit Planes

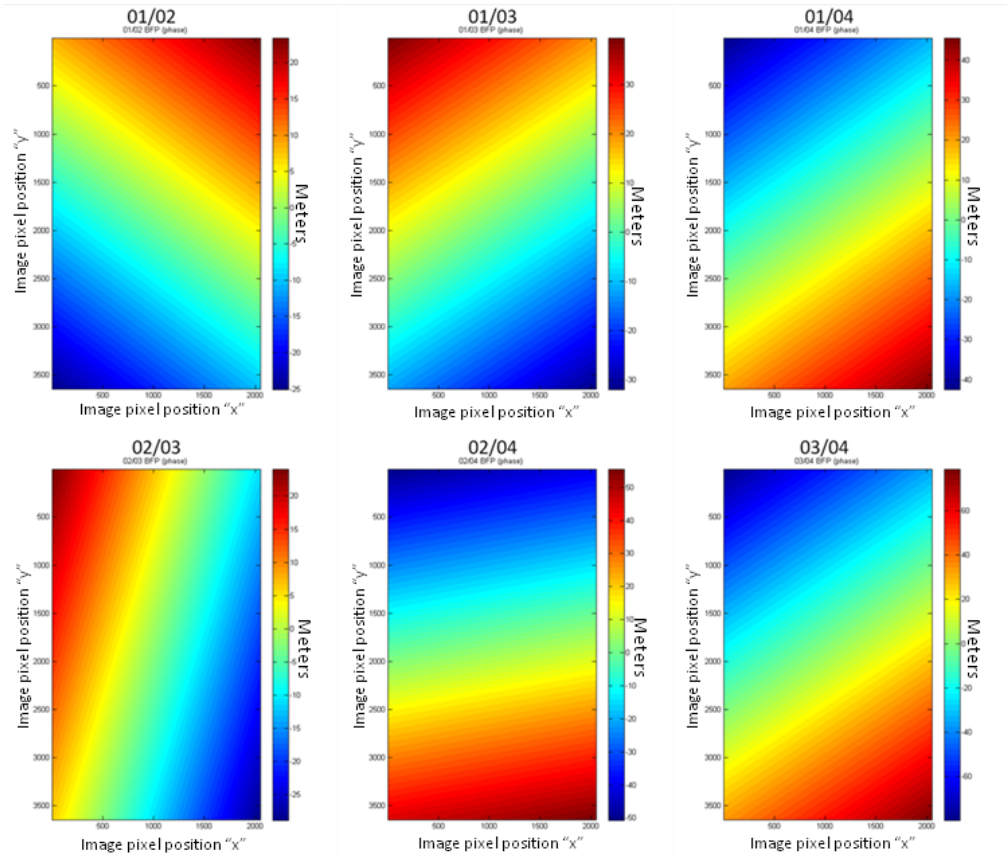


Figure 110. This figure demonstrates the relationship between the normalized snow depth error for each of the six interferometric image pairs and the pattern of the BFP derived from those interferograms.

After the snow depth errors were normalized, it appeared that they generally follow the same pattern as that seen in the coherence images (Figure 109). In other words, after the normalization, the first eight show a high bias and the second show a low bias or the opposite configuration. It should be noted that this signal is not strong in all the cases such as SAR image pairs 01/04 and 03/4, while it is very strong in others. While the mechanism for this is not understood, it appears that there may be some relationship between this and the range phase, similar to that which was seen for the azimuth phase relative to the overall high or low average error. When observing Figure 110, note that when the range phase slopes up toward the north; the first eight snow depth sites tend to be greater than the normalized line while the second eight tend to be less than the normalized line. When the range phase slopes toward the south or toward the radar platform the opposite is the case. The signal does tend to be weak in pair 03/04 and nonexistent in image pair 01/04. Again this does not show causality but the consistency of the pattern cannot be ignored. Therefore there appears to be a potential link to either the coherence, or the cause of the coherence pattern, and the particular flight geometry.

Another observation was made for three of the six SAR image pairs. Observing Figure 107, note that in image pairs 01/03, 02/03, and 02/04, the absolute snow depth errors show a stair-step pattern for every four measurements. This pattern is also similar in SAR image pair 01/02, but the signal is not as strong. Each of these stairs corresponds with one of the rows in which the snow depths were measured manually. The lower position number indicates a measurement further north or further from the radar, and the higher position number being further south or closer to the antenna. For example, the eastward row of four snow depths had the “1” position as the most northerly component. Each successive location went south through location “4” and started over again at position “5” at the top of the collection scene on the next row.

In each of these four cases the snow depth error decreases as the position moves south. This held true for every row regardless of whether there was a high or low bias. It also held true regardless of the amount of coherence. There are a couple of possibilities that could account for this. The first one is that there may be an error in the overall slope of the underlying Snow Off DEM. Recall that the Snow Off DEM is subtracted from the

Snow On DEMs. An error in the average slope of the Snow Off DEM may account for this pattern. The same pattern is not apparent in the other two scenes, which raises questions about the validity of this line of thinking. Another potential explanation is that the error is contained in the slope derived from the 10m DEM. Recall that the 10m DEM slope was added back into both the Snow On and Snow Off BFPR images. If the slope has the wrong tilt it would be indicated as an increase in error in a particular direction. The weakness to that argument is that the same wrong slope is added to both the Snow On and Snow Off images. That should cancel the error out when those images are subtracted from each other. Another potential source lies with the BFP generated in the Snow On images. It is assumed that average elevation slope for the Snow On image is the same as that of the Snow Off. This would be a good assumption if the snow laid evenly across the scene. We know that is not entirely true. The BFPR images from the Snow On cases may actually have a different average terrain slope. After the Snow On BFPR is linearized, it is added back in to the 10m DEM slope. It is assumed that the BFPR image is a deviation from the average slope and that the Snow On and Snow Off images have the same average slope. If in fact they don't, this will cause a regularly increasing error in a particular direction. For example, if the snow depth increases on average as one moves from the southern part of the image to the northern part of the image, the snow covered terrain slope will be steeper than that of the slope calculated from the 10m DEM. This would mean that there would be an error in the slope that is added back in.

THIS PAGE INTENTIONALLY LEFT BLANK

VI. COHERENCE OBSERVATION

In the course of this research there were a couple unexpected observations. Recall that one of the reasons that SAR has not been used to determine snow depth is that it is nearly impossible to get images with strong coherence where snow is involved. This is because any changes in the surface cause decorrelation. Typically, SAR imagery pairs are taken over periods of time that ensure that the surface properties will change. The SAR acquisitions are often separated by at least several days. Because of the design of this research (using multiple acquisitions closely placed in time) temporal decorrelation was not an issue. The acquisitions were taken successively one after another insuring there would never be more than a handful of minutes between the acquisitions. The greatest time difference between acquisitions for the included images was 17 minutes for pair 01/04. Visually inspecting the images demonstrated that there were some differences in the coherence. There is no discernible pattern, however, until the images are put in order of increasing time difference between the acquisition of two images used in the generation of the interferometric pair. This can be seen in Figure 111.

INSAR Scan Time Difference and Coherence

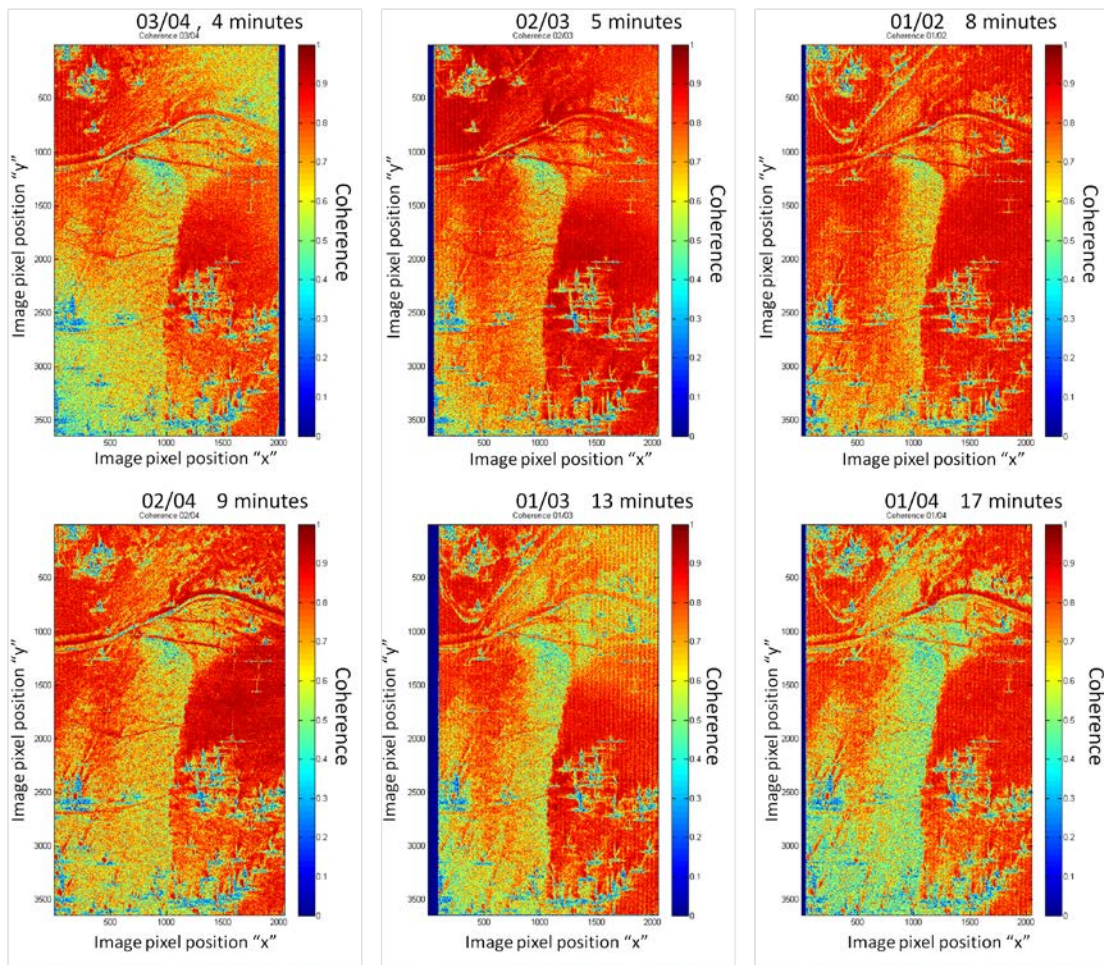


Figure 111. Time series of coherence images ordered by time between image pairs. Note the decrease in coherency over time. Mammoth Mountain study site, ($37^{\circ}37.7'N$, $119^{\circ}02.7'N$).

With the exception of image pair 03/04 with a time difference of only 4 minutes, there appears to be a very clear signal of increasing decorrelation between successive pairs as the time difference increases between the pairs. It is difficult to determine the exact cause of this increased decorrelation or why image pair 03/04 does not seem to follow the pattern. It is hypothesized that the surface's dielectric properties were changing rapidly enough that it could be seen in the coherence. Air temperature at the collection site was recorded to be $8^{\circ} C$ at 1200 local time or at the end of the SAR collection period by the General Atomics flight crew. In addition to that it was a sunny

day. It is believed that the surface of the snow was increasing its liquid water content from surface melting at a rate that was observable in the coherence images. It was also noted by the researcher that at the beginning of the SAR data collection that the snow was too dry to make a snow ball that held together. By the end of the SAR collection, there was no difficulty in making a solid snow ball. This may be an indication that the liquid content was increasing as the data were being taken. Unfortunately the time difference between snowballs was not noted and no snow moisture measurements (or dielectric measurements) were recorded. It is believed that potentially a change in the liquid water content of the surface may have resulted in a change of SAR penetration into the surface resulting in a change (decrease) in the path length, thereby changing the phase recorded at the surface. This would most likely result in decorrelation between images. Greater differences in time would result in greater changes in path length and increased decorrelation.

THIS PAGE INTENTIONALLY LEFT BLANK

VII. CONCLUSIONS, RECOMMENDATIONS AND FUTURE WORK

A. CONCLUSIONS

The goal of the SNODAR research was to explore the viability of using Multi-pass Single Look Complex InSAR to determine snow depth. Two different approaches were taken towards deriving Snow Off and Snow On DEMs that could be differenced to determine a change in elevation of snow depth. The first approach required the calculation of the baseline for the interferometric pair. The second approach bypassed the need for the baseline knowledge and took a perturbation or decomposition of parts approach. The SAR datasets were acquired by General Atomics using a Lynx II radar from a platform flying approximately 10km to the south of the study area.

1. Baseline Method

The Baseline method approach ultimately ended up being problematic. The method attempted to determine the baseline between SAR collections by solving a system of equations using ground control points and their associated phases. The DEMs generated from this approach were ultimately unrepresentative of the real terrain. The problem revolved around the ability to get a correct baseline. This was determined by observing that the removal of the flat earth phase from interferogram did not result in a match to known terrain characteristics. The flat earth phase is wholly dependent on an accurate knowledge of the baseline. Sensitivity tests indicate that there was very little room for input error when calculating the baseline.

The sensitivity of the Baseline method to measurement error is a challenging problem. Limitations in the ability to accurately quantify the input data will be difficult to overcome. Changing the baseline configuration of the flight paths to increase the baseline will decrease the sensitivity to potential measurement error. There are, however, limits to the size of the baseline before coherence becomes an issue. In addition, there may be approaches that will improve the input data for the system of equations used to calculate the baseline. The baseline calculations proved to be most sensitive to the

vertical component or Δz difference between the ground control points. It was shown that small potential errors could result in large errors in the flat earth phase calculations.

This method was mathematically rigorous and complicated both from a theoretical point of view and a computational point of view. This complexity interjected many opportunities for either error in the processing or error in the computations. It is not clear from this research why the Baseline method did not work in this case, and it is believed that the fundamentals are still there for a successful application of the method. This is a topic for future research—several suggestions are offered below and in the Recommendations section.

2. Best Fit Plane Removed Method

The Best Fit Plane Removed method showed greater success relative to the baseline method. The BFPR method bypassed the requirement for the baseline knowledge by taking a perturbation or decomposition approach. This was done by generating a best fit plane to the interferometric image and then removing it from the total phase data. This isolated the interferometric phase caused by the terrain that deviated from the mean slope. It also removed the flat earth phase that was an issue with the Baseline method. The phase was compared to the difference of the elevation at GCPs relative to the average elevation slope. The average slope was determined using a relatively low resolution DEM to generate the mean slope and comparing it to survey grade GPS elevations. A linear regression was performed and applied to the “Best Fit Plane Removed” image to convert phase to elevation. That image was then added back to the average slope, resulting in a DEM. A Snow Off DEM compared well to the real world 10m DEM. After computing DEMs from both Snow On and Snow Off scenes they were differenced to calculate snow depth.

The snow depth results of six Snow On SAR pairs were compared to 16 manually measured snow depth locations with varying degrees of success. The SAR image pairs showed an average error of -8cm, 95cm, -49cm, 175cm 87cm and 42cm for the respective six SAR pairs. The results also indicated that coherence of the unwrapped InSAR image played a role in the DEM generation. Of the 16 locations manually

measured, eight fell in a high coherence regime indicated by coherences greater than 0.7 and the others fell in a regime indicated by coherence less than 0.7. In almost all of the cases the magnitude of the error for each of the SAR image pairs fell in two categories determined by this regime.

There did appear to be a consistent pattern of either high or low bias in the BFPR-calculated snow depth results. Four of the SAR image pairs demonstrated a low average for the snow depths while the other two pairs demonstrated a high average. The pattern indicates that errors may be either related to or indicated by the BFPs produced from the unwrapped interferograms. There appear to be two different biases. The first is that the slope of the azimuth aspect of the BFP affects the direction of the bias. It was observed that an eastward tilt in the BFP was consistent with SAR pairs with a bias towards low snow depth errors. Those with a westward tilt demonstrated a bias towards high snow depth errors. The second bias is not as well defined but does appear to exist in this dataset. This bias appears to relate coherence in the image and the range slope of the BFP. After normalizing the error there was a clear difference between the snow depth locations with high and low coherence. Additionally, the determination of whether the high or low coherence was above or below the normalization line appeared to be determined by the range tilt of the BFP. This pattern is not fully understood. Furthermore, the observed pattern does not necessarily indicate causality. Additional SAR image pairs should be tested to ensure that the pattern holds.

Another observation was made in four of the six SAR image pairs. It appeared that regardless of the coherence, the calculated error decreased as the observations moved southward or in the direction toward the sensor. This is indicative of an issue in the slope of one or more of the BFPR elements. Slope issues could arise from the calculation of the BFP, accuracy of the low resolution DEM used to determine the deviation of the high frequency terrain from the average slope, or an issue with representativeness of the low resolution DEM relative to the true slope of the snow covered terrain.

Furthermore this research demonstrates that the Ku-band radar is capable of discerning the snow air interface (minimal penetration). This is evident in both its ability to see features on the snow surface such as tracks in the snow from the researchers, and

the representative DEMs that consistently showed the terrain or snow surface. The DEMs also consistently showed the Snow On terrain to be higher than that of the Snow Off terrain.

3. Coherence Observation

One final observation was unexpected. It was assumed from the beginning of this research that the decorrelation normally associated with InSAR pairs from more traditional collections with time separation of multiple days would be nonexistent. The greatest time difference between SAR image pairs was 17 minutes with the shortest time difference being 4 minutes. It was observed that when the coherence images were ordered according to increasing time between the images, that the coherence decreased from one image to the next. This indicated that decorrelation was occurring on a very short time scale. This suggests that the dielectric properties of the snow surface were rapidly changing during the SAR data acquisition. This is only speculative, however, since no specific snow-moisture or other measurements were taken of the surface as a function of time.

4. Implications

While perfect results were not achieved, the BFPR method shows promise. The ground work has been laid for further investigation. In addition, while penetration into the snow pack by the Ku-band radar was not directly tested, it appears that it was minimal. The greatest challenge in this research was achieving good DEMs utilizing multiple SAR passes with an aircraft with only one antenna and an unknown baseline. SAR acquisition using an aircraft equipped with a bistatic antenna system with a frequency in the Ku-band or higher would greatly simplify the process and increase the probability of successful snow depth determination. While one of the main goals was to derive a method that could be used with operational monostatic platforms, it would benefit future research to test these techniques with a system that is better suited for making DEMs. The nature of the technique would not then be dependent on the ability to derive DEMs using monostatic SAR platforms with the attendant baseline determination

problems. Once SAR interaction with the snow surfaces is better codified; the focus could transition to the platforms with only one antenna.

B. RECOMMENDATIONS AND FUTURE WORK

1. Baseline Recommendations

While the Baseline method proved to be problematic, there are still some potential things that can be done to move it toward success. Changing the flight parameters such as lengthening baseline should reduce sensitivity to any introduced measurement error. Additionally, the placement of the GCPs in a manner that increases the difference in the vertical should minimize ambiguity caused by the CR elevations being too close together.

2. Explore the causes of the Best Fit Plane Removed Biases

The BFPR method has shown potential but still has aspects that are not fully understood. The noted biases appeared to either be caused by or indicated by the BFP determined from the unwrapped interferogram. While the bias pattern was quite consistent across all six SAR image pairs, it does not prove causality. The mechanisms are not understood. Collection and analysis of additional data sets would help determine if this bias to BFP relationship holds. In addition, once these biases are understood, it should lead to increased accuracy.

3. Circumvent the biases

If the hypothesized biases hold to be true, there may be a way to circumvent them. Recall that the flat earth phase pattern is determined by the baseline of the aircraft pair flight geometry. The interferograms are generated from a master/slave relationship. If this relationship is reversed, the resulting interferogram will have a reversed BFP in both the range and azimuth directions. If this happens and the biases are related to SAR geometry, one should be able get the exact opposite bias when the data are processed. The results from the opposite master/slave relationships with the presumed opposite biases should be able to be averaged for the correct solution.

4. Bistatic Antenna

The purpose of this research was to determine if snow depth could be determined from SAR interferometry. Generating a good DEM was the greatest challenge in this research because of limitations imposed by the use of the monostatic (single antenna) SAR system. The monostatic configuration is commonly used for SAR imagery acquisition and those data were what was available for this research. An aircraft with a bistatic antenna (dual antenna) configuration would be much better suited for DEM generation. The baseline would always be known to a high degree of precision. Knowing the baseline would make much of the DEM generation significantly easier and allow for the focus of the research to be on the SAR interaction with the snow.

5. Negation of ground data

To be a viable technique, this capability will eventually need to be able to be performed without highly quantified GCPs. Different methods should be explored to determine if this is possible.

6. Snow conditions

Snow conditions affect the ability to get returns from the surface and have the potential to affect the overall accuracy. Varying snow conditions from different times of the season with different properties should be explored to determine the effects on this technique.

7. Collection method

There are several aspects of the collection that should be explored. The baseline configuration as mentioned above may play a role in the BFPR method. Additionally collecting data using a strip-map approach to cover large areas of land should be considered as should using differing resolutions.

8. Perturbation isolation

The BFPR approach was used to isolate the terrain phase perturbation for this research. Other approaches are possible. For example a fast Fourier transform (FFT)

could be used to separate the low frequency terrain slope from the higher frequency terrain detail (Shurong et al. 2009). Examination of this FFT approach may provide additional insight to the BFPR results.

THIS PAGE INTENTIONALLY LEFT BLANK

APPENDIX A. BASELINE TO M/RAD SENSITIVITY

Based on Eq 6.10					
Sensitivity of M/Rad to change in Baseline (Potential Error analysis)					
baseline in meters	θ degrees	lambda	height in meters	P to H	M/Rad
1	77	0.018	2334.5	0.0155	64.3879
2	77	0.018	2334.5	0.0311	32.1940
3	77	0.018	2334.5	0.0466	21.4626
4	77	0.018	2334.5	0.0621	16.0970
5	77	0.018	2334.5	0.0777	12.8776
6	77	0.018	2334.5	0.0932	10.7313
7	77	0.018	2334.5	0.1087	9.1983
8	77	0.018	2334.5	0.1242	8.0485
9	77	0.018	2334.5	0.1398	7.1542
10	77	0.018	2334.5	0.1553	6.4388
11	77	0.018	2334.5	0.1708	5.8534
12	77	0.018	2334.5	0.1864	5.3657
13	77	0.018	2334.5	0.2019	4.9529
14	77	0.018	2334.5	0.2174	4.5991
15	77	0.018	2334.5	0.2330	4.2925
16	77	0.018	2334.5	0.2485	4.0242
17	77	0.018	2334.5	0.2640	3.7875
18	77	0.018	2334.5	0.2796	3.5771
19	77	0.018	2334.5	0.2951	3.3888
20	77	0.018	2334.5	0.3106	3.2194
21	77	0.018	2334.5	0.3261	3.0661
22	77	0.018	2334.5	0.3417	2.9267
23	77	0.018	2334.5	0.3572	2.7995
24	77	0.018	2334.5	0.3727	2.6828
25	77	0.018	2334.5	0.3883	2.5755
26	77	0.018	2334.5	0.4038	2.4765
27	77	0.018	2334.5	0.4193	2.3847
28	77	0.018	2334.5	0.4349	2.2996
29	77	0.018	2334.5	0.4504	2.2203
30	77	0.018	2334.5	0.4659	2.1463
31	77	0.018	2334.5	0.4815	2.0770
32	77	0.018	2334.5	0.4970	2.0121

1 meter change in base line	Difference in Height (z) to Phase ($\Delta\phi$) ratio, M/Rad change
1 to 2	32.194
2 to 3	10.731
3 to 4	5.366
4 to 5	3.219
5 to 6	2.146
6 to 7	1.533
7 to 8	1.150
8 to 9	0.894
9 to 10	0.715
10 to 11	0.585
11 to 12	0.488
12 to 13	0.413
13 to 14	0.354
14 to 15	0.307
15 to 16	0.268
16 to 17	0.237
17 to 18	0.210
18 to 19	0.188
19 to 20	0.169
20 to 21	0.153
21 to 22	0.139
22 to 23	0.127
23 to 24	0.117
24 to 25	0.107
25 to 26	0.099
26 to 27	0.092
27 to 28	0.085
28 to 29	0.079
29 to 30	0.074
30 to 31	0.069
31 to 32	0.065
32 to 33	0.061

33	77	0.018	2334.5	0.5125	1.9511	33	to	34	0.057
34	77	0.018	2334.5	0.5280	1.8938	34	to	35	0.054
35	77	0.018	2334.5	0.5436	1.8397	35	to	36	0.051
36	77	0.018	2334.5	0.5591	1.7886	36	to	37	0.048
37	77	0.018	2334.5	0.5746	1.7402	37	to	38	0.046
38	77	0.018	2334.5	0.5902	1.6944	38	to	39	0.043
39	77	0.018	2334.5	0.6057	1.6510	39	to	40	0.041
40	77	0.018	2334.5	0.6212	1.6097	40	to	41	0.039
41	77	0.018	2334.5	0.6368	1.5704	41	to	42	0.037
42	77	0.018	2334.5	0.6523	1.5330	42	to	43	0.036
43	77	0.018	2334.5	0.6678	1.4974	43	to	44	0.034
44	77	0.018	2334.5	0.6834	1.4634	44	to	45	0.033
45	77	0.018	2334.5	0.6989	1.4308	45	to	46	0.031
46	77	0.018	2334.5	0.7144	1.3997	46	to	47	0.030
47	77	0.018	2334.5	0.7300	1.3700	47	to	48	0.029
48	77	0.018	2334.5	0.7455	1.3414	48	to	49	

Table 14. The left table demonstrates the sensitivity of the height to phase ratio in an interferogram based on the change in the baseline length. The right table demonstrates the actual change height to phase relationship from 1meter in baseline to the next.

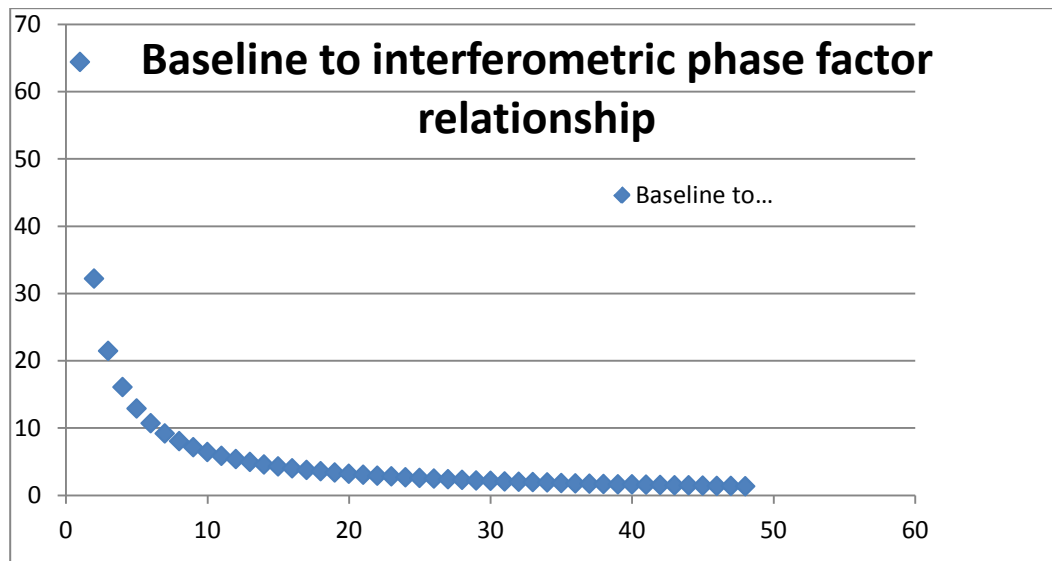


Figure 112. Baseline length to interferometric phase factor relationship based on Table 14.

APPENDIX B. BASELINE COMPONENT SENSITIVITY TO GROUND DIFFERENCE ERROR

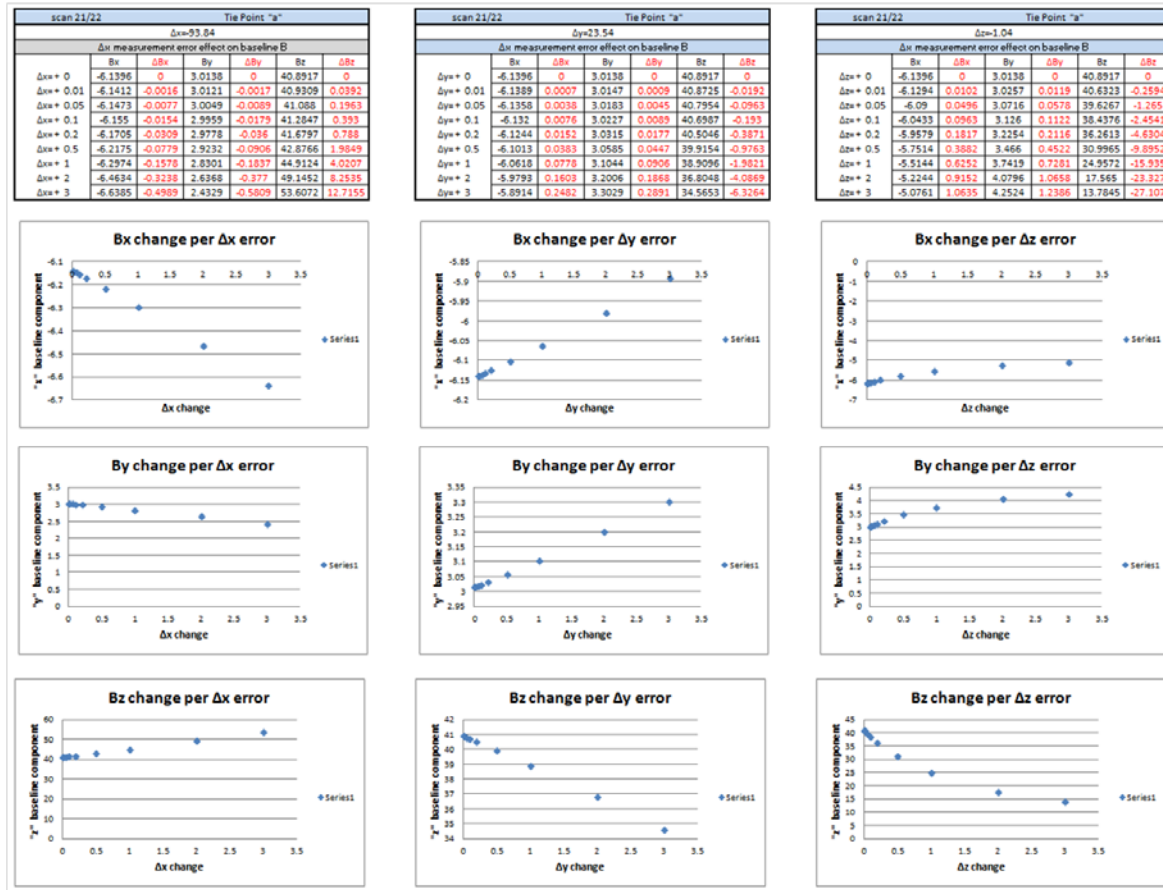


Figure 113. This figure demonstrates the change that the input values of the Δx , y , and z elements into the baseline calculation system of equations has on the length of the calculated baseline.

THIS PAGE INTENTIONALLY LEFT BLANK

APPENDIX C. CALCULATED SNOW DEPTH

Calculated Snow depth (cm)							
	Manual	01/02	01/03	01/04	02/03	02/04	03/04
1	175	220	339	206	626	-13	156
2	164	168	270	125	428	-28	112
3	164	169	259	131	349	-6	120
4	130	144	224	86	235	-16	112
5	184	196	361	135	634	-13	131
6	183	177	327	97	527	20	126
7	164	183	308	119	463	47	149
8	239	210	331	115	431	111	172
9	209	198	353	215	620	161	164
10	180	160	268	195	488	185	137
11	166	138	224	170	330	195	133
12	154	120	203	98	188	151	111
13	169	149	242	88	171	117	86
14	135	110	176	69	43	142	109
15	136	108	167	18	-19	117	100
16	130	104	150	30	-21	127	97
Off grid snow depths (trees present)							
17...18	126	216	202	79	78	157	163
18...19	133	167	195	96	165	0.89	169
19...20	138	115	208	59	312	-29	163
20...21	133	87	152	146	313	173	134
21...22	162	109	149	109	43	167	139

Table 15. Calculated snow depth for each location for each of the six SAR image pairs for Best Fit Plane Removed Method.

THIS PAGE INTENTIONALLY LEFT BLANK

APPENDIX D. SNOW DEPTH ERROR

Error in Snow Depth Calculated (cm)						
	01/02	01/03	01/04	02/03	02/04	03/04
1	45	164	31	451	-188	-19
2	4	106	-39	264	-192	-52
3	5	95	-33	185	-170	-44
4	14	94	-44	105	-146	-18
5	12	177	-49	450	-197	-53
6	-6	144	-86	344	-163	-57
7	19	144	-45	299	-117	-15
8	-29	92	-124	192	-128	-67
9	-11	144	6	411	-48	-45
10	-20	88	15	308	5	-43
11	-28	58	4	164	29	-33
12	-34	49	-56	34	-3	-43
13	-20	73	-81	2	-52	-83
14	-25	41	-66	-92	7	-26
15	-28	31	-118	-155	-19	-36
16	-26	20	-100	-151	-3	-33
Average Grid	-8.00	95.00	-49.06	175.69	-86.56	-41.69
Off grid snow depths (trees present)						
17...18	90	76	-47	-48	31	37
18...19	34	62	-37	32	-132.11	36
19...20	-23	70	-79	174	-167	25
20...21	-46	19	13	180	40	1
21...22	-53	-13	-53	-119	5	-23
Average all	-6.00	82.57	-47.05	144.29	-76.58	-28.14

Table 16. Calculated error in the snow depth for each location for each of the six SAR image pairs for the Best Fit Plane Removed method.

THIS PAGE INTENTIONALLY LEFT BLANK

LIST OF REFERENCES

- Air Force Weather Agency, 2012: AFWA Algorithm Description Document (ADD) for the Air Force Weather Agency (AFWA) Snow Depth Analysis Model (SNODEP).
- Air Force Weather Agency, 2012: AFWA Fact Sheet on Snow Depth and Sea Ice Analysis Model, [Available online at https://weather.afwa.af.mil/static/about_info/about_snow.html.].
- American Avalanche Association, 2004: Snow, Weather, and Avalanches: Observational Guidelines for Avalanche Programs in the United States. 3–22.
- Carrara, W. G., Goodman, R.S., Majewski R. M., 1995: *Spotlight Synthetic Aperture Radar Signal Processing Algorithms*. 1st ed. Artech House, 554 pp.
- Google Earth, “California.” Map. *Google Maps*. Web. Jun 2012: [Available online at <http://www.google.com/earth/index.html>.]
- Foster, J. L. et al., 2011: A blended global snow product using visible, passive microwave and scatterometer satellite data, *International Journal of Remote Sensing*, **32**, 1371–1395
- Granite Island Group, Cross Section (RCS), cited July 2013: [Available online at <http://www.tscm.com/rcc.pdf>.]
- Goldstein R. M., Zebker H. A., and Werner C. L., 1988: Satellite radar interferometry: Two-dimensional phase unwrapping. *Radio Science*, **4**, 713–720.
- GPS.gov, cited April 2012: GPS Accuracy. [Available online at <http://www.gps.gov/systems/gps/performance/accuracy/>]
- General Atomics Aeronautical, Sensor Systems, Lynx Multi-mode Radar, cited Dec 2012: [Available online at http://www.ga-asi.com/products/sensor_systems/lynxsar.php.]
- Groisman, P. Y., Karl, T. R., Knight, R. W. 1994: Changes of Snow Cover, Temperature, and Heat Balance over the Northern Hemisphere, *Journal of Climate*, **7** 1633–1656.
- Hodgson, M. E., Jensen, J., Raber, G., Tullis, J., Davis, B. A., Thompson, G., Schuckman, K., 2005: An Evaluation of Lidar-derived Elevation and Terrain Slope in Leaf-Off Conditions. *Photogrammetric Engineering & Remote Sensing*, **71**, 817–823.

- Hopkinson, C., Sitar, M., Chasmer, L., and Treitz, P., 2004: Mapping Snowpack Depth beneath Forest Canopies Using Airborne LiDAR. *Photogrammetric Engineering & Remote Sensing*, **70**, 323–330.
- Jakowatz, C.V., Wahl, D. E., Eichel, P. H., Ghiglia, D. C., and Thompson, P. A., 1996: *Spotlight-Mode synthetic Aperture Radar: A signal Processing Approach*. Kluwer Academic Publishers Norwell, MA, USA, 429 pp.
- Jet Propulsion Laboratory, SIR-C/X-SAR Flight Statistics, cited Aug 2012: [Available online at http://southport.jpl.nasa.gov/sir-c/getting_data/missions_stats.html.]
- Jet Propulsion Laboratory, What is SIR-C/X-SAR, cited Aug 2012: [Available online at <http://southport.jpl.nasa.gov/desc/SIRCdesc.html>.]
- Marshall, H-P., Koh, G., and Foster, R. R., 2005: Estimating alpine snowpack properties using FMCW radar. *Annals of Glaciology*, **40**, Issue 1, 157–162.
- Marshall, H. P., Birkeland, K., Elder, K., and Meiners, T., 2008: Helicopter-Based Microwave Radar Measurements in Alpine Terrain. *Proc. of the 2008 Int. Snow Science Workshop*, Whistler, British Columbia, Canada, Telus Whistler Conference Center
- Mathematics-Online lexicon, Rotation of a Cartesian Coordinate System, cited July 2013: [Available online at <http://www.mathematics-online.org/inhalt/aussage/aussage444/>.]
- MathWorks, MATLAB and Simulink for Technical Computing, cited July 2013: [Available online at <http://www.mathworks.com/index.html>.]
- MathWorks, Image Processing Toolbox, cited July 2013: [Available online at <http://www.mathworks.com/products/image/>.]
- MathWorks, Fitting an Orthogonal Regression Using Principal Components Analysis, cited July 2013: [Available online at <http://www.mathworks.com/help/stats/examples/fitting-an-orthogonal-regression-using-principal-components-analysis.html>.]
- MathWorks, GoldsteinUnwrap2D_r1, cited July 2013: [Available online at <http://www.mathworks.com/matlabcentral/fileexchange/29497-goldsteinunwrap2dr1>.] Smith, Carey.
- Northrop Grumman, 2010: Algorithm and Data User Manual (ADUM) for the Special Sensor Microwave Imager/Sounder (SSMIS), Report-12621F CAGE/Facility Ident: 70143, 77 pp.
- Osterhuber, R., Howle, J., and Bawden, G., 2008: Snow Measurement Using Ground-Based Tripod LiDAR. *Western Snow Conference 2008*. Hood River, OR.

- Richards, J. A., 2009: *Remote sensing with Imaging Radar*. 1st ed. Springer-Verlag, 361 pp.
- Richards, M., 2007: A Beginner's Guide to Interferometric SAR Concepts and Signal Processing. *IEEE A&E Systems Magazine*, Vol. NO. 9, 5–11.
- Rosen, P., 2009: InSAR Principles and Theory. *UNAVCO Short Course Series- InSAR: An introduction to Processing and Applications for Geoscientists*, Boulder, Colorado, [Available on line at <http://cws.unavco.org:8080/cws/learn/uscs/2009/2009insar/.>]
- Schweizer, J. and Kronholm, K., 2006: Snow cover spatial variability at multiple scales: Characteristics of a layer of buried surface hoar. *Cold Regions Science and Technology*, **47**, 207–223.
- Shi, J. and Dozier J., 1996: Estimation of Snow Water Equivalence Using SIR-C/X-SAR. In *IEEE, International Geoscience and Remote Sensing Symposium, Remote Sensing for a Sustainable Future*, **4**, 2002–2004.
- Shi, J. and Dozier J., 2000: Estimation of Snow Water Equivalence Using SIR-C/X-SAR, Part I: Inferring Snow Density and Subsurface Properties. *IEEE Transactions on Geoscience and Remote Sensing*, **38**, 2465–2474.
- Shi, J. and Dozier J., 2000: Estimation of Snow Water Equivalence Using SIR-C/X-SAR, Part II: Inferring Snow Depth and Particle Size. *IEEE Transactions on Geoscience and Remote Sensing*, **38**, 2475–2488.
- Shurong, P., Kexue, H., Yaonan, W., Juan, L., Jiwei, D., and Haixia, X., 2009: A High Accurate Approach for InSAR Flat Earth Effect Removal: *IEEE 2009, International Conference on Measuring Technology and Mechatronics Automation (ICMTMA '09)*, v.3, p. 742-745.
- Stofan, E.R, et al., 1995: Overview of Results of Spacebourne Imaging Radar-C, X-Band Synthetic Aperture Radar (Sir-C/X-SAR). *IEEE Transactions on Geoscience and Remote Sensing*, **33**, 817–828.
- Trimble, GeoExplorer 6000 Series Handhelds, cited July 2013: [Available online at <http://www.trimble.com/mappingGIS/geo6.aspx?dtID=applications&.>]
- Tsunoda, S. I., Pace, F., Stence, J., Woodring, M., Hensely, W. H., Doerry, A. W., and Walker, B.C., 1999: Lynx: A high-resolution synthetic aperture radar. *SPIE Aeroense*, **3704**, 1–8.
- Ulaby, F. T., Moore, R. K., Fung, A. K., 1982: *Microwave Remote Sensing Active and Passive Volume II Radar Remote Sensing and Surface Scattering and Emission Theory*. Addison-Wesley Publishing Company, Inc., 850 pp.

United States Department of Agriculture, Geospatial Data Gateway, cited July 2013:
[Available online at <http://datagateway.nrcs.usda.gov/GDGOrder.aspx>.]

Yankielum, N., Rosenthal, W., and Davis, R.E., 2004:Alpine snow depth measurements from aerial FMCW radar. *Cold Regions Science and Technology*, **40**, 123–134.

INITIAL DISTRIBUTION LIST

1. Defense Technical Information Center
Ft. Belvoir, Virginia
2. Dudley Knox Library
Naval Postgraduate School
Monterey, California